HOKKAIDO UNIVERSITY

Title	Solar Energy Mediated Methane Conversion over Nanometals/Semiconductors Catalysts
Author(s)	,
Citation	. ( ) 13806
Issue Date	2019-09-25
DOI	10.14943/doctoral.k13806
Doc URL	http://hdl.handle.net/2115/79298
Type	theses (doctoral)
File Information	Hui_Song.pdf

Instructions for use

Solar Energy Mediated Methane Conversion over Nanometals/Semiconductors Catalysts

(太陽光エネルギーを利用したナノ金属/半導体触媒によるメタン転換反応に関する研究)

Hui Song

Graduate School of Chemical Sciences and Engineering

Hokkaido University

2019

Contents

Contents

Chapter 5 Direct photocatalytic oxidation of methane to liquid oxygenates with molecular oxygen over nanometals/ZnO catalysts 109

Abstract

Methane, the predominant component in natural gas, is not only a clean fuel among fossil fuels but also an important chemical source. The conversion of methane to higher-value chemicals is a promising technology in the supply of chemicals and energy. The current commercial methane conversion technology suffers substantially from intense energy consumption. It is highly desirable to develop novel technologies for methane conversion with improved efficiency and lower cost. Solar energy, the most abundant and clean renewable energy, has been utilized as a new stimulus to drive methane activation and conversion under mild conditions. However, the efficiency of methane conversion mediated by solar energy are still low and direct photocatalytic conversion of methane with molecular oxygen to liquid oxygenates remains a key challenge. Thus, this thesis focused on rational design of plasmonic nanometals-based catalysts for photo-enhanced thermocatalytic methane conversion at mild temperatures by coupling solar energy and thermal energy as well as design of nanometals cocatalysts/semiconductors for photocatalytic oxidation of methane to liquid oxygenates with oxygen at room temperature.

In chapter 1, a general background of methane conversion and the fundamentals of photo-activation of methane is introduced. Then, the recent development of methane conversion driven or promoted by solar energy are summarized.

In chapter 2, coupling of solar energy and thermal energy for steam methane reforming (SMR) was investigated over Rh/TiO_2 catalysts, in order to improve the efficiency of methane conversion under mild conditions. It was found that visible light illuminated TiO_2 supported Rh nanoparticles could enhance methane activation and conversion in SMR at mild operating temperatures (below 300 °C), with a ~50% decrease in apparent activation energy compared to that of pure thermal process. Characterization results show an ultrafast separation of hot carriers excited from Rh at the $Rh-TiO_2$ interface, resulting in the formation of electron-deficient state of $Rh^{\delta+}$ at surface for the successive CH_4 activation at low temperatures.

In chapter 3, bimetal plasmonic catalysts consisting of Pt and Au nanoparticles were developed for carbon dioxide reforming of methane (CRM) with UV-vis light illumination at mild temperatures

to efficiently convert methane and carbon dioxide into valuable chemicals (H_2 and CO). Due to the effective plasmonic coupling effect of Pt and Au nanoparticles, the activation energies for CH_4 conversion are reduced ~30% below thermal activation energies and the reaction rate is 2.3 times higher than that of the thermal-catalytic reaction rate at 400 °C. Experimental and theoretical results reveal that effective coupling plasmonic effect generates strong local electric fields and excite hot carriers to activate the reactants and intermediate species, reduce the activation energies and accelerate the reaction rate.

In chapter 4, TaN was employed as an optical support to replace noble Au plasmonic promoter and to investigate the activities of its supported Pt and other group VIII metal catalysts in CRM at reaction temperature of 500 °C with visible light assistance. Experimental results show that the activities of TaN supported group VIII metal-based catalysts were enhanced with visible light irradiation, and the activity enhancement ratios (2.3-2.7 times) were higher than that achieved by adopting expensive Au as plasmonic promoter (1.6 times). Theoretical results reveal that polarity of TaN is regarded to facilitate electron-hole separation and ultimately be responsible for the activity enhancement.

In chapter 5, to convert methane to liquid chemicals without any additional thermal energy input, photocatalytic oxidation of methane to methanol and formaldehyde with molecular oxygen was achieved over ZnO loaded with cocatalysts (Pt, Pd, Au or Ag) catalysts in pure water at room temperature. The activity for production of total liquid oxygenates including methyl hydroperoxide, methanol and formaldehyde on 0.1 wt% Au/ZnO reached approximately 12,545 micromoles per gram catalyst per hour ($\mu mol\ g^{-1}\ h^{-1}$), with 95% selectivity. Experiments with isotopically labeled oxygen and water reveal that molecular oxygen, rather than water, was the oxygen source of methanol formed. Experimental and theoretical results demonstrate that the photocatalytic oxidation of methane to liquid oxygenates is a radical process where surface active oxygen (hole center, O^-) of photo-excited ZnO plays the dominated role for the methane activation to methyl radicals, a rate-limiting step for methane oxidation, with selectivity for methanol controlled by co-catalysts.

In chapter 6, in order to improve the selectivity of methanol in photocatalytic oxidation of methane with molecular oxygen, TiO_2 loaded with different amounts of Pt, Pd, Au and Ag nanoparticles were investigated. It was found that the loading amount of cocatalysts played an

important role for the production of methanol; both the yield and selectivity of methanol increased gradually with increasing the loading amount. In addition, reducing the concentration of $^{\bullet}$OH radicals generated in the reaction solution via the formation of electron-deficient state of $Au^{\delta+}$ on the surface of TiO_2 could inhibit the over-oxidation of methanol to formaldehyde and carbon dioxide. The activity for production of the primary products (methyl hydroperoxide and methanol) on the optimized photocatalysts amounts to 2,845 µmol g^{-1} h^{-1}, with approximately 73% selectivity.

In chapter 7, an overall summary of this dissertation work was provided. This thesis carried out a systematic study on solar energy mediated methane conversion over nanometals/semiconductors photocatalysts, including photo-enhanced thermocatalytic SMR and CRM at low temperatures, and partial oxidation of methane with oxygen to liquid oxygenates at room temperature. Photo-thermocatalytic methane converieson shows high reaction rates and low activation energies in comparison with conventional thermocatalysis; hot carriers generated from plasmonic nanometals enable the activation of methane, leading to an enhanced activity and reduced activation energy. In room temperature photocatalytic methane conversion, methane is mainly activated by surface active oxygen of photoexcited wide bandgap oxide semiconductors, and reducing the concentration of $^{\bullet}$OH in reaction solution contributes to inhibit deep-oxidation of liquid oxygenates to carbon dioxide. This study opens a promising pathway towards efficient C-H bond activation chemistry by the construction of active and energy-efficient nanometals/semiconductors catalysts.

Chapter 1 Introduction

1.1 General background of methane conversion

Methane, the predominant component in natural gas and biogas, has received increasing attention as an alternative and promising resource for chemical commodities production as worldwide consumption of crude oil resources increases. In particular, large amounts of shale gas, methane hydrate and coalbed methane reserves have recently been discovered, providing the opportunity to reduce reliance on crude oil.[1] According to U.S. Energy Information Administration, world natural gas consumption would increase by 43% from 2015 to 2040 (Figure 1.1).[2] However, since the locations of methane extraction sites are mainly in remote areas, methane gas must be transported over long distances. It is inconvenient to liquefy methane gas for transportation since the boiling point of methane is as low as 109 K under atmospheric pressure.[3] Therefore, technologies for transforming methane on-site and on a large-scale are in high demand.
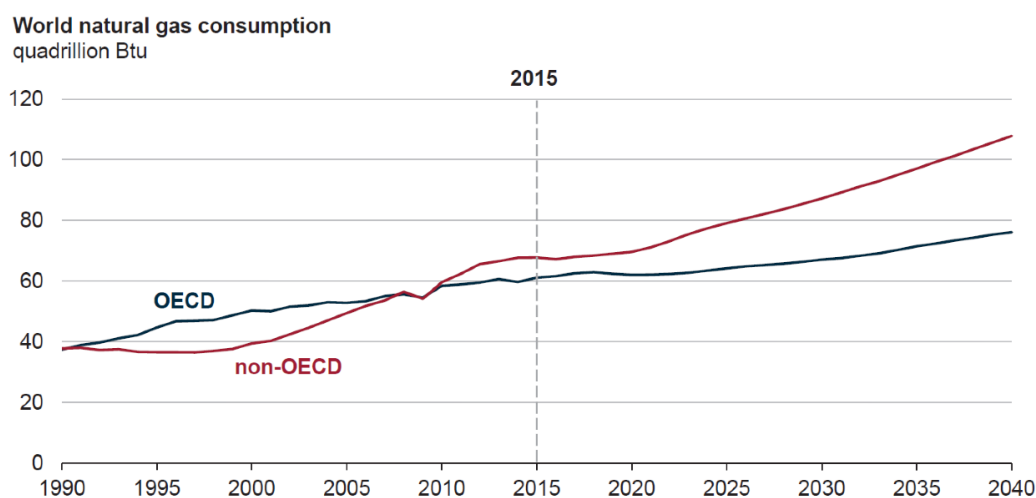
Figure 1.1 World natural gas consumption in quadrillion (10^{15}) Btu with history data during 1990-2015 and projected data during 2015-2040.[2]

Methane is a very stable and inert molecule due to its unique molecular configuration.[4] The symmetrical tetrahedral structure with four equal C–H bonds endows methane with low electron and proton affinity (-1.9 eV),[5] weak acidity and low polarizability (2.8×10^{-40} C^2 m^2 J^{-1}).[6] The strength of the C-H bonds in methane is high, with the first dissociation energy at 439 kJ mol^{-1}.[7] Methane also demonstrates a high ionization energy (12.6 eV),[8] implying that it is difficult to remove even the most

4

loosely bound electron of methane. The energy level of the highest occupied molecular orbital (HOMO) is low and that of the lowest unoccupied molecular orbital (LUMO) is high, which makes it difficult to remove electrons from the HOMO for oxidation or to donate electrons to the LUMO for reduction. All of these structural properties indicate that reactions involving proton or electron transfer are unfavourable for methane. High temperatures are usually required to activate the C-H bonds, which always results in the occurrence of radical reactions with inherently low selectivity.[9,10] Both sufficient energy input and appropriate catalysts are necessary for methane conversion reactions. In the last decade, various innovative means using the design of novel catalytic systems have been developed for driving methane conversion under mild conditions, which is considered the "Holy Grail" in the chemical community.[1,11]

There are two main routes for transforming methane into valuable fuels and chemicals.[11] One is the indirect conversion route, or synthesis gas (syngas, H_2/CO) route, which is the current commercial route for large-scale transformation of methane.[12] This route converts methane into syngas through steam reforming of methane (SRM) and utilizes the obtained syngas in downstream processes such as Fischer-Tropsch synthesis or methanol synthesis.[13-16] The other is the direct conversion route, in which methane is converted directly into liquid oxygenates or higher hydrocarbons.[17-22] The representative direct conversion process is partial oxidation of methane (POM) to methanol.[23-29] The indirect route is the industrialized route for methane conversion and is economically competitive on large scales, but it is an energy-intensive process because high operating temperatures (700 - 1100 °C) are required to drive the endothermic SRM reaction.[30-33] Low-temperature direct oxidation of methane to methanol is a promising process because it can be operated at much lower temperatures, reducing thermal energy input and capital costs that are required in the indirect steam reforming step. However, the oxygenated products such as methanol and formaldehyde are more reactive than methane and can be easily over-oxidized into undesired CO_2,[34-36] leading to low yield and poor selectivity of oxygenates. Inhibiting the propensity for over-oxidation remains a great challenge for direct methane conversion to valuable products. Therefore, innovative catalysts and reaction systems should be developed to reduce the reaction temperature of methane conversion.

To date, many technologies have been employed to convert methane at low temperature, including thermocatalysis,[37-41] photocatalysis,[42-45] electrochemical catalysis,[46,47] biocatalysis based

on enzymes,[48] plasma and other technologies.[49-51] For example, in the early 1970s, the thermocatalytic oxidation of methane to methanol with the use of an oxidant (K_2PtCl_6) at lower temperature (120 °C) was first reported by Shilov et al.[52] The activation and functionalization of C-H bonds over complexes of transition metals such as Pt, Pd, Rh, Ru and Ir under mild conditions were further developed by Bercaw[53] and Bergman.[54] To solve the issues of low activity and stability of catalysts in the Shilov system, Periana et al. developed a catalyst of Pt complexes ((2,2'-bipyrimidine)$PtCl_2$) that transformed methane to methyl bisulfate in the presence of concentrated sulfuric acid with nearly 81% selectivity and 90% methane conversion at 220 °C.[19] Among these various technologies, photocatalysis based on plasmonic metal nanostructures and/or semiconductors photocatalysts has emerged as a promising approach to drive methane conversion under mild conditions.[55-60]

1.2 The fundamentals of photo-activation of methane

The dissociation of the first C-H bond in methane is considered to be the rate-limiting step for the activation of methane.[27] Under pure thermal conditions, a temperature of at least hundreds of degrees Celsius is normally needed to overcome the high activation barriers and break the first C-H bond due to the high dissociation energy of the C-H bond and its non-polar character. Exploring low- or room-temperature methane activation approaches is a potential approach to lower the requirement of operating temperatures, i.e., reducing thermal energy input, and avoid deactivation caused by coke formation and catalyst sintering in high operating temperature reactions.

1.2.1 Photothermal methane activation

As the most studied and most commonly used catalysts, metals have intrinsic properties for selectively and efficiently catalysing various chemical reactions, such as organic transformations, oxidation, hydrogenation and dehydrogenation.[61] More importantly, many metal nanostructures (such as those of Cu, Ag, Au, Rh and Pt) show strong and tunable light absorption properties via the well-known localized surface plasmon resonance (LSPR).[62] LSPR is visualized as the resonant oscillation of the surface conduction charge carriers in the conductive nanostructures stimulated by incident light. The intensity and resonant wavelength of LSPR over metal nanostructures could be finely tuned by modifying the size and shape of the nanostructures. Plasmonic metal nanoparticles are generally used as catalytically active sites and/or light absorber materials in photo-thermocatalytic reactions, where

some conventional thermocatalytic reactions can proceed without heat energy input or at lower reaction temperatures, leading to reduced energy consumption, extended catalyst stability and lower activation energy.[63-65]

a

Indirect hot carrier transfer

b

Direct hot carrier transfer
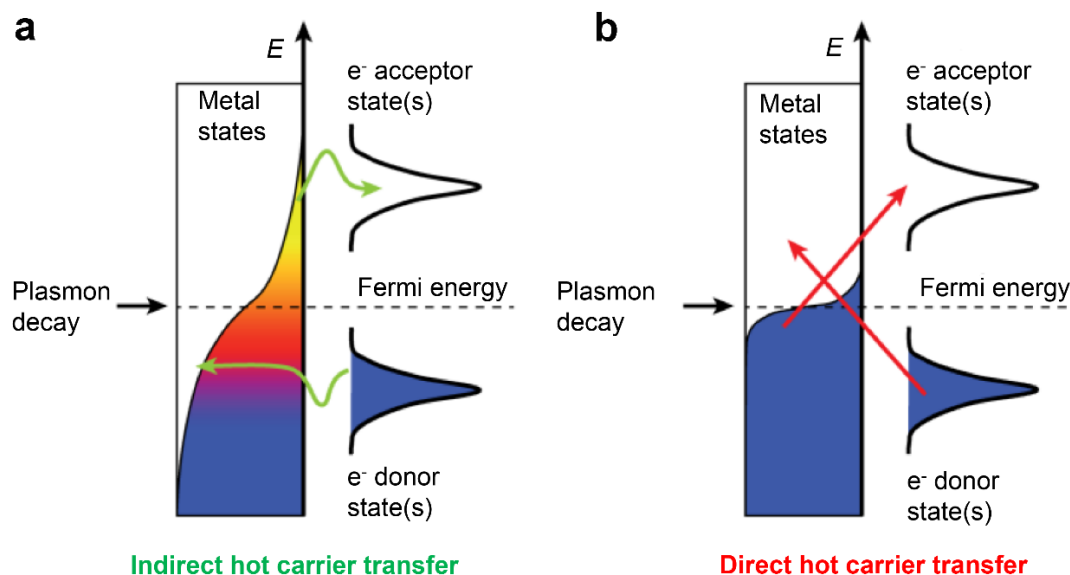
Figure 1.2 Schematic illustrations of the two main mechanisms for the transfer of hot carriers to adsorbate states. (A) Indirect hot carrier transfer mechanism. Plasmon decay first generates hot carriers in the metal that then transfer to adsorbate states at the metal/adsorbate interface.[68] (B) Direct hot carrier transfer mechanism. Plasmon decay enables the direct excitation of hot carriers to the adsorbate states through interfacial electronic transitions.[68] The arrow directions represent the direct charge carrier transfer processes, i.e., the direct charge transfer between the plasmonic nanoparticles and the adsorbates.

On the other hand, plasmon excitation provides an alternative approach for facilitating the activation of methane on metal nanostructures. The excitation of surface plasmons leads to the formation of energetic charge carriers (hot carriers) in the metal.[66-68] Then, the hot carriers can be injected from the surface of the metal to the accessible orbitals of the adsorbates (Figure 1.2a). Alternatively, the interactions between nanometals and absorbates lead to the formation of hybridized electronic states at the interface. Photo-excitation of these interfacial hybridized states leads to direct charge transfer between adsorbates and nanometals and realizes reactant activation (Figure 1.2b). Compared to the indirect hot carrier transfer mechanism, this direct interfacial charge carrier transfer avoids the generation of hot carriers in the nanometals. Plasmon excitation also leads to the production of enhanced electric fields within metal nanoparticles with maximum field intensities at

the surface.[63,69] Polarizing methane by local electric fields will change the charge distribution and molecular structure of CH_4 to alter the absorption and activation of CH_4.[1,70] Photo-induced charge transfer and elevated electric fields contribute to methane activation over plasmonic metal nanoparticles in photothermal methane conversion.

1.2.2 Photocatalytic methane activation

In thermocatalytic methane conversion, high temperatures are required to trigger reaction in the gaseous phase (Figure 1.3a, orange reaction pathway). Different from thermocatalysis or photo-thermocatalysis, in photocatalysis, the active intermediates are readily generated upon the excitation of photons with the energy of several eV, and C-H bond cleavage can be then initiated by the active intermediates at a much lower temperature with a markedly decreased energy barrier (Figure 1.3b, green reaction pathway). By employing appropriate photocatalysts with efficient active sites, high-temperature methane conversion reactions that are thermodynamically unfavourable can be carried out feasibly with solar energy mediation.

Under solar light irradiation, a flux of photons with energy equivalent to or exceeding the bandgap (E_g) of the semiconductor can be absorbed, resulting in the excitation of an electron from the valence band (VB) to the conduction band (CB), which then forms a vacancy regarded as a hole.[71-74] The high-energy electrons and holes can diffuse towards the interface between the semiconductor and reacting environment to drive redox reactions. To drive methane conversion, oxide semiconductors are widely used. The VB of oxide semiconductors is composed of O2p orbitals, which generally show much positive potential (ca. +3 V vs. SHE) and can ensure strong oxidation capability upon a photoexcitation process to produce reactive oxygen species, such as surface reactive oxygen species (O^-, photogenerated holes) or hydroxyl radicals ($^\bullet OH$ from water photooxidation) (Figure 1.3b).[44,75] These species are highly electrophilic for abstracting the H atom from the C-H bond of methane at room temperature (Equations 1 and 2). In addition, it has been reported that coordination complexes of transition metals can produce alkoxyl radicals ($^\bullet OR$) via photoinduced ligand-to-metal charge transfer (LMCT) in a homogeneous system.[45] Methane activation is realized by alkoxyl radicals through hydrogen atom transfer (HAT) catalysis to produce methyl radicals (Equation 3). Generally, Equations 1-3 proceed rapidly due to their highly exothermic nature. Since the activation barriers of hydrogen abstraction processes are quite low, these processes are thermodynamically

controllable. Taking a hydroxyl radical as an example, the homolytic cleavage of methane's C-H bond by a hydroxyl radical is a highly exothermic (ΔH = -60 kJ mol^{-1}) reaction and takes place with an activation energy of 15 kJ mol^{-1} to produce water and a methyl radical.[76] Therefore, the generation of an electrophilic reactive oxygen species is crucial for methane activation in photocatalysis.

$$CH_4 + M^{(n-1)+}\text{-}O^- \rightarrow {}^{\bullet}CH_3 + M^{(n-1)+}\text{-}OH \qquad (1)$$

$$CH_4 + {}^{\bullet}OH \rightarrow {}^{\bullet}CH_3 + H_2O \qquad (2)$$

$$CH_4 + {}^{\bullet}OR \rightarrow {}^{\bullet}CH_3 + HOR \qquad (3)$$
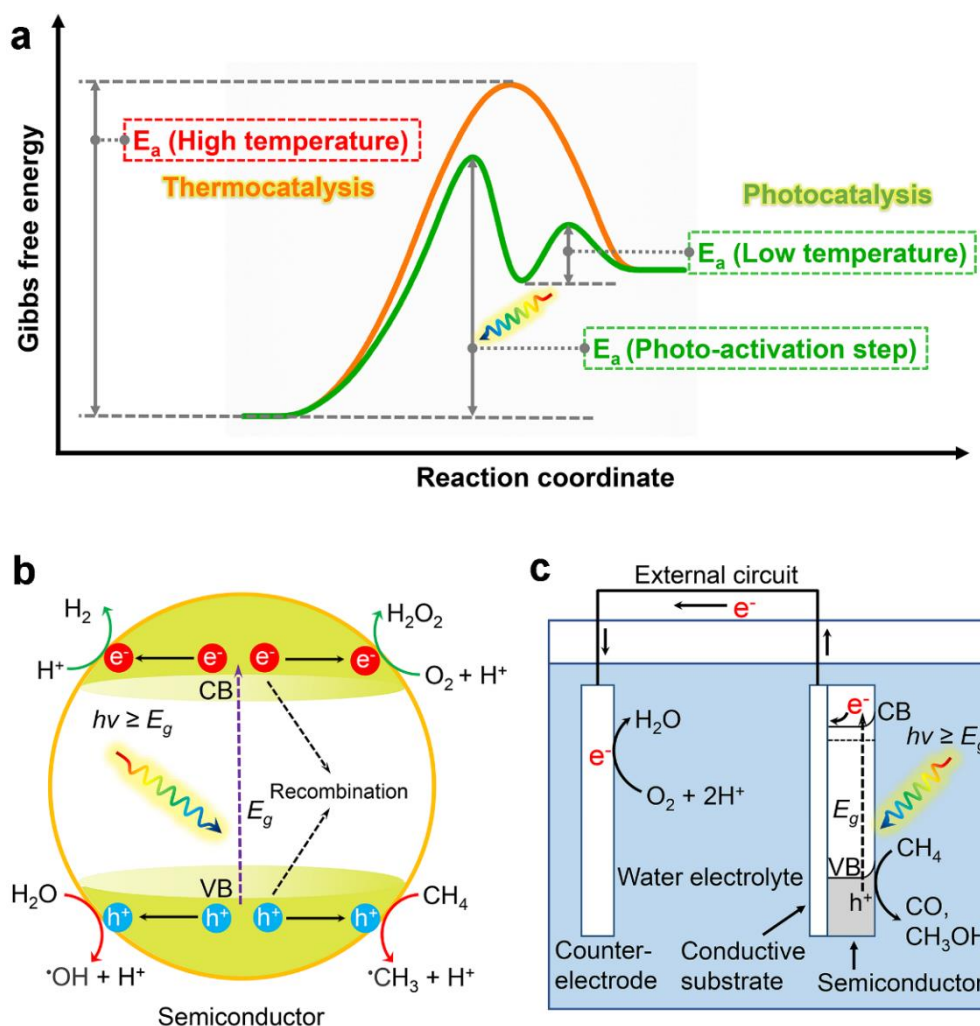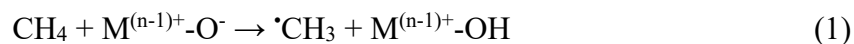
Figure 1.3 Photocatalytic and photoelectrochemical methane activation. (a) The kinetic progress of methane activation in thermocatalysis and photocatalysis pathways. Figure 1.3a only exhibits the process of rate-limiting steps of methane activation instead of the complete steps involved in methane conversion. (b) Methane activation over semiconductor-based photocatalysts. (c) Photoelectrochemical cell design for methane conversion.

In addition, reactive oxygen species, such as $^{\bullet}$OH, also have the ability to further oxidize the products. Thus, controlling the availability of oxidative species (photo-generated holes in the VB or $^{\bullet}$OH in aqueous solution) is important for improving selectivity towards desired products.

According to the reactive environments and the type of photocatalysts, the produced methyl radicals can self-couple to produce ethane and hydrogen via non-oxidative coupling of methane (NOCM) or further react with oxygen, water and carbon dioxide to generate methanol, hydrogen and carbon monoxide via partial oxidation of methane (POM), steam reforming of methane (SRM) and dry reforming of methane (DRM).

1.2.3. Photoelectrocatalytic methane activation

Photoelectrochemical cells, combining the advantages of photocatalysis and electrocatalysis, provide another alternative route for methane activation. In these systems, an n-type semiconductor deposited on a conductive substrate is employed as a photoanode, and an external circuit achieves a current loop between two electrodes and an aqueous electrolyte. As shown in Figure 1.3c, upon light illumination, charge carriers are excited in the semiconductor and are further separated by the space charge layer formed at the interface of the semiconductor and electrolyte. Electrons transfer to the counter electrode, where they take part in the reduction reaction, whereas the holes move to the semiconductor/electrolyte interface, where they perform oxidation.

Under electrolytic conditions, the photoexcited charge transfer reactions could be accelerated, and the reaction intermediate species on the surface of the catalyst may be potentially stabilized, thus affecting the selectivity towards the products.[77] The design of a photoelectrode can simultaneously couple solar and electrical energy to break the high barrier of C-H bond activation and overcome the disadvantages of photocatalysis and electrocatalysis, i.e., only photoexcitation cannot obtain the effective oxidation potential and only electricity cannot produce the catalytically active sites. Therefore, photoelectrochemical cells are meaningful for methane activation and conversion.

1.3 Previous research on solar energy mediated methane conversion

In recent years, more and more work emerges in methane conversion promoted or driven by solar energy. In this part, I highlight the recent achievements on solar energy mediated catalytic

methane conversion. I focus on methane conversion in photoenhanced thermocatalytic systems, photocatalytic systems, photoelectrochemical systems.

1.3.1 Photo-enhanced thermocatalytic conversion of methane

Recently, photo-thermocatalysis over nanometals has received much attention. Photo-thermocatalysis can simultaneously couple solar energy and thermal energy to efficiently promote catalytic reactions to achieve high catalytic performance at mild operating temperatures. Metal nanostructures generally have a broad light absorption region for effective utilization efficiency of solar light. It is generally acknowledged that photoexcitation on nanometals influences the rate-limiting steps of reaction, and heating plays a role in facilitating the dissociation and desorption of intermediate species.[64] Thus, photo-thermocatalysis generally shows higher reaction rates than photocatalytic reactions and reduced reaction temperatures in comparison with conventional thermocatalysis.
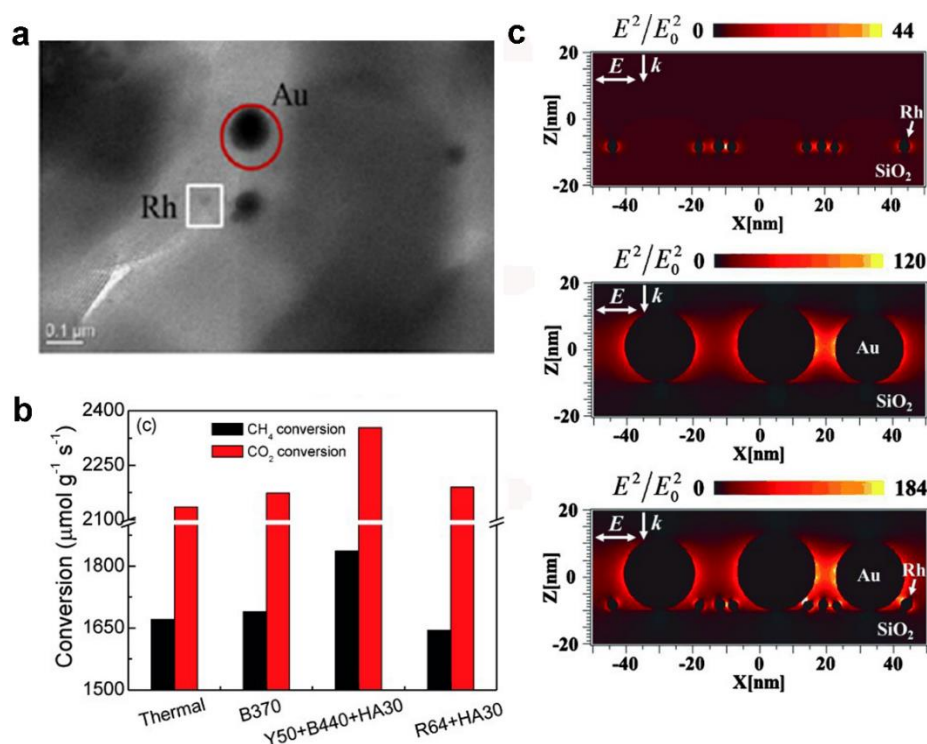
Figure 1.4 Photo-enhanced DRM over bimetallic catalysts. (a) TEM image of Rh-Au/SBA-15 catalyst.[55] (b) CH_4 and CO_2 conversion rate in DRM on Rh-Au/SBA-15 with different wavelength light illumination.[55] (c) FDTD simulation results of electromagnetic field distribution on Rh or/and Au loaded SiO_2 catalysts under a light illumination of 530 nm.[55]
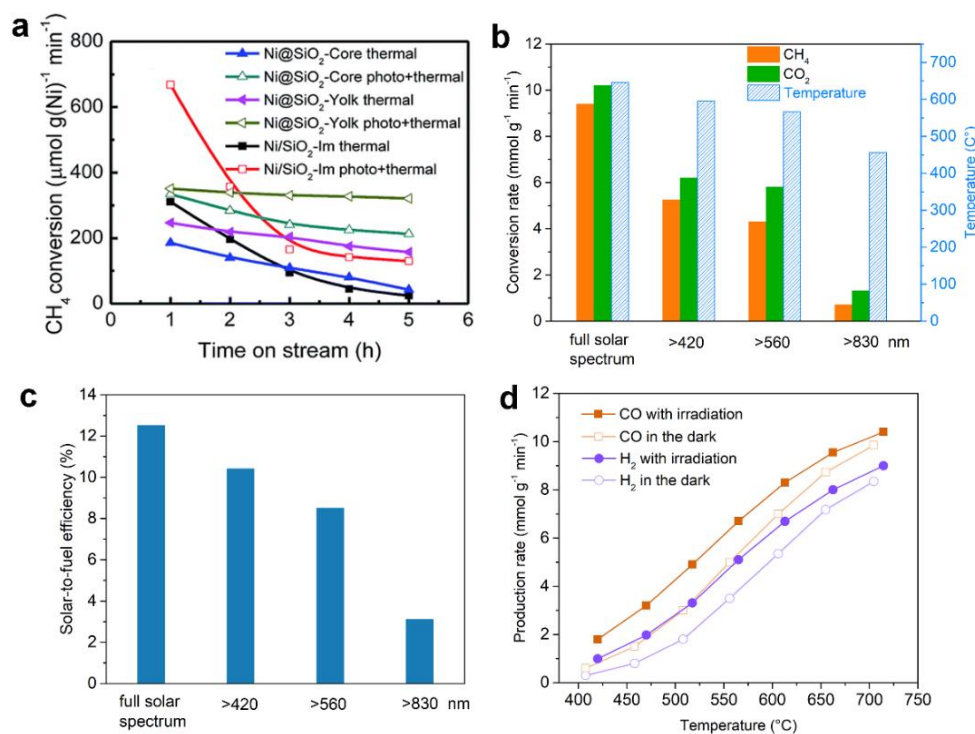
Figure 1.5 Photo-enhanced DRM over Ni-based catalysts. (a) CH_4 conversion on different structured $Ni@SiO_2$ catalysts in DRM under light irradiation and in the dark condition.[80] (b) CH_4 and CO_2 conversion rate and equilibrium temperature and (c) solar-to-fuel efficiency of SiO_2 modified Ni catalyst under different wavelength light irradiation from the xenon lamp.[81] (d) The catalytic performance of the SiO_2 modified Ni catalyst in DRM at different temperatures under light illumination and in the dark condition.[81]

For conventional thermal energy-driven DRM, high temperatures (700-1000 °C) are required to break the large reaction energy barrier related to the successive activation of CH_4 and CO_2 for the production of syngas.[55] To reduce the reaction temperatures, our group discovered that a dramatically visible light-enhanced methane conversion rate was observed over a Rh catalyst, a highly active catalyst towards DRM in thermocatalysis, when co-loaded with a visible light plasmonic Au nanoparticle promoter on SAB-15 at 500 °C (Figure 1.4a).[55] However, only the Rh catalyst exhibited no enhancement in activity under the same reaction conditions because its plasmonic resonant wavelength is primarily in the UV region. Control experiments showed that enhanced photoactivity was observed with 490-550 nm light irradiation, corresponding to the resonant wavelength of Au nanoparticles, as shown in Figure 1.4b. Finite-difference time-domain (FDTD) simulations revealed that when Au nanoparticles were loaded on a Rh/SAB-15 catalyst, the electric field was enhanced

approximately 4-fold and 1.5-fold compared to that of Rh/SAB-15 and Au/SAB-15, respectively, with 530 nm visible light irradiation as a result of the near-field coupling effect between Au and Rh nanoparticles (Figure 1.4c). The strong electric field over Rh-Au/SAB-15 provided a stronger ability to polarize and activate CH_4 and CO_2, resulting in enhanced methane conversion. In addition, our group further developed a PdAu alloy catalyst that showed long-term catalytic activity in DRM under visible light irradiation.[78] The electronic structure of the active Pd catalyst gradually became electronic deficient with increasing amounts of the plasmonic Au promoter; additionally, hot carriers induced from excitation of the plasmonic PdAu alloy could facilitate the activation of CH_4 and CO_2, both of which gave rise to enhanced catalytic activity and stability over the optimized $Pd_{90}Au_{10}$ alloy catalyst.

In addition to group IB metals, such as Au, as a plasmonic promoter for the DRM reaction, Ni, as a cheap metal, endows a strong LSPR band in the visible light region and exhibits light-enhanced catalytic activity in the DRM reaction.[79,80] In a representative experiment, the activity of a $10Ni/Al_2O_3$ catalyst under low-intensity (60 mW cm^{-2}) visible light irradiation was 1.3 times greater than that under dark conditions, with a quantum efficiency of 19.0% (Figure 1.5a).[80] The effect of the morphology of the Ni catalyst in the photo-enhanced DRM reaction was also investigated by constructing core-shell and yolk-shell $Ni@SiO_2$ catalysts. In addition to the promoted activity originating from the activation of CH_4 and CO_2 by plasmonic excited hot carriers, enhanced long-term stability over $Ni@SiO_2$-yolk and $Ni@SiO_2$-core catalysts was also observed under light irradiation due to the decrease in the amount of deposited active carbon species. A similar result was also achieved by Li et al.[81] The authors designed SiO_2-modified Ni nanocrystals that showed a highly efficient solar energy-driven DRM reaction process. Under the illumination of solar light (Figure 1.5b), a CH_4 conversion rate of 9.5 mmol g^{-1} min^{-1} was achieved under a GHSV (GHSV = the volumetric flow rate of the feedstock divided by the mass of the catalyst) of 293086 mL^{-1} g$_{cat}^{-1}$ h^{-1}, corresponding to a CH_4 conversion of 41%. The solar-to-fuel efficiency was estimated to be 12.5% (Figure 1.5c). The irradiation of the full solar spectrum of light enabled the excitation of the LSPR of the Ni nanocrystals and increased the temperature of the Ni nanocrystals (646 °C), which together led to a high DRM reaction rate (Figure 1.5d). The average temperature of the Ni nanocrystal catalyst was measured by a thermocouple, which was placed in close contact with the catalyst powder.

Additionally, a nanocomposite Ni/CeO_2 catalyst also had excellent catalytic activity and durability in DRM with UV-Vis-IR light illumination without any thermal energy input.[82]

1.3.2 Photocatalytic conversion of methane

Although methane conversion can be improved in photo-thermocatalytic systems at mild temperatures, external heating is still required to elevate reaction temperature. Photocatalysis or photoelectrochemical catalysis provides an approach to proceed methane conversion at room temperature.

1.3.2.1 Non-oxidative coupling of methane (NOCM)

NOCM is a promising way to directly transform methane into hydrogen and ethane. The change in Gibbs free energy is positive in NOCM (Equation 4), indicating that this thermodynamically unfavourable reaction has difficulty taking place at low temperatures. Recently, many studies have used solar energy-driven methane dehydrogenation to produce ethane and hydrogen over oxide photocatalysts, and these reactions have been reported at room temperature.[70,83-85]

$$2CH_4 \rightarrow C_2H_6 + H_2, \Delta G^0_{298K} = 68.6 \text{ kJ mol}^{-1} \qquad (4)$$
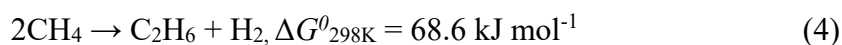
Yoshida et al. discovered that a variety of silica-supported highly dispersed oxides, such as SiO_2-Al_2O_3,[86] SiO_2-Al_2O_3-TiO_2,[87,88] Ce/SiO_2,[89-91] MgO/Al_2O_3,[92] Ga_2O_3/SiO_2[93] and ZrO_2/SiO_2[94,95], were capable of promoting NOCM to form C_2H_6 and H_2 with light irradiation at approximately room temperature, with C_2H_4 and C_3H_8 as minor products. The authors deduced that highly dispersed metal oxides, such as Ti oxide, were the reactive sites for photocatalytic NOCM. Photoexcitation occurred via electron transfer from oxygen to Ti, forming Ti^{3+}-O^- species.[56] The active oxygen species cleaved C-H bonds from methane at room temperature, and the coupling of formed methyl radicals produced C_2H_6 as the main product.

The catalytic performance of the above photocatalysts mainly depended on the transient photogenerated electron-hole pairs, which usually underwent severe recombination, resulting in low methane conversion (< 4% under UV light irradiation for 90 h). Deep UV light (λ < 270 nm) was also imperative in these reaction systems. The creation of univalent metal species has been developed to obtain high activity. For example, Chen et al. reported that Zn^+-modified zeolite achieved 24%

methane conversion with approximately 99% selectivity for C_2H_6 after irradiation with a high-pressure mercury lamp (Figure 1.6a).[85] Importantly, this photocatalyst also exhibited activity under visible light illumination. The authors proposed a two-stage catalytic process where the electrons were first excited from the zeolite to the 4s orbital of Zn^{2+} under UV light ($\lambda < 390$ nm) irradiation, forming (Zn^+, Zn^{2+})-ZSM-5$^-$. Then, the electrons in the 4s orbitals of Zn^+ ions were excited by visible light ($\lambda < 700$ nm) to the empty orbitals of CH_4 to dissociate the C-H bond. Consequently, H_2 and C_2H_6 were produced by coupling of methane (Figure 1.6b). The generated Zn species (Zn^+) act as the active sites in this photocatalytic NOCM system and should only be stable under oxygen-free conditions. An M-C σ bond can be formed between Zn^+ and methane, and electrons can be injected from Zn^+ to methane to activate the C-H bond upon light irradiation. In addition, Ga^{3+}-, Zn^{2+}-, Fe^{3+}- and Al^{3+}-modified titanosilicate (EST-10) zeolites were found to be effective in photocatalytic NOCM.[84] Ga^{3+}-modified EST-10 showed a methane conversion of approximately 30 μmol g^{-1} h^{-1} with UV ($\lambda < 390$ nm) light irradiation, which was 3 times higher than that of the Zn^+-modified ZSM-5 photocatalyst. This high performance was attributed to the synergistic effect of the strong C-H bond polarization by Ga^{3+} cations and hydrogen abstraction from CH_4 by photoinduced $^{\bullet}OH$.

Long and co-workers fabricated a photocatalyst consisting of Au nanoparticles and ZnO with exposed (001) facets, which achieved a high NOCM conversion rate under simulated solar light irradiation.[70] The optimized Au/ZnO photocatalyst showed a C_2H_6 production rate of approximately 11 μmol g^{-1} h^{-1} and a H_2 evolution rate of 10 μmol g^{-1} h^{-1} with solar light illumination for 4 h (Figure 1.6c). The authors thought that strong polarization and the intrinsic electric field of ZnO play important roles in photocatalytic NOCM. The authors also inferred that the C-H bond in CH_4 absorbed on the polar surface of ZnO was first activated and oxidized to form $^{\bullet}CH_3$ and H^+ intermediates. Subsequently, two $^{\bullet}CH_3$ combined to form C_2H_6, while H^+ intermediates were reduced by electrons to form H_2 (Figure 1.6d). Additionally, the exposed polar *m*-plane of Si-doped GaN nanowires was reported to transform methane into hydrogen and benzene with approximately 9/1 stoichiometry under UV light illumination.[83]

Notably, although no oxidant was used in the above photocatalytic NOCM reaction, oxygen absorbed on the surface of oxide photocatalysts or lattice oxygen inevitably participated in the reaction, rendering the frequent detection of CO or CO_2 as byproducts. Employing non-reducible

photocatalysts or eliminating surface absorbed oxygen was essential to achieve the desired stoichiometric ratio of hydrogen and hydrocarbons.[71,73]
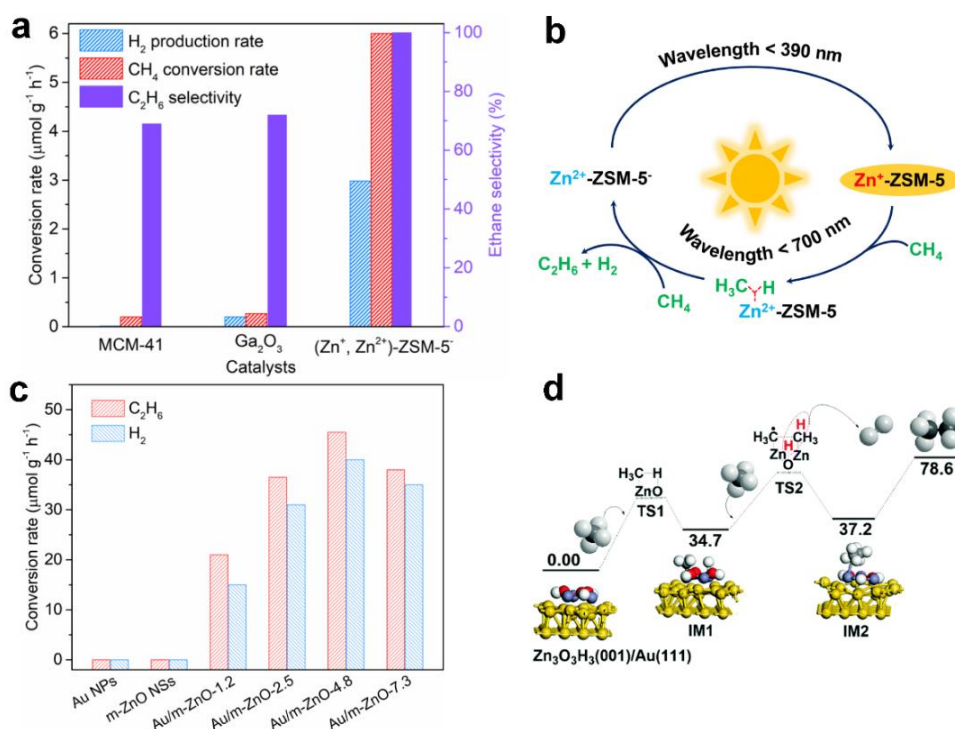
Figure 1.6 Photocatalytic NOCM. (a) CH$_4$ conversion rate, H$_2$ production rate and C$_2$H$_6$ selectivity achieved in the NOCM reaction catalyzed by different catalysts under light irradiation in 8 h.[85] (b) Proposed mechanisms for photocatalytic NOCM over the Zn^{2+}-ZSM-5 catalyst.[85] (c) Photocatalytic NOCM activity over Au/ZnO photocatalysts with solar light illumination in 4 h.[70] (d) Energy profiles for CH$_4$ coupling reaction on Zn$_3$O$_3$H$_3$(001)/Au(111) surfaces.[70]

1.3.2.2 Partial oxidation of methane (POM)

POM is a potential approach for the revalorization of methane by forming valuable oxygenates, e.g., methanol, formaldehyde, formic acid, and methanol precursors. Due to the participation of oxygen, this approach is easier to carry out thermodynamically (Equation 5). In addition to molecular oxygen, NO and H$_2$O$_2$ can be utilized as oxidants in POM.[75,96-98]

$$2CH_4 + O_2 \rightarrow 2CH_3OH, \Delta G^0_{298K} = -223 \text{ kJ mol}^{-1} \tag{5}$$
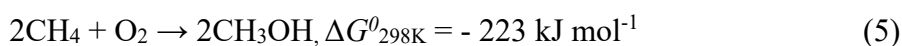
Photocatalytic POM to methanol or formic acid with molecular oxygen can proceed over oxide photocatalysts such as TiO$_2$, VO$_x$/SiO$_2$ and MoO$_3$.[96,97] It is proposed that photogenerated active O$^-$ sites on the surface of photocatalysts are responsible for methane activation by abstracting hydrogen

from methane. Corma et al. proved that photoirradiation enabled the homolytic dissociation of surface O-H bonds over silica zeolite, resulting in siloxyl radicals (Si-O$^{\bullet}$) that were capable of producing methyl radicals from CH_4.[99] When molecular oxygen was introduced as a co-reactant, the selectivity for C1 products, including methanol, formic acid and formaldehyde, was above 95%.

Compared with molecular oxygen, nitric oxide (NO) is a milder oxidant. Anpo et al. discovered that upon UV light ($\lambda > 270$ nm) irradiation over highly dispersed vanadium oxide supported on MCM-41 at room temperature, selective formation of methanol occurred in the presence of NO, while over-oxidation of methane into water and CO_2 occurred in the presence of molecular oxygen.[98] The photoexcited triplet state of vanadium oxides was considered to be the active site for methanol production from methane and NO.
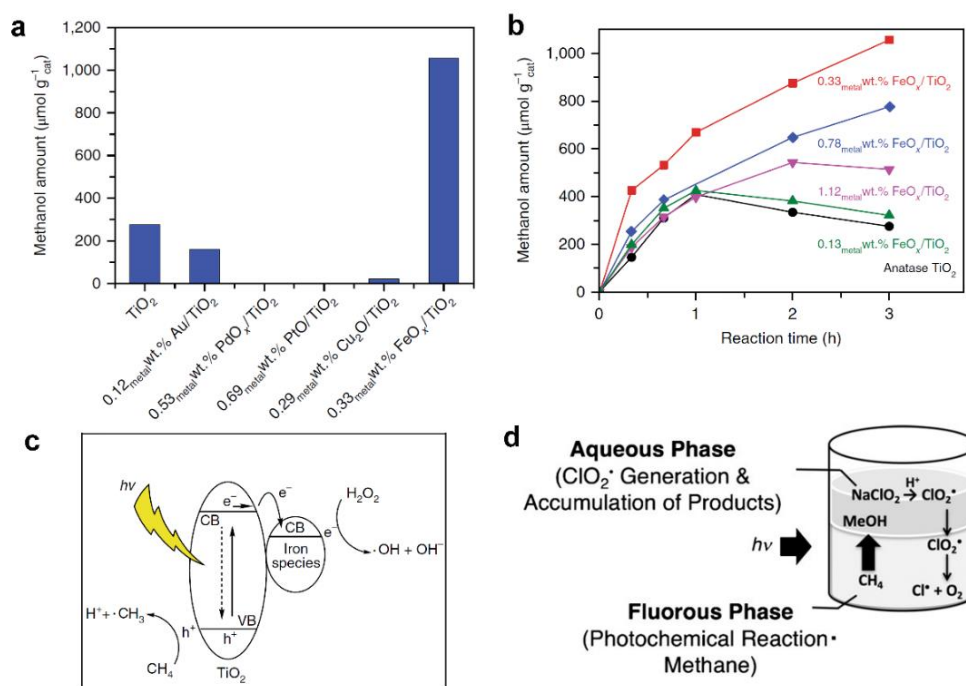
Figure 1.7 Photocatalytic POM. (a) CH_3OH yields of different metal-loaded TiO_2 catalysts after 3 h of light irradiation.[75] (b) CH_3OH production rate over a series of iron-oxide-species-loaded TiO_2 catalysts under light irradiation.[75] (c) Proposed mechanism of photocatalytic methane oxidation over FeO_x/TiO_2 using H_2O_2 as an oxidant.[75] (d) Photooxidation of CH_4 by $NaClO_2$ in a two-phase reaction system.[101]

H_2O_2, a strong oxidant, has been widely used for POM to synthesize methanol in thermocatalysis and has a large impact on the photocatalytic oxidation of methane.[18,65] Tang et al. discovered that, by adding an adequate amount of H_2O_2, FeO_x/TiO_2 served as an excellent photocatalyst for the

transformation of methane into methanol under ambient conditions, as shown in Figure 1.7a.[75] The optimized FeO_x/TiO_2 catalyst showed a high methanol yield of 1056 µmol g^{-1} after 3 h of 300 W Xe lamp irradiation (Figure 1.7b) in a batch reactor purged with 70 µmol CH_4, with nearly 90% selectivity for methanol and 15% CH_4 conversion. The existence of iron oxide species could significantly facilitate the separation of photoinduced electrons and holes as well as decrease the energy barrier for H_2O_2 reduction, resulting in the production of $^\bullet OH$. These holes could then react with methane to produce $^\bullet CH_3$, finally forming methanol through the reaction of $^\bullet CH_3$ and $^\bullet OH$ (Figure 1.7c).

Currently, it is still a great challenge to achieve oxygenated products with high yield and selectivity in photocatalytic POM because the C-H bond dissociation energies of oxygenates (e.g., ~397 kJ mol^{-1} in methanol) are lower than those of methane (439 kJ mol^{-1}), inevitably leading to over-oxidation of oxygenates into CO_2.[100] A strategy to increase product selectivity is to protect the product from over-oxidation. For example, Periana et al. reported that methane can be first oxidized to stable methyl bisulfate using catalysts of Pt complexes with high yields, which could then be converted to methanol by facile hydrolysis.[19] In addition to employing an appropriate photocatalyst, rationally designing reaction systems to selectively separate the product is an alternative approach to improve product selectivity. For instance, when a two-phase reaction system consisting of perfluorohexane (PHF) and water was adopted, a methane conversion of 99% with 14% and 85% selectivity for methanol and formic acid, respectively, was obtained using chlorine dioxide radical ($ClO_2^\bullet$) as the oxidizing agent (Figure 1.7d).[101] $ClO_2^\bullet$ was prepared by mixing $NaClO_2$ and HCl aqueous solutions. Then, upon light irradiation ($\lambda > 290$ nm), $ClO_2^\bullet$ can produce oxygen and $Cl^\bullet$ radicals. $Cl^\bullet$ could dissociate the C-H bond in methane to generate $^\bullet CH_3$, and the subsequent addition of oxygen resulted in the generation of oxygenated products. CH_4 and O_2 are well soluble in PHF, whereas water and the oxygenated products (CH_3OH and $HCOOH$) are poorly soluble in PHF. Therefore, the reaction of methane oxidation occurred in the PHF, and the products were then transferred into the aqueous solution, thereby avoiding deep oxidation to CO_2.

1.3.2.3 Steam reforming of methane (SRM)

Since methane has the largest H/C ratio among hydrocarbons, it has been widely used as a good hydrogen source in industry through SRM at high operating temperatures.[12] Recently, it has been

reported that hydrogen production can be promoted photocatalytically over metal-cocatalysed semiconductors in the presence of methane and water at approximately room temperature, as shown in Equation 6.[102-104] Considering that the reaction could proceed at room temperature, some oxygenated products such as methanol could also be formed through Equation 7 without complete oxidation in a solid-liquid phase reaction system.

$$CH_4 + 2H_2O \rightarrow CO_2 + 4H_2, \Delta G^0{}_{298K} = 114 \text{ kJ mol}^{-1} \tag{6}$$

$$CH_4 + H_2O \rightarrow CH_3OH + H_2, \Delta G^0{}_{298K} = 117 \text{ kJ mol}^{-1} \tag{7}$$
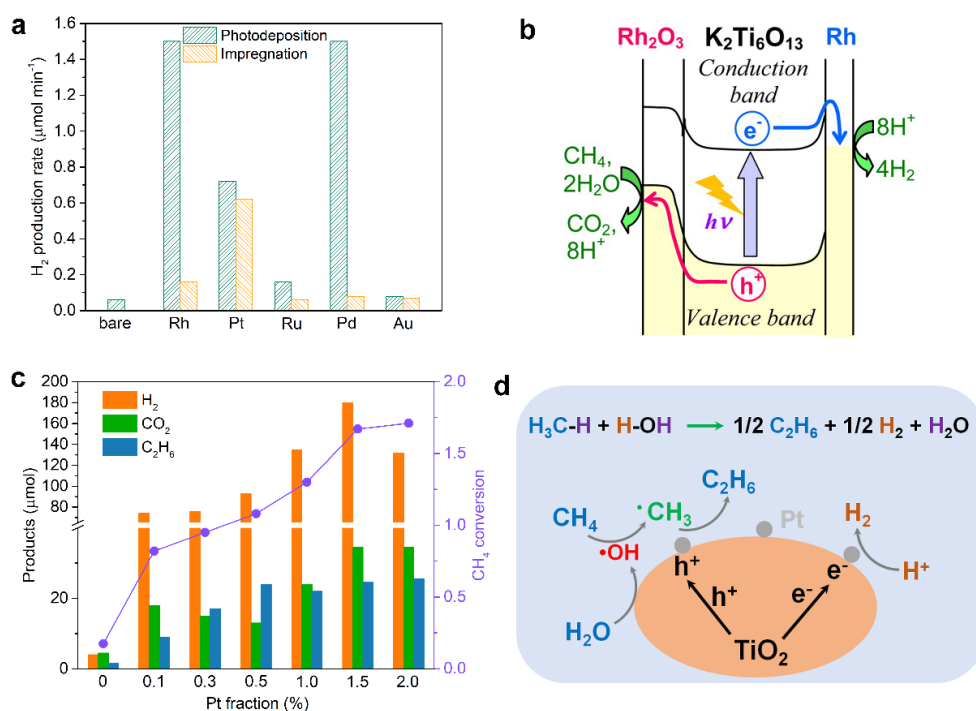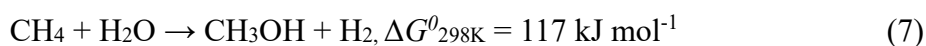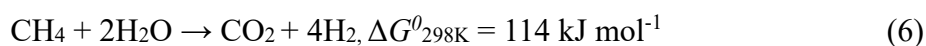
Figure 1.8 H_2 generation in photocatalytic SRM. (a) H_2 generate rate over the bare $K_2Ti_6O_{12}$ and co-catalyst-loaded $K_2Ti_6O_{12}$ photocatalysts synthesized by different methods.[103] (b) Proposed mechanism of photocatalytic SRM over the $Rh/Rh_2O_3/K_2Ti_6O_{12}$ photocatalyst.[103] (c) The production rate of H_2, C_2H_4 and CO_2 as well as CH_4 conversion rate over Pt/TiO_2 photocatalysts with different Pt loadings.[102] (d) Proposed mechanism of photocatalytic methane conversion over the Pt/TiO_2 photocatalyst.[102]

SRM to H_2 and CO_2. Previous studies on photocatalytic hydrogen production through Equation 6 mostly come from Yoshida's group and are mainly concentrated on noble metal-loaded wide bandgap semiconductor photocatalysts, e.g., Pt/TiO_2,[104] $Pt/NaTaO_3:La$,[105] $Pt/CaTiO_3$,[106] Pt/β-Ga_2O_3[107] and $Rh/K_2Ti_6O_{13}$.[103] The reactions were generally carried out in a flow-type reactor at

atmospheric pressure and approximately 75 °C in reactant gases (1 - 3% H_2O and 50% CH_4 with Ar balance) under irradiation from a 300 W Xe lamp. Due to the irradiation of the full-spectrum Xe lamp, the reaction temperatures were higher than room temperature (~75 °C). Under these reaction conditions, only H_2 and CO_2 were generated, and no byproducts, such as CO, C_2H_6 and CH_3OH, were formed, revealing that photocatalytic SRM could be selectively driven.

Noble metal co-catalysts play critical roles not only in improving photoexcited charge carrier separation and catalysing H_2 production but also in the activation of methane. For example, Rh as a co-catalyst has the best potential to selectively promote photocatalytic SRM when loaded on a K_2TiO_{13} photocatalyst by a photodeposition method compared with other co-catalysts, such as Pd, Pt, Au and Ru (Figure 1.8a).[103] The H_2 production rate on Rh/K_2TiO_{13} was approximately 1.9 μmol min^{-1} g^{-1}, with methane conversion of ~0.18%. The Rh co-catalyst in Rh/K_2TiO_{13} existed as a mixture of RhO_x nanoparticles and Rh nanoparticles, which acted as co-c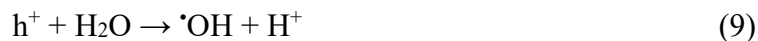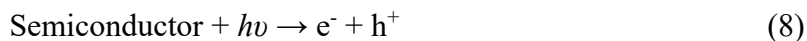atalysts for reductive and oxidative reactions, respectively, thereby effectively promoting photocatalytic SRM (Figure 1.8b). Li et al. reported that in a circulating system containing methane and water, Pt-loaded TiO_2 catalysts generated not only H_2 and CO_2 but also C_2H_6 under UV light irradiation, indicating that both SRM and NOCM occurred under those reaction conditions.[102] Loading an appropriate amount of Pt co-catalysts on TiO_2 significantly enhanced the yields of H_2 and C_2H_6 (Figure 1.8c). Pt co-catalysts provided catalytically active sites where H^+ was reduced to H_2 and methane was activated by $^{\bullet}OH$ to form $^{\bullet}CH_3$, followed by C_2H_6 production (Figure 1.8d).

The exploration of alternative non-noble metal co-catalysts with high efficiency is in high demand. Doping or modifying Ga_2O_3 with metal cations, such as Mg^{2+}, Zn^{2+}, In^{3+} and Al^{3+}, was reported as an effective way to promote H_2 production.[105] In addition, increasing the reaction temperature could promote the hydrogen generation rate over β-Ga_2O_3 photocatalysts by facilitating the migration of photoinduced charge carriers.[108]

Methanol production. In addition to H_2 and CO_2, organic oxygenates such as methanol can be generated in photocatalytic SRM by using an appropriate photocatalyst for the liquid-phase reaction system because the low reaction temperature inhibits over-oxidation of these organic oxygenates.[42,109,110] The mechanism is related to the formation of $^{\bullet}OH$ and its ability to activate CH_4 to produce several free radicals, finally leading to the production of methanol (Equations 8-10).

$$\text{Semiconductor} + h\upsilon \rightarrow e^- + h^+ \qquad (8)$$

$$h^+ + H_2O \rightarrow {}^\bullet OH + H^+ \qquad (9)$$

$$CH_4 + {}^\bullet OH \rightarrow CH_3OH + {}^\bullet H \qquad (10)$$

Prior research regarding photocatalytic methanol production from methane and water has mainly concentrated on WO_3-based photocatalysts with irradiation of ultraviolet C (UVC, 100-280 nm) or strong laser light.[111-115] Typically, the conversion of methane was maintained at 4% over La-doped WO_3 under milder reaction conditions (atmospheric pressure and ~ 94 °C) with UV light irradiation, and 53.12 mmol g^{-1} h^{-1} CH_3OH was produced.[112] Mesoporous La-modified WO_3 exhibited a 2-fold enhancement in the production of methanol compared with that of WO_3 under UVC-visible light illumination, whereas the production of CO_2 was markedly inhibited. This activity enhancement probably resulted from the generation of oxygen vacancies, which enhanced water adsorption and changed the concentration of ${}^\bullet OH$. It should be noted that in a methane oxidation process irradiated with UVC-visible light, oxygenated products could also be produced without photocatalysts because the UVC light was capable of directly photolyzing water into ${}^\bullet OH$, which would activate methane to ${}^\bullet CH_3$, thus forming methanol and other products.[116,117]

In addition to WO_3 materials, other semiconductors such as $BiVO_4$ and Bi_2WO_6 have been studied as photocatalysts for the conversion of methane to methanol.[42,110,118] Murcia-López et al. investigated the activities of methanol production over $BiVO_4$, Bi_2WO_6, and Bi_2WO_6/TiO_2 photocatalysts under UVC-visible light illumination at 55 °C and ambient pressure.[42] The prepared $BiVO_4$ exhibited higher methanol yield and selectivity compared to the other two photocatalysts, while the over-oxidation of methane to CO_2 was enhanced remarkably over the Bi_2WO_6/TiO_2 catalyst (Figure 1.9a). However, the CH_4 conversion of all these photocatalysts was low (< 0.4%). Sadtler et al. fabricated $BiVO_4$ microcrystals with bipyramidal and platelet morphologies for the transformation of methane with water to methanol at 65 °C by 350 W Xe lamp irradiation.[118] As shown in Figure 1.9b, bipyramidal $BiVO_4$ consisting of (012) and (102) facets showed a higher activity for methanol production (112 μmol h^{-1} g^{-1}) with an improved selectivity in 1 h compared to platelet $BiVO_4$ exposing (001) facets. The higher activity and improved selectivity towards methanol were attributed to the larger surface area of bipyramidal $BiVO_4$ for extracting photogenerated holes. Beta zeolite was also

an efficient catalyst for photocatalytic methanol production using methane and water under UVC light irradiation, even though the main product was CO_2.[110] Loading V_2O_5 and $BiVO_4$ on beta zeolite modified the surface acidic-basic properties of beta zeolite by decreasing the amount of acidic Al-O units and surface Si-OH, thereby inhibiting CO_2 production and achieving a better selectivity towards methanol (6.5%) with a CH_4 conversion rate of 0.2% (Figure 1.9c).
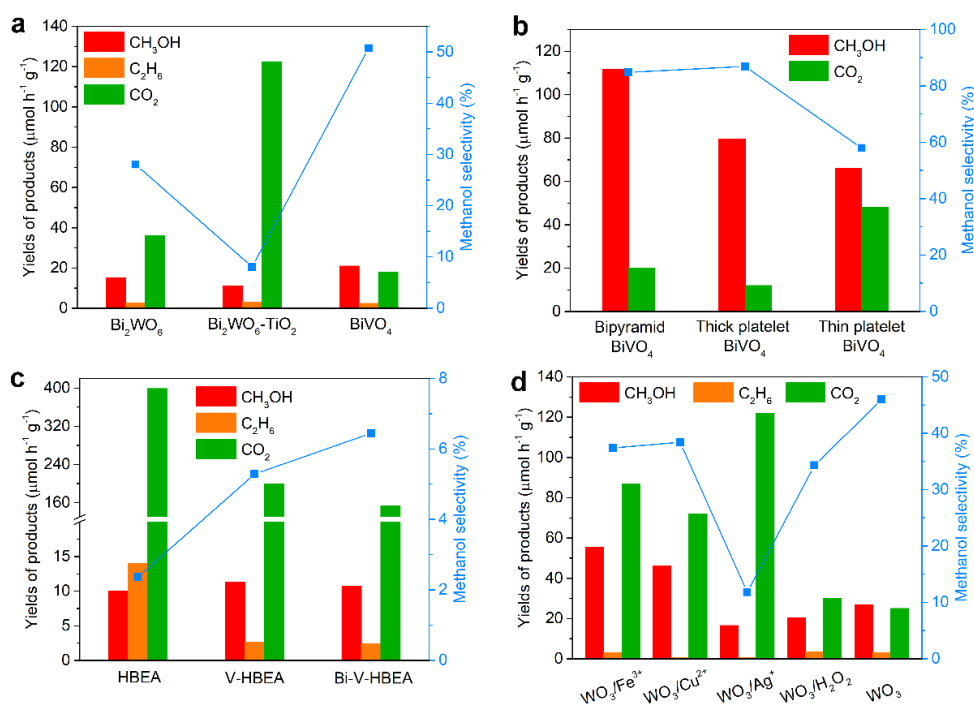
Figure 1.9 Methanol production in photocatalytic conversion of methane with water. (a) The production rate of CH_3OH, C_2H_6 and CO_2 as well as CH_3OH selectivity over Bi_2WO_6, Bi_2WO_6-TiO_2, and $BiVO_4$ photocatalysts, respectively.[42] (b) The production rate of CH_3OH and CO_2 as well as CH_3OH selectivity over different structured $BiVO_4$ with bipyramid, thick platelet, and thin platelet morphologies, respectively.[118] (c) The production rate of CH_3OH, C_2H_6 and CO_2 as well as CH_3OH selectivity over HBEA, V-HBEA and Bi-V-HBEA photocatalysts, respectively.[110] (d) The production rate of CH_3OH, C_2H_6 and CO_2 as well as CH_3OH selectivity over WO_3 with addition of Fe^{3+}, Cu^{2+}, Ag^+ and H_2O_2, respectively.[119]

The addition of electron scavengers such as Ag^+, Fe^{3+}, Cu^{2+} and O_2 was shown to have a remarkable influence on the activity of the catalyst and its selectivity towards methanol. Villa et al. found that the addition of an adequate amount of Fe^{3+} and Cu^{2+} ions resulted in significant enhancements (2.0-fold for Fe^{3+} and 1.7-fold for Cu^{2+}) in methanol production compared to pure

mesoporous WO_3 due to the efficient separation of electron-hole pairs (Figure 1.9d).[119] However, the selectivity for methanol dropped slightly to 38% with a CH_4 conversion of approximately 0.4% due to the production of a larger amount of CO_2. A similar effect was detected when O_2 and Fe^{3+} were added into a reaction solvent containing Bi_2VO_6 photocatalyst because of the considerable production of highly oxidant radicals to over-oxidize methane to CO_2.[42] However, Murcia-López et al. discovered that in the presence of nitrite (NO_2^-) ions (1 mM), the production of undesired CO_2 was inhibited over $BiVO_4$ photocatalysts.[120] The photocatalytic reaction was conducted in an aqueous solution containing 300 mL water and a certain amount of catalyst (1 g/L). In the case of tests with nitrite ions, certain amounts of $NaNO_2$ were added into the aqueous solution. As a scavenger of $^\bullet OH$, NO_2^- ions can be used to control the concentration of $^\bullet OH$ and prevent further oxidation of the desired product methanol, thereby decreasing the generation of CO_2 and achieving high selectivity for methanol (greater than 90%) with CH_4 conversion of approximately 0.03%. Therefore, carefully controlling the production of $^\bullet OH$ in the reactive solvent is crucial to achieve a compromise between product selectivity and methane conversion.

1.3.2.4 Functionalization of methane

Recently, photoredox catalysis has been regarded as a promising technology to directly activate and functionalize organic molecules such as methane HAT and LMCT.[121,122] LMCT excitation is a process that photoexcites π electrons from a ligand to transfer to the d orbitals of a metal centre, forming ligand-based radical intermediates with a reduced metal centre.[123] This distinct excitation process in LMCT allows more efficient use of light energy by avoiding intermediate states and enables targeted oxidation reactions to proceed only at the transiently oxidizing ligands, thereby improving the selectivity of the targeted products. The HAT process induced from the photoexcited catalyst can produce amine, aminium and other active radicals for C-H bond functionalization.[124,125]

Zuo et al. recently used LMCT catalysis to produce the alkoxy radical (R-O$^\bullet$, where R=CH_3, CH_2CCl_3, CH_2CF_3) from cerium salt and an alcohol under blue LED (λ=400 nm) irradiation, which could efficiently activate and functionalize methane.[45] The HAT process, in which R-O$^\bullet$ cleaved a C-H bond followed by forming an alcohol (R-OH) and a $^\bullet CH_3$, was thermodynamically viable. The dissociation energy of the C-H bond in methane equals the dissociation energy of the O-H bond in methanol (439 kJ mol^{-1}). The polarity-matching effect made the HAT process from the solvent

(CH$_3$CN) unfavourable due to the electrophilic property of both R-O$^\bullet$ and $^\bullet$CH$_2$CN (Figure 1.10a). The $^\bullet$CH$_3$ species readily coupled with a C=N or an N=N bond of the other substrate to form a new bond with a radical intermediate, which was then reduced by the Ce(III) species. Finally, the active Ce(IV) species was regenerated, and the functionalization of methane was achieved (Figure 1.10b). In a typical experiment, methane coupled with di-*tert*-butylazodicarboxylate substrate was transformed into the desired product with a turnover number (TON) of 2900 without over-functionalization products being detected.
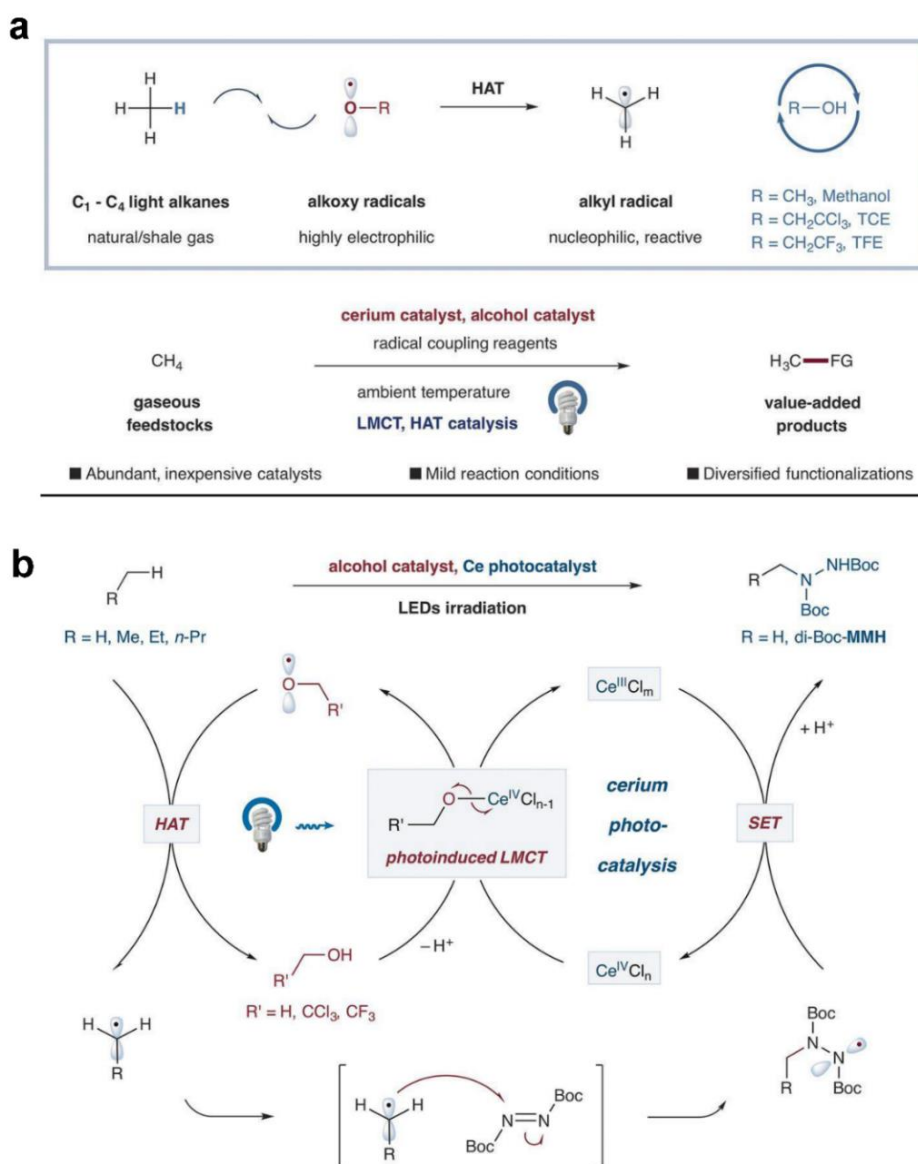

Figure 1.10 Photocatalytic functionalization of methane. (a) Alkoxy radical-mediated hydrogen atom transfer activation resulted in various selective functionalization of gaseous alkanes.[45] (b) Proposed mechanism for the functionalization of CH$_4$ and other alkanes over cerium-based catalyst.[45]

1.3.3 Photo-electrochemical conversion of methane

Direct electrocatalytic conversion of methane is an alternative method to produce valuable chemicals and fuels. Electrocatalysis has the ability to overcome the chemical inertness of methane and control the product selectivity by applying a potential to a catalyst surface under mild conditions. Recently, many studies regarding electrocatalysts and electrocatalytic systems for the selective oxidation of methane to methanol have been reported.[126-128] For example, it was reported that the yield of methanol over a gas diffusion electrode consisting of $TiO_2/RuO_2/V_2O_5$ was approximately 297 mg L^{-1} at an applied potential of 2.0 V *vs.* standard calomel electrode, with high selectivity towards methanol (97%).[128] On the basis of electrocatalysis, introducing solar light that provides additional driving forces, i.e., photoelectrochemical catalysis, can reduce the required amount of energy input in the methane conversion process. Photoelectrode materials play a critical role in methane conversion by absorbing solar light to produce electron-hole pairs and by providing active sites for the activation of methane and the stabilization of useful adsorbed species.[129]

In practical applications, Wang and co-workers recently developed a process of selective conversion of methane to CO by a photoelectrochemical method in which methane oxidation occurred at the interface of the photoanode and electrolyte with light irradiation and an applied potential at room temperature (Figure 1.11a).[130] The separation of photoinduced electron-hole pairs could be reinforced by the externally applied bias. A high yield for CO production of 81.9% was achieved over atomic layer deposition (ALD)-grown TiO_2 photoelectrodes, whereas remarkably low yields of CO (<4%) were obtained over anatase TiO_2 or P25 materials, as shown in Figure 1.11b. The significant difference in CO selectivity was attributed to the function of the Ti^{3+} species. The TiO_2 photoanode prepared by ALD possessed a high concentration of Ti^{3+} sites, which could be verified by the EPR results. The existence of the Ti^{3+} species favourably led to the generation of Ti^{3+}-C bonds, resulting in the selective formation of CO through the synergistic effect between adjacent Ti^{3+} and Ti^{4+} sites that could facilitate the transfer of C=O-Ti to O=C-Ti. In contrast, the Ti^{4+} sites would be conducive to the production of Ti^{4+}-O-C bonds, readily leading to the over-oxidation of methane to form carbonates (Figure 1.11c). Similar key steps for CO_2 reduction could be achieved based on the studied methane oxidation process. *In situ* characterizations detected the presence of several critical reaction intermediates such as H_3C-O-Ti, H_2C=O-Ti and Ti-CO in photoelectrochemical oxidation of methane,

providing strong evidence to support the proposed mechanism. Computational studies further revealed that the pathway of production of CO was thermodynamically more advantageous than that of over-oxidation (carbonate). In addition, the selectivity for CO could be tuned by regulating the applied potential. The lower the applied potential was, the higher the selectivity towards CO.
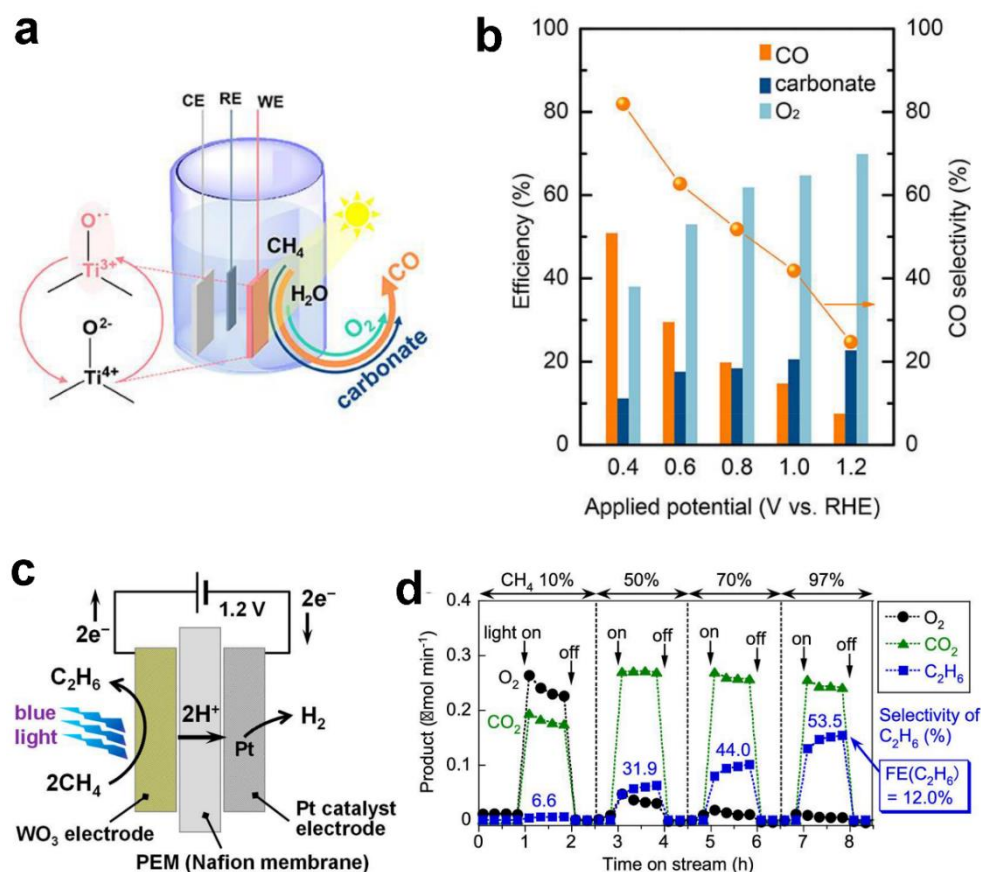
Figure 1.11 Photo-electrochemical conversion of methane on a TiO₂ photoelectrode. (a) Schematic illustration of photocatalytic oxidation of CH_4 over a TiO_2-based photoelectrode. [130] (b) The efficiency and selectivity of CO under different applied potentials. [130] (c) Proposed mechanisms of CH_4 oxidation over TiO_2 photoelectrodes. [130] (d) Photoelectrochemical system for CH_4 conversion in the gas phase. (e) Time course of product generation on the photoanode under different concentrations of CH_4 ($CH_4/H_2O/Ar$=10-97/3/balance). [131]

Amano and co-workers recently reported that methane was converted to ethane on a WO_3 photoanode in a gas-phase photoelectrochemical system under irradiation of a 453 nm LED at room temperature, accompanying the production of H_2 on the cathode with an approximately 100% Faraday efficiency (Figure 1.11d). [131] At an applied bias of 1.2 V, IPCE was 11%. The concentration of methane played a central role in the photocatalytic activity. When 10 vol% CH_4 was introduced into the reactor,

water oxidation to O_2 evolution was the main reaction. In contrast, when the concentration of CH_4 was increased to 97 vol%, water oxidation was suppressed and the ethane selectivity increased to 54% with 0.1% CH_4 conversion (Figure 1.11e).

1.4 Research motivation and thesis organization

Catalytic conversion of methane to value-added chemicals and fuels by a sustainable method is a highly attractive goal that still has significant challenges in catalysis. Solar energy can be employed with photocatalysts to activate methane and drive methane conversions. Compared with conventional thermocatalysis, there are several advantages in solar energy mediated CH_4 conversion. First, solar energy is an energy input that can reduce fossil fuel consumption and CO_2 emissions in driving methane conversion. Second, the utilization of photoenergy and appropriate photocatalysts could easily overcome the reaction barriers (such as C-H bond activation) to realize methane conversion at lower temperatures or even room temperature. Third, lower reaction temperatures would lead to significant environmental and process benefits, such as reduced thermal energy inputs, wider choice of catalysts, milder catalyst stability requirements, lower reactor cost and enhanced safety. However, most of reported photocatalysts suffered from low efficiency, poor sustainability and harsh reaction conditions. Furthermore, the mechanism investigations of methane activation and conversion on semiconductors remains in the preliminary stages. Thus, in this dissertation, I focused on develop nanometals/semiconductors-based catalysts that can use solar energy along with excellent C-H activation ability, thereby achieving a efficient, selective and energy-efficient methane conversion under mild conditions.

The dissertation is divided into seven chapters. A summary of the remaining six chapters is as follows:

Chapter 2 Visible-light-mediated methane activation for steam methane reforming over Rh/TiO$_2$ catalysts under mild conditions

Recent studies have found that the activation of reactants via the interactions between molecules and energetic hot carriers (electrons and holes) at photo-excitation of metallic nanostructures provide a potential route to boost the thermocatalytic activity at mild reaction temperatures. In this chapter,

TiO$_2$ supported Rh nanoparticles catalysts were constructed for steam methane reforming under visible light irradiation at mild operating temperature (below 300 °C). TiO$_2$ is a good candidate as electron acceptor because of relatively low energy level of conduction band. It can be expected that the hot electrons generated from the interband transition of Rh nanoparticles could transfer into TiO$_2$, lead to the formation of electron-deficient state of Rh$^{\delta+}$ at surface for the successive CH$_4$ activation. Therefore, the activity of methane conversion is expected to be enhanced under the assistance of both thermal and solar energy at mild operating temperatures.

Chapter 3 Light-enhanced carbon dioxide reforming of methane by effective plasmonic coupling effect of Pt and Au nanoparticles

Our group recently found that plasmonic Au nanoparticles could effectively enhance the catalytic activity of Rh/SBA-15 in carbon dioxide reforming of methane (CRM) reaction at 500 °C under visible light irradiation because Au could act as a plasmonic promoter to facilitate CRM. Meanwhile, the reaction rate enhancement is closely related to the energy and distribution of hot electrons. In this chapter, SiO$_2$ supported Pt and Au NPs catalysts were investigated for catalytic CRM under both UV and visible light irradiation. It is expected that surface plasmonic coupling of Pt and Au nanoparticles with different excited LSPR peaks may be effectively utilize solar energy and induce more energetic hot electrons to inject into the adsorbates and/or specific reaction intermediates, thereby reducing activation energies and promoting reaction rates at mild reaction temperatures.

Chapter 4 Visible light-promoted carbon dioxide reforming of methane over Pt/TaN catalysts

Tantalum mononitride (TaN), even though there were already some researches on investigating its optical properties, up to now, there were no reports on harnessing the optical property of TaN in photocatalytic reactions. In this chapter, TaN was employed as an optical support to investigate the activities of its supported group VIII metal catalysts in CRM with visible light assistance at 500 °C. TaN exhibits an obvious optical absorption in the visible region. The polarity of TaN is expected to facilitate electron-hole separation and possibly results in the activity enhancement.

Chapter 5 Direct photocatalytic oxidation of methane to liquid oxygenates with molecular oxygen over nanometals/ZnO catalysts

Previous studies demonstrate that ZnO-based photocatalysts show high activity for catalytic complete oxidation of methane to carbon dioxide in gas phase under simulated sunlight illumination. No work has been reported on photocatalytic conversion of methane to liquid oxygenates over ZnO photocatalysts in aqueous solution. In this chapter, in order to convert methane to liquid chemicals without any additional thermal energy input, ZnO nanocatalysts loaded with Pt, Pd, Au and Ag nanoparticles were developed, and their photocatalytic performance for oxidation of methane to liquid oxygenates such as methanol and formaldehyde in aqueous solution with O_2 as an oxidant was investigated at room temperature. Due to the formation of surface lattice O^- ions by photo-excited holes on ZnO, a reactive oxygen species that have high electrophilic ability, the activation of CH_4 could be achieved. Isotope experiments using $^{18}O_2$ and $H_2^{18}O$ were performed and in situ characterization methods were employed to investigated the mechanism of photocatalytic methane oxidation.

Chapter 6 Selective photocatalytic oxidation of methane to methanol with molecular oxygen over nanometals/TiO₂ catalysts

TiO_2 has been widely studied as the photocatalysts for many reactions such as organic transformation, water splitting and CO_2 reduction. Previous studies about photocatalytic oxidation of methane to methanol over TiO_2 is very limited, especially for using O_2 as an oxidant. This chapter investigated the TiO_2 loaded with different amount of Pt, Pd, Au and Ag as co-catalysts for selective photocatalytic oxidation of methane to methanol in aqueous solution with O_2 as an oxidant at room temperature. Developing the strategies to modify the surface electronic state of the co-catalyst is expected to avoid the complete oxidation of methanol to CO_2 and achieve appreciable methanol production activity.

Chapter 7 General conclusion and future prospects

This chapter makes an overall summary of the achievements in this dissertation, and presents the prospects for further work.

References

1. Schwach, P., Pan, X., and Bao, X. (2017). Direct Conversion of Methane to Value-Added Chemicals over Heterogeneous Catalysts: Challenges and Prospects. Chem. Rev. *117*, 8497-8520.

2. U.S. Energy Information Administration, International Energy Outlook 2018, U.S. Energy Information Administration, Washington, DC, 2018.

3. Ravi, M., Ranocchiari, M., and van Bokhoven, J.A. (2017). The direct catalytic oxidation of methane to methanol-A critical assessment. Angew. Chem. Int. Ed. *56*, 16464-16483.

4. Olivos-Suarez, A.I., Szécsényi, À., Hensen, E.J.M., Ruiz-Martinez, J., Pidko, E.A., and Gascon, J. (2016). Strategies for the Direct Catalytic Valorization of Methane Using Heterogeneous Catalysis: Challenges and Opportunities. ACS Catal. *6*, 2965-2981.

5. Zhan, C.-G., Nichols, J.A., and Dixon, D.A. (2003). Ionization potential, electron affinity, electronegativity, hardness, and electron excitation energy: molecular properties from density functional theory orbital energies. J. Phys. Chem. A *107*, 4184-4195.

6. Amos, R. (1979). An accurate ab initio study of the multipole moments and polarizabilities of methane. Mol. Phys. *38*, 33-45.

7. Luo, Y. R. *Comprehensive handbook of chemical bond energies*; CRC press, 2007. pp 19-145.

8. Berkowitz, J., Greene, J., Cho, H., and Ruscić, B. (1987). The ionization potentials of CH_4 and CD_4. J. Phys. Chem. *86*, 674-676.

9. Dietl, N., Engeser, M., and Schwarz, H. (2010). Competitive Hydrogen-Atom Abstraction versus Oxygen-Atom and Electron Transfers in Gas-Phase Reactions of $[X_4O_{10}]^{.+}$(X= P, V) with C_2H_4. Chem. Eur. J. *16*, 4452-4456.

10. Dietl, N., Schlangen, M., and Schwarz, H. (2012). Thermal hydrogen-atom transfer from methane: the role of radicals and spin states in oxo-cluster chemistry. Angew. Chem. Int. Ed. *51*, 5544-5555.

11. Tang, P., Zhu, Q., Wu, Z., and Ma, D. (2014). Methane activation: the past and future. Energy Environ. Sci. *7*, 2580-2591.

12. Angeli, S.D., Monteleone, G., Giaconia, A., and Lemonidou, A.A. (2014). State-of-the-art catalysts for CH_4 steam reforming at low temperature. Int. J. Hydrog. Energy *39*, 1979-1997.

13. Behrens, M., Studt, F., Kasatkin, I., Kühl, S., Hävecker, M., Abild-Pedersen, F., Zander, S., Girgsdies, F., Kurr, P., and Kniep, B.-L. (2012). The active site of methanol synthesis over $Cu/ZnO/Al_2O_3$ industrial catalysts. Science *336*, 893-897.

14. Alvarez-Galvan, M., Mota, N., Ojeda, M., Rojas, S., Navarro, R., and Fierro, J. (2011). Direct methane conversion routes to chemicals and fuels. Catal. Today *171*, 15-23.

15. Schulz, H. (1999). Short history and present trends of Fischer–Tropsch synthesis. Appl. Catal., B *186*, 3-12.

16. Khodakov, A.Y., Chu, W., and Fongarland, P. (2007). Advances in the development of novel cobalt Fischer-Tropsch catalysts for synthesis of long-chain hydrocarbons and clean fuels. Chem. Rev. *107*, 1692-1744.

17. Snyder, B.E., Vanelderen, P., Bols, M.L., Hallaert, S.D., Bottger, L.H., Ungur, L., Pierloot, K., Schoonheydt, R.A., Sels, B.F., and Solomon, E.I. (2016). The active site of low-temperature methane hydroxylation in iron-containing zeolites. Nature *536*, 317-321.

18. Agarwal, N., Freakley, S.J., McVicker, R.U., Althahban, S.M., Dimitratos, N., He, Q., Morgan, D.J., Jenkins, R.L., Willock, D.J., Taylor, S.H., et al. (2017). Aqueous Au-Pd colloids catalyze selective CH_4 oxidation to CH_3OH with O_2 under mild conditions. Science *358*, 223-227.

19. Periana, R.A., Taube, D.J., Gamble, S., Taube, H., Satoh, T., and Fujii, H. et al. (1998). Platinum catalysts for the high-yield oxidation of methane to a methanol derivative. Science *280*, 560-564.

20. Sushkevich, V.L., Palagin, D., Ranocchiari, M., and van Bokhoven, J.A. (2017). Selective anaerobic oxidation of methane enables direct synthesis of methanol. Science *356*, 523-527.

21. Hashiguchi, B.G., Konnick, M.M., Bischof, S.M., Gustafson, S.J., Devarajan, D., Gunsalus, N., Ess, D.H., and Periana, R.A. (2014). Main-group compounds selectively oxidize mixtures of methane, ethane, and propane to alcohol esters. Science *343*, 1232-1237.

22. Guo, X., Fang, G., Li, G., Ma, H., Fan, H., Yu, L., Ma, C., Wu, X., Deng, D., Wei, M. et al. (2014). Direct, Nonoxidative Conversion of Methane to Ethylene, Aromatics, and Hydrogen. Science *344*, 616-619.

23. Osadchii, D., Olivos Suarez, A.I., Szécsényi, Á., Li, G., Nasalevich, M.A., Dugulan, A.I., Serra-Crespo, P., Hensen, E.J., Veber, S.L., and Fedin, M.V. (2018). Isolated Fe sites in Metal Organic Framework catalyze the direct conversion of methane to methanol. ACS Catal. *8*, 5542-5548.

24. Szécsényi, Á., Li, G., Gascon, J., and Pidko, E.A. (2018). Mechanistic Complexity of Methane Oxidation with H_2O_2 by Single-Site Fe/ZSM-5 Catalyst. ACS Catal. *8*, 7961-7972.

25. Ab Rahim, M.H., Forde, M.M., Jenkins, R.L., Hammond, C., He, Q., Dimitratos, N., Lopez-Sanchez, J.A., Carley, A.F., Taylor, S.H., Willock, D.J. et al. (2013). Oxidation of methane to methanol with hydrogen peroxide using supported gold-palladium alloy nanoparticles. Angew. Chem. Int. Ed. *52*, 1280-1284.

26. Huang, W., Zhang, S., Tang, Y., Li, Y., Nguyen, L., Li, Y., Shan, J., Xiao, D., Gagne, R., Frenkel, A.I. et al. (2016). Low-Temperature Transformation of Methane to Methanol on Pd_1O_4 Single Sites Anchored on the Internal Surface of Microporous Silicate. Angew. Chem. Int. Ed. *55*, 13441-13445.

27. Kwon, Y., Kim, T.Y., Kwon, G., Yi, J., and Lee, H. (2017). Selective Activation of Methane on Single-Atom Catalyst of Rhodium Dispersed on Zirconia for Direct Conversion. *J. Am. Chem. Soc. 139*, 17694-17699.

28. Zuo, Z., Ramirez, P.J., Senanayake, S., Liu, P., and Rodriguez, J.A. (2016). Low-Temperature Conversion of Methane to Methanol on CeO_x/Cu_2O catalysts: Water Controlled Activation of the C-H Bond. J. Am. Chem. Soc., *136*, 13810-13813.

29. Hutchings, G.J. (2016). Methane Activation by Selective Oxidation. Top. Catal. *59*, 658-662.

30. Che, F., Gray, J.T., Ha, S., and McEwen, J.-S. (2016). Improving Ni Catalysts Using Electric Fields: A DFT and Experimental Study of the Methane Steam Reforming Reaction. ACS Catal. *7*, 551-562.

31. Che, F., Ha, S., and McEwen, J.-S. (2016). Elucidating the field influence on the energetics of the methane steam reforming reaction: A density functional theory study. Appl. Catal., B *195*, 77-89.

32. Kechagiopoulos, P.N., Angeli, S.D., and Lemonidou, A.A. (2017). Low temperature steam reforming of methane: A combined isotopic and microkinetic study. Appl. Catal., B *205*, 238-253.

33. Ligthart, D.A.J.M., van Santen, R.A., and Hensen, E.J.M. (2011). Influence of particle size on the activity and stability in steam methane reforming of supported Rh nanoparticles. J. Catal. *280*, 206-220.

34. Cui, X., Li, H., Wang, Y., Hu, Y., Hua, L., Li, H., Han, X., Liu, Q., Yang, F., He, L. (2018). Room-Temperature Methane Conversion by Graphene-Confined Single Iron Atoms. Chem *4*, 1902-1910.

35. Ikuno, T., Zheng, J., Vjunov, A., Sanchez-Sanchez, M., Ortuno, M.A., Pahls, D.R., Fulton, J.L., Camaioni, D.M., Li, Z., Ray, D. (2017). Methane Oxidation to Methanol Catalyzed by Cu-Oxo Clusters Stabilized in NU-1000 Metal-Organic Framework. J. Am. Chem. Soc. *139*, 10294-10301.

36. Tang, Y., Li, Y., Fung, V., Jiang, D.E., Huang, W., Zhang, S., Iwasawa, Y., Sakata, T., Nguyen, L., Zhang, X. (2018). Single rhodium atoms anchored in micropores for efficient transformation of methane under mild conditions. Nat. Commun. *9*, 1231.

37. Bozbag, S.E., Šot, P., Nachtegaal, M., Ranocchiari, M., van Bokhoven, J.A., and Mesters, C. (2018). Direct Stepwise Oxidation of Methane to Methanol over Cu-SiO$_2$. ACS Catal. *8*, 5721-5731.

38. Xie, P., Pu, T., Nie, A., Hwang, S., Purdy, S.C., Yu, W., Su, D., Miller, J.T., and Wang, C. (2018). Nanoceria-Supported Single-Atom Platinum Catalysts for Direct Methane Conversion. ACS Catal. *8*, 4044-4048.

39. Chan, S.I., Lu, Y.J., Nagababu, P., Maji, S., Hung, M.C., Lee, M.M., Hsu, I.J., Minh, P.D., Lai, J.C.H., and Ng, K.Y. (2013). Efficient oxidation of methane to methanol by dioxygen mediated by tricopper clusters. Angew. Chem. Int. Ed. *125*, 3819-3823.

40. Newton, M.A., Knorpp, A.J., Pinar, A.B., Sushkevich, V.L., Palagin, D., and van Bokhoven, J.A. (2018). On the Mechanism Underlying the Direct Conversion of Methane to Methanol by Copper Hosted in Zeolites; Braiding Cu K-Edge XANES and Reactivity Studies. J. Am. Chem. Soc. *140*, 10090-10093.

41. Upham, D.C., Agarwal, V., Khechfe, A., Snodgrass, Z.R., Gordon, M.J., Metiu, H., and McFarland, E.W. (2017). Catalytic molten metals for the direct conversion of methane to hydrogen and separable carbon. Science *358*, 917-921.

42. Murcia-López, S., Villa, K., Andreu, T., and Morante, J.R. (2014). Partial Oxidation of Methane to Methanol Using Bismuth-Based Photocatalysts. ACS Catal. *4*, 3013-3019.

43. Yuliati, L., and Yoshida, H. (2008). Photocatalytic conversion o.f methane. Chem. Soc. Rev. *37*, 1592-1602.

44. Chen, X., Li, Y., Pan, X., Cortie, D., Huang, X., and Yi, Z. (2016). Photocatalytic oxidation of methane over silver decorated zinc oxide nanocatalysts. Nat. Commun. *7*, 12273.

45. Hu, A., Guo, J.-J., Pan, H., and Zuo, Z. (2018). Selective functionalization of methane, ethane, and higher alkanes by cerium photocatalysis. Science *361*, 668-672.

46. Lee, B., and Hibino, T. (2011). Efficient and selective formation of methanol from methane in a fuel cell-type reactor. J. Catal. *279*, 233-240.

47. Arnarson, L., Schmidt, P.S., Pandey, M., Bagger, A., Thygesen, K.S., Stephens, I.E.L., and Rossmeisl, J. (2018). Fundamental limitation of electrocatalytic methane conversion to methanol. Phys. Chem. Chem. Phys. *20*, 11152-11159.

48. Zakaria, Z., and Kamarudin, S.K. (2016). Direct conversion technologies of methane to methanol: An overview. Renew. Sust. Energ. Rev. *65*, 250-261.

49. Gür, T.M. (2016). Comprehensive review of methane conversion in solid oxide fuel cells: Prospects for efficient electricity generation from natural gas. Prog. Energy Combust. Sci. *54*, 1-64.

50. Reddy, P.V.L., Kim, K.-H., and Song, H. (2013). Emerging green chemical technologies for the conversion of CH4 to value added products. Renew. Sust. Energ. Rev. *24*, 578-585.

51. Wang, L., Yi, Y., Wu, C., Guo, H., and Tu, X. (2017). One-Step Reforming of CO_2 and CH_4 into High-Value Liquid Chemicals and Fuels at Room Temperature by Plasma-Driven Catalysis. Angew. Chem. Int. Ed. *56*, 13679-13683.

52. Shilov, A.E., and Shul'pin, G.B. (1997). Activation of C-H bonds by metal complexes. Chem. Rev. *97*, 2879-2932.

53. Labinger, J.A., and Bercaw, J.E. (2002). Understanding and exploiting C-H bond activation. Nature *417*, 507-514.

54. Bromberg, S.E., Yang, H., Asplund, M.C., Lian, T., McNamara, B., Kotz, K., Yeston, J., Wilkens, M., Frei, H., and Bergman, R.G. (1997). The mechanism of a C-H bond activation reaction in room-temperature alkane solution. Science *278*, 260-263.

55. Liu, H., Meng, X., Dao, T.D., Zhang, H., Li, P., Chang, K., Wang, T., Li, M., Nagao, T., and Ye, J. (2015). Conversion of Carbon Dioxide by Methane Reforming under Visible-Light Irradiation: Surface-Plasmon-Mediated Nonpolar Molecule Activation. Angew. Chem. Int. Ed. *54*, 11545-11549.

56. Shimura, K., and Yoshida, H. (2014). Semiconductor photocatalysts for non-oxidative coupling, dry reforming and steam reforming of methane. Catalysis surveys from Asia *18*, 24-33.

57. Kuang, Y., Yamada, T., and Domen, K. (2017). Surface and interface engineering for photoelectrochemical water oxidation. Joule *1*, 290-305.

58. Tavasoli, A., and Ozin, G. (2018). Green Syngas by Solar Dry Reforming. Joule *2*, 571-575.

59. Chen, S., Qi, Y., Li, C., Domen, K., and Zhang, F. (2018). Surface strategies for particulate photocatalysts toward artificial photosynthesis. Joule *2*, 2260-2288.

60. Shih, C.F., Zhang, T., Li, J., and Bai, C. (2018). Powering the future with liquid sunshine. Joule *2*, 1925-1949.

61. Zhang, Y., He, S., Guo, W., Hu, Y., Huang, J., Mulcahy, J.R., and Wei, W.D. (2017). Surface-Plasmon-Driven Hot Electron Photochemistry. Chem. Rev. *116*, 2927-2954.

62. Linic, S., Christopher, P., and Ingram, D.B. (2011). Plasmonic-metal nanostructures for efficient conversion of solar to chemical energy. Nat. Mater. *10*, 911-921.

63. Linic, S., Aslam, U., Boerigter, C., and Morabito, M. (2015). Photochemical transformations on plasmonic metal nanoparticles. Nat. Mater. *14*, 567-576.

64. Christopher, P., Xin, H., and Linic, S. (2011). Visible-light-enhanced catalytic oxidation reactions on plasmonic silver nanostructures. Nat. Chem. *3*, 467-472.

65. Meng, X., Liu, L., Ouyang, S., Xu, H., Wang, D., Zhao, N., and Ye, J. (2016). Nanometals for Solar-to-Chemical Energy Conversion: From Semiconductor-Based Photocatalysis to Plasmon-Mediated Photocatalysis and Photo-Thermocatalysis. Adv. Mater. *28*, 6781-6803.

66. Kale, M.J., Avanesian, T., and Christopher, P. (2013). Direct Photocatalysis by Plasmonic Nanostructures. ACS Catal. *4*, 116-128.

67. Christopher, P., and Moskovits, M. (2017). Hot charge carrier transmission from plasmonic nanostructures. Ann. Rev. Phys. Chem. *68*, 379-398.

68. Kale, M.J., and Christopher, P. (2015). Plasmons at the interface. Science *349*, 587-588.

69. Aslam, U., Rao, V.G., Chavez, S., and Linic, S. (2018). Catalytic conversion of solar to chemical energy on plasmonic metal nanostructures. Nat. Catal. *1*, 656-665.

70. Meng, L., Chen, Z., Ma, Z., He, S., Hou, Y., Li, H.-H., Yuan, R., Huang, X.-H., Wang, X., and Wang, X. (2018). Gold plasmon-induced photocatalytic dehydrogenative coupling of methane to ethane on polar oxide surfaces. Energy Environ. Sci. *11*, 294-298.

71. Tong, H., Ouyang, S., Bi, Y., Umezawa, N., Oshikiri, M., and Ye, J. (2012). Nano-photocatalytic materials: possibilities and challenges. Adv. Mater. *24*, 229-251.

72. Kudo, A., and Miseki, Y. (2009). Heterogeneous photocatalyst materials for water splitting. Chem. Soc. Rev. *38*, 253-278.

73. Chen, X., Shen, S., Guo, L., and Mao, S.S. (2010). Semiconductor-based photocatalytic hydrogen generation. Chem. Rev. *110*, 6503-6570.

74. Hisatomi, T., Kubota, J., and Domen, K. (2014). Recent advances in semiconductors for photocatalytic and photoelectrochemical water splitting. Chem. Soc. Rev. *43*, 7520-7535.

75. Xie, J., Jin, R., Li, A., Bi, Y., Ruan, Q., Deng, Y., Zhang, Y., Yao, S., Sankar, G., and Ma, D. (2018). Highly selective oxidation of methane to methanol at ambient conditions by titanium dioxide-supported iron species. Nat. Catal. *1*, 889-896.

76. Margitan, J., Kaufman, F., and Anderson, J. (1974). The reaction of OH with CH_4. Geophys. Res. Lett. *1*, 80-81.

77. Yu, Q., Meng, X., Wang, T., Li, P., and Ye, J. (2015). Hematite films decorated with nanostructured ferric oxyhydroxide as photoanodes for efficient and stable photoelectrochemical water splitting. Adv. Funct. Mater. *25*, 2686-2692.

78. Liu, H., Li, M., Dao, T.D., Liu, Y., Zhou, W., Liu, L., Meng, X., Nagao, T., and Ye, J. (2016). Design of PdAu alloy plasmonic nanoparticles for improved catalytic performance in CO_2 reduction with visible light irradiation. Nano Energy *26*, 398-404.

79. Liu, H., Dao, T.D., Liu, L., Meng, X., Nagao, T., and Ye, J. (2017). Light assisted CO_2 reduction with methane over group VIII metals: Universality of metal localized surface plasmon resonance in reactant activation. Appl. Catal., B *209*, 183-189.

80. Liu, H., Meng, X., Dao, T.D., Liu, L., Li, P., Zhao, G., Nagao, T., Yang, L., and Ye, J. (2017). Light assisted CO_2 reduction with methane over SiO_2 encapsulated Ni nanocatalysts for boosted activity and stability. J. Mater. Chem. A *5*, 10567-10573.

81. Huang, H., Mao, M., Zhang, Q., Li, Y., Bai, J., Yang, Y., Zeng, M., and Zhao, X. (2018). Solar-Light-Driven CO_2 Reduction by CH_4 on Silica-Cluster-Modified Ni Nanocrystals with a High Solar-to-Fuel Efficiency and Excellent Durability. Adv. Energy Mater. *8*, 1702472.

82. Zhang, Q., Mao, M., Li, Y., Yang, Y., Huang, H., Jiang, Z., Hu, Q., Wu, S., and Zhao, X. (2018). Novel photoactivation promoted light-driven CO_2 reduction by CH_4 on Ni/CeO_2 nanocomposite with high light-to-fuel efficiency and enhanced stability. Appl. Catal., B *239*, 555-564.

83. Li, L., Fan, S., Mu, X., Mi, Z., and Li, C.-J. (2014). Photoinduced conversion of methane into benzene over GaN nanowires. J. Am. Chem. Soc. *136*, 7793-7796.

84. Li, L., Cai, Y.Y., Li, G.D., Mu, X.Y., Wang, K.X., and Chen, J.S. (2012). Synergistic Effect on the Photoactivation of the Methane C-H Bond over Ga^{3+}-Modified ETS-10. Angew. Chem. Int. Ed. *51*, 4702-4706.

85. Li, L., Li, G.D., Yan, C., Mu, X.Y., Pan, X.L., Zou, X.X., Wang, K.X., and Chen, J.S. (2011). Efficient Sunlight-Driven Dehydrogenative Coupling of Methane to Ethane over a Zn^+-Modified Zeolite. Angew. Chem. Int. Ed. *50*, 8299-8303.

86. Kato, Y., Yoshida, H., and Hattori, T. (1998). Photoinduced non-oxidative coupling of methane over silica-alumina and alumina around room temperature. Chem. Commun. 2389-2390.

87. Yoshida, H., Matsushita, N., Kato, Y., and Hattori, T. (2003). Synergistic active sites on SiO_2-Al_2O_3-TiO_2 photocatalysts for direct methane coupling. J. Phys. Chem. B *107*, 8355-8362.

88. Kato, Y., Matsushita, N., Yoshida, H., and Hattori, T. (2002). Highly active silica-alumina-titania catalyst for photoinduced non-oxidative methane coupling. Catal. Commun. *3*, 99-103.

89. Yuliati, L., Itoh, H., and Yoshida, H. (2006). Modification of highly dispersed cerium oxides on silica with highly dispersed titanium oxides as a new photocatalyst design for nonoxidative direct methane coupling. Chem. Lett. *35*, 932-933.

90. Yuliati, L., Hamajima, T., Hattori, T., and Yoshida, H. (2008). Nonoxidative coupling of methane over supported ceria photocatalysts. J. Phys. Chem. C *112*, 7223-7232.

91. Yuliati, L., Hamajima, T., Hattori, T., and Yoshida, H. (2005). Highly dispersed Ce (III) species on silica and alumina as new photocatalysts for non-oxidative direct methane coupling. Chem. Commun. 4824-4826.

92. Yuliati, L., Hattori, T., and Yoshida, H. (2005). Highly dispersed magnesium oxide species on silica as photoactive sites for photoinduced direct methane coupling and photoluminescence. Phys. Chem. Chem. Phys. *7*, 195-201.

93. Yuliati, L., Hattori, T., Itoh, H., and Yoshida, H. (2008). Photocatalytic nonoxidative coupling of methane on gallium oxide and silica-supported gallium oxide. J. Catal. *257*, 396-402.

94. Yoshida, H., Chaskar, M.G., Kato, Y., and Hattori, T. (2002). Fine structural photoluminescence spectra of silica-supported zirconium oxide and its photoactivity in direct methane conversion. Chem. Commun. 2014-2015.

95. Yoshida, H., Chaskar, M., Kato, Y., and Hattori, T. (2003). Active sites on silica-supported zirconium oxide for photoinduced direct methane conversion and photoluminescence. J. Photochem. Photobiol. A *160*, 47-53.

96. Ward, M.D., Brazdil, J.F., Mehandru, S., and Anderson, A.B. (1987). Methane photoactivation on copper molybdate: an experimental and theoretical study. J. Phys. Chem. *91*, 6515-6521.

97. Kaliaguine, S., Shelimov, B., and Kazansky, V. (1978). Reactions of methane and ethane with hole centers O^-. J. Catal. *55*, 384-393.

98. Hu, Y., Higashimoto, S., Takahashi, S., Nagai, Y., and Anpo, M. (2005). Selective photooxidation of methane into methanol by nitric oxide over V-MCM-41 mesoporous molecular sieves. Catal. Lett. *100*, 35-37.

99. Sastre, F., Fornés, V., Corma, A., and García, H. (2011). Selective, room-temperature transformation of methane to C1 oxygenates by deep UV photolysis over zeolites. J. Am. Chem. Soc. *133*, 17257-17261.

100. Labinger, J.A. (2004). Selective alkane oxidation: hot and cold approaches to a hot problem. J. Mol. Catal. A: Chem. *220*, 27-35.

101. Ohkubo, K., and Hirose, K. (2018). Light-Driven C-H Oxygenation of Methane into Methanol and Formic Acid by Molecular Oxygen Using a Perfluorinated Solvent. Angew. Chem. Int. Ed. *130*, 2148-2151.

102. Yu, L., Shao, Y., and Li, D. (2017). Direct combination of hydrogen evolution from water and methane conversion in a photocatalytic system over Pt/TiO_2. Appl. Catal., B *204*, 216-223.

103.   Shimura, K., Kawai, H., Yoshida, T., and Yoshida, H. (2012). Bifunctional rhodium cocatalysts for photocatalytic steam reforming of methane over alkaline titanate. ACS Catal. *2*, 2126-2134.

104.   Yoshida, H., Hirao, K., Nishimoto, J.-i., Shimura, K., Kato, S., Itoh, H., and Hattori, T. (2008). Hydrogen production from methane and water on platinum loaded titanium oxide photocatalysts. J. Phys. Chem. C *112*, 5542-5551.

105.   Shimura, K., Kato, S., Yoshida, T., Itoh, H., Hattori, T., and Yoshida, H. (2010). Photocatalytic steam reforming of methane over sodium tantalate. J. Phys. Chem. C *114*, 3493-3503.

106.   Shimura, K., and Yoshida, H. (2010). Hydrogen production from water and methane over Pt-loaded calcium titanate photocatalyst. Energy Environ. Sci. *3*, 615-617.

107.   Shimura, K., Yoshida, T., and Yoshida, H. (2010). Photocatalytic activation of water and methane over modified gallium oxide for hydrogen production. J. Phys. Chem. C *114*, 11466-11474.

108.   Shimura, K., Maeda, K., and Yoshida, H. (2011). Thermal acceleration of electron migration in gallium oxide photocatalysts. J. Phys. Chem. C *115*, 9041-9047.

109.   Villa, K., Murcia-López, S., Morante, J.R., and Andreu, T. (2016). An insight on the role of La in mesoporous WO_3 for the photocatalytic conversion of methane into methanol. Appl. Catal., B *187*, 30-36.

110.   Murcia-López, S., Bacariza, M.C., Villa, K., Lopes, J.M., Henriques, C., Morante, J.R., and Andreu, T. (2017). Controlled Photocatalytic Oxidation of Methane to Methanol through Surface Modification of Beta Zeolites. ACS Catal. *7*, 2878-2885.

111.   Noceti, R.P., Taylor, C.E., and D'Este, J.R. (1997). Photocatalytic conversion of methane. Catal. Today *33*, 199-204.

112.   Taylor, C., and Noceti, R. (2000). New developments in the photocatalytic conversion of methane to methanol. Cataly. Today *55*, 259-267.

113.   Gondal, M., Hameed, A., and Suwaiyan, A. (2003). Photo-catalytic conversion of methane into methanol using visible laser. Appl. Catal., A *243*, 165-174.

114.   Taylor, C.E. (2003). Methane conversion via photocatalytic reactions. Cataly. Today *84*, 9-15.

115.   Gondal, M., Hameed, A., Yamani, Z., and Arfaj, A. (2004). Photocatalytic transformation of methane into methanol under UV laser irradiation over WO_3, TiO_2 and NiO catalysts. Chem. Phys. Lett. *392*, 372-377.

116   Ogura, K., Migita, C.T., and Fujita, M. (1988). Conversion of methane to oxygen-containing compounds by the photochemical reaction. Ind. Eng. Chem. Res. *27*, 1387-1390.

117.   Ogura, K., and Kataoka, M. (1988). Photochemical conversion of methane. J. Mol. Cataly. *43*, 371-379.

118.   Zhu, W., Shen, M., Fan, G., Yang, A., Meyer, J.R., Ou, Y., Yin, B., Fortner, J., Foston, M., and Li, Z. (2018). Facet-Dependent Enhancement in the Activity of Bismuth Vanadate Microcrystals for the Photocatalytic Conversion of Methane to Methanol. ACS Appl. Nano Mater. *1*, 6683-6691.

119.   Villa, K., Murcia-López, S., Andreu, T., and Morante, J.R. (2015). Mesoporous WO_3 photocatalyst for the partial oxidation of methane to methanol using electron scavengers. Appl. Catal., B *163*, 150-155.

120.   Murcia-López, S., Villa, K., Andreu, T., and Morante, J.R. (2015). Improved selectivity for partial oxidation of methane to methanol in the presence of nitrite ions and $BiVO_4$ photocatalyst. Chem. Commun. *51*, 7249-7252.

121.   Hu, A., Guo, J.-J., Pan, H., Tang, H., Gao, Z., and Zuo, Z. (2018). δ-Selective Functionalization of Alkanols Enabled by Visible-Light-Induced Ligand-to-Metal Charge Transfer. J. Am. Chem. Soc. *140*, 1612-1616.

122.   Guo, J.J., Hu, A., Chen, Y., Sun, J., Tang, H., and Zuo, Z. (2016). Photocatalytic C-C Bond Cleavage and Amination of Cycloalkanols by Cerium (III) Chloride Complex. Angew. Chem. Int. Ed. *55*, 15319-15322.

123.   Balzani, V., Ceroni, P., and Juris, A. (2014) Photochemistry and photophysics: Concepts, Research, Applications; John Wiley & Sons.

124.   Choi, G.J., Zhu, Q., Miller, D.C., Gu, C.J., and Knowles, R.R. (2016). Catalytic alkylation of remote C-H bonds enabled by proton-coupled electron transfer. Nature *539*, 268-271.

125.   Jeffrey, J.L., Terrett, J.A., and MacMillan, D.W. (2015). O-H hydrogen bonding promotes H-atom transfer from α C-H bonds for C-alkylation of alcohols. Science *349*, 1532-1536.

126. Arnarson, L., Schmidt, P.S., Pandey, M., Bagger, A., Thygesen, K.S., Stephens, I.E., and Rossmeisl, J. (2018). Fundamental limitation of electrocatalytic methane conversion to methanol. Phys. Chem. Chem. Phys. *20*, 11152-11159.

127. Xie, S., Lin, S., Zhang, Q., Tian, Z., and Wang, Y. (2018). Selective electrocatalytic conversion of methane to fuels and chemicals. J. Energy Chem. *27*, 1629-1636.

128. Rocha, R.S., Reis, R.M., Lanza, M.R., and Bertazzoli, R. (2013). Electrosynthesis of methanol from methane: The role of V_2O_5 in the reaction selectivity for methanol of a $TiO_2/RuO_2/V_2O_5$ gas diffusion electrode. Electrochimi. Acta *87*, 606-610.

129. Baltrusaitis, J., Jansen, I., and Schuttlefield Christus, J.D. (2014). Renewable energy based catalytic CH_4 conversion to fuels. Catal. Sci. Technol. *4*, 2397-2411.

130. Li, W., He, D., Hu, G., Li, X., Banerjee, G., Li, J., Lee, S.H., Dong, Q., Gao, T., and Brudvig, G.W. (2018). Selective CO Production by Photoelectrochemical Methane Oxidation on TiO_2. ACS Cent. Sci. *4*, 631-637.

131. Amano, F., Shintani, A., Tsurui, K., Mukohara, H., Ohno, T., and Takenaka, S. (2019). Photoelectrochemical Homocoupling of Methane under Blue Light Irradiation. ACS Energy Lett. *4*, 502-507.

Chapter 2 Visible-light-mediated methane activation for steam methane reforming over Rh/TiO$_2$ catalysts under mild conditions

2.1 Introduction

Methane (CH$_4$) is well known as a highly available and abundant fuel stock, the utilization of which is very important in today's industry.[1-3] However, the direct activation of methane remains a grand challenge because of the high C-H bond energy (104 kcal mol^{-1}) in CH$_4$ and its intrinsic non-polar nature.[4,5] Nowadays the major industrial route for CH$_4$ utilization to produce hydrogen requires high-temperature (700-1000 °C) steam methane reforming (SMR, CH$_4$ + H$_2$O → 3H$_2$ + CO, ΔH$_{289 K}$ = + 206 kJ mol^{-1}) and subsequent low-temperature (<300 °C) water-gas shift reaction (WGS, CO + H$_2$O → H$_2$ + CO$_2$, ΔH$_{289 K}$ = - 41 kJ mol^{-1}).[6,7] Hydrogen is produced from both methane and water. Exploring low temperature activation of CH$_4$ technologies is an important subject since it can simplify process layout and reduce energy input.[8] Great efforts devoted to enhance the catalytic performance for SMR at low temperatures are mainly via modification of metal catalysts and supports to optimize catalysts, and few studies have been done with respect to energy input.[8-11] Recently, the use of non-thermal plasmas as the energy input to drive thermodynamically unfavorable dry reforming of methane at room temperature has been attracted much attention.[12,13] Therefore, it is of great significant to develop energy-efficient catalytic processes for CH$_4$ activation through providing new form of energy input to enhance the catalytic performance and reduce the reaction activation energy.

The activation of reactants via the interactions between molecules and energetic hot carriers (electrons and holes) at photo-excitation of metallic nanostructures provide another route to boost the catalytic activity.[14-17] As shown in Figure 2.1a, under light illumination, hot carriers can be readily injected into the antibonding orbitals of molecules absorbed on the metal surface, in which energy was deposited into adsorbates to facilitate chemical reaction.[14,18] Linic *et al.*, found that plasmon-excited hot electrons from Ag nanostructures could promote the activation of O$_2$ as the rate-limiting step in aerobic oxidation reaction by visible light irradiation.[17,19] Halas *et al.*, demonstrated that hot electrons generated via photoexcitation of Au/SiO$_2$ and Al/Al$_2$O$_3$ catalysts can trigger H$_2$

dissociation.[20,21] Moreover, the excited hot electrons in the metals can be injected into the conduction band (CB) of neighboring semiconductors through metal-semiconductor interfaces when the metal nanostructures was coupled with appropriate semiconductor (Figure 2.1b).[22] The Schottky barrier (Φ_{SB}) formed at the metal-semiconductor interface helps trap the hot electrons transferred to the CB of semiconductors by retarding them from transferring back to metals. The hot electrons gathered at the metal-semiconductor interface are consumed by the reduction reaction,[23] while the positive hot holes are remained on the metal surface to oxidize adsorbates.[24] This strategy effectively separate hot electrons and holes and extends their lifetimes in driving various surface chemical reactions, such as aerobic oxidation,[25,26] H_2O splitting,[27,28] CO_2 reduction,[29] etc.[30]
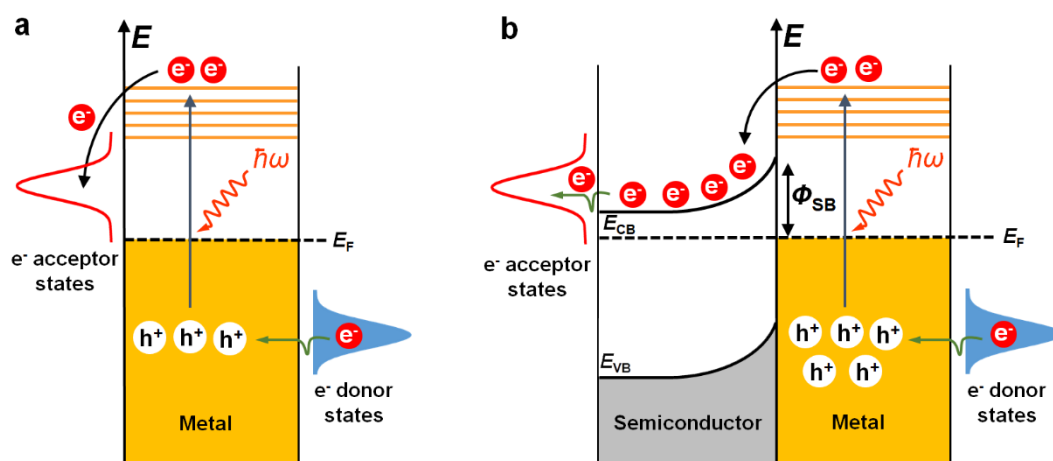

Figure 2.1 Schematic of photo-induced hot carrier generation and transfer process in metal and metal-semiconductor system. (a) In clean metal system, hot electrons and holes are first generated in a metal by photoexcitation and then hot electrons can transfer into electron acceptor state (and hot holes can transfer into electron donor state). (b) In metal-semiconductor system, hot electrons excited in a metal with sufficient energy can transfer into the conduction band (CB) of the adjacent semiconductor. The Schottky barrier (Φ_{SB}) formed at the metal-semiconductor interface can capture the transferred hot electrons and therefore prolong hot carrier lifetimes and make them capable of facilitating surface chemical reactions. E_{VB} represents for the top of valence band. E_{CB} represents for the bottom of conduction band. E_f represents for Fermi level.

Recent studies have found that the electron-deficient state of metals can be regarded as the active sites to activate the C-H bond.[3,7,31] Flytzani-Stephanopoulos *et al.*,[3] supposed that isolated Rh^+ cations can promote the activation of CH_4 by forming $Rh-CH_3$ species in H_2O and O_2. Xu *et al.*,[31] reported that the electron-deficient state of $Rh^{\delta+}$ had a higher ability to grab electrons of CH_4 and dissociate the C-H bond. This inspire us to use light energy to promote CH_4 activation by finely modulating the

surface electronic state of metal nanostructures through hot electrons transfer between metal nanostructures and semiconductors under light irradiation. Rhodium Rh nanoparticles (NPs) have been demonstrated to exhibit strong light absorption in visible region, which is mainly dominated by interband transition.[32,33] At the same time, metal oxide-supported Rh nanocatalysts have been widely investigated in the SMR reaction, especially in the low temperature SMR reaction.[8-10] However, until now, no report has been noticed on utilizing light energy to enhance CH_4 conversion over Rh NPs in SMR reaction.

In this chapter, I report that Rh nanoparticles supported on TiO_2 can be used as a photocatalyst to activate CH_4 and drive chemical transformation of CH_4 into H_2 through SMR reaction at mild operating temperature (below 300 °C). Our results demonstrate that hot electrons, derived from the excitation of interband transition on Rh NPs, are transferred quickly to the TiO_2 within 250 fs, leaving $Rh^{\delta+}$ with electron-deficient state at Rh surface, which can promote C-H bond activation at low temperatures. Under visible light (420~800 nm, ~580 mW cm^{-2}) illumination, the H_2 production rates were remarkably enhanced and the apparent activation energy for SMR reaction was reduced by ~50% compared to that under dark condition.

2.2 Experimental section

2.2.1 Chemicals and materials

Rhodium (III) chloride hydrate (RhCl$_3$ • 3H$_2$O) was supplied by Sigma-Aldrich. Commercially TiO_2 (AEROXIDE TiO_2 P25, Lot No. 614041498) was purchased from Evonik-Degussa. Zirconium oxide (ZrO_2), silicon dioxide (SiO_2), anatase and rutile TiO_2 were purchased from Wako Co.

2.2.2 Preparation of catalysts

All catalysts were prepared via the impregnation method. In general, for synthesis of Rh/TiO_2 catalysts with different Rh weight loadings, 1 g TiO_2 was added into 20.0 mL of an aqueous solution of RhCl$_3$·3H$_2$O (2.43, 4.86, 7.29, 9.72, 14.58 and 24.23 mM). After stirring for 1 h, the samples were dried at 60 °C and calcined at 400 °C for 2 h with a heating rate of 5 °C min^{-1}. Then, the catalysts were reduced at 400 °C for 1 h in flowing H_2 (10 ml min^{-1}) under atmospheric pressure. The obtained catalysts were named as x% Rh/TiO_2 (x=0.5-5 wt.%, representing for the Rh weight loadings). The

preparation of 2% Rh/ZrO_2 and 2% Rh/SiO_2 with 2 wt.% Rh loadings was similar to the above method in addition to adding the corresponding supports. In this chapter, unless otherwise stated, Rh/TiO_2 was referred to the catalysts with the Rh loading of 2.0 wt.%.

2.2.3 Characterization

The structures of as-prepared samples were analyzed by X-ray diffractometer with Cu Kα radiation (PANalytical). TEM and HR-TEM were carried out on a Tecnai G 2 F30 transmission electron microscope. HAADF-STEM images were taken on using a JEOL 2100F microscope. The XPS spectra were collected using a Thermo ESCALAB-250 spectrometer. The XPS peaks of Rh were calibrated by the C 1s feature of the adventitious carbon (284.8 eV). UV-vis absorption spectra of the samples were measured by a Shimadzu UV-2600 spectrophotometer. The light intensity and wavelength distribution of the irradiation light source were analyzed by USR-40 spectrophotometer. The ultrafast transient absorption spectra were measured via the pump and probe method utilizing an amplified Ti Sapphire femtosecond laser (Spitfire Ace, Spectra Physics, 35 fs (FWHM), 1 kHz).

2.2.4 Photocatalytic activity measurements

The photocatalytic SRM reaction tests was measured at atmospheric pressure in a homemade fixed-bed flow-type reactor (height 3 mm, diameter 8.5 mm) equipped with a quartz window to allow visible light irradiation, as shown in Figure 2.2. Typically, 20 mg catalyst was dispersed uniformly in the reaction cell. Then, the reactor cell was flushed with pure Ar gas for 2 h to remove the air in the cell. Subsequently, the catalysts were first activated at 400 °C for 2 h under the reaction gas, a mixture of CH_4 (10%)/Ar and H_2O vapor (3%) with a flow rate of 10 mL min^{-1}. After that, the activated catalysts were cooled to the desired reaction temperature to reach stable catalytic performances. All products were quantified by gas chromatograph (GC) equipped with thermal conductivity detector and flame ionization detector. LA-251 Xe lamp were used as light source. A HA30 filter and a L42 filter were utilized to remove infrared and UV ($\lambda < 420$ nm) light, respectively. The temperature was detected by a thermocouple under the reactor and controlled by TC-1000 temperature controller to mitigate heating effect caused by light irradiation. The apparent quantum efficiency AQE (AQE) was calculated as: AQE (%)= [{(Y_{light}-Y_{dark})×2}/(number of incident photos)]×100, where Y_{light} and Y_{dark} are the amounts of H_2 production under light illumination and in the dark conditions, respectively.
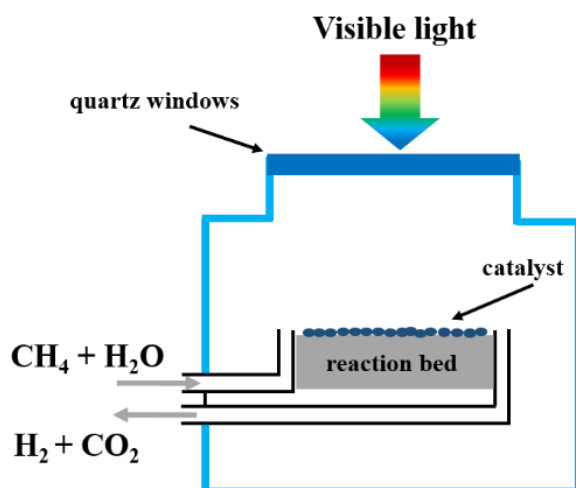
Figure 2.2 Photo-thermocatalytic SMR system. Schematic diagram of home-made photo-thermocatalytic reactor system.

2.2.5 Isotopic labelling experiments

The isotopic labeling experiments for SMR were measured using CD_4 (Cambridge Isotope Laboratories, Inc.) at 260 °C. The reactant gas mixture was 10% CH_4 (or CD_4) and 3% H_2O vapor in Ar. The steady state rates of product formation were measured by gas chromatograph (GC) equipped with thermal conductivity detector and flame ionization detector. The kinetic isotope effect (KIE) was calculated according to the reaction rates with CH_4 and CD_4 reactants.

2.2.6 Computational details

2.2.6.1 Methods

First principles molecular dynamics simulation were done within the Car-Parrinello framework (CPMD) using an unrestricted spin (Local Spin Density: LSD) approach and including gradient corrections on the exchange and correlation functional after Becke-Lee-Yang-Parr (BLYP).[34,35] The valence-core interaction was modeled by norm-conserving Troullier-Martins (TM) pseudopotentials[36] for Rh, Ti, Si, C, O and H atoms. The electrons of Rh 5s, 4d; Ti 4s, 3d; Si 3s, 3p; C 2s, 2p; O 2s, 2p; H 1s were treated as valence electrons and Rh 5p, Si 3d wavefunctions is also included in addition to those electron wavefunctions. For Rh and Ti, non-linear core corrections were taken into account. Those wavefunctions are expanded in a plane-wave basis set with an energy cut-off of 80 Ry, with the sampling of the Brillouin restricted to the   point. A fictitious electronic mass of 1200 a.u. and an integration step of 5.0 a.u. ensured a good control of the conserved quantities.

The configuration of electrons and wavefunctions in solving Kohn-Sham equations were similar as those in dynamical simulations but some unoccupied states are included (number of unoccupied states: 530, number of occupied states: 1765) in the Kohn-Sham calculation to investigate unoccupied states.

2.2.6.2 Models

Rh metal crystal with face-centered cubic lattice, whose lattice length a is 3.803 Å (ICSD code 650222), was quarried in the size of 4a (15.212 Å) × 4a × 3a (11.409 Å) and was placed at the bottom of the simulation cell whose size was 4a × 4a × 24 Å. One surficial Rh atom at the (001) surface was exchanged for Ti and Si. Then the two methane molecules and four water molecules were put in the open space (~ 14 Å in thickness) of the cell with keeping moderate distances between molecules each other and between the slab surface and the molecules to avoid undesirable bias. The number of atoms of Rh, Ti, Si, C, O, and H included in the cell box are 190, 1, 1, 2, 4, and 16, respectively.

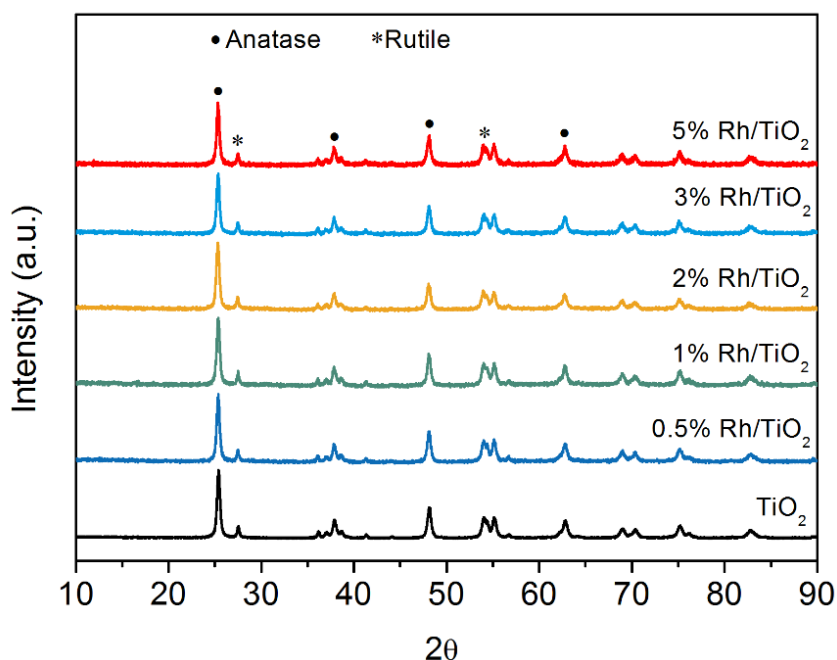## 2.3 Results

2.3.1 Catalyst characterization

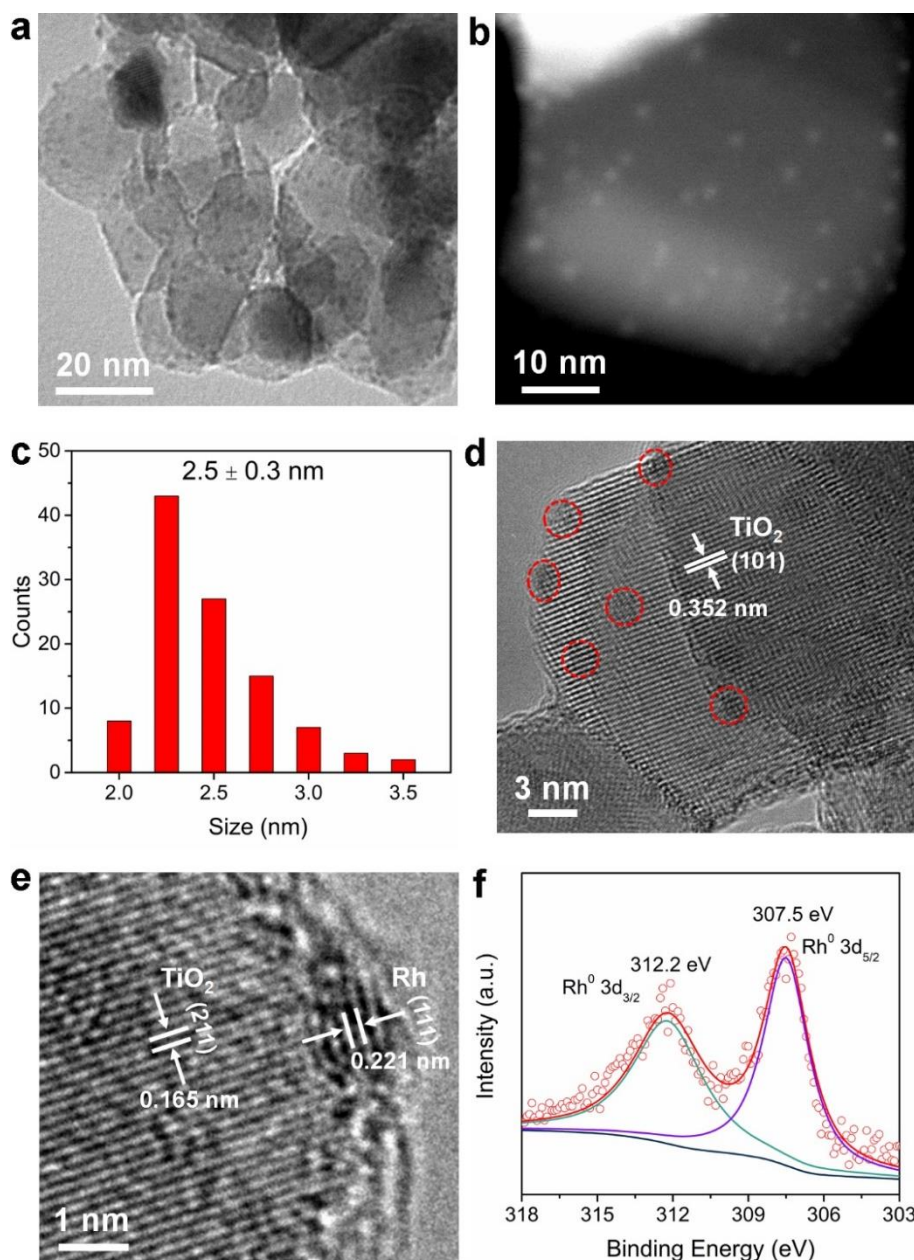**Figure 2.3** XRD patterns of different Rh loadings of Rh/TiO$_2$ catalysts.

Figure 2.4 Characterizations of 2% Rh/TiO₂ catalyst. (a) TEM and (b) HAADF-STEM images. (c) Size distribution of Rh NPs. (d and e) HRTEM images; Rh NPs are marked with red circles. (f) Rh 3d XPS spectra.

The x% Rh/TiO₂ (the mass percentage x = 0.5-5) catalysts were prepared by impregnation method, followed by hydrogen reduction at 400 °C for 1 h. X-ray diffraction (XRD) pattern (Figure 2.3) show that TiO₂ consists of anatase and rutile phases in all samples while no diffraction peaks can be observed for Rh because of low loading percentages and fine particle size. Transmission electron microscopy (TEM) and high-angle annular dark-field scanning transmission electron microscopy (HAADF-STEM) images (Figure 2.4a and b) of 2% Rh/TiO₂ catalyst clearly demonstrate that the Rh

NPs dispersed uniformly on the surface of TiO_2 with an average particle size of ~2.5 nm (Figure 2.4c). Two groups of lattice fringes with $d = 0.352$ nm and $d = 0.168$ nm shown in the high resolution TEM (HRTEM) images (Figure 2.4d and e) agree well with the (101) plane of anatase TiO_2 and the (211) plane of rutile TiO_2.[37] The lattice fringe with interplanar distance of 0.221 nm can be attributed to the (111) plane of Rh.[38] The Rh 3d XPS spectra (Figure 2.4f) of 2% Rh/TiO_2 catalyst show that Rh NPs are in a metallic state, but the binding energy of Rh NPs shifted slightly to higher values (307.5 eV for Rh $3d_{5/2}$ and 312.2 eV for Rh $3d_{3/2}$) compared to those of metallic bulk Rh (307.0-307.1 eV for Rh $3d_{5/2}$ and 311.8-311.9 eV for Rh $3d_{3/2}$).[40-42] Since the Rh NPs are very small, large proportion of Rh atoms in the Rh NPs are located at the vicinity of Rh/TiO_2 interface and will be affected by the interaction with O atoms on TiO_2 surface.[43] The Rh-O interaction leads to the charge transfer from Rh to O and contributes the shift of binding energy of Rh to higher values.[43-44]

2.3.2 Photo-enhanced catalytic activity

The SMR measurements were performed on a fixed-bed reactor equipped with a quartz window at atmospheric pressure. Figure 2.5a show the ultraviolet-visible (UV-VIS) absorption spectra of bare TiO_2 and 2% Rh/TiO_2. The bare TiO_2 show no photoabsorption at the visible light range ($\lambda > 400$ nm). By contrast, after loading Rh NPs, Rh/TiO_2 exhibits obvious and broad absorption in the visible light region. The board absorption band can be ascribed to the interband transitions in Rh NPs.[32] To rule out the influence of UV-light-excitation of TiO_2 on the catalytic activity, only visible light ($420 < \lambda < 800$ nm, Figure 2.5b) with an intensity of ~580 mW cm^{-2} was used in all measurements. Figure 2.5c shows the steady-state reaction rate (H_2 production rate) at a temperature fixed at 260 °C with and without visible light irradiation. It is obvious that, when the light was turned on, the H_2 production rate increased by ~3 times compared to that of the pure thermocatalytic process. This visible-light-enhanced H_2 production rate over Rh/TiO_2 was reversible. The reaction was also performed at temperatures ranging from 220 to 300 °C. As shown in Figure 2.5d, the H_2 production rate was consistently higher than that under dark condition. This enhancement can be also observed in terms of CO_2 and CO production (Figure 2.5e and f). It should be pointed out that CO_2 was the main product due to the existence of water-gas shift reaction (CO + $H_2O \rightarrow H_2 + CO_2$) as side reaction.[9-11] The ratio of H_2 to CO_2 is below the ideal ratio of 4:1, which may be because some intermediates were produced or the lattice oxygen from the reducible TiO_2 support participated in the reaction.[8,31]
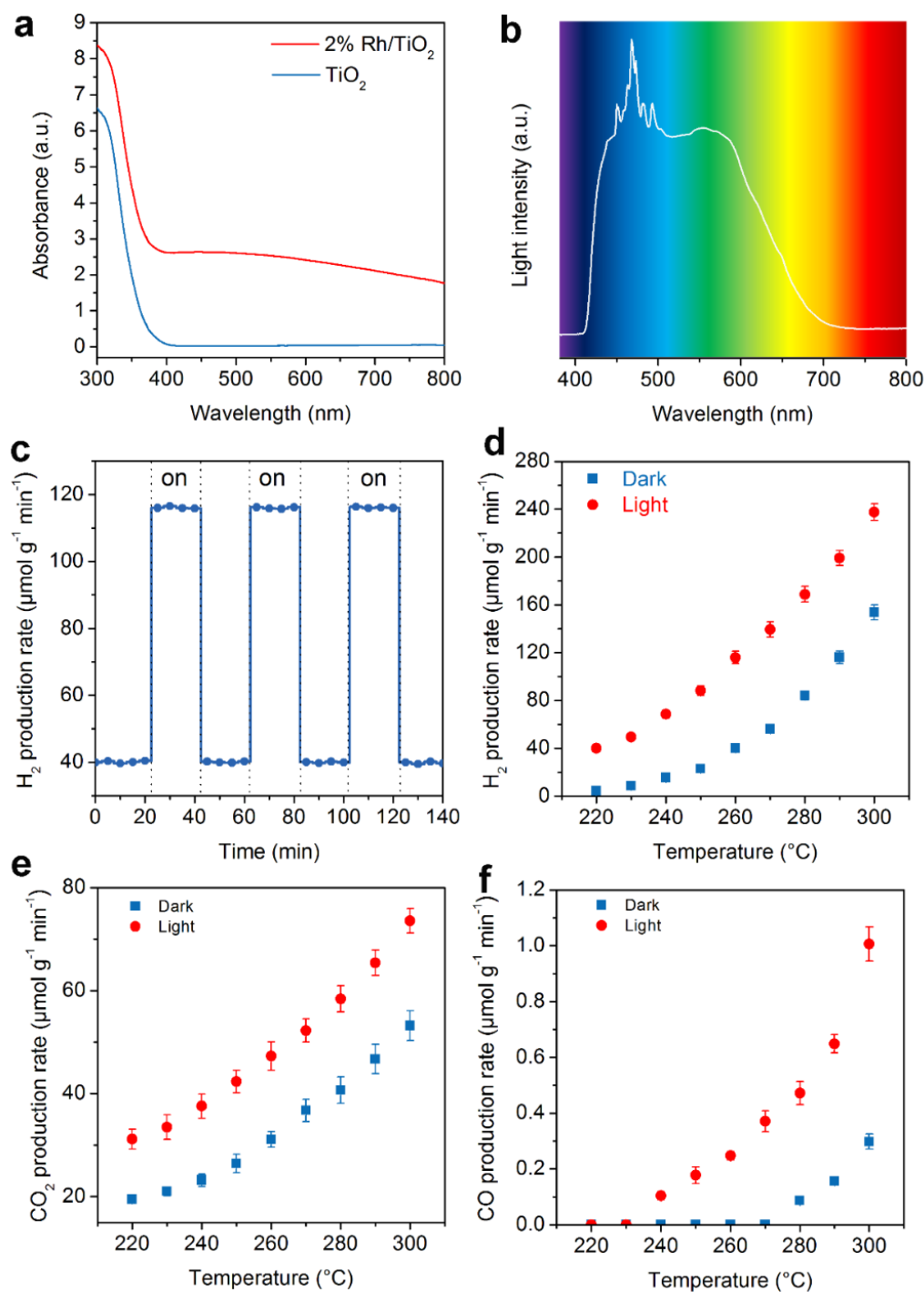
Figure 2.5 Photo-enhanced SMR reaction. (a) UV-VIS absorption spectra of Rh/TiO_2 and TiO_2 catalysts. (b) The output irradiance of light source in the experiment. (c) The H_2 production rate at 260 °C on Rh/TiO_2 catalyst with and without visible light irradiation. (d)-(f) The reaction rate of H_2 CO_2, and CO production on Rh/TiO_2 catalyst as a function of temperature in the purely thermal condition and under visible light illumination.

Figure 2.6a shows that the H_2 production rate enhancement (calculated by the reaction rate with

light divided by the reaction rate without light) declined from ~8.9 to ~1.6 times as the reaction temperature increased from 220 °C to 300 °C, suggesting the superiority of photo-activation of reaction at low temperature. The rate difference (Figure 2.6b, calculated by subtracting the reaction rate without light from the reaction rate with light) significantly increased with reaction temperature and was almost stable beyond 280 °C. In order to achieve reaction rate equivalent to the reaction under visible light illumination, a temperature increase of 20-40 °C is needed under purely thermal condition. Therefore, visible light illumination on Rh/TiO_2 catalyst remarkably increased H_2 production rate in SMR. Figure 2.6c shows that the crystal phase of TiO_2 has a negligible effect on the activity under both dark and light conditions. In addition, as shown in Figure 2.6d, Rh/TiO_2 catalyst shows excellent catalytic stability under dark and light condition.
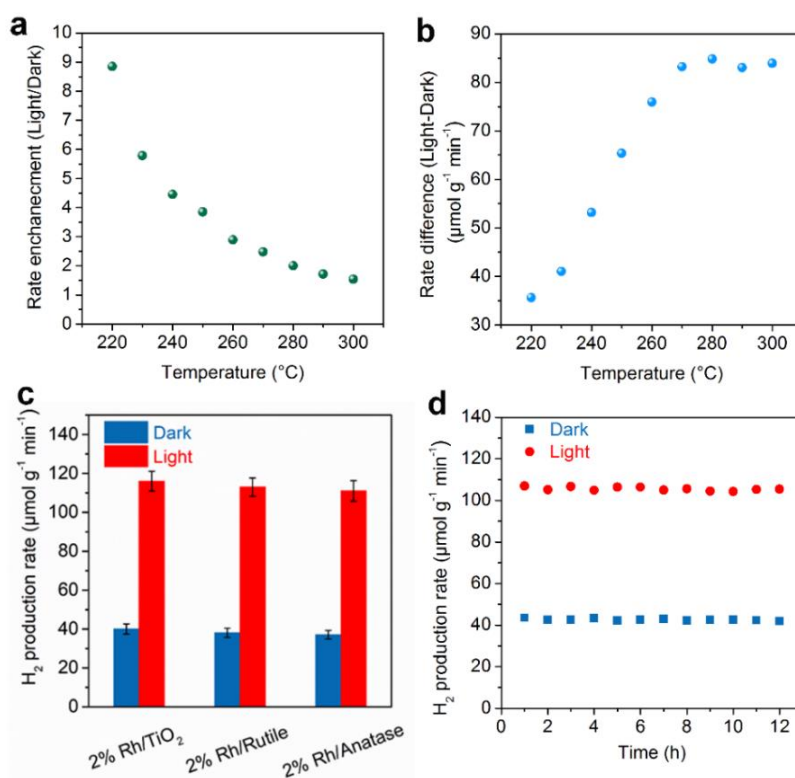

Figure 2.6 The enhancement and stability in photo-thermocatalytic SMR reaction. (a) Rate enhancement (the H_2 production rate ratio of light condition to the purely thermal condition) as a function of temperature. (b) Difference in H_2 production rate between dark and light condition as a function of temperature. (c) The H_2 production rate of 2% Rh/TiO_2, 2% Rh/Anatase and 2% Rh/Rutile at 260 °C in the dark and light conditions. (d) The H_2 production rate under the dark and under light conditions versus reaction time over Rh/TiO_2 catalyst at 260 °C.
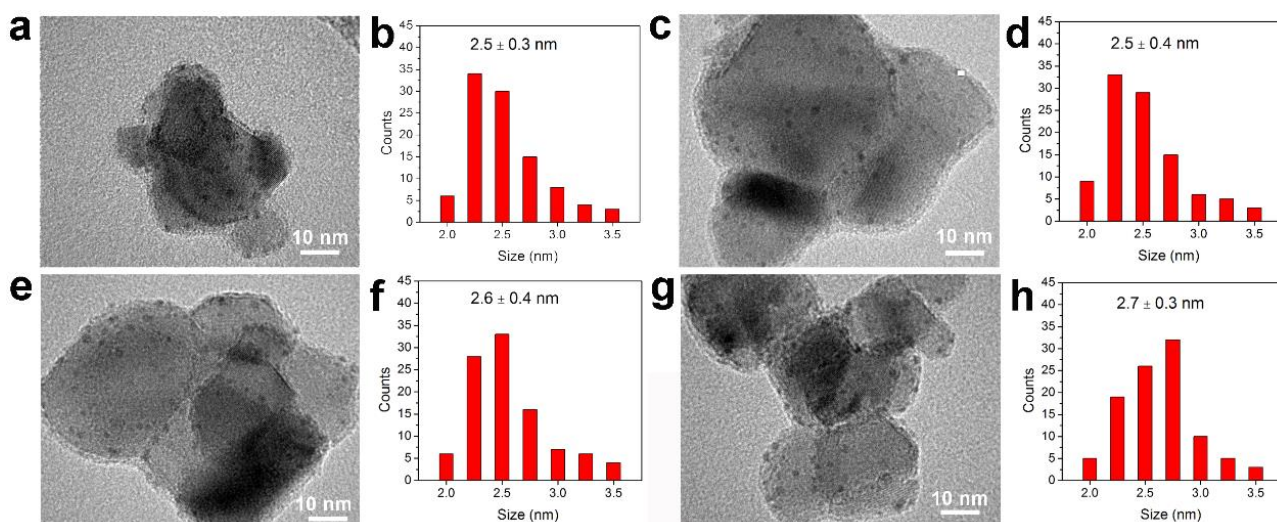
Figure 2.7 The size of Rh NPs in Rh/TiO₂. (a), (c), (e) and (g) TEM images of 0.5% Rh/TiO₂, 1% Rh/TiO₂, 3% Rh/TiO₂ and 5% Rh/TiO₂ catalysts; (b), (d), (f) and (h) are their corresponding size distribution of Rh NPs. All the catalysts were first annealed at 400 °C in air for 2 h and then reduced by H₂ at 400 °C for 1 h.
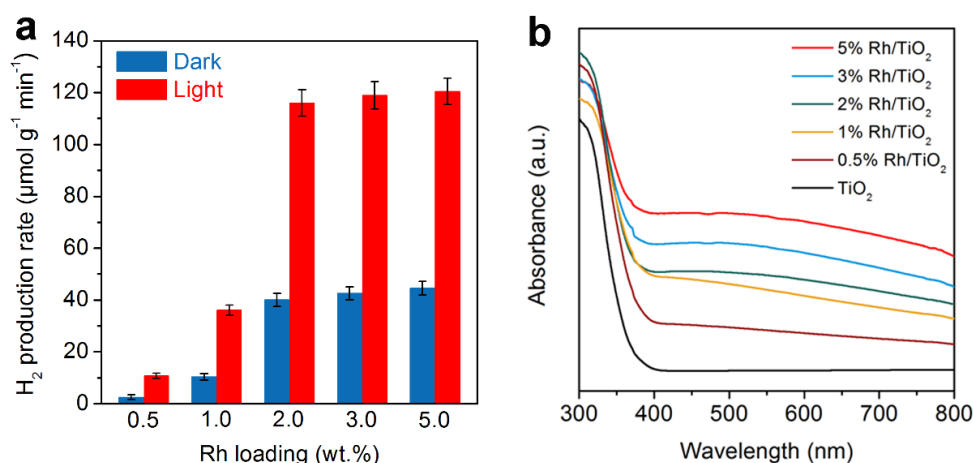

Figure 2.8 (a) Rh loading amount dependent H₂ production activity at 260 °C under the dark and light conditions. (b) UV-visible absorption spectra of catalysts with different Rh loadings.

The loading amount of Rh has obvious influence on the catalytic performance of Rh/TiO₂ catalysts in SMR reaction. As shown in Figure 2.7, with increasing Rh loadings from 0.5 to 5.0 wt.%, the size of Rh NPs increased from 2.0 to 2.9 nm. The H₂ production rate under dark and light condition (Figure 2.8a) increased with the catalytically active sites (Rh NPs) as well as the number of hot carriers generated by the interband transition of Rh NPs. Figure 2.8b shows that the light absorption intensity of the Rh/TiO₂ catalysts gradually increased with Rh loading. Further increasing Rh loadings

(larger than 2.0 wt%), the rate enhancement was nearly stable under present reaction condition. The catalytic activity is influenced by the size of Rh NPs. As shown in Figure 2.9 and 2.10, the activities under dark and light conditions decrease with the increase of Rh NPs size. The increase in size reduces the number of coordinatively unsaturated Rh surface atoms, leading to a decrease in activity. Moreover, with the increase of gas flow rates of reactant (CH_4), the reaction rates were also improved accordingly (Figure 2.11).
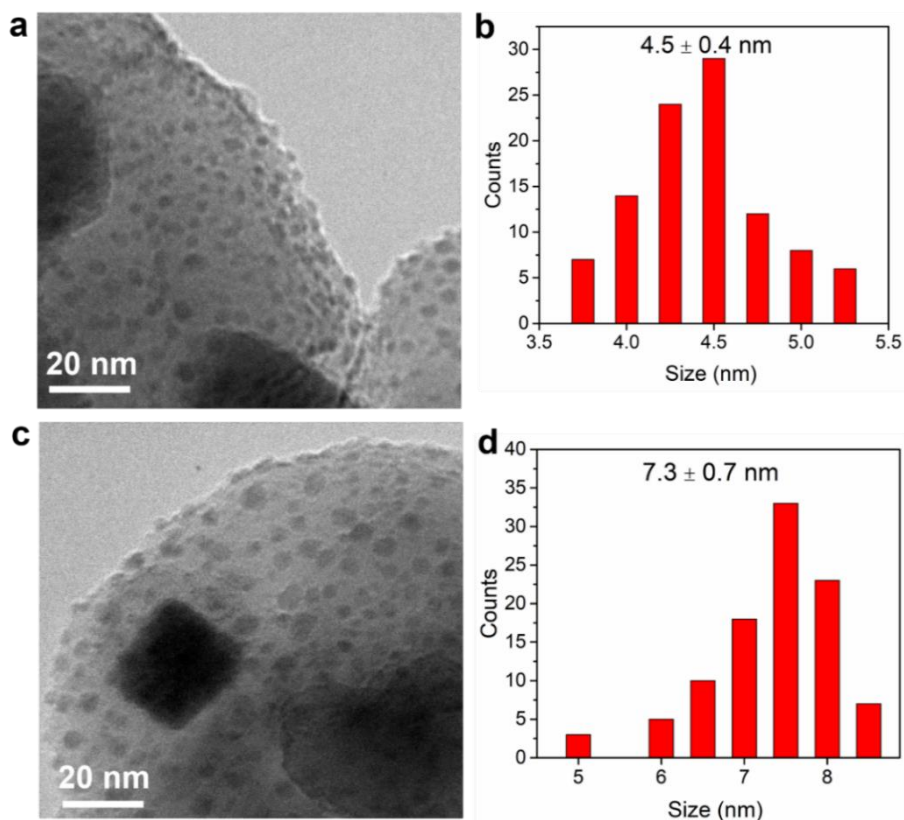

Figure 2.9 TEM images of 5% Rh/TiO_2 annealed at 550 (a) and 700 °C (c); (b) and (d) are their corresponding size distribution of Rh NPs. The catalysts were first annealed at 550 and 700 °C in air for 2 h, respectively, and then reduced by H_2 at 400 °C for 1 h.

To understand the mechanism of the observed rate enhancement induced by photo-irradiation in SRM reaction, insulators, ZrO_2 and SiO_2 with high conduction bands, supported Rh NPs catalysts (2% Rh/ZrO_2 and 2% Rh/SiO_2) were synthesized and their catalytic activities were examined. The average particle size of Rh NPs is 3.2 nm in 2% Rh/ZrO_2 and 3.5 nm in 2% Rh/SiO_2 (Figure 2.12). The Rh 3d XPS spectra (Figure 2.13) of Rh/ZrO_2 and Rh/SiO_2 exhibit that Rh NPs existed in a metallic state in both 2% Rh/ZrO_2 and 2% Rh/SiO_2 catalysts.[40-42] Broad photoabsorption could be also observed in the visible light region for both catalysts (Figure 2.14a). The Rh/TiO_2 catalysts showed higher

activities than those of Rh/SiO₂ and Rh/ZrO₂ catalysts under dark condition, which can be explained by the strong interaction between metal Rh and TiO₂ support and the adsorption of H₂O on the different catalytic surface.[1,45,46] Under visible light illumination, both Rh/ZrO₂ and Rh/SiO₂ exhibit improved reaction activities (Figure 2.14b), but the rate enhancements are much less pronounced than Rh/TiO₂ catalyst.
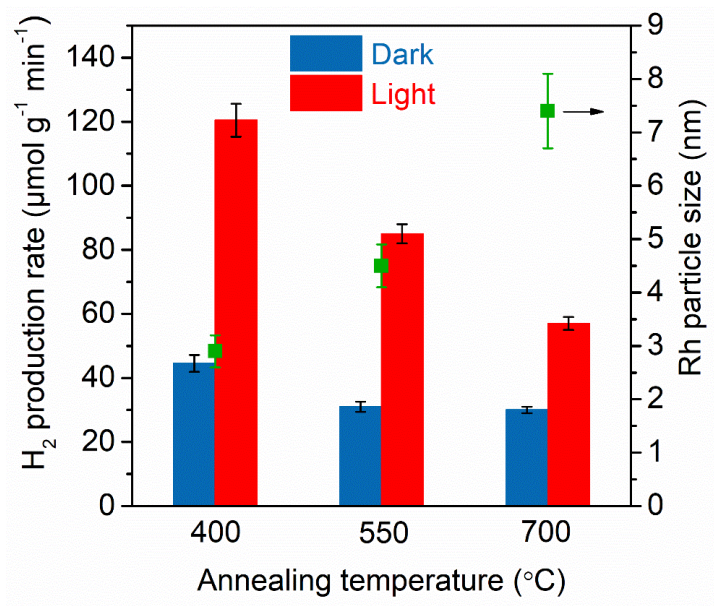

Figure 2.10 Effect of Rh NPs size on the H₂ production rate over 5% Rh/TiO₂ catalyst at 260 °C in the dark and light conditions.
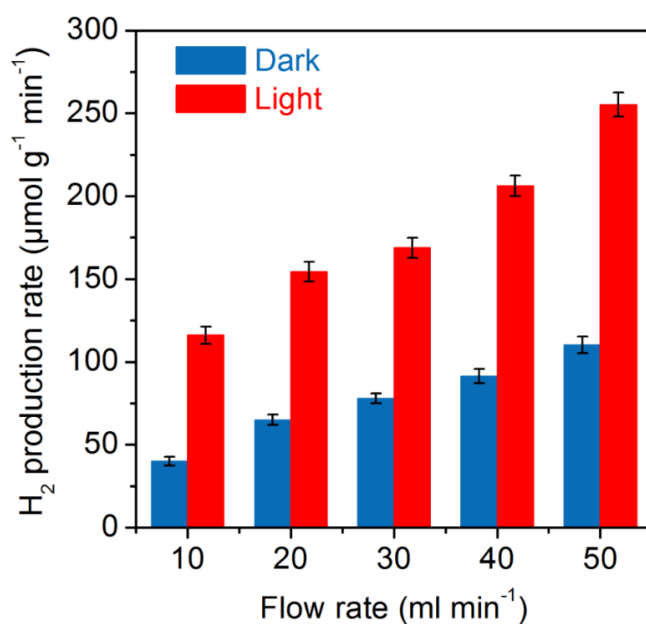

Figure 2.11 Effect of the gas flow rate on the H₂ production rate over 2% Rh/TiO₂ catalyst at 260 °C in the dark and light conditions.
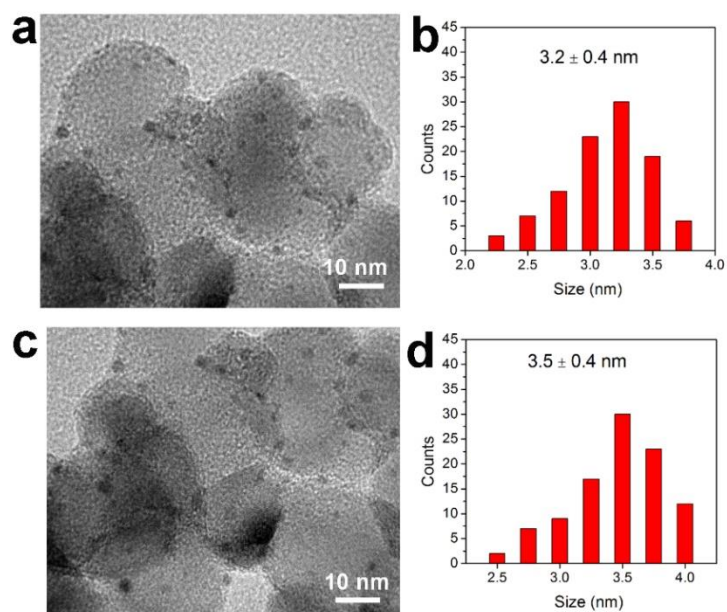
Figure 2.12 (a) and (c) TEM images of 2% Rh/ZrO$_2$ and 2% Rh/SiO$_2$ catalysts; (b) and (d) are their corresponding size distribution of Rh NPs.
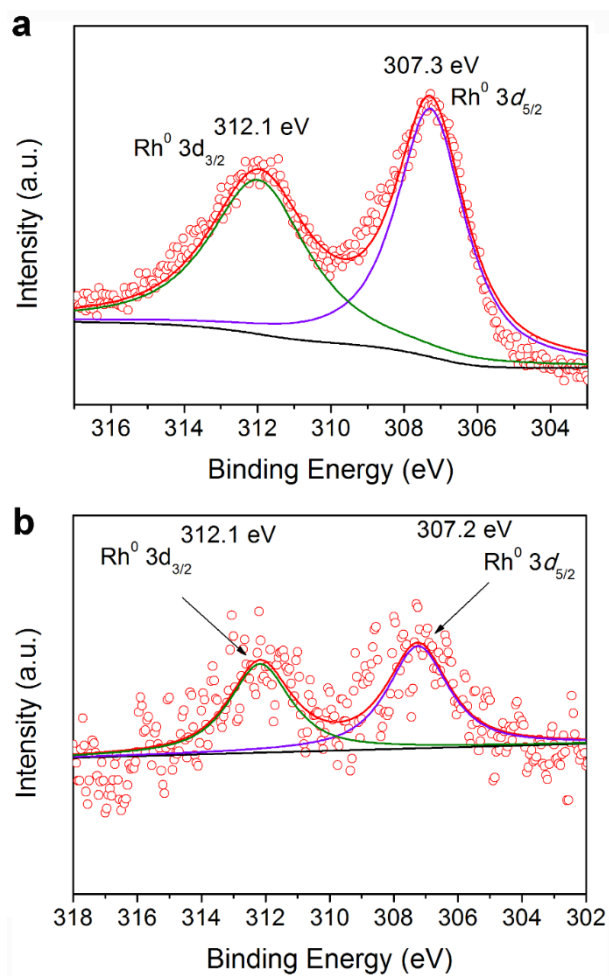

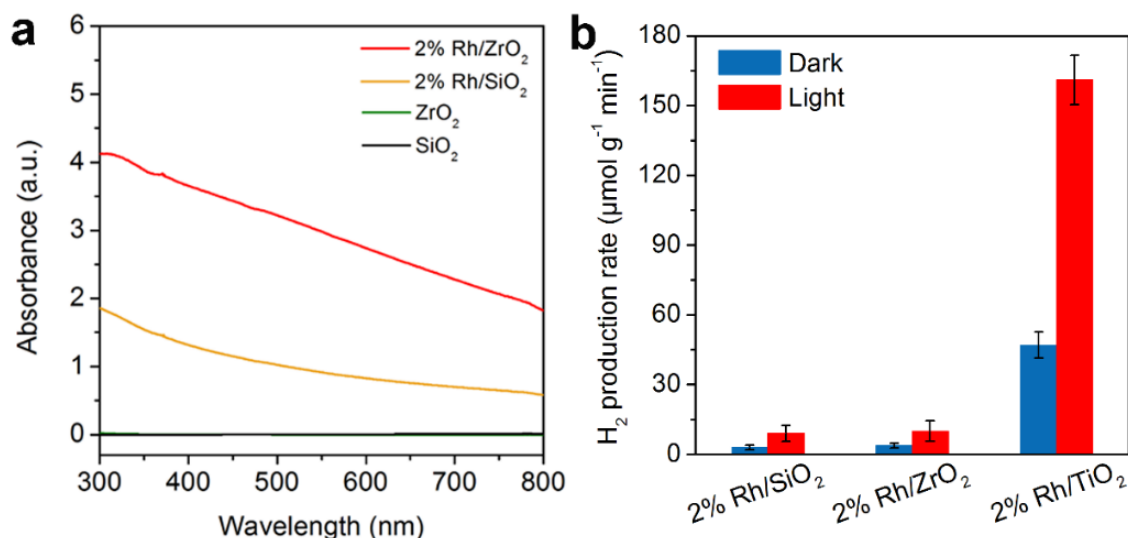**Figure 2.13** Rh 3d XPS spectra of (a) 2% Rh/ZrO$_2$ and (b) 2% Rh/SiO$_2$.

Figure 2.14 (a) UV-visible absorption spectra of 2% Rh/ZrO$_2$ and 2% Rh/SiO$_2$ catalysts. (b) The reaction rate of H$_2$ production on oxide supported Rh catalysts at 260 °C under the dark and light condition.

The dependence of H$_2$ production rate on visible-light intensity over Rh/TiO$_2$ catalyst shows a linear relationship (Figure 2.15a). This linear dependence validates that the reaction was driven by the number of hot carriers excited by the light irradiation.[15,17] As shown in Figure 2.15b, the AQE for H$_2$ production over Rh/TiO$_2$ catalyst is well consistent with the optical absorption spectrum of Rh/TiO$_2$, indicating that the interband transition of Rh NPs is responsible for the photo-enhancement reaction rate.[47]

It has been widely accepted that the activation of CH$_4$, exactly the C-H bond cleavage, is the rate-limiting step for CH$_4$ reforming processes.[8,48] For SMR reaction on Rh-based catalysts, the rate limiting step is the cleavage of C-H bonds of CH$_4$ to form intermediate species (CH$_x$*, x=0-3).[8] Kinetic isotope effect can be employed to distinguish hot carrier driven chemical reactions from thermal driven reactions since carrier-driven surface reactions over metallic nanostructures show higher kinetic isotope effects compare to thermal-driven counterparts.[17] To confirm this assumption, the kinetic isotope effect (KIE, CH$_4$ rate/CD$_4$ rate) were performed by comparing the rates of H$_2$ production using either CH$_4$ or CD$_4$ as the reactant (Figure 2.15c). The KIE under the dark condition is 1.55, agreeing well with previous work on Rh-based catalysts[8,48] and revealing that the activation of CH$_4$ is the rate limiting step in SMR. Under visible light irradiation, a larger KIE of 1.69 was obtained. Therefore, the KIE study reveals that hot carriers formed from interband transition of Rh
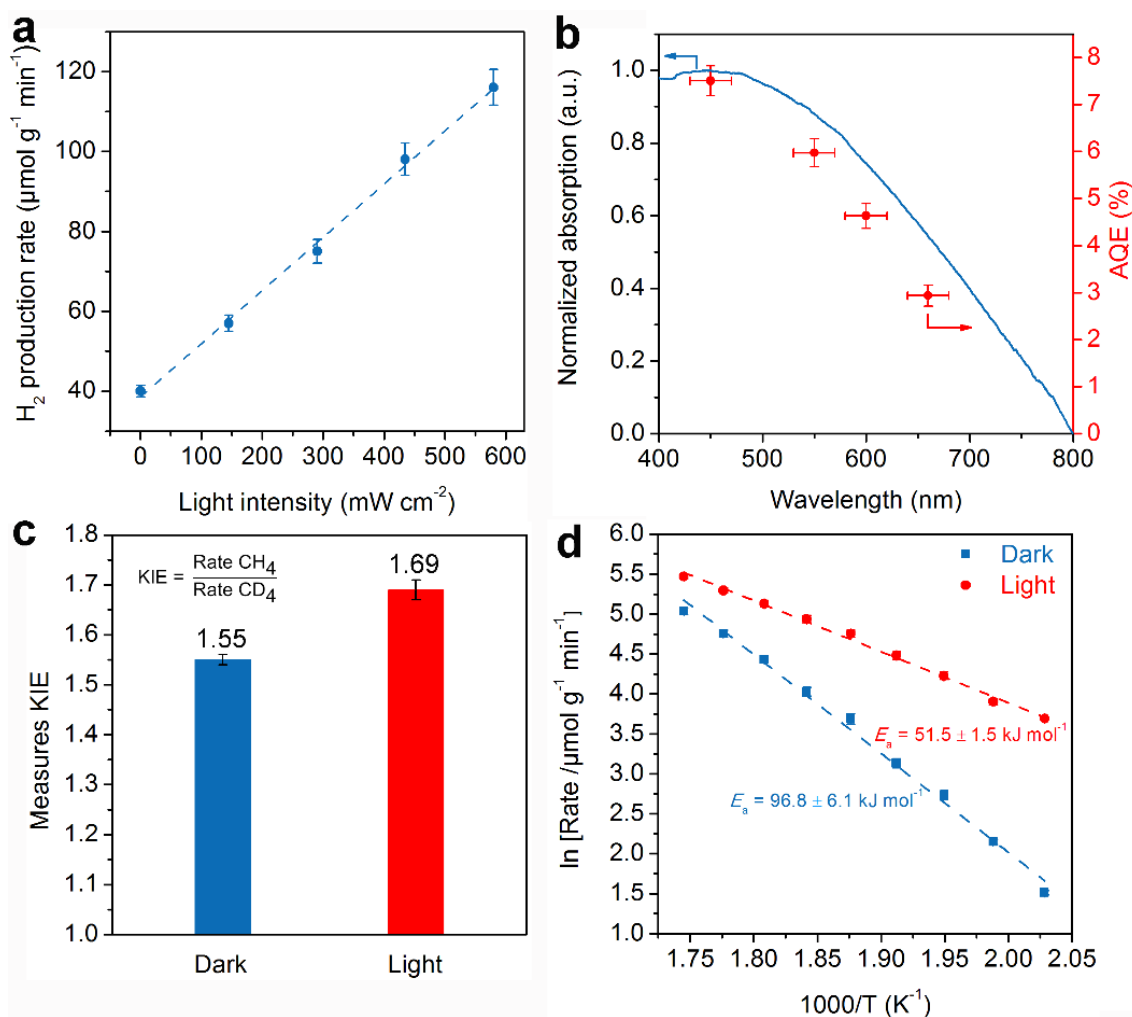
accelerated the reaction rates.

Figure 2.15 Features of hot carrier-driven reaction. (a) Dependence of H_2 production rate of Rh/TiO$_2$ at 260 °C on light intensity. (b) Normalized absorption and AQE values of Rh/TiO$_2$ at 260 °C with light irradiation of different wavelength ranges. (c) Influence of visible light illumination on kinetic isotope effects (KIEs) (CH$_4$ rate/CD$_4$ rate) over Rh/TiO$_2$ at 260 °C. (d) Arrhenius plots for H_2 production rate under dark and light conditions over Rh/TiO$_2$ catalysts. Error bars represent the standard deviation of three measurements with the same catalyst.

To understand the underlying mechanism, the reaction kinetics of SMR reaction over Rh/TiO$_2$ catalyst under dark condition and with light irradiation were investigated experimentally in the reaction temperature from 220 to 300 °C. The apparent activation energy was calculated by fitting the measured reaction rate (r) with Arrhenius equation (ln r = - E_a/RT + ln A), as shown in Figure 2.15d. The apparent activation energy under the dark was 96.8 kJ mol^{-1}, which is consistent with the

previous reports on the Rh-based catalysts.[48,49] By contrast, the apparent activation energy under light illumination was remarkably reduced to 51.5 kJ mol^{-1}, demonstrating that the photo-excitation of Rh intraband transition greatly assisted the activation process of CH$_4$.

2.4 Discussion

The above results reveal that hot carriers excited at Rh NPs play the key role in enhancing catalytic rates of SMR over Rh/TiO$_2$ catalyst. The Rh NPs were loaded on TiO$_2$ support by impregnation method, thus the way of Rh NPs depositing on the facets of TiO$_2$ is random. However, the hot electrons can be transferred from Rh NPs to the facets where Rh NPs were loaded as long as the hot electron energy is sufficiently high. From Figure 2.1, a positively charged surface states will be formed after the excitation hot electrons at Rh NPs and subsequent injection to the neighboring TiO$_2$ support. A consistent conclusion drawn by many latest studies has demonstrated that electron-deficient Rh (Rh$^+$ or Rh$^{\delta+}$) could facilitate the activation of C-H bond and boost the reaction activity of CH$_4$ reforming.[3,7,31] The femtosecond transient absorption (TA) spectroscopy was employed to track the electron transfer dynamics process at Rh-TiO$_2$ interface. As shown in Figure 2.16, the transient absorption spectra at 5000 nm for Rh/TiO$_2$, Rh/ZrO$_2$, and Rh/SiO$_2$ after 450 nm excitation reveal that the hot carrier separation process at Rh-ZrO$_2$ and Rh-SiO$_2$ interfaces were inhibited, while an ultrafast charge separation process was obviously identified by the fast-transient absorption rise. The transient absorption trace of Rh/TiO$_2$ was fitted with a rise time of 250 fs and a multi-exponential decay with time constants of 5.87 ps (58.19%), 40.84 ps (25.44%), 354.73 ps (10.14%) and 4995.43 ps (6.23%) (Table 2.1). As depicted by Figure 2.1, the hot carrier separation at metal-oxide interface is determined by the height of Schottky barrier. The oxide supports such as ZrO$_2$ and SiO$_2$ with extremely high CB restrains the hot electrons transfer from Rh to their CB. By contrast, TiO$_2$ with low CB favors the visible light-induced hot electron injection from Rh NPs into TiO$_2$. The formation of this transient absorption was within 250 fs, which is comparable to that of Au NPs/TiO$_2$ system (240 fs),[50] manifesting that hot electron injection process was completed promptly within 250 fs. The decay of the hot electrons can be assigned to the back-transfer process from TiO$_2$ to Rh NPs. The lifetimes of hot electrons are remarkably longer than the transfer process, suggesting that the Schottky junction at the Rh/TiO$_2$ interface can retard the hot carrier recombination process. Due to the hot electron injection to TiO$_2$, an electron-deficient state will be retained within the hot carrier lifetime at

Rh NPs counterpart, which plays the key role in reactant activation during the photo-oxidation process over nanometals.[24,25]
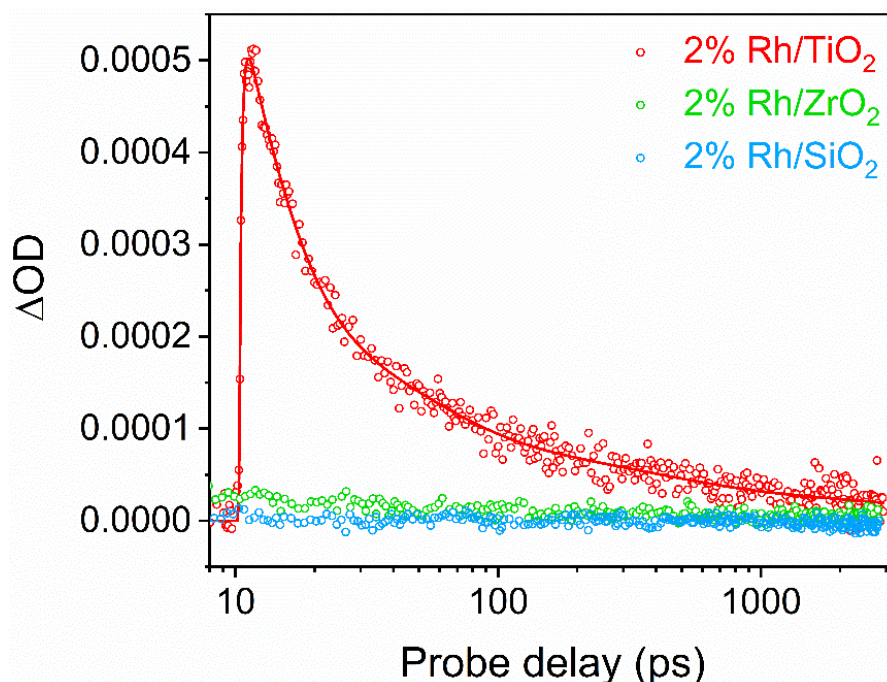

Figure 2.16 Ultrafast hot electron transfer. Transient absorption kinetics at 5000 nm of Rh/TiO_2 (red), Rh/ZrO_2 (green), Rh/SiO_2 (blue) catalysts under photoexcitation at 450 nm.

Table 2.1 Kinetics parameters of decays observed for 450 nm excited 2% Rh/TiO_2.

sample	τ_1 (ps)	τ_2 (ps)	τ_3 (ps)	τ_4 (ps)
2% Rh/TiO_2	5.87 ps (58.19%)	40.84 ps (25.44%)	354.73 ps (10.14%)	4995.43 ps (6.23%)

To further validate the transfer process of hot electrons from Rh to TiO_2, first principles molecular dynamics simulation[51] and the electronic structure calculations based on the density functional theory within local density approximation (DFT-LDA) were carried out. To mimic the reaction conditions and compare different support (TiO_2 and SiO_2) systems, the model consisting a metallic Rh slab, which was doped with Ti and Si at the surface (190 Rh, 1 Ti, and 1 Si atom), and the reactant molecules of $2CH_4$ and $4H_2O$ was employed. The snapshot and the electronic structure of the equilibrium structure at 247 °C are presented in Figure 2.17a and b. The CH_4 molecule was spontaneously dissociated at 247 °C at the surface. For the electronic properties[52,53], only significant

components are presented. The electrons in the system occupies up to -6.2 eV as indicated by the solid line. Both the occupied states and the unoccupied states (-6.0 to -5.0 eV) are mainly composed of Rh 4d orbitals. When investigating the components of the unoccupied Ti3d states and the unoccupied H1s states of the adsorbates produced by dissociative adsorptions, some interesting electronic properties were found. The unoccupied Ti 3d band is situated in the energy range from -5.0 to -3.0 eV and the unoccupied H 1s components originating in the absorbed -H on the Rh-based metallic slab are located just around the Ti 3d band. Therefore, electrons in Rh 4d orbitals can be excited to the unoccupied 4d, 5s, or 5p orbitals under visible light irradiation, followed by transfer into the unoccupied 3d band of Ti or injection into the unoccupied H1s orbitals. The photo-excited electrons are easily transferred to Ti 3d band with suppressing the recombination, leading to Rh surface in the electron-deficient state. The calculation results also demonstrate that although the concentration of Ti is very small (1/192 in atomic ratio) in the Rh based alloy, the Ti 3d component is very large (~0.15 at most in the energy range from -5 to -3 eV) and the band location in energy axis matches well the location of the band of unoccupied H1s. In addition, the maximum component of Si 3s and 3p are less than 0.01 and 0.025, indicating that hot electrons can hardly be transferred to SiO_2.
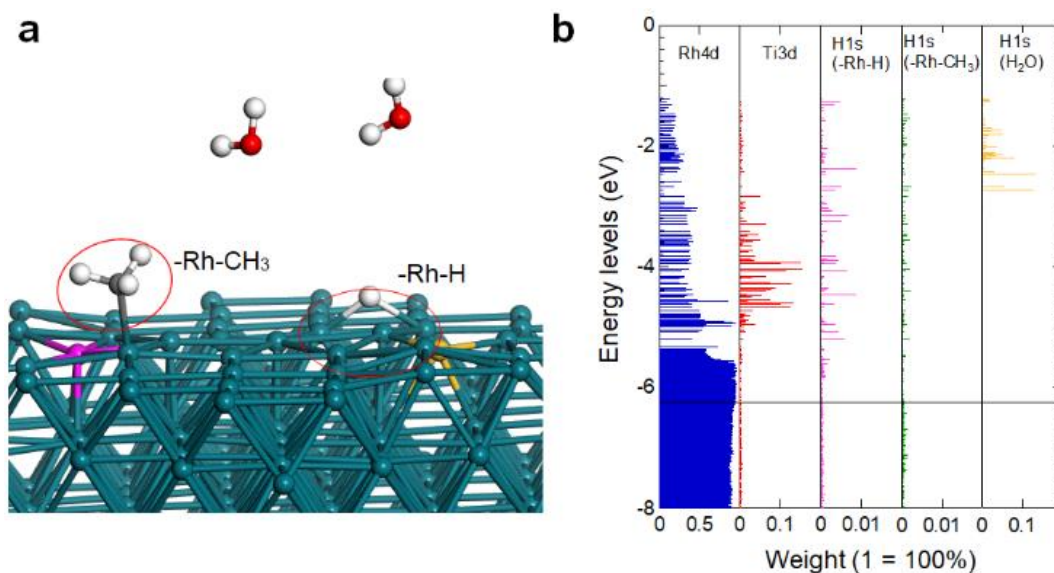
Figure 2.17 DFT calculations of Rh/TiO₂ in the reactant molecules of CH₄ and H₂O. (a) Snapshot of the equilibrium structure at 247 °C of the Rh metal doped with Ti and Si atom, which is intended to mimic the boundary area of Rh/TiO₂ and Rh/SiO₂ systems in the presence of CH₄ and H₂O. The color code is white for H, red for O, gray for C, aquamarine for Rh, pink for Ti and yellow for Si. (b) The corresponding electronic structure of the (a) system. A black solid line indicates the Fermi level.

Figure 2.18 Mechanism of hot carrier-enhanced SMR. (a) Schematic of energy transfer from phot-excited hot carriers to adsorbate states. Visible light-excited hot carriers can be separated quickly at the Rh/TiO2 surface; the positive charged Rh surface facilitates C-H bond activation, while the electron-rich sites at the interface favor the reduction process. (b) Proposed mechanism for SMR reaction on Rh/TiO2 under visible light illumination.
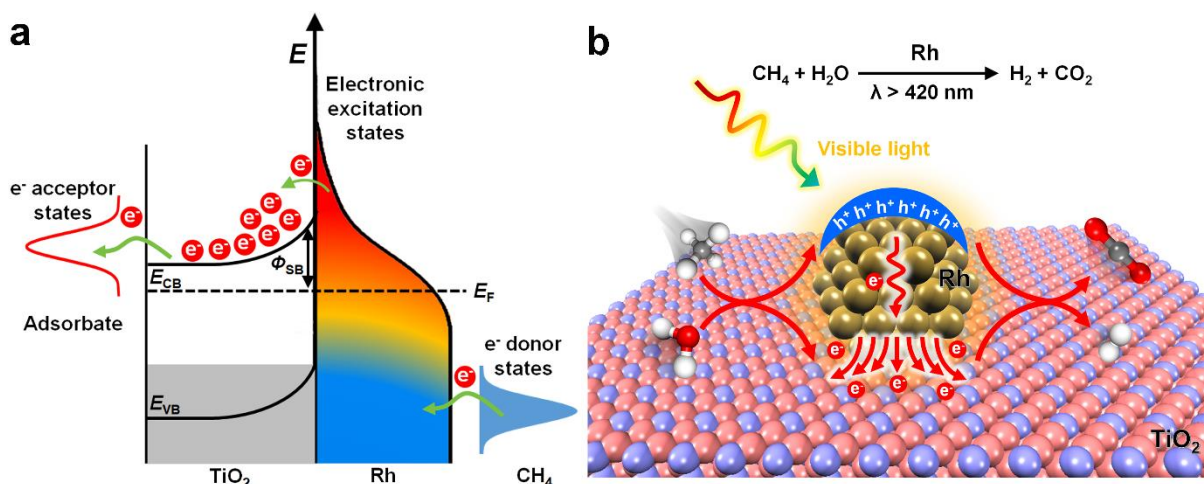
Figure 2.18 shows the proposed mechanism of hot carrier-driven SMR reaction on Rh/TiO2. For the thermal energy-driven SMR reaction, CH4 can be dissociated to H* and CH*x (x=0-3) species, and H2O is dissociated to H* and OH* species. After that, H2 and CO2 are generated through a sequence of intermediate reactions. The cleavage of C-H bonds of CH4 to form intermediate species (CHx*, x=0-3) is the rate limiting step and the thermal energy is mainly used to activate the C-H bond.[8,48] In the photo-thermocatalytic reaction, the SMR reaction on Rh/TiO2 catalysts is supposed to proceed the thermal energy-driven process. However, under visible light illumination, the electrons in the 4d orbitals of Rh NPs can be excited to high energy levels, generating hot electron-hole pairs. These hot electrons with high energies can be injected quickly into the CB of TiO2 within 250 fs (Figure 2.16). The Schottky junction at the Rh-TiO2 interface could trap the transferred hot electrons and delay them from transferring back to Rh NPs under continuous visible light irradiation. Thus, the electron-rich sites can be formed at the interface between Rh and TiO2, while the surface electronic state of Rh NPs are positively charged due to electronic depletion, leading to the formation of electron-deficient $Rh^{+\delta}$ sites at Rh surface. The electron-rich sites at Rh/TiO2 interface mediate the reduction of H* or OH* species into H2, and activate the adsorbates by depositing their energy into antibonding orbitals. At the same time, the electron-deficient counterpart, $Rh^{+\delta}$ sites are more liable

to accept σ electrons of CH_4 and facilitated C-H bond cleavage to yield CO_2 and H* species.[3,7,31] For Rh/ZrO$_2$ and Rh/SiO$_2$ catalysts, hot electrons excited from the interband transitions of Rh NPs are incapable of transferring into ZrO_2 and SiO_2 and forming spatial separation from the hot holes, so the surface electronic state of Rh NPs almost remain in the neutral state, which results in the lower visible light-driven photocatalytic activities compared to those of Rh/TiO$_2$.

2.5 Conclusions

In conclusion, I demonstrates that visible light excitation process of energetic hot carrier in TiO_2 supported Rh nanoparticles catalysts greatly assisted CH_4 activation for H_2 production via steam methane reforming at low temperature. The reaction apparent activation energy decreased by ~50% under light irradiation compared to that under dark condition. Ultrafast hot carriers separation occurred within 250 fs at Rh-TiO$_2$ interface, leading to the formation of a positively charged Rh surface state for the activation of C-H bond. The results demonstrated that the activation and conversion of CH_4 can be enhanced by controlling the surface electronic state of nanocatalysts by way of hot carriers transfer at the interface of catalytically active nanometal and its support. This study opens a new avenue towards the activation of commercially useful and tough reactions by constructing energy-efficient nanometal photocatalysts and using solar light.

References

1. Pakhare, and D., Spivey, J. (2014). A review of dry (CO$_2$) reforming of methane over noble metal catalysts. Chem. Soc. Rev. *43*, 7813-7837.

2. Agarwal, N., Freakley, S. J., McVicker, R. U., Althahban, S. M., Dimitratos, N., He, Q., Morgan, D. J., Jenkins, R. L., Willock, D. J., Taylor, S. H. , Kiely, C. J., and Hutchings, G. J. (2017). Aqueous Au-Pd colloids catalyze selective CH_4 oxidation to CH_3OH with O_2 under mild conditions. Science *358*, 223-227.

3. Shan, J., Li, M., Allard, L. F., Lee, S., and Flytzani-Stephanopoulos, M. (2017). Mild oxidation of methane to methanol or acetic acid on supported isolated rhodium catalysts. Nature *551*, 605-608.

4. Zuo, Z., Ramirez, P. J., Senanayake, S., Liu, P., and Rodriguez, J. A. (2016). The Low-Temperature Conversion of Methane to Methanol on CeO_x/Cu_2O catalysts: Water Controlled Activation of the C-H Bond. J. Am. Chem. Soc. *138*, 13810-13813.

5. Chen, X., Li, Y., Pan, X., Cortie, D., Huang, X., and Yi, Z. (2016). Photocatalytic oxidation of methane over silver decorated zinc oxide nanocatalysts. Nat. Commun. *7*, 12273.

6. Che, F., Gray, J. T., Ha, S., and McEwen, J.-S. (2017). Improving Ni Catalysts Using Electric Fields: A DFT and Experimental Study of the Methane Steam Reforming Reaction. ACS Catal. *7*, 551-562.

7. Olivos-Suarez, A. I., Szécsényi, À., Hensen, E. J. M., Ruiz-Martinez, J., Pidko, E. A., and Gascon, J. (2016). Strategies for the Direct Catalytic Valorization of Methane Using Heterogeneous Catalysis: Challenges and Opportunities. ACS Catal. *6*, 2965-2981.

8. Kechagiopoulos, P. N., Angeli, S. D., and Lemonidou, A. A. (2017). Low temperature steam reforming of methane: A combined isotopic and microkinetic study. Appl. Catal., B *205*, 238-253.

9. Halabi, M. H., de Croon, M. H. J. M., van der Schaaf, J., Cobden, P. D., and Schouten, J. C. (2010). Intrinsic kinetics of low temperature catalytic methane-steam reforming and water-gas shift over $Rh/Ce_\alpha Zr_{1-\alpha}O_2$ catalyst. Appl. Catal., A *389*, 80-91.

10. Halabi, M. H., de Croon, M. H. J. M., van der Schaaf, J., Cobden, P. D., and Schouten, J. C. (2010). Low temperature catalytic methane steam reforming over ceria-zirconia supported rhodium. Appl. Catal., A *389*, 68-79.

11. Angeli, S. D., Monteleone, G., Giaconia, A., and Lemonidou, A. A. (2014). State-of-the-art catalysts for CH_4 steam reforming at low temperature. Int. J. Hydrogen Energy *39*, 1979-1997.

12. Chung, W.-C., and Chang, M.-B. (2016). Review of catalysis and plasma performance on dry reforming of CH_4 and possible synergistic effects. Renewable and Sustainable Energy Rev. *62*, 13-31.

13. Wang, L., Yi, Y., Wu, C., Guo, H., and Tu, X. (2017). One-Step Reforming of CO_2 and CH_4 into High-Value Liquid Chemicals and Fuels at Room Temperature by Plasma-Driven Catalysis. Angew. Chem. Int. Ed. *56*, 13679-13683.

16. Zhang, Y., He, S., Guo, W., Hu, Y., Huang, J., Mulcahy, J. R., and Wei, W. D. (2017). Surface-Plasmon-Driven Hot Electron Photochemistry. Chem. Rev. *118*, 2927-2954.

15. Li, K., Hogan, N. J., Kale, M. J., Halas, N. J., Nordlander, and P., Christopher, P. (2017). Balancing Near-Field Enhancement, Absorption, and Scattering for Effective Antenna-Reactor Plasmonic Photocatalysis. Nano Lett. *17*, 3710-3717.

(16) Aslam, U., Chavez, S., and Linic, S. (2017). Controlling energy flow in multimetallic nanostructures for plasmonic catalysis. Nat. Nanotechnol. *12*, 1000-1005.

17. Christopher, P., Xin, H., and Linic, S. (2011). Visible-light-enhanced catalytic oxidation reactions on plasmonic silver nanostructures. Nat. Chem. *3*, 467-472.

18. Kale, M. J., Avanesian, T., and Christopher, P. (2013). Direct Photocatalysis by Plasmonic Nanostructures. ACS Catal. *4*, 116-128.

19. Christopher, P., Xin, H., Marimuthu, A., and Linic, S. (2012). Singular characteristics and unique chemical bond activation mechanisms of photocatalytic reactions on plasmonic nanostructures. Nat. Mater. *11*, 1044-1050.

20. Mukherjee, S., Zhou, L., Goodman, A. M., Large, N., Ayala-Orozco, C., Zhang, Y., Nordlander, P., and Halas, N. J. (2014). Hot-electron-induced dissociation of H_2 on gold nanoparticles supported on SiO_2. J. Am. Chem. Soc. *136*, 64-67.

21. Zhou, L., Zhang, C., McClain, M. J., Manjavacas, A., Krauter, C. M., Tian, S., Berg, F., Everitt, H. O., Carter, E. A., Nordlander, P., and Halas, N. J. (2016). Aluminum Nanocrystals as a Plasmonic Photocatalyst for Hydrogen Dissociation. Nano Lett. *16*, 1478-1484.

22. Clavero, C. (2014). Plasmon-induced hot-electron generation at nanoparticle/metal-oxide interfaces for photovoltaic and photocatalytic devices. Nat. Photon. *8*, 95-103.

23. Bian, Z., Tachikawa, T., Zhang, P., Fujitsuka, M., and Majima, T. (2014). Au/TiO_2 Superstructure-Based Plasmonic Photocatalysts Exhibiting Efficient Charge Separation and Unprecedented Activity. J. Am. Chem. Soc. *136*, 458-465.

24. Li, H., Qin, F., Yang, Z., Cui, X., Wang, J., and Zhang, L. (2017). New reaction pathway induced by plasmon for selective benzyl alcohol oxidation on BiOCl possessing oxygen vacancies. J. Am. Chem. Soc. *139*, 3513-3521.

25. Tsukamoto, D., Shiraishi, Y., Sugano, Y., Ichikawa, S., Tanaka, S., and Hirai, T. (2012). Gold nanoparticles located at the interface of anatase/rutile TiO_2 particles as active plasmonic photocatalysts for aerobic oxidation. J. Am. Chem. Soc. *134*, 6309-6315.

26. Sugano, Y., Shiraishi, Y., Tsukamoto, D., Ichikawa, S., Tanaka, S., and Hirai, T. (2013). Supported Au-Cu Bimetallic Alloy Nanoparticles: An Aerobic Oxidation Catalyst with Regenerable Activity by Visible-Light Irradiation. Angew. Chem. Int. Ed. *52*, 5295-5299.

27. Cushing, S. K., and Wu, N. (2016). Progress and Perspectives of Plasmon-Enhanced Solar Energy Conversion. J. Phys. Chem. Lett. *7*, 666-675.

28. Warren, S. C., and Thimsen, E. (2012). Plasmonic solar water splitting. Energy Environ. Sci. *5*, 5133-5146.

29. Robatjazi, H., Zhao, H., Swearer, D. F., Hogan, N. J., Zhou, L., Alabastri, A., McClain, M. J., Nordlander, P., and Halas, N. J. (2017). Plasmon-induced selective carbon dioxide conversion on earth-abundant aluminum-cuprous oxide antenna-reactor nanoparticles. Nat. Commun. *8*, 27.

30. Wang, C., and Astruc, D. (2014). Nanogold plasmonic photocatalysis for organic synthesis and clean energy conversion. Chem. Soci. Rev. *43*, 7188-7216.

31. Wang, R., Xu, H., Liu, X., Ge, Q., and Li, W. (2006). Role of redox couples of $Rh^0/Rh^{\delta+}$ and Ce^{4+}/Ce^{3+} in CH_4/CO_2 reforming over $Rh-CeO_2/Al_2O_3$ catalyst. Appl. Catal., A *305*, 204-210.

32. Zhang, X., Li, X., Zhang, D., Su, N. Q., Yang, W., Everitt, H. O., and Liu, J. (2017). Product selectivity in plasmonic photocatalysis for carbon dioxide hydrogenation. Nat. Commun. *8*, 14542.

33. Sarina, S., Zhu, H. Y., Xiao, Q., Jaatinen, E., Jia, J., Huang, Y., Zheng, Z., and Wu, H. (2004). Viable Photocatalysts under Solar-Spectrum Irradiation: Nonplasmonic Metal Nanoparticles. Angew. Chem. Int. Ed. *53*, 2935-2940.

34. Becke, A. D. (1988). Density-functional exchange-energy approximation with correct asymptotic behavior. Phys. Rev. A *38*, 3098-3100.

35. Lee, C., Yang, W., and Parr, R. G. (1988). Development of the Colle-Salvetti correlation-energy formula into a functional of the electron density. Phys. Rev. B *37*, 785-789.

36. Troullier, N., and Martins, J. L. (1991). Efficient pseudopotentials for plane-wave calculations. Phys. Rev. B *43*, 1993-2006.

37. Kawahara, T., Konishi, Y., Tada, H., Tohge, N., Nishii, J., and Ito, S. (2002). A patterned TiO_2 (anatase)/TiO_2 (rutile) bilayer-type photocatalyst: effect of the anatase/rutile junction on the photocatalytic activity. Angew. Chem. Int. Ed. *41*, 2811-2813.

38. Zettsu, N., McLellan, J. M., Wiley, B., Yin, Y., Li, Z. Y., and Xia, Y. (2006). Synthesis, Stability, and Surface Plasmonic Properties of Rhodium Multipods, and Their Use as Substrates for Surface-Enhanced Raman Scattering. Angew. Chem. Int. Ed. *45*, 1288-1292.

39. Pan, X., Yang, M, Fu, X., Zhang, N., and Xu, Y.-J. (2013). Defective TiO_2 with oxygen vacancies: synthesis, properties and photocatalytic applications. Nanoscale *5*, 3601-3614.

40. Ojeda, M., Granados, M. L., Rojas, S., Terreros, P., García-García, F. J., and Fierro, J. L. G. (2004). Manganese-promoted Rh/Al_2O_3 for C_2-oxygenates synthesis from syngas: Effect of manganese loading. Appl. Catal., A *261*, 47-55.

41. Suárez, S., Yates, M., Petre, A., Martin, J., Avila, P., and Blanco, J. (2010).   Development of a new Rh/TiO_2-sepiolite monolithic catalyst for N_2O decomposition. Appl. Catal., B 2006, *64*, 302-311.

42. Larichev, Y. V., Netskina, O., Komova, and O., Simagina, V. (2010). Comparative XPS study of Rh/Al_2O_3 and Rh/TiO_2 as catalysts for $NaBH_4$ hydrolysis. Int. J. Hydrogen Energy *35*, 6501-6507.

43. Novák, É., Fodor, K., Szailer, T., Oszkó, A., and Erdöhelyi, A. (2002). CO_2 hydrogenation on Rh/TiO_2 previously reduced at different temperatures. Top Catal. *20*, 107-117.

44. Ahmadi, M., Mistry, H., and Cuenya, B. R. (2016). Tailoring the Catalytic Properties of Metal Nanoparticles via Support Interactions. J. Phys. Chem. Lett., *7*, 3519–3533.

45. Park, J. Y., Baker, L. R., and Somorjai, G. A. (2015). Role of hot electrons and metal-oxide interfaces in surface chemistry and catalytic reactions. Chem. Rev. *115*, 2781-2817.

46. Che, F., Gray, J. T., Ha, S., Xu, H., and McEwen, J.-S. (2016). Reducing Reaction Temperature, Steam Requirements, and Coke Formation During Methane Steam Reforming Using Electric Fields: A Microkinetic Modeling and Experimental Study. ACS Catal. 2017*, 7,* 6957–6968.

47. Meng, X., Liu, L., Ouyang, S., Xu, H., Wang, D., Zhao, N., and Ye, J. (2016). Nanometals for Solar-to-Chemical Energy Conversion: From Semiconductor-Based Photocatalysis to Plasmon-Mediated Photocatalysis and Photo-Thermocatalysis. Adv. Mater. *28*, 6781-6803.

48. Wei, J., and Iglesia, E. (2004). Structural requirements and reaction pathways in methane activation and chemical conversion catalyzed by rhodium. J. Catal. *225*, 116-127.

49. Zeppieri, M., Villa, P. L., Verdone, N., Scarsella, M., and De Filippis, P. (2010). Kinetic of methane steam reforming reaction over nickel- and rhodium-based catalysts. Appl. Catal., A *387*, 147-154.

50. Furube, A., Du, L., Hara, K., Katoh, R., and Tachiya, M. (2007). Ultrafast plasmon-induced electron transfer from gold nanodots into TiO_2 nanoparticles. J. Am. Chem. Soc. *129*, 14852-14853.

51. Car, R., and Parrinello, M. (1985). Unified approach for molecular dynamics and density-functional theory. Phys. Rev. Lett. *55*, 2471-2474.

52. Oshikiri, M., Ye, J., and Boero, M. (2014). Inhomogeneous RVO_4 Photocatalyst Systems (R = Y, Ce, Pr, Nd, Sm, Eu, Gd, Tb, Dy, Ho, Er, Tm, Yb, Lu). J. Phys. Chem. C *118*, 8331-8341.

53. Johnson, B. G., Gill, P. M., and Pople, J. A. (1993). The performance of a family of density functional methods. *J. Chem. Phys. 98*, 5612-5626.

Chapter 3 Light-enhanced carbon dioxide reforming of methane by effective plasmonic coupling effect of Pt and Au nanoparticles

3.1 Introduction

The increasing of atmospheric carbon dioxide (CO_2) coming from excessive consumption of fossil fuels have generated much concerns about the consequent effects on the global climate change.[1-3] Photocatalytic CO_2 reduction on semiconductors, utilizing photo-induced electrons and holes to propel the simultaneous processes of CO_2 photoreduction and H_2O photooxidation, offer a promising and attractive route to take the advantage of abundant solar energy and recycle CO_2 resource.[4-8] However, the extreme inertness of CO_2 ($\Delta_f G^0 = -396$ kJ mol^{-1}) and the sluggish kinetics of multiple e^-/H^+ transfer process result in low energy conversion efficiency and uncontrollable selectivity for CO_2 photoreduction, indicating that it is still a great challenge to reduce CO_2 only using semiconductors and solar energy.[9-11] Currently, carbon dioxide reforming of methane (CRM) reaction based on Group VIII metal (Pt, Rh, Ru, Pd, Ni, etc.) catalysts can convert CH_4 by utilizing CO_2, one of the most abundant greenhouse gases, to produce industrially important syngas (H_2 and CO).[12-14] However, this reaction requires operating temperatures of 1100-1300 K to activate the reactants and achieve high equilibrium conversion of CH_4 and CO_2 to syngas, which waste a lot of heat energy and shorten catalyst lifetime via sintering deterioration and carbon deposition.[15] Great efforts have been devoted to improve conversion efficiency in CRM at lower temperatures over past few years,[13] but most of the reported ways were limited and few strategies were reported to directly reduce the activation energies of CRM reaction. Significant catalytic advances to reduce activation energies of reaction for simultaneously lowering reaction temperatures and boosting conversion efficiency are highly desirable.

Recently, it has been reported that plasmonic metallic nanostructures can efficiently drive chemical reactions with photo-excited charge carriers to overcome activation barriers, exhibiting a linear or super-linear dependence of reaction rates on incident light intensity.[16-20] Plasmonic nanostructures of metals (such as Ag, Au, Cu, Pd, Pt and Rh) exhibit strong light absorption through

an excitation of localized surface plasmon resonances (LSPR), which can be spectrally tuned throughout the UV or visible light by modulating the shape and size of metallic nanostructures.[21, 22] Interestingly, LSPR excitation produces a large number of energetic electrons (hot electrons) at the nanostructured surfaces that can transfer to adsorbates and promote reaction rates.[23-25] Recent studies have shown that Pt nanoparticles (NPs) as photocatalysts can drive catalysis and enhanced catalytic performances under light irradiation.[26, 27] We recently found that plasmonic Au NPs could effectively enhance the catalytic activity of Rh/SBA-15 in CRM reaction under visible light irradiation because Au could act as a plasmonic promoter to facilitate CRM.[28] Meanwhile, the reaction rate enhancement is closely related to the energy and distribution of hot electrons, which rely on the energy of the incident photon and the LSPR of metallic nanostructures as well as the local density-of-states in the nanostructures and the associated band structure. Therefore, it is expected that surface plasmonic coupling of two metal NPs with different excited LSPR peaks may be effectively utilize solar energy and induce more energetic hot electrons to inject into the adsorbates and/or specific reaction intermediates, thereby reducing activation energies and promoting reaction rates.[29-31]

In this chapter, I report that the plasmonic coupling effect of Pt and Au NPs can significantly reduce activation energies and enhance reaction rates of CH_4 conversion in CRM reaction. Under low-intensity light (300~800 nm, ~0.6 W cm^{-2}) irradiation, the activation energies for CH_4 conversion are reduced ~30% below thermal activation energies and the reaction rate is 2.3 times higher than that of the thermal-catalytic reaction rate at 400 °C. The wavelength-dependent performances show that not only UV but also visible light play important roles in facilitating CH_4 conversion rate. Finite-difference time-domain (FDTD) simulation indicate that effective coupling LSPR effect of Pt and Au NPs generates intense electric fields and hot electrons by absorbing UV and visible light. The transfer of hot electrons generated on the photoactivated Pt and Au surfaces to the adsorbed reactants and intermediate species can weaken the chemical bonds and reduce surface coverage of adsorbed species, reducing the activation energies of CH_4 and facilitating the reaction rates. The lower species coverage was detected by in situ DRIFTS analysis. Our research that effective coupling LSPR effect of Pt and Au NPs promote the CRM reaction via reducing the activation energies opens a new avenue for photo-mediated reactions on plasmonic metal NPs by utilizing solar energy.

3.2 Experimental section

3.2.1 Chemicals and materials

Chloroplatinic acid hexahydrate ($H_2PtCl_6 \cdot 6H_2O$), gold chloride trihydrate ($HAuCl_4 \cdot 3H_2O$), sodium carbonate (Na_2CO_3) and urea (CN_2OH_4) were purchased from Wako Co. Silicon dioxide, (SiO_2, nanopowder 5-15 nm (BET), 99.5% metals basis) was purchased from Sigma-Aldrich.

3.2.2 Preparation of catalysts

Preparation of Au/SiO$_2$: Au/SiO$_2$ catalysts with different loadings were prepared with urea-precipitation method. In general, 1.0 g SiO$_2$ was added into 100.0 mL of an aqueous solution of HAuCl$_4$ (0.51 mM) and urea (11.4 g). The suspension was maintained at 80 °C with vigorous stir for 4 h, then centrifuged, washed, dried and calcined at 400 °C for 4 h. The theoretical loadings of Au was 1.0 wt%.

Preparation of Pt-Au/SiO$_2$: Pt was loaded on Au/SiO$_2$ via the impregnation method. In general, 1.0 g Au/SiO$_2$ was added into 10.0 mL of an aqueous solution of H$_2$PtCl$_6$ (2.56, 5.13 and 7.69 mM)) and Na$_2$CO$_3$ (the weight ratio of Na and Pt is 2).   After impregnation, excess water was removed at 50 °C until dryness. Then samples were calcined at 400 °C for 4 h. The theoretical loadings of Pt were from 0.5 to 1.5 wt%.

Preparation of Pt/SiO$_2$ and Pt (No Na)/SiO$_2$: For Pt/SiO$_2$, 1.0 g SiO$_2$ was added into 10.0 mL of an aqueous solution of H$_2$PtCl$_6$ (2.56, 5.13 and 7.69 mM) and Na$_2$CO$_3$ (the weight ratio of Na and Pt is 2). Then, the sample was dried and calcined at 400°C. After that, Pt/SiO$_2$ with loadings of Pt from 0.5 to 1.5 wt% were obtained. The preparation of Pt (No Na)/SiO$_2$ was similar to the above method in addition to not adding Na$_2$CO$_3$.

In this paper, all the catalysts were *in-situ* reduced for 1h during CRM reaction. Unless otherwise stated, Pt-Au/SiO$_2$, Pt/SiO$_2$ and Au/SiO$_2$ were referred to the catalysts with Na modification and the theoretical Pt and Au loading of 0.5 and 1.0 wt%.

3.2.3 Characterization

The crystallographic phases of as-prepared samples were analyzed by X-ray diffraction (XRD)

method on an X'Pert PRO diffractometer with Cu Kα radiation. TEM and HR-TEM were employed on a FEI Tecnai G 2 F20 transmission electron microscope operated at 300 kV. HAADF-STEM images were taken on a JEOL 2100F microscope. The XPS spectra were analyzed on a Thermo ESCALAB-250 spectrometer using a monochromatic Al Kα radiation source (1486.6 eV) and the binding energies determined by XPS were corrected by reference to the adventitious carbon peak (284.7 eV) for every sample. The diffuse reflection spectra of the catalysts were investigated by ultraviolet–visible spectrophotometer (UV-2600, SHIMADZU Co., Japan). N_2 adsorption-desorption experiments were performed at 77 K to examine the Brunauer-Emmett-Teller surface area.

3.2.4 Photocatalytic activity measurements

The photocatalytic reaction was carried out at atmospheric pressure in a fixed-bed reactor system. Typically, 20 mg photocatalyst was used for each test and was placed uniformly in the alumina cell (diameter 8.5 mm, height 3 mm). In the experiments, the Pt and Au NPs and the SiO_2 were in well thermal equilibrium with each other due to their good thermal contact. The temperature was precisely measured and controlled by a thermocouple and TC-1000 temperature controller (JASCO), conducting the resistive heater to mitigate heating induced by light irradiation and keep the catalyst at the desired temperature. LA-251 Xe lamp equipped with HA30 filter (remove the IR light) was used to provide the light energy input. CO_2 and CH_4 (the molar ratio of 1:1) flowed into the reactor at a total flowrate of 20.0 ml/min. Firstly, the catalysts were *in-situ* reduced in CRM reaction for one hour. After the catalytic reactions were carried out for one hour, the effluent gas streams were analyzed using gas chromatograph (GC) equipped with a thermal conductivity (TCD) and a flame ionization detector (FID) to gain the relative amounts of CO_2, CH_4, CO and H_2.

3.2.5 In situ DRIFTS analysis

The DRIFTS analysis were measured at 400 °C by a FT/IR-6300 system (JASCO Corp.), equipped with an insitu DR cell and a liguid nitrogen cooled mercury-cadmium-telluride detector (MCT) (see details in Figure 3.1). The wavenumber resolution is 4 cm^{-1}. The catalyst (20 mg) was placed uniformly in the DR cell, then Ar (20 mL min^{-1}) was introduced into the cell at 400 °C for 30 min to acquired the background spectrum of the sample. Then CO_2+CH_4+Ar (1:1:2) mixture (10.0 mL min^{-1}) was introduced at 400 °C for 60 min. After that, the spectra were recorded at 400 °C under

CO_2+CH_4+Ar (1:1:2) mixture (10.0 mL min^{-1}) in the dark and light condition.
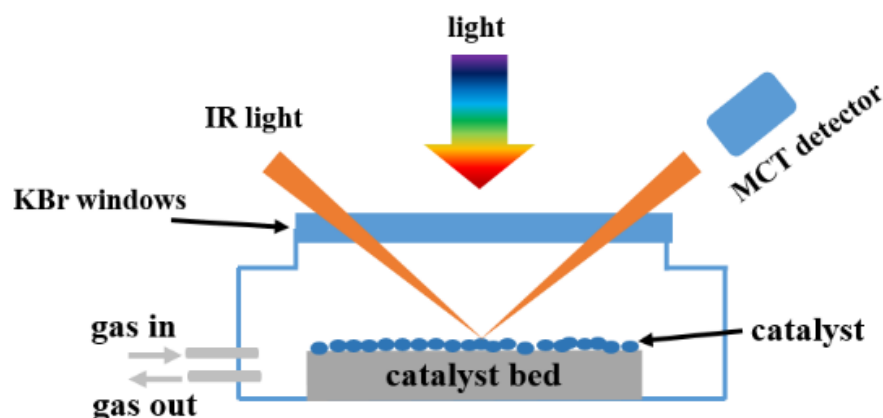

Figure 3.1 Schematic diagram of reactor cell for the in situ DRIFTS analysis.

3.2.6 Electromegnetic field simulation

The electromagnetic fields distributed around plasmonic Pt and Au nanoparticles were conducted using finite-difference time-domain (FDTD) methods (FullWAVE, Synopsys'RSoft). The dielectric functions of Rh, Au and SiO_2 were taken from the literature.[32]

3.3 Results

3.3.1 Catalyst characterization

Pt and Au with different loadings were loaded on SiO_2 (BET surface area, 436 m^2 g^{-1}) by impregnation and precipitation method and the actual Pt and Au loadings characterized by ICP-OES method were similar to the theoretical values (Table 3.1). Note that sodium ions (Na$^+$) were added in the process of loading Pt, since the addition of sodium ions could stabilize the dispersed Pt NPs and thereby improve the catalytic activity for CRM in thermal process.[35, 36] The representative high-angle annular dark-field scanning transmission electron microscopy (HAADF-STEM) images are shown in Figure 3.2. Without Na-modification, the average size of Pt NPs in Pt(Na free)/SiO_2 is around 3.0~4.0 nm, while the average size of Pt NPs in Pt/SiO_2 is around 1.5~2.5 nm with Na-modification. Figure 3.3 show that the catalytic activities of Pt/SiO_2 were remarkable improved after Na-modification.

Table 3.1 Elemental analysis of the catalysts

Samples	Pt (wt. %)[a]	Na (wt. %)[a]	Au (wt. %)[a]

0.5 wt. % Pt(Na free)/SiO$_2$	0.54	-	-
0.5 wt. % Pt/SiO$_2$	0.54	1.22	-
1.0 wt. % Pt(Na free)/SiO$_2$	0.98	-	-
1.0 wt. % Pt/SiO$_2$	1.01	2.34	-
1.5 wt. % Pt(Na free)/SiO$_2$	1.45	-	-
1.5 wt. % Pt/SiO$_2$	1.44	3.23	-
1.0 wt. % Au/SiO$_2$	-	-	0.89
0.5 wt. % Pt-1.0 wt. % Au/SiO$_2$	0.51	1.37	0.86

a, analyzed by ICP-OES method.

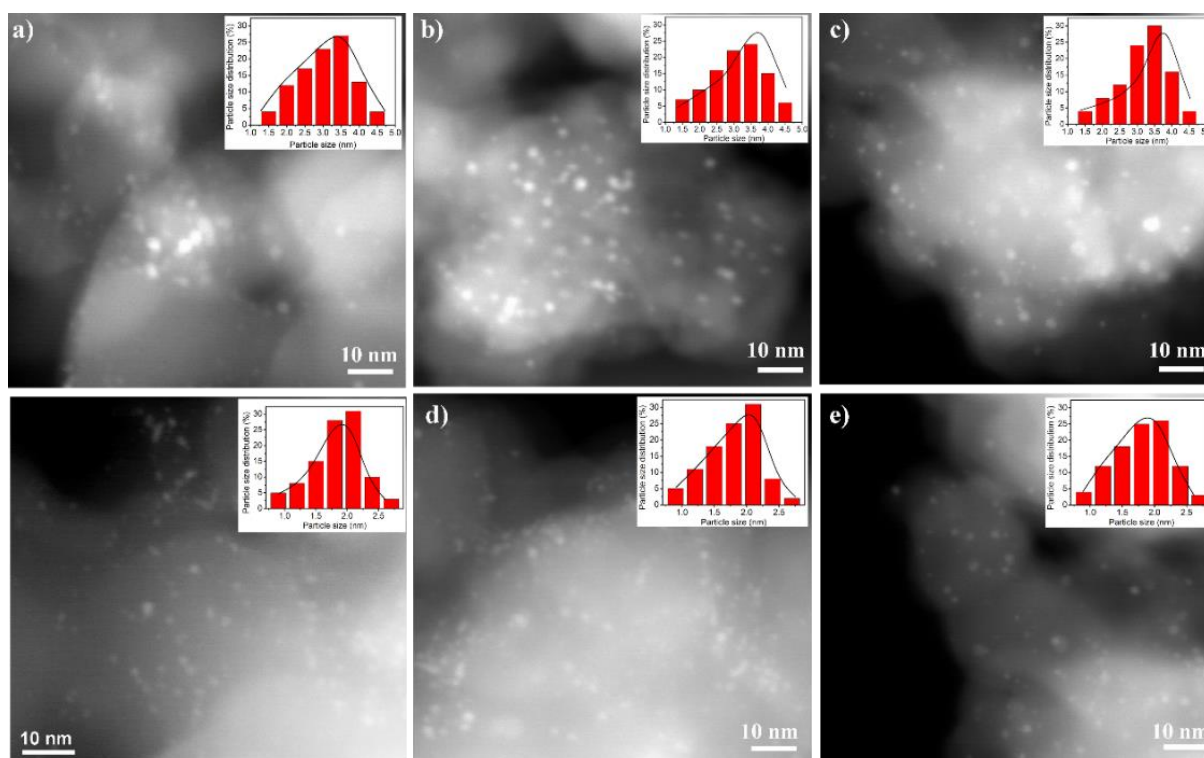**Figure 3.2** a, b, c, d, e and f are HAADF-STEM images of 0.5 wt. % Pt(Na free)/SiO$_2$, 1.0 wt. % Pt(Na free)/SiO$_2$, 1.5 wt. % Pt(Na free)/SiO$_2$, 0.5 wt. % Pt/SiO$_2$, 1.0 wt. % Pt/SiO$_2$ and 1.5 wt. % Pt/SiO$_2$, respectively.
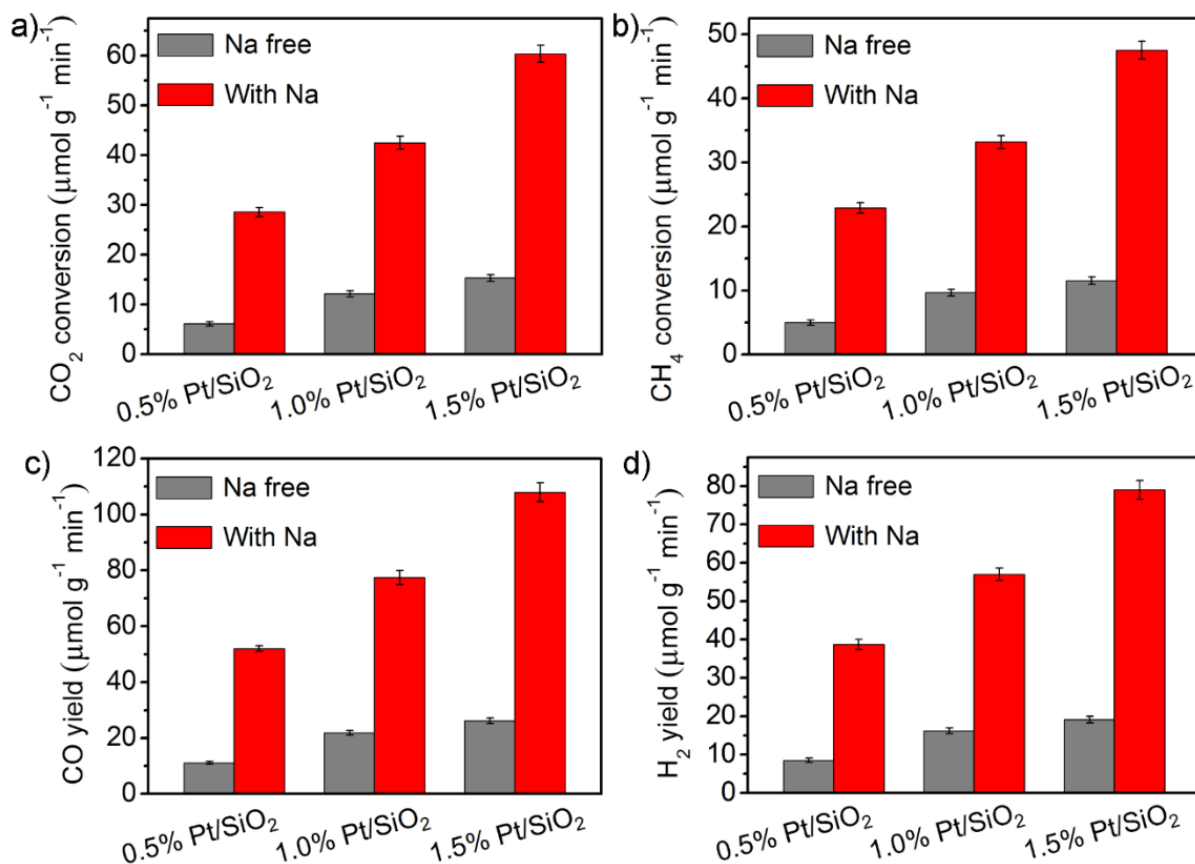
Figure 3.3 The catalytic activities of the catalysts in CRM reaction under thermal process (without light irradiation). (a) CO_2 conversion, (b) CH_4 conversion, (c) CO yield, and (d) H_2 yield. Reaction conditions: 20 mg catalyst, $CO_2/CH_4=1$, flowrate 20.0 mL min^{-1}, 400 °C.

Figure 3.4a and b present the representative HAADF-STEM and TEM images of Au/SiO$_2$. The size of Au NPs was in the range of 10-30 nm. Figure 3.4c and d show the HAADF-STEM image of Pt-Au/SiO$_2$. The size of Pt NPs almost remains unchanged and Pt NPs were indeed deposited on Au NPs except those directly deposited on SiO$_2$ support, while not all the Au NPs were loaded with Pt NPs. It is noted that this Pt-Au contact aggregate structures are thermodynamically stable and Au-Pt surface alloy is difficult to form.[37, 38] The crystalline structures of the catalysts were determined by XRD analysis (Figure 3.4e). The broad peak centered at 20-30° was ascribed to the amorphous SiO$_2$. The peaks located at 38.2°, 44.3°, 64.6° and 77.5° were assigned to the Au NPs. No peaks of Pt can be observed because of its low amount and small size. But XPS (Figure 3.4f) and ICP-OES analysis (Table 3.1) of the catalysts can detect the presence of Pt. XPS data also show that Pt and Au existed in a metallic state when loaded on the SiO$_2$ support.[39, 40]
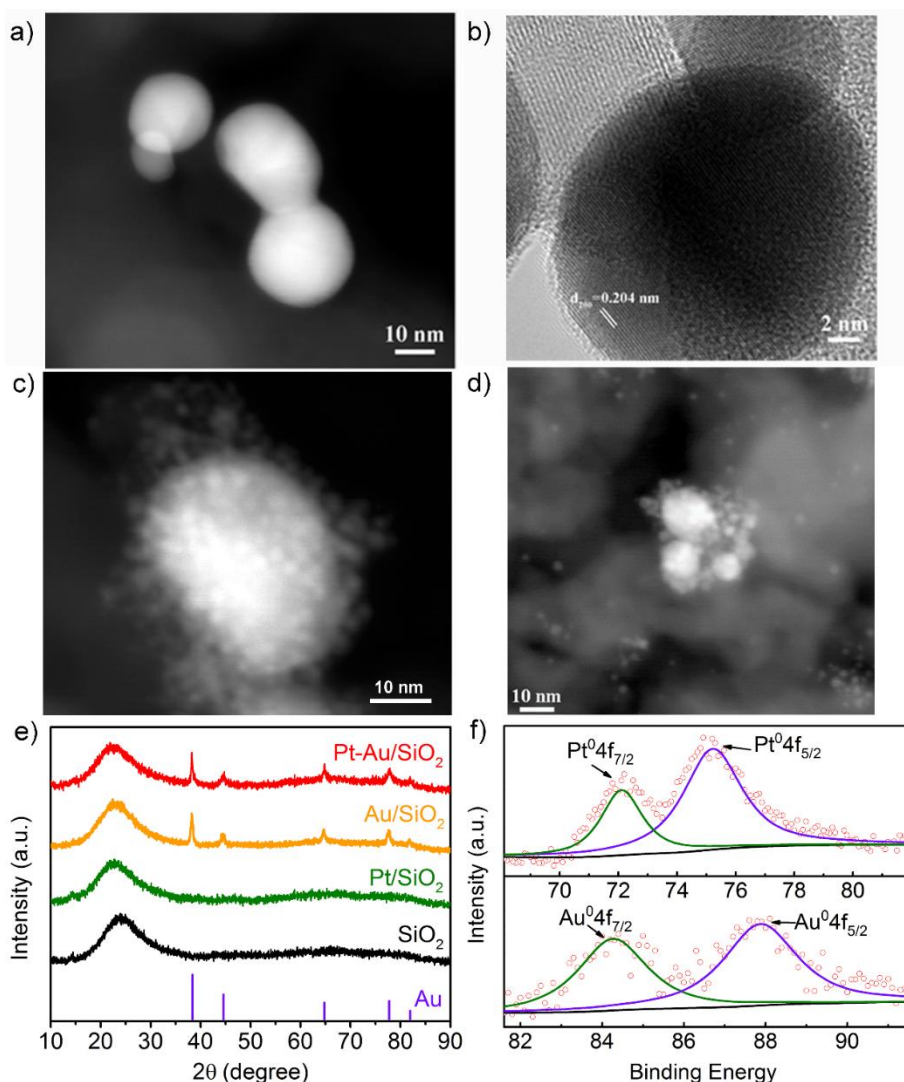
Figure 3.4 (a) HAADF-STEM and (b) TEM images of 1.0 wt. %Au/SiO2. (c) and (d) HAADF-STEM images of Pt-Au/SiO2. The Pt and Au NPs can be identified by their higher contrast. (e) XRD patterns of the catalysts. (f) Pt 4f and Au 4f XPS spectra of the spent Pt-Au/SiO2.

3.3.2 Photo-enhanced catalytic activity

The catalytic activities of the catalysts in CRM reaction with light irradiation (300 nm$<\lambda<$800 nm) at the same reaction temperature (400 °C) are shown in Figure 3.5 and Figure 3.6. As shown in Figure 3.5, for Pt/SiO2 catalysts with different Pt loadings, the catalytic activities were enhanced under UV-visible light irradiation (Figure 3.5a). The rate enhancement was around 1.6 when the content of Pt was lower than 1.0 wt%, which slightly reduced when Pt loadings was higher than 1.0 wt% (Figure 3.5b). Moreover, without light illumination, the thermal-catalytic activities of Pt-Au/SiO2 and Pt/SiO2 were almost the same, while the Au/SiO2 showed almost no performance in CRM reaction, which were in well agreement with our earlier report that Au could not activate the

reaction of CRM.[28] However, the reaction rates of Pt/SiO_2, $Pt-Au/SiO_2$ and Au/SiO_2 were all improved under irradiation of light. The reaction rates of Pt/SiO_2 and $Pt-Au/SiO_2$ exhibited a nearly linear dependence on the light intensity, and the increased slop of $Pt-Au/SiO_2$ was larger than that of Pt/SiO_2. The linear dependence of catalytic activity on the light intensity agrees well with the mechanism of photo-induced reactions driven by hot electrons.[17, 19, 31] The linear dependence further provides an indication that the localized heating, which usually induce an exponential dependence, is negligible in these reactions.[19] Additionally, the reaction rates of $Pt-Au/SiO_2$ were clearly greater than the sum of the reaction rates of Pt/SiO_2 and Au/SiO_2 at the same light intensity. Under light illumination (0.6 W cm^{-2}), the CH_4 conversion rates of $Pt-Au/SiO_2$ and Pt/SiO_2 were 55.1 and 37.4 $\mu mol\ g^{-1}\ min^{-1}$, which were about 2.3 and 1.6 times higher than those of the thermal-catalytic process (24 and 22.9 $\mu mol\ g^{-1}\ min^{-1}$), respectively. The catalyst undergone a little deactivation over 6 hours (Figure 3.7). It should be noted that CO_2 conversions were a little higher than CH_4 conversion and the sum of conversion of CO_2 and CH_4 is larger than the sum of yield of CO and H_2 because of the existing reverse water gas shift-reaction ($CO_2 + H_2 \rightarrow CO + H_2O$) as side reaction.[13] Meanwhile, the yields of CO and H_2 displayed similar increasing trends compared with the conversions of CH_4 and CO_2, and the mass balance was almost 100%. From the above results, it could be speculated that Pt and Au LSPR might have coupling effect to facilitate the activation of CH_4 and CO_2 and improve the catalytic activities in CRM reaction.
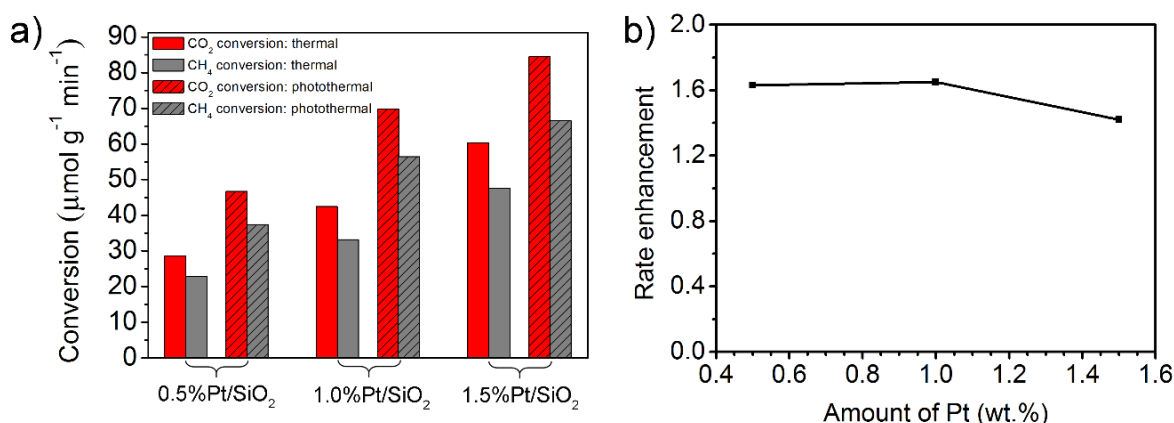

Figure 3.5 (a) CO_2 and CH_4 conversion of catalysts in thermal and photothermal process, (b) corresponding rate enhancement calculated by dividing the rate of the photothermal process by the rate of the thermal process. Reaction conditions: 20 mg catalyst, $CO_2/CH_4=1$, flowrate 20.0 mL min^{-1}, light intensity 0.6 W cm^{-2}, 400 °C, incident wavelength 300~800 nm.
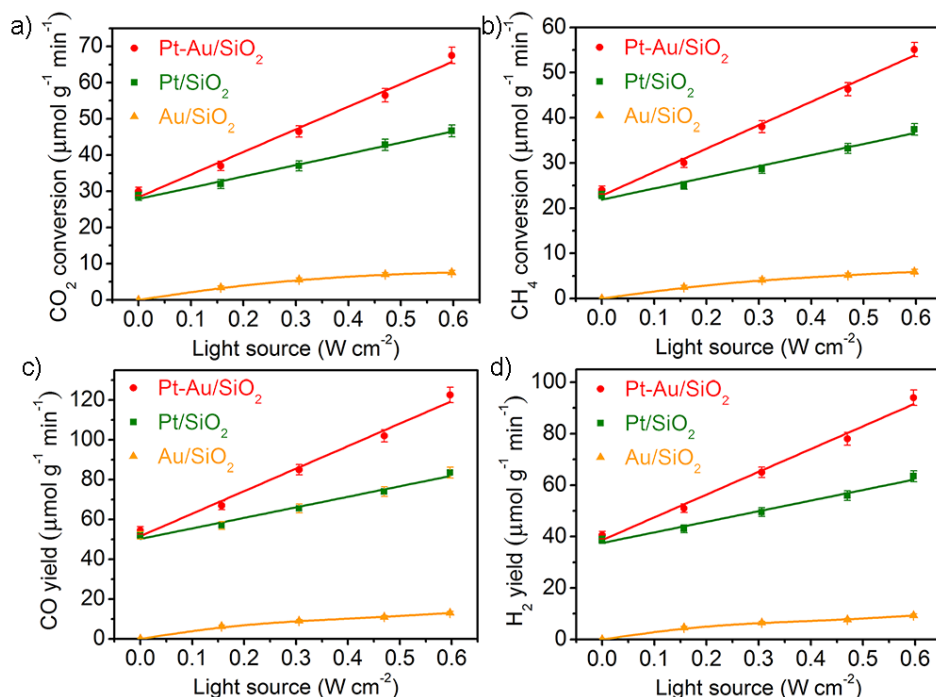
Figure 3.6 (a) CO_2 conversion, (b) CH_4 conversion, (c) CO yield, and d) H_2 yield. Reaction conditions: 20 mg catalyst, $CO_2/CH_4=1$, flowrate 20.0 mL min^{-1}, 400 °C, incident wavelength 300~800 nm.
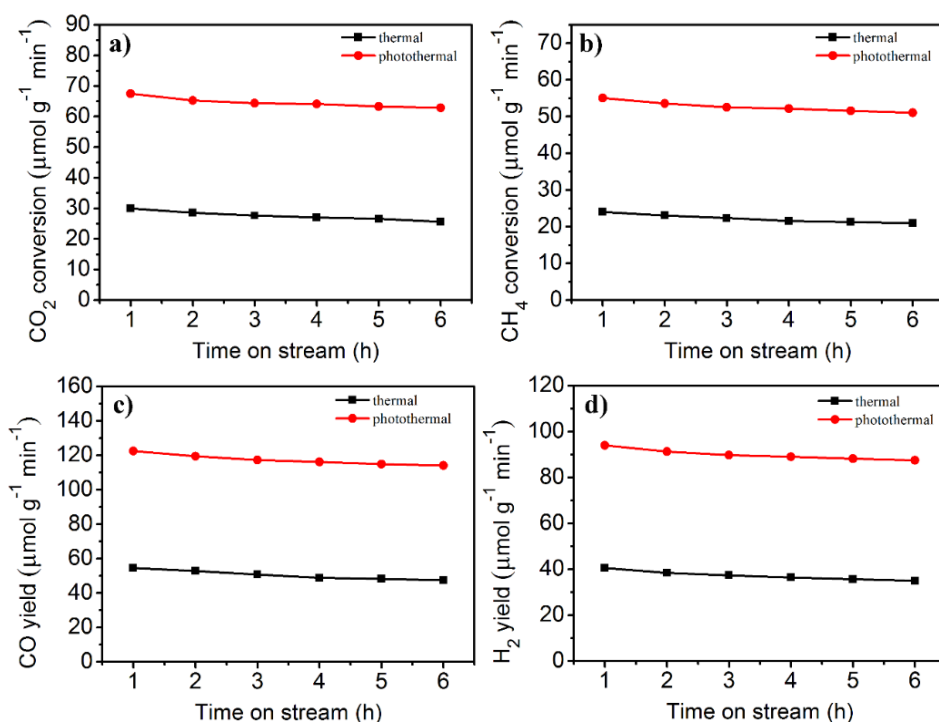

Figure 3.7 (a) CO_2 conversion, (b) CH_4 conversion, (c) CO yield, and (d) H_2 yield of Pt-Au/SiO$_2$ in thermal and photothermal process. Reaction conditions: 20 mg catalyst, $CO_2/CH_4=1$, flowrate 20.0 mL min^{-1}, light intensity 0.6 W cm^{-2}, 400 °C, incident wavelength 300~800 nm.
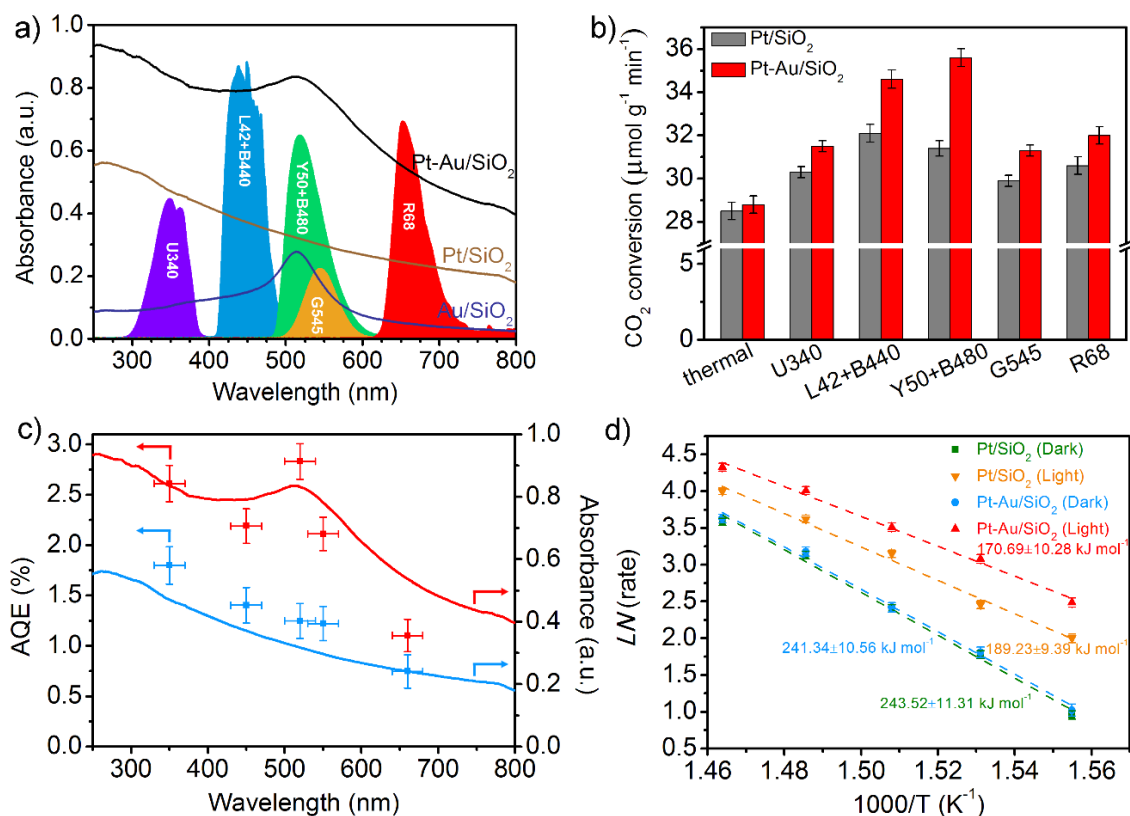
Figure 3.8 (a) UV-vis absorption spectra of (solid line) of Pt-Au/SiO₂, Pt/SiO₂ and Au/SiO₂; overlaid with spectra of light source obtained with filters U340, L42+B440, Y50+B480, G545 and R68. (b) CO₂ conversion rate (c) UV-vis absorption spectra and AQE values of Pt-Au/SiO₂ and Pt/SiO₂ without or with light irradiation of different wavelength ranges. (d) Arrhenius plot for CO₂ conversion rate under light and dark conditions for CRM reaction over Pt-Au/SiO₂ and Pt/SiO₂ catalysts; the intensity of y-axis is the natural logarithm of reaction rate at different reaction temperature. Reaction conditions: 20 mg catalyst, $CO_2/CH_4=1$, flowrate 20.0 mL min^{-1}, 400 °C, using different filters to obtain the desired wavelength range.

In order to demonstrate the observed photo-enhancement activities resulting from LSPR coupling effect of Pt and Au NPs, the impact of different irradiation wavelength on the catalytic activities of Pt-Au/SiO₂ and Pt/SiO₂ were performed (utilizing filters U340, L42+B440, Y50+B480, G545 and R68 to obtain the desired wavelength range, Figure 3.8a). By the irradiation of light, Pt/SiO₂ exhibited a broad SPR absorption from the range of UV to visible regions with a peak of around 275 nm (Figure 3.8a).[41, 42] Notably, interband transitions of Pt NPs can also contribute to the visible absorption.[43] While Au/SiO₂ displayed a strong SPR absorption peak centered at 520 nm (Figure 3.8a).[44] Interestingly, Pt-Au/SiO₂ also showed a broad absorption and two peaks locating at

275 and 520 nm (Figure 3.8a), combining the SPR absorption characteristics of both Pt/SiO_2 and Au/SiO_2, and the absorption intensity was remarkably enhanced and exceeded that of Pt/SiO_2 and Au/SiO_2. The catalytic activities of Pt/SiO_2 and $Pt-Au/SiO_2$ with the irradiation of different wavelengths of light were illustrated in Figure 3.8b. Clearly, the CH_4 conversion rates of Pt/SiO_2 and $Pt-Au/SiO_2$ were all improved under different wavelengths of light irradiation. Furthermore, the dependencies of the apparent quantum efficiency (AQE) of $Pt-Au/SiO_2$ and Pt/SiO_2 on the wavelength of irradiation showed the similar trend to the light absorption spectra of $Pt-Au/SiO_2$ and Pt/SiO_2, respectively (Figure 3.8c). Thus, it can be concluded that the observed activity enhancement was induced by the excitation of hot carrier. In addition, the AQE of $Pt-Au/SiO_2$ at the wavelength of 520 nm were higher than those at the other four wavelengths and higher than that of Pt/SiO_2 at 520 nm, indicating that surface plasmon and catalytic activity of Pt/SiO_2 were significantly enhanced by introducing Au NPs. It is also worth noting that plasmonic heating effect may also partly contribute to the enhanced activity, but due to the lack of accurate determination of the local surface temperature on Pt and Au NPs in this work, the relative contributions of hot carriers and plasmonic heating effect to the catalytic activity needs further investigation. All the above results suggested that the coupling LSPR effect of Pt and Au NPs both in UV and visible light range indeed promoted CRM reaction.

To understand the mechanism of CRM reaction under light irradiation, the reaction kinetics test on $Pt-Au/SiO_2$ and Pt/SiO_2 in light and dark were carried out. Figure 3.8d shows Arrhenius-type plots for the CO_2 conversion rate *versus* temperature. The apparent activation energy (E_a) of Pt/SiO_2 (243.52±11.31 kJ mol^{-1}) and $Pt-Au/SiO_2$ (241.34±10.56 kJ mol^{-1}) are similar under dark condition. Intriguingly, the E_a over Pt/SiO_2 and $Pt-Au/SiO_2$ decreased to 189.23±9.39 and 170.69±10.28 kJ mol^{-1} under light illumination, respectively. These changes in E_a suggested that the coupling LSPR effect changed the energetics of CRM reaction.[45]

In order to reveal the underlying mechanism, FDTD methods were conducted to calculate the intensity of electric near-field of catalysts. Figure 3.9 shows the electric fields distributions of the $Pt-Au/SiO_2$, Pt/SiO_2 and Au/SiO_2 under light excitation of 350 and 530 nm. The enhancement of the intensity of electric fields ($|E|^2$) at the surface of Pt NPs in Pt/SiO_2 can be clearly observed (Figure 3.9a and d). The enhancement of electric fields intensity in Pt/SiO_2 at the 530 nm wavelength was larger than that at the 350 nm wavelength because the near-field peak for $|E|^2$ were red-shifted with

respect to the far-field peak (absorption efficiency) (Figure 3.10), which was consistent with the previous report.[46] While the enhancement of electric fields intensity at the surface of Au NPs in Au/SiO$_2$ at the 530 nm wavelength (Figure 3.9b) was greater than that at the 350 nm wavelength (Figure 3.9e) due to its plasmon resonance in the visible light region (Figure 3.8a). When Au/SiO$_2$ was loaded with Pt NPs, the LSPR of Pt-Au/SiO$_2$ system was located in the UV and visible region (Figure 3.8a and 11). The intensities of electric fields on Pt-Au/SiO$_2$ at the 350 and 530 wavelengths were significantly higher than those of Pt/SiO$_2$ and Au/SiO$_2$ (Figure 3.9c and f), respectively, which could be explained by the strong near-field coupling between Pt and Au NPs. The generated strong electric fields yield high concentrations of hot electrons at the surface of the Pt and Au NPs. These electrons tend to be more energetic under thermal excitation (400 °C) and might play a vital role in activating chemical bonds in chemical transformations.
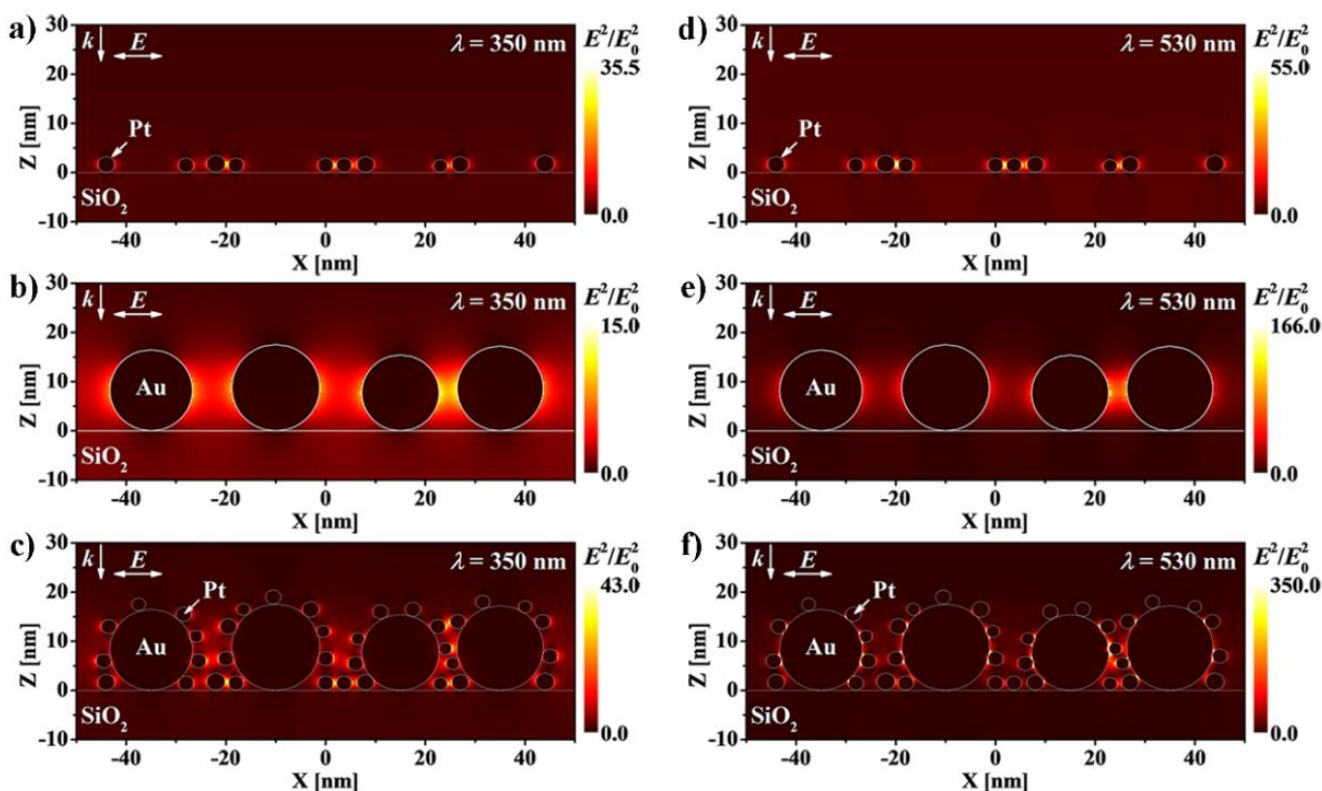

Figure 3.9 Spatial distribution of the enhancement of electric field intensity at the wavelength of 350 and 530 nm, from FDTD simulation of a and d) Pt/SiO$_2$, b and e) Au/SiO$_2$, and c and f) Pt-Au/SiO$_2$.
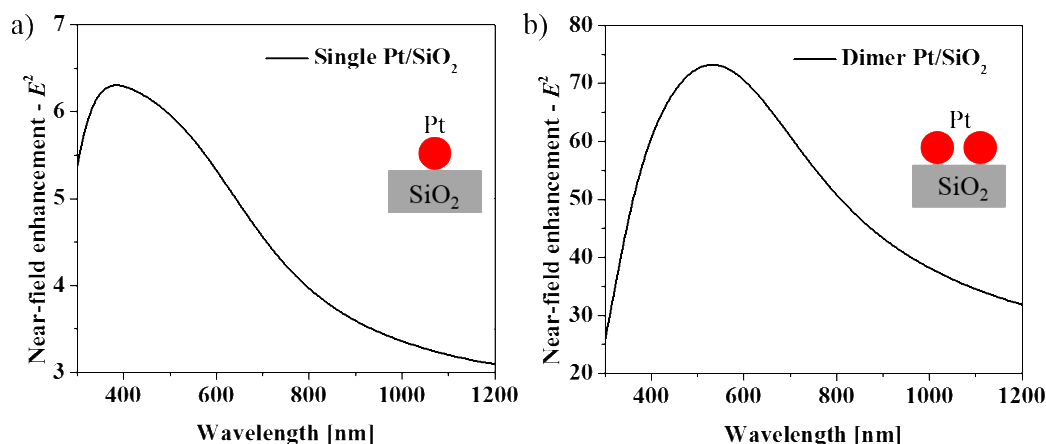
Figure 3.10 The near-field enhancement spectra of (a) single Pt nanoparticle/SiO_2 and (b) dimer Pt nanoparticles/SiO_2. The coupling between Pt nanoparticles with small gap could lead to a red-shift of the near-field enhancement spectrum.
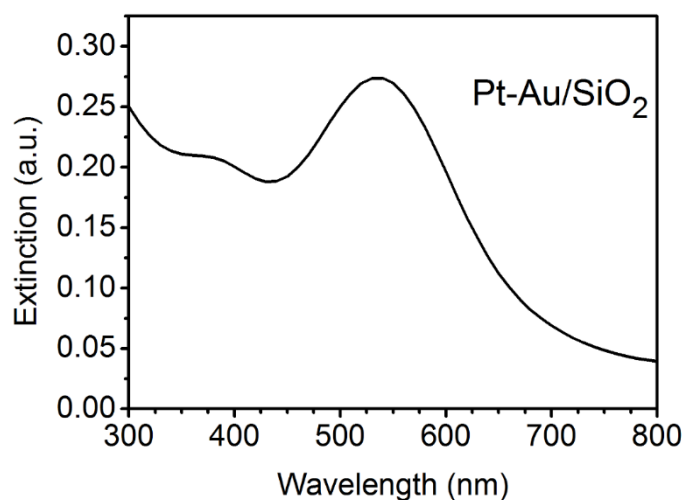

Figure 3.11 Simulated plasmonic absorption of Pt-Au/SiO_2.

To further determine how light influences the catalytic performances and examine the formed intermediate species in the reaction condition, the interaction between catalysts and CO_2 + CH_4 were investigated at 400 °C by DRIFTS. Figure 3.12 shows the infrared (IR) adsorption spectra of Pt/SiO_2 and Pt-Au/SiO_2 in dark and light conditions at 400 °C under CO_2 + CH_4 mixture. It could be seen that apart from the reactant gas phase contributions (CH_4 centered at ca. 3015 cm^{-1}, CO_2 centered at ca. 2349 cm^{-1}),[47] several peaks can also be observed. The broad peak centered at ca. 1500 cm^{-1} is characteristic of carbonate types species adsorbed on the support at high temperature.[47] The broad band at 2043 cm^{-1} is assigned to the CO stretch frequency of linearly bound, while the broad band at 1935 cm^{-1} is characteristic of 2-fold bridges (bridge-bonded) CO species (CO*) on Pt,[48] which can further desorb to form CO. In addition, the broad peak at 3500-3750 cm^{-1} is assigned to the surface

adsorbed hydroxyl (OH*) groups[49] and the peaks at 1309 and 1363cm^{-1} are characteristic of the adsorbed formate (COOH*) species.[50] The above results suggest that the HCOO*, CO* and OH* species are the main intermediate species in the process of CRM reaction. Moreover, the intensity of these peaks did not change with time in the reaction (Figure 3.13). Interestingly, the intensity of characteristic peaks of CO* and HCOO* species were obviously decreased under light illumination, resulting in the lower surface coverage of absorbed CO* and COOH* species. The lower species coverage means that the adsorbed CO* and COOH* species are more easily desorbed to form CO and H_2 under light irradiation, which could explain the enhancement of catalytic activities and the lower activation energy in CRM reaction.
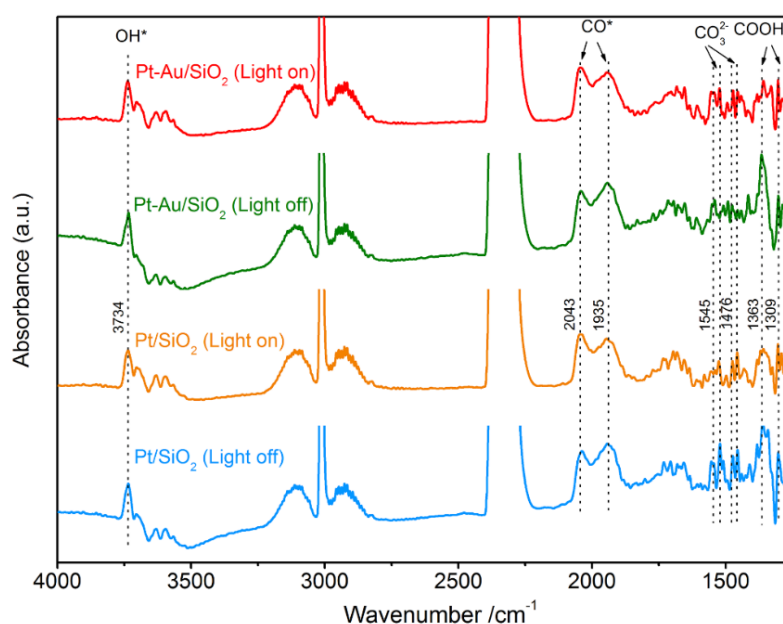

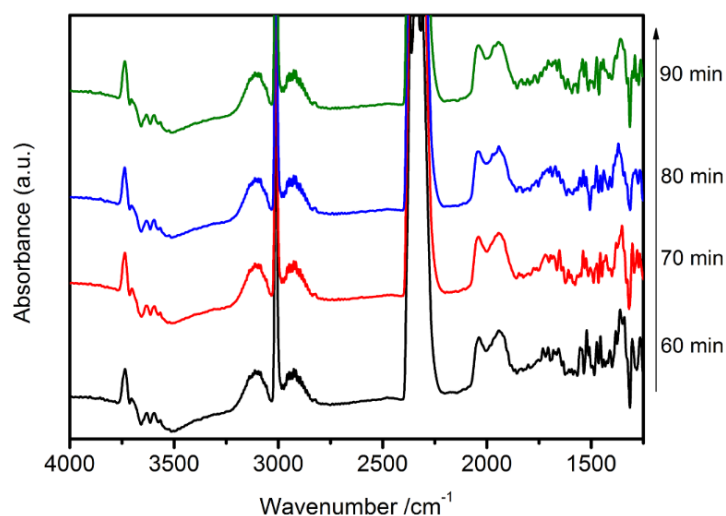**Figure 3.12** DRIFTS spectra of Pt-Au/SiO$_2$ and Pt/SiO$_2$ in the dark and light condition at 400 °C.

Figure 3.13 DRIFTS spectra of Pt-Au/SiO$_2$ and Pt/SiO$_2$ in the dark condition at 400 °C.

3.4 Discussion

The speculated mechanism of thermal and photo-thermal catalytic CRM reaction on Pt-Au/SiO2 can be explained by Figure 3.14. In the thermal catalytic reactions, CH_4 adsorbed on Pt surface are firstly dissociated to $CH*_{x(x=0-3)}$ and H*, then the adsorbed CO_2 react with H* to form COOH* species (Figure 3.14B.b) and subsequently generate CO* and OH* species (Figure 3.14B.c). After that, these intermediate species are subjected to a series of reactions to produce CO and H_2 (Figure 3.14B.h and i).[51-53] In these reactions, the dissociation of CH_4 are the main rate-determining step (RDS) in CRM reaction.[51, 54] For the photo-thermal reactions, as the catalysts were controlled and kept at the desired temperature (400 °C) even with irradiation of light, the CRM reaction over Pt-Au/SiO2 was also supposed to proceed via the thermally activated process (400 °C K). However, Pt-Au/SiO2 shows a broad LSPR absorption band covering the UV-to-visible spectral range. Under UV-visible light irradiation, the LSPR of Pt and Au are excited and the electric field intensities at Pt and Au NPs surface are significantly enhanced due to the presence of plasmonic coupling effect of Pt and Au. The induced strong electric field can effectively make the Pt surface sites more active.[31] Furthermore, the excited LSPR energy of Pt and Au can selectively dissipate through the active Pt surface sites and the energetic charge carriers (hot electrons and holes) are excited during LSPR-decay process and interband transitions of Pt NPs. The hot electrons can overcome the activation energy barrier and transfer to the LUMO (lowest unoccupied molecular orbital) of the adsorbed CO_2 and CH_4 molecules (Figure 3.14A and 3.14B.e) forming transient negative ions CO_2^- and CH_4^-, then decay back to the metal, which has been considered as one possible mechanism for plasmon-mediated chemical reaction in recent researches.[17, 19, 20] As a result, the energy originating from energetic carriers can deposit to C=O and C-H bonds to cause vibrational excitation and the bond elongation of C=O and C-H bonds, resulting in weakening the C=O and C-H bonds and facilitating bonds dissociation (RSD) and promoting CRM reaction rates. In a similar way, the hot electrons can also transfer to the adsorbed CO_2 and intermediate COOH* and CO* species (Figure 3.14A and 3.14B.e and f) to weaken the chemical bonds, lower surface coverage of adsorbed CO* and COOH* species (Figure 3.13) and accelerate the desorption of CO and H_2, resulting in reducing the activation energy for CO_2 reduction.[45] In addition, The mechanism of photo-thermal catalytic CRM reaction over Pt/SiO2 are similar to that of Pt-Au/SiO2, except that Pt-Au/SiO2 yield stronger electric field and generate more

energetic hot electrons compared with Pt/SiO$_2$ under irradiation of UV-visible light.
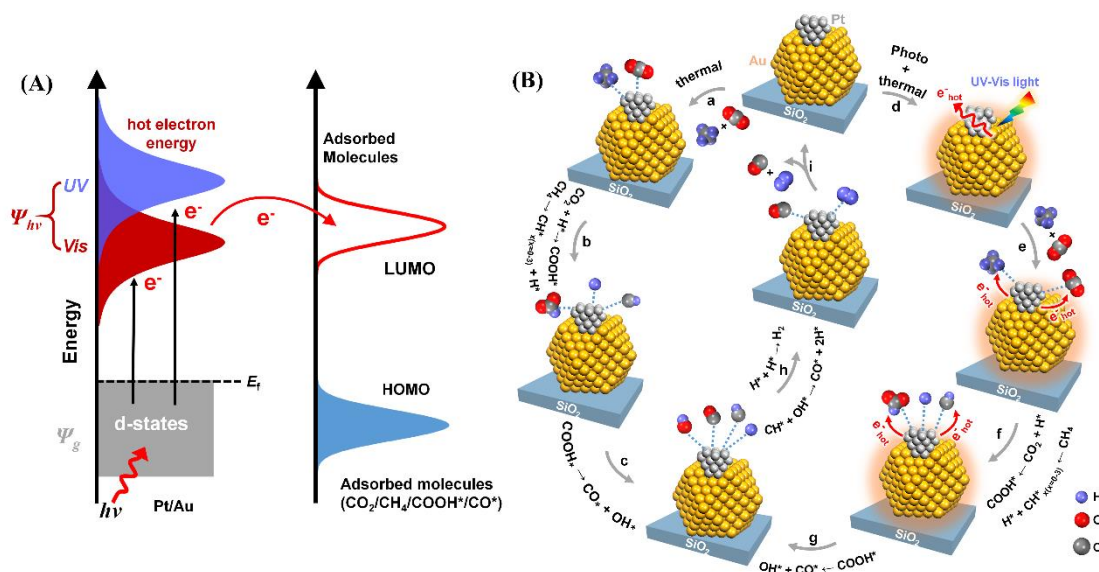

Figure 3.14 (A) Schematic of energy transfer from phot-excited plasmon states to molecular states. Light-excited hot electrons can be directly injected into the antibonding orbitals of the adsorbed reactants and intermediate species to weaken the chemical bonds and accelerate the desorption of products. (B) Proposed mechanism for CRM reaction on Pt-Au/SiO$_2$ in the dark or under UV-visible light illumination.

3.5 Conclusions

In conclusion, I have demonstrated the coupling of Pt and Au LSPR effect for efficient CH$_4$ conversion in CRM reaction using UV-vis light illumination. The plasmonic coupling effect reduces the activation energies and changes the energetics of the CRM reaction mechanism, with a reaction rate 2.3 times higher than that of the thermocatalytic reaction rate. Compared with our previous work on Rh-Au/SBA-15, in this work, I for first time utilized FDTD simulations, DFT calculations and in-situ DRIFTS experiments to demonstrate that both UV and visible light absorption of Pt-Au/SiO$_2$ generates stronger electric fields and excites high concentrations of hot electrons via effective coupling LSPR effect of Pt and Au NPs to activate the adsorbed reactants and intermediate species and facilitate the reaction rate. My findings suggest that it is possible to design more active bimetal plasmonic catalysts through rational combination of plasmonic metal promoter and reaction-selective metal catalyst.

References

1. Wang, W.-H., Himeda, Y., Muckerman, J. T., Manbeck, G. F., and Fujita, E. (2015). CO_2 Hydrogenation to Formate and Methanol as an Alternative to Photo-and Electrochemical CO_2 Reduction. Chem. Rev. *115*, 12936-12973.

2. Liang, L., Lei, F., Gao, S., Sun, Y., Jiao, X., Wu, J., Qamar, S., and Xie, Y. (2015). Single Unit Cell Bismuth Tungstate Layers Realizing Robust Solar CO_2 Reduction to Methanol. Angew. Chem. Int. Ed. *54*, 13971-13974.

3. Yu, J., Low, J., Xiao, W., Zhou, P., and Jaroniec, M. (2014). Enhanced Photocatalytic CO_2-Reduction Activity of Anatase TiO_2 by Coexposed {001} and {101} Facets. J. Am. Chem. Soc. *136*, 8839-8842.

4. Li, H., Shang, J., Zhu, H., Yang, Z., Ai, Z., and Zhang, L. (2016). Oxygen Vacancy Structure Associated Photocatalytic Water Oxidation of BiOCl. ACS Catal. *6*, 8276-8285.

5. Kuriki, R., Matsunaga, H., Nakashima, T., Wada, K., Yamakata, A., Ishitani, O., Maeda, K. Ishitani, and K. Maeda. (2016). Nature-Inspired, Highly Durable CO_2 Reduction System Consisting of a Binuclear Ruthenium (II) Complex and an Organic Semiconductor Using Visible Light. J. Am. Chem. Soc. *138*, 5159-5170.

6. Hoch, L. B., O'Brien, P. G., Jelle, A., Sandhel, A., Perovic, D. D., Mims, and C. A., Ozin. (2016). Nanostructured Indium Oxide Coated Silicon Nanowire Arrays: A Hybrid Photothermal/Photochemical Approach to Solar Fuels. ACS Nano *10*, 9017-9025.

7. Meng, X., Wang, T., Liu, L., Ouyang, S., Li, P., Hu, H., Kako, T., Iwai, H., Tanaka, A., and Ye, J. (2014). Photothermal Conversion of CO_2 into CH_4 with H_2 over Group VIII Nanocatalysts: An Alternative Approach for Solar Fuel Production. Angew. Chem. Int. Ed. *126*, 11662-11666.

8. Faunce, T., Styring, S., Wasielewski, M. R., Brudvig, G. W., Rutherford, A. W., Messinger, J., Lee, A. F., Hill, C. L., Fontecave, M., and MacFarlane, D. R. (2013). Artificial Photosynthesis as a frontier Technology for Energy Sustainability. Energy Environ. Sci. *6*, 1074-1076.

9. Zhang, H., Wang, T., Wang, J., Liu, H., Dao, T. D., Li, M., Liu, G., Meng, X., Chang, K., Shi, L., and Ye, J. (2013). Surface-Plasmon-Enhanced Photodriven CO_2 Reduction Catalyzed by Metal-Organic-Framework-Derived Iron Nanoparticles Encapsulated by Ultrathin Carbon Layers. Adv. Mater. *28*, 3703-3710.

10. Shi, H., Chen, G., Zhang, C., and Zou, Z. (2014). Polymeric g-C_3N_4 Coupled with $NaNbO_3$ Nanowires toward Enhanced Photocatalytic Reduction of CO_2 into Renewable Fuel. ACS Catal. *4*, 3637-3643.

11. Kondratenko, E. V., Mul, G., Baltrusaitis, J., Larrazábal, G. O., and Pérez-Ramírez, J. (2013). Status and Perspectives of CO_2 Conversion into Fuels and Chemicals by Catalytic, Photocatalytic and Electrocatalytic Processes. Energy Environ. Sci. *6*, 3112-3135.

12. Liu, H., Li, M., Dao, T. D., Liu, Y., Zhou, W., Liu, L., Meng, X., Nagao, T., and Ye, J. (2016). Design of PdAu Alloy Plasmonic Nanoparticles for Improved Catalytic Performance in CO_2 Reduction with Visible Light Irradiation. Nano Energy *26*, 398-404.

13. Pakhare, D., and Spivey, J. (2014). A Review of Dry (CO_2) Reforming of Methane over Noble Metal Catalysts. Chem. Soc. Rev. *43*, 7813-7837.

14. Wang, N., Shen, K., Huang, L., Yu, X., Qian, W., and Chu, W. (2013). Facile Route for Synthesizing Ordered Mesoporous Ni-Ce-Al Oxide Materials and Their Catalytic Performance for Methane Dry Reforming to Hydrogen and Syngas. ACS Catal. *3*, 1638-1651.

15. Rodriguez, J. A., Grinter, D. C., Liu, Z., Palomino, R. M., and Senanayake, S. D. (2017). Ceria-Based Model Catalysts: Fundamental Studies on the Importance of the Metal-Ceria Interface in CO oxidation, the Water-Gas Shift, CO_2 Hydrogenation, and Methane and Alcohol Reforming. Chem. Soc. Rev. *46*, 1824-1841.

16. Kale, M. J., Avanesian, T., and Christopher, P. (2013). Direct Photocatalysis by Plasmonic Nanostructures. ACS Catal. *4*, 116-128.

17. Christopher, P., Xin, H., Marimuthu, A., and Linic, S. (2012). Singular Characteristics and Unique Chemical Bond Activation Mechanisms of Photocatalytic Reactions on Plasmonic Nanostructures. Nat. Mater. *11*, 1044-1050.

18. Linic, S., Christopher, P., and Ingram, D. B. (2011). Plasmonic-Metal Nanostructures for Efficient Conversion of Solar to Chemical Energy. Nat. Mater. *10*, 911-921.

19. Christopher, P., Xin, H., and Linic, S. (2011). Visible-Light-Enhanced Catalytic Oxidation Reactions on Plasmonic Silver Nanostructures. Nat. Chem. *3*, 467-472.

20. Linic, S., Aslam, U., Boerigter, C., Morabito, M. Photochemical Transformations on Plasmonic Metal Nanoparticles. (2015). Nat. Mater. *14*, 567-576.

21. Meng, X., Liu, L., Ouyang, S., Xu, H., Wang, D., Zhao, N., and Ye, J. (2016). Nanometals for Solar-to-Chemical Energy Conversion: From Semiconductor-Based Photocatalysis to Plasmon-Mediated Photocatalysis and Photo-Thermocatalysis. Adv. Mater. *28*, 6781-6803.

22. Jiang, R., Li, B., Fang, C., and Wang, J. (2014). Metal/Semiconductor Hybrid Nanostructures for Plasmon-Enhanced Applications. Adv. Mater. *26*, 5274-5309.

23. Swearer, D. F., Zhao, H., Zhou, L., Zhang, C., Robatjazi, H., Martirez, J. M. P., Krauter, C. M., Yazdi, S., McClain, M. J., and Ringe, E. (2016). Heterometallic Antenna-Reactor Complexes for Photocatalysis. Proc. Natl Acad. Sci. USA *113*, 8916-8920.

24. Willets, K. A., and Van Duyne, R. P. (2007). Localized Surface Plasmon Resonance Spectroscopy and Sensing. Annu. Rev. Phys. Chem. *58*, 267-297.

25. Hutter, E., and Fendler, J. H. (2004). Exploitation of Localized Surface Plasmon Resonance. Adv. Mater. *16*, 1685-1706.

26. Kale, M. J., Avanesian, T., Xin, H., Yan, J., and Christopher, P. (2014). Controlling Catalytic Selectivity on Metal Nanoparticles by Direct Photoexcitation of Adsorbate-Metal Bonds. Nano Lett. *14*, 5405-5412.

27. Sarina, S., Zhu, H. Y., Xiao, Q., Jaatinen, E., Jia, J., Huang, Y., Zheng, Z., and Wu, H. (2014). Viable Photocatalysts under Solar-Spectrum Irradiation: Nonplasmonic Metal Nanoparticles. Angew. Chem. Int. Ed. *53*, 2935-2940.

28. Liu, H., Meng, X., Dao, T. D., Zhang, H., Li, P., Chang, K., Wang, T., Li, M., Nagao, T., and Ye, J. (2015). Conversion of Carbon Dioxide by Methane Reforming under Visible-Light Irradiation: Surface-Plasmon-Mediated Nonpolar Molecule Activation. Angew. Chem. Int. Ed. *54*, 11545-11549.

29. Aslam, U., Chavez, S., and Linic, S. (2017). Controlling Energy Flow in Multimetallic Nanostructures for Plasmonic Catalysis. Nat. Nanotechnol. *12*, 1000-1005.

30. Robatjazi, H., Zhao, H., Swearer, D. F., Hogan, N. J., Zhou, L., Alabastri, A., McClain, M. J., Nordlander, P., and Halas, N. J. (2017). Plasmon-Induced Selective Carbon Dioxide Conversion on Earth-Abundant Aluminum-Cuprous Oxide Antenna-Reactor Nanoparticles. Nat. Commun. *8*. 27.

31. Li, K., Hogan, N. J., Kale, M. J., Halas, N. J., Nordlander, P., and Christopher, P. (2017). Balancing Near-Field Enhancement, Absorption, and Scattering for Effective Antenna-Reactor Plasmonic Photocatalysis. Nano Lett. *17*, 3710-3717.

32. Palik, E. D. Handbook of optical constants of solids, Academic press, 1998, Vol. 3.

33. Kresse, G., and Furthmüller, J. (1996). Efficiency of Ab-Initio Total Energy Calculations for Metals and Semiconductors Using a Plane-Wave Basis Set. Comput. Mater. Sci. *6*, 15-50.

34. Grimme, S. (2006). Semiempirical GGA-Type Density Functional Constructed with a Long-Range Dispersion Correction. J. Comput. Chem. *27*, 1787-1799.

35. Zhang, C., Liu, F., Zhai, Y., Ariga, H., Yi, N., Liu, Y., Asakura, K., and Flytzani-Stephanopoulos, M., and He, H. (2012). Alkali-Metal-Promoted Pt/TiO_2 Opens a More Efficient Pathway to Formaldehyde Oxidation at Ambient Temperatures. Angew. Chem. Int. Ed. *51*, 9628-9632.

36. Zhai, Y., Pierre, D., Si, R., Deng, W., Ferrin, P., Nilekar, A. U., Peng, G., Herron, J. A., Bell, D. C., and Saltsburg, H. (2010). Alkali-Stabilized Pt-OHx Species Catalyze Low-Temperature Water-Gas Shift Reactions. Science *329*, 1633-1636.

37. Massalski, T. B., Murray. J. L., Bennett, H., and Baker, H. *Binary Alloy Phase Diagram*, Vol. 1, American society for metals, Metals Park, OH 1986.

38. Zhou, S., Jackson, G. S., and Eichhorn, B. (2007). AuPt Alloy Nanoparticles for CO-Tolerant Hydrogen Activation: Architectural Effects in Au-Pt Bimetallic Nanocatalysts. Adv. Funct. Mater. *17*, 3099-3104.

39. Wang, Y., Yu, J., Xiao, W., and Li, Q. (2014). Microwave-Assisted Hydrothermal Synthesis of Graphene Based $Au-TiO_2$ Photocatalysts for Efficient Visible-Light Hydrogen Production. J. Mater. Chem. A. *2*, 3847-3855.

40. Zhai, Q., Xie, S., Fan, W., Zhang, Q., Wang, Y., Deng, W., and Wang, Y. (2013). Photocatalytic Conversion of Carbon Dioxide with Water into Methane: Platinum and Copper (I) Oxide Co-catalysts with a Core-Shell Structure. Angew. Chem. Int. Ed. *125*, 5888-5891.

41. Zoric, I., Zäch, M., Kasemo, and B., Langhammer, C. (2011). Gold, Platinum, and Aluminum Nanodisk Plasmons: Material Independence, Subradiance, and Damping Mechanisms. ACS Nano 2011, *5*, 2535-2546.

42. Bigall, N. C., Härtling, T., Klose, M., Simon, P., Eng, L. M., and Eychmüller, A. (2008). Monodisperse Platinum Nanospheres with Adjustable Diameters from 10 to 100 nm: Synthesis and Distinct Optical Properties. Nano Lett. *8*, 4588-4592.

43. Bohren, C. F. (1983). How Can a Particle Absorb More Than the Light Incident on It?. Am. J. Phys. *51*, 323-327.

44. Mukherjee, S., Libisch, F., Large, N., Neumann, O., Brown, L. V., Cheng, J., Lassiter, J. B., Carter, E. A., Nordlander, P., and Halas, N. J. (2013). Hot Electrons Do the Impossible: Plasmon-Enduced Dissociation of H_2 on Au. Nano Lett. *13*, 240-247.

45. Upadhye, A. A., Ro, I., Zeng, X., Kim, H. J., Tejedor, I., Anderson, M. A., Dumesic, J. A., and Huber, G. W. (2015). Plasmon-Enhanced Reverse Water Gas Shift Reaction over Oxide Supported Au Catalysts. Catal. Sci. Technol. *5*, 2590-2601

46. Sanz, J., Ortiz, D., Alcaraz De La Osa, R., Saiz, J., González, F., Brown, A., Losurdo, M., Everitt, H., and Moreno, F. (2013). UV Plasmonic Behavior of Various Metal Nanoparticles in the Near- and Far-Field Regimes: Geometry and Substrate Effects. J. Phys. Chem. C *117*, 19606-19615.

47. Ferreira-Aparicio, P., Rodrıguez-Ramos, I., Anderson, J., and Guerrero-Ruiz, A. (2000). Mechanistic Aspects of the Dry Reforming of Methane over Ruthenium Catalysts. Appl. Catal., A *202*, 183-196.

48. Zhu, X., Huo, P., Zhang, Y.-p., Cheng, D.-g., and Liu, C.-j. (2008). Structure and Reactivity of Plasma Treated Ni/Al_2O_3 Catalyst for CO_2 Reforming of Methane. Appl. Catal., B *81*, 132-140.

49. Lin, H., Long, J., Gu, Q., Zhang, W., Ruan, R., Li, Z., and Wang, X. (2012). In situ IR Study of Surface Hydroxyl Species of Dehydrated TiO_2: towards Understanding Pivotal Surface Processes of TiO_2 Photocatalytic Oxidation of Toluene. Phys. Chem. Chem. Phys. *14*, 9468-9474.

50. Bai, S., Shao, Q., Wang, P., Dai, Q., Wang, X., and Huang, X. (2017). Highly Active and Selective Hydrogenation of CO_2 to Ethanol by Ordered Pd-Cu Nanoparticles. J. Am. Chem. Soc. *139*, 6827-6830.

51. Niu, J., Du, X., Ran, J., and Wang, R. (2016). Dry (CO_2) Reforming of Methane over Pt Catalysts Studied by DFT and Kinetic Modeling. Appl. Surf. Sci. *376*, 79-90.

52. Tang, W., Hu, Z., Wang, M., Stucky, G. D., Metiu, H., and McFarland, E. W. (2010). Methane Complete and Partial Oxidation Catalyzed by Pt-Doped CeO_2. J. Catal. *273*, 125-137.

53. Laosiripojana, N., and Assabumrungrat, S. (2005). Catalytic Dry Reforming of Methane over High Surface Area Ceria. Appl. Catal., B *60*, 107-116.

54. Wei. J., and Iglesia, E. (2004). Mechanism and Site Requirements for Activation and Chemical Conversion of Methane on Supported Pt Clusters and Turnover Rate Comparisons among Noble Metals. J. Phys. Chem. B. *108*, 4094-4103.

Chapter 4 Visible light-promoted carbon dioxide reforming of methane over Pt/TaN catalysts

4.1 Introduction

Photo-catalytically converting CH_4 into valuable fuels is beneficially for solar energy utilization and environmental protection.[1-4] Recently, photo-enhanced carbon dioxide reforming of methane (CRM) has emerged as a promising avenue for CH_4 and CO_2 utilization and attracted the attentions of scientists, since it is a thermodynamically uphill reaction and produces syngas with a suitable ratio for the down-stream Fischer-Tropsch process.[5,6] Plasmonic group 8 and 11 elements were mainly used as the optical component of the catalysts for photo-enhanced reaction systems.[7,8] It was reported that, with appropriate light-absorber (Au) in the catalyst, light irradiation was capable of enhancing the activity of a catalyst in CRM at low temperatures.[9] However, the light-absorbers, especially the noble plasmonic metals, are expensive and not applicable for large-scale industrial utilization. In this sense, it is of great significance to explore cheap and suitable optical materials as alternatives.

Tantalum mononitride (TaN), even though there were already some researches on investigating its optical properties, to the best of my knowledge, up to now, there were no reports on harnessing the optical property of TaN in photocatalytic reactions.[10-12] In this chapter, it was discovered that, in spite that TaN itself was inactive in CRM, TaN was a suitable optical support to enhance the activities of its supported group 8 metal catalysts in CRM with visible light assistance. To give a reasonable explanation about the interesting phenomena, the origination of the optical property of TaN and mechanism study were investigated via a theoretical study.

4.2 Experimental section

4.2.1 Chemicals and materials

$H_2PtCl_6 \cdot 6H_2O$, $HAuCl_4 \cdot 4H_2O$ (Wako, 99.9%), TaN, Ta_2O_5, GaN, ZnO, TiN and ZrN were purchased from Wako.

4.2.2 Preparation of catalysts

Pt/TaN, Pt/Ta$_2$O$_5$, Pt/GaN, Pt/ZnO, Pt/TiN and Pt/ZrN were prepared by loading a certain amount of H$_2$PtCl$_4$ on support by wetness impregnation method. After impregnating for 10 h, the samples were evaporated and dried at 80 °C and calcined at 500 °C for 1 h. Pd/TaN and Ir/TaN were prepared by a similar method.

As a reference, Pt-Au/Ta$_2$O$_5$ was prepared by impregnating Pt/Ta$_2$O$_5$ with H$_2$AuCl$_4$ aqueous solution, and the theoretical loading of Au is 1.0 wt%.

4.2.3 Characterization

The crystalline structures of TaN and the supported catalysts were analyzed by X-ray diffraction (XRD) method, on an X-Pert diffractometer equipped with graphite monochromatized Cu-Kα radiation. The specific surface areas were determined with a surface area analyzer (BEL Sorp-II mini, BEL Japan Co., Japan) by the Brunauer-Emmett-Teller (BET) method. The morphology and the sizes of Pt particles were observed on transmission electron microscope JEM-2100 (JEOL Ltd, Japan). The diffuse reflection spectra of the catalysts were measured by UV-visible spectrophotometer (UV-2600, SHIMADZU Co., Japan) from 200 nm to 800 nm. The contents of Pt on the catalysts were analyzed by inductively coupled plasma optical emission spectrometry (ICP-OES, SPS3520UV-DD, SII nano technology Inc., Japan). The existences and the valence states of Pt over the catalysts were identified by X-ray photoelectron spectroscopy (XPS, PHI Quantera SXM, ULVAC-PHI Inc., Japan).

4.2.4 Photocatalytic activity measurements

CRM reaction was conducted in a fixed-bed reactor under atmospheric pressure. A 0.10 g portion of catalyst without dilution was packed uniformly in the alumina cell. Both TC-1000 temperature controller (Jacso) and LA-251Xe lamp (Hayashi) with L42+HA30 filters (visible light) were employed to provide the energy input. CH$_4$ and CO$_2$ with the molar ratio of 1/1 were introduced into the reactor at a total flowrate of 20.0 mL/min (STP). The effluent gas was analyzed by gas chromatographs (GC) to obtain the relative amounts of CH$_4$, CO, CO$_2$ and H$_2$, and the flowrate of the effluent gas was measured with a flowmeter.

4.2.5 DFT theoretical calculations

Similar with the method proposed by Kumar et al, the dielectric function for absorption coefficient calculations in this study also includes both parts from interband transition and localized surface plasmon resonance (LSPR).[11]

$$\varepsilon(\omega) = \varepsilon^{interband}(\omega) + \varepsilon^{LSPR}(\omega)$$

The contribution of interband excitations to the dielectric function, $\varepsilon^{interband}(\omega)$ was obtained from electronic band structure calculation by evaluating matrix elements for direct electronic transitions between occupied and unoccupied states as discussed by Kumar *et al.*[13]

While for the dielectric function from LSPR, $\varepsilon^{LSPR}(\omega)$ was evaluated by approximating it with the Drude expression for a given plasma frequency (ω_p) and damping constant (γ),[14]

$$\varepsilon^{LSPR}(\omega) = 1 - \frac{\omega_P^2}{\omega^2 + i\gamma\omega}$$

The real ($\varepsilon_1^{LSPR}(\omega)$) and imaginary ($\varepsilon_2^{LSPR}(\omega)$) components of this dielectric function are given by

$$\varepsilon_1^{LSPR}(\omega) = 1 - \frac{\omega_P^2\tau^2}{1 + \omega^2\tau^2}$$

$$\varepsilon_2^{LSPR}(\omega) = \frac{\omega_P^2\tau^2}{\omega(1 + \omega^2\tau^2)}$$

where τ ($\gamma = 1/\tau$) represents a relaxation time obtained from a higher order calculations, while ω_p is the plasma frequency calculated from the band structure.[15]

In details, all calculations were performed with the Vienna ab-initio Simulation Package (VASP) based on the density functional theory (DFT).[16] The generalized gradient approximation (GGA) of Perdew-Burke-Ernzerhof (PBE) was chosen for the exchange-correlation potential.[17] The lattice vectors and atomic coordinates were relaxed until the Hellmann-Feynman force was reduced to 0.01 eV/Å and the total energy converged within an error of 1×10^{-5} eV/atom. An energy cutoff of 500 eV and the Monkhorst-Pack scheme with 28×28×48 k-points mesh along with a sufficient number of conduction bands was used for optical properties calculations.

4.3 Results and discussion
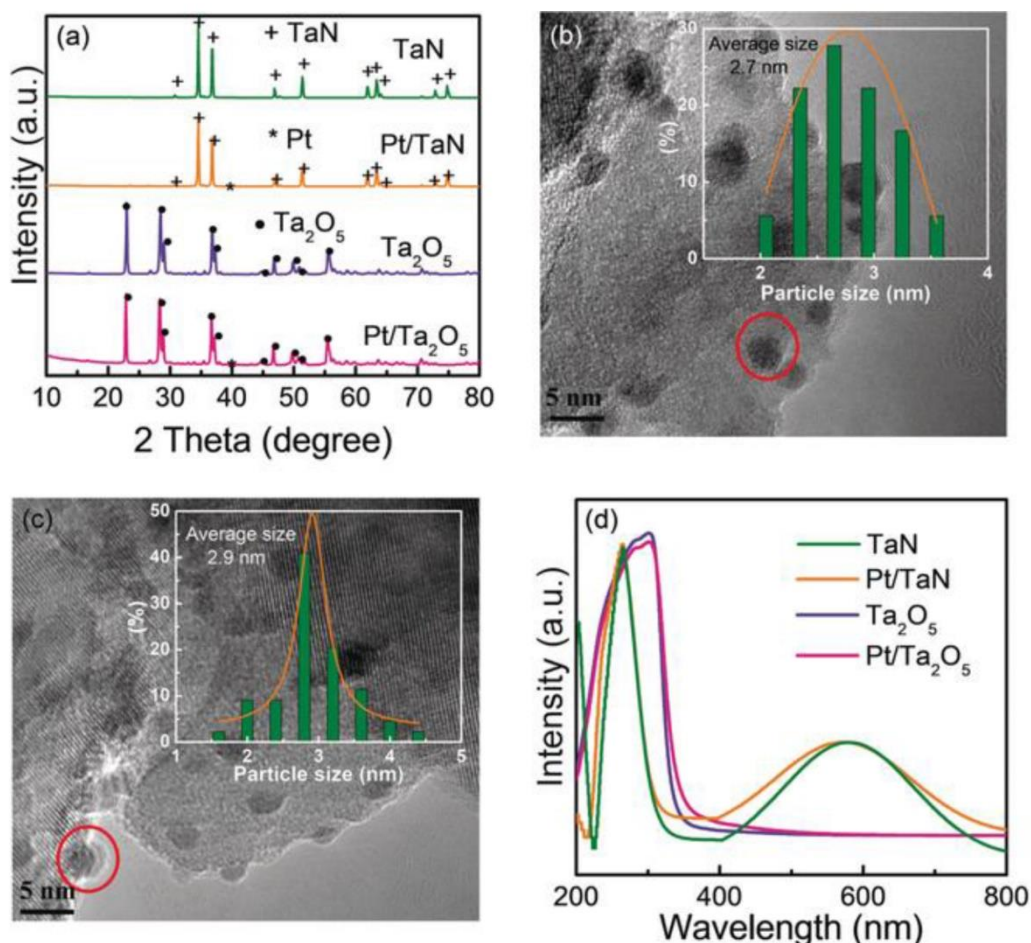
4.3.1 Catalyst characterization

Figure 4.1 (a) XRD patterns of TaN, Ta_2O_5 and the Pt-based catalysts, (b) and (c) TEM images of Pt/TaN and Pt/Ta_2O_5, with Pt particle size distributions as insets, and (d) UV-visible spectra of TaN, Ta_2O_5 and the Pt-based catalysts.

TaN of hexagonal phase (Figure 4.1a) and with a specific surface area of 13.7 m^2 g^{-1} (Table 4.1) was commercial and used as received. Ta_2O_5 with a similar specific surface area was adopted as reference (Table 4.1). The active components, with Pt being taken as an example in the main text, were loaded on the supports TaN and Ta_2O_5 via incipient wetness impregnation method. The successful loading of Pt could be confirmed by the diffraction peaks at 39.8º attributed to Pt in the XRD profiles in Fig. 1a and the Pt 4f peaks in the XPS spectra shown in Figure 4.2. The results in Figure 4.2 indicated that Pt existed over the Pt/Ta_2O_5 and Pt/TaN catalysts. The different binding energy of the Pt species over the Pt/Ta_2O_5 and Pt/TaN catalysts might be related to the interactions

between Pt and support. The actual contents of Pt on the catalysts were 0.82 wt% and 1.2 wt% (Table 4.1), and the average sizes of Pt nanoparticles were 2.7 nm and 2.9 nm over Pt/TaN and Pt/Ta$_2$O$_5$ (Figure 4.1b, 4.1c and Table 4.1), respectively. The optical properties of TaN, Ta$_2$O$_5$ and the Pt-based catalysts were characterized by UV-visible spectroscopy with the results displayed in Figure 4.1d. It could be seen that, there was an absorption peak in the visible light region (400-800 nm) over TaN whereas the optical absorption of Ta$_2$O$_5$ was located in the ultraviolet region. The loading of Pt influenced little on the optical absorption of the supports owing to the weak absorption of Pt in the ultraviolet region[18,19] and the low loadings of Pt on the catalysts (Table 4.1).

Table 4.1 Physicochemical properties of supports and the Pt-based catalysts.

Catalysts	S_{BET} (m^2 g^{-1})[a]	Pt loading (wt%)[b]	Pt sizes (nm)[c]
TaN	13.7	-	-
Pt/TaN	8.6	0.82	2.7
Ta$_2$O$_5$	19.5	-	-
Pt/Ta$_2$O$_5$	18.5	1.2	2.9

a, obtained by N$_2$ adsorption-desorption method through Brunauer-Emmett-Teller (BET) equation;

b, analyzed by ICP-OES method;

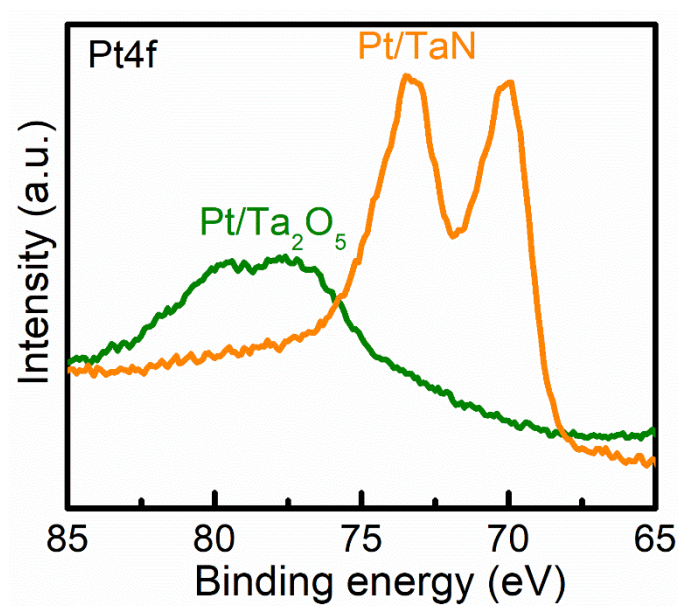c, obtained from the TEM images in Figure 4.1b and 4.1c.

Figure 4.2 Pt4f XPS spectra of the Pt/Ta$_2$O$_5$ and Pt/TaN catalysts.
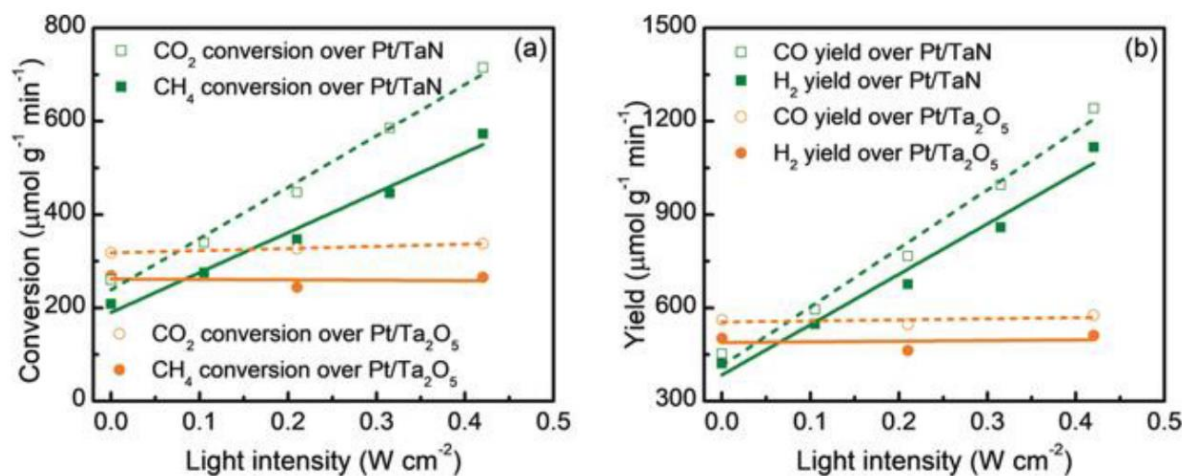
4.3.2 Photo-enhanced catalytic activity

Figure 4.3 Catalytic performance of Pt/TaN and Pt/Ta$_2$O$_5$ in CRM, (a) CH$_4$ and CO$_2$ conversions, and (b) CO and H$_2$ yields. Reaction conditions: 0.10 g catalyst, 500 °C, reactant 20.0 mL min^{-1}, with or without visible light irradiation.

The effect of the optical property of TaN on the photocatalytic performances of its supported catalysts was studied in visible light assisted CH$_4$ conversion with CO$_2$. It is apparent that, in spite that TaN and Ta$_2$O$_5$ were inert in CRM, both Pt/TaN and Pt/Ta$_2$O$_5$ were effective in CRM at 500 °C without visible light irradiation (Figure 4.3, 4.4 and 4.5). On the other hand, with visible light assistance, CH$_4$ and CO$_2$ conversions over Pt/TaN were further improved whereas the performances of Pt/Ta$_2$O$_5$ remained nearly constant. For all cases, the conversions of CO$_2$ were always higher than those of CH$_4$ owing to the coexistence of reverse water gas shift reaction (Figure 4.3b).[20] Meanwhile, the selectivities to CO and H$_2$, and the mass balances were nearly 100 %. The yields to CO and H$_2$ exhibited analogous trend with the conversions of CO$_2$ and CH$_4$ (Figure 4.3). Noticeably from Figure 4.3, compared with the catalytic activities and yields of Pt/TaN evaluated under thermal-driven conditions, the catalytic performance was about 2.7 times enhanced with 0.42 W cm^{-2} visible light assistance. The activity enhancement ratio obtained over Pt/TaN with visible light irradiation (2.7 times) was much higher than that achieved by introducing the expensive and thermal-driven inactive Au as plasmonic promoter to visible-light-inert Pt/Ta$_2$O$_5$ (1.6 times, Figure 4.6). It revealed that TaN is an excellent optical material in improving the catalytic activity of its supported catalyst with visible light irradiation. The superiority of TaN as optical catalyst promoter could also be evidenced by TaN supported other group VIII metal catalysts with visible light irradiation (Ir/TaN in Figure 4.7 and

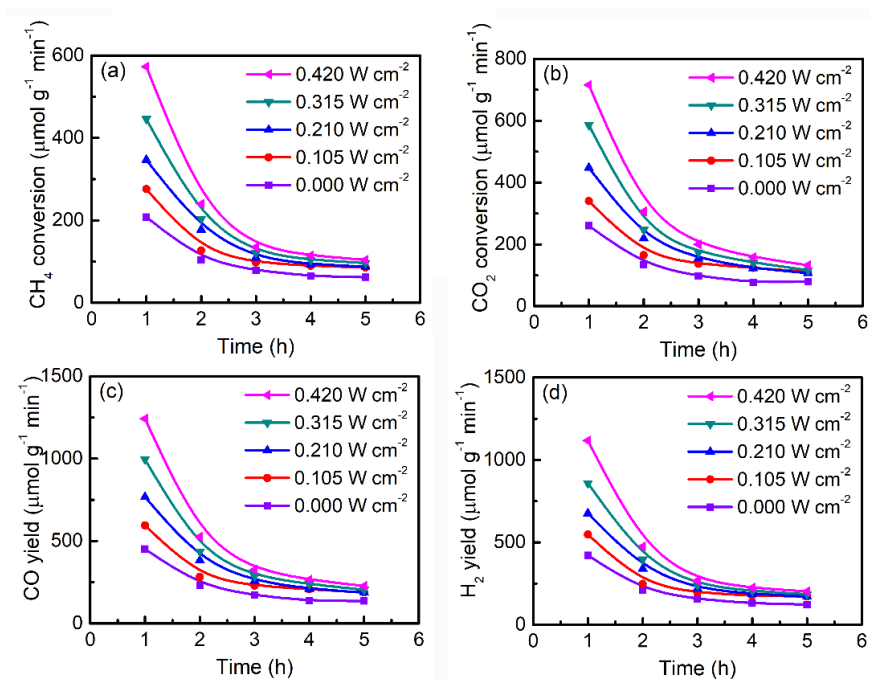Pd/TaN in Figure 4.8), and the light induced activity enhancement ratios were in the range of 2.3-2.7.

Figure 4.4 Catalytic performance of Pt/TaN in CRM, (a) CH_4 conversion, (b) CO_2 conversion, (c) CO yield and (d) H_2 yield. Reaction conditions: 0.10 g catalyst, 500 °C, reactant 20.0 mL min^{-1}, with or without visible light irradiation.

Figure 4.5 Catalytic performance of Pt/Ta$_2$O$_5$ in CRM, (a) CH_4 conversion, (b) CO_2 conversion, (c) CO yield and (d) H_2 yield. Reaction conditions: 0.10 g catalyst, 500 °C, reactant 20.0 mL min^{-1}, with or without visible light irradiation.
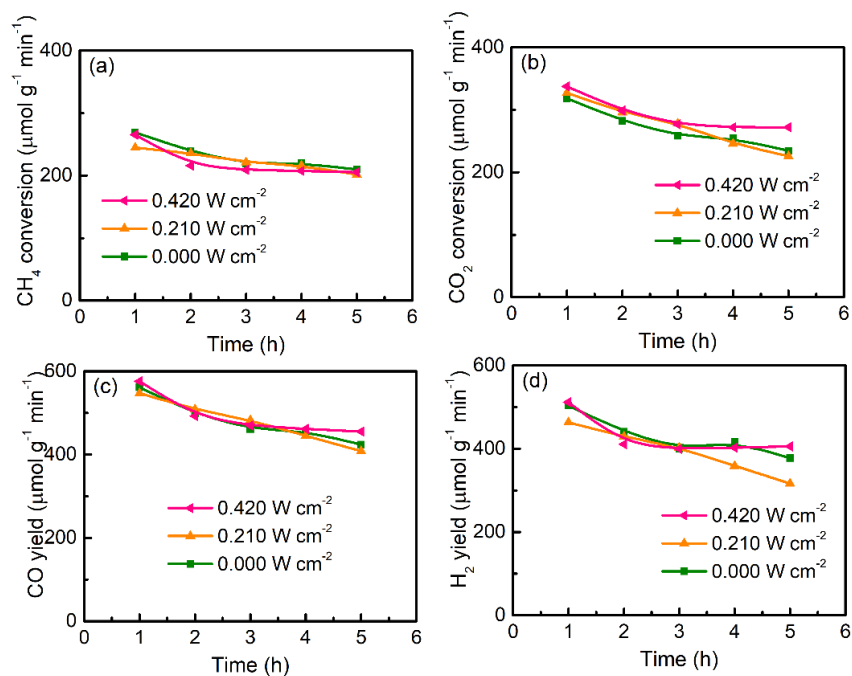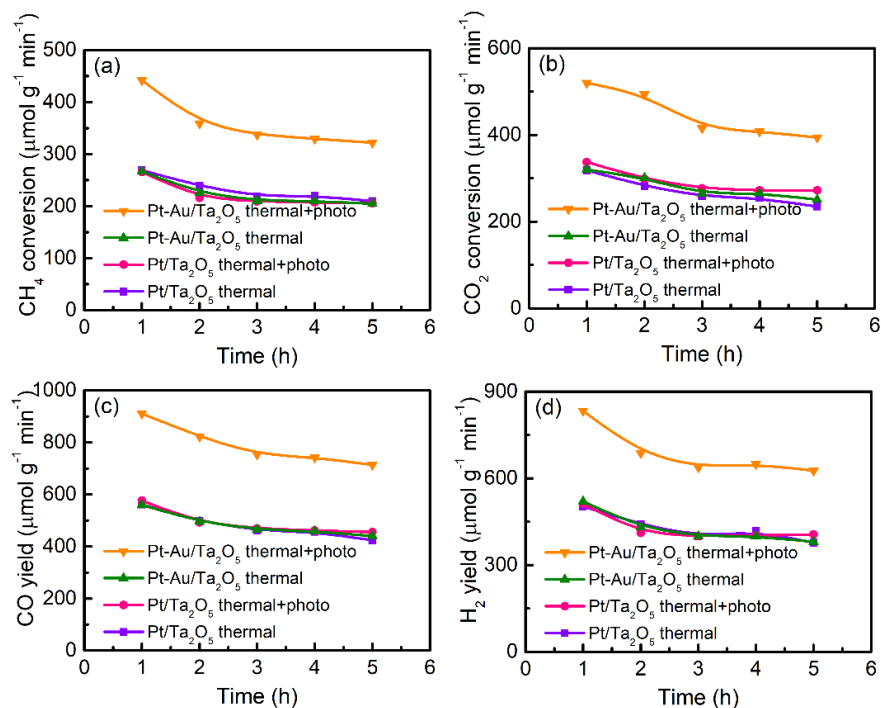
Figure 4.6 Catalytic performance of Pt/Ta$_2$O$_5$ and Pt-Au/Ta$_2$O$_5$ in CRM, (a) CH$_4$ conversion, (b) CO$_2$ conversion, (c) CO yield and (d) H$_2$ yield. Reaction conditions: 0.10 g catalyst, 500 °C, reactant 20.0 mL min^{-1}, with or without 0.420 W cm^{-2} visible light irradiation.

Figure 4.7 Catalytic performance of Ir/TaN in CRM, (a) CH$_4$ conversion, (b) CO$_2$ conversion, (c) CO yield and (d) H$_2$ yield. Reaction conditions: 0.10 g catalyst, 500 °C, reactant 20.0 mL min^{-1}, with or without 0.42 W cm^{-2} visible light irradiation.
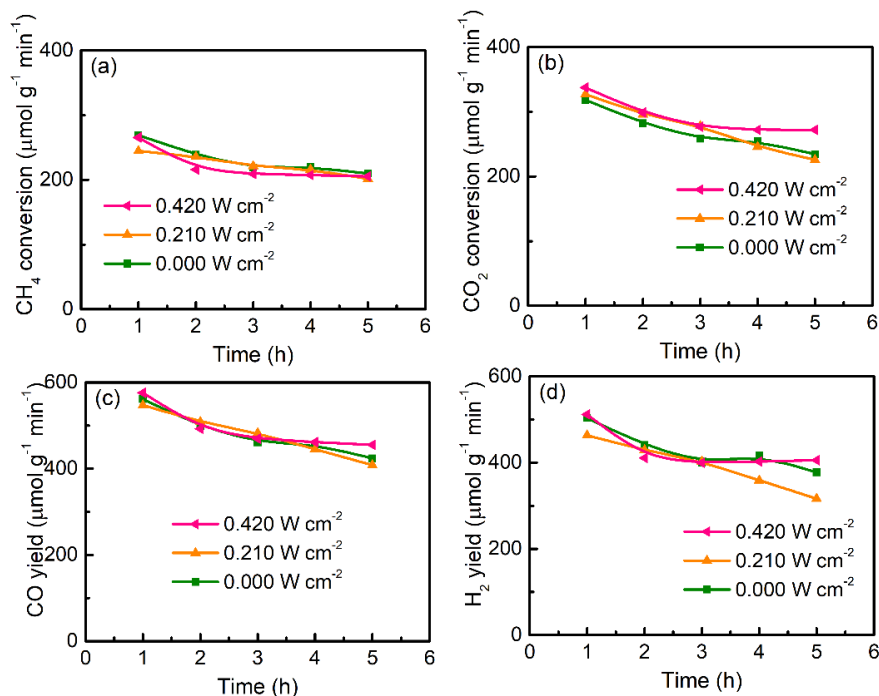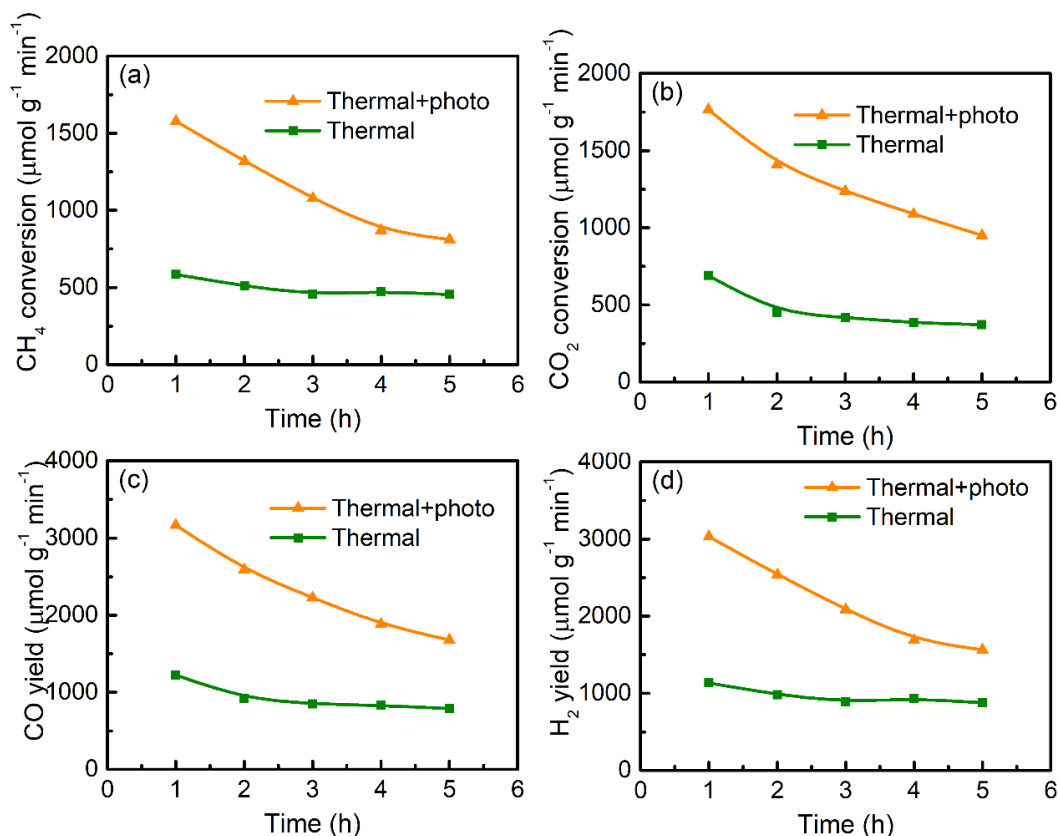
Figure 4.8 Catalytic performance of Pd/TaN in CRM, (a) CH_4 conversion, (b) CO_2 conversion, (c) CO yield and (d) H_2 yield. Reaction conditions: 0.10 g catalyst, 500 $^{\circ}$C, reactant 20.0 mL min^{-1}, with or without 0.420 W cm^{-2} visible light irradiation.

The values observed over the temperature detector revealed that the reaction temperature was well controlled, together with the uninfluenced catalytic performance over Pt/Ta$_2$O$_5$ (Figure 4.3), Pt/ZrN (Figure 4.9) and Pt/TiN (Figure 4.10) in CRM with visible light assistance, it indicated that visible light introduction did not induce temperature increase or local heating to the thermal-driven reaction system. Even though ZrN and TiN could absorb visible light (ZrN and TiN, Figure 4.11),[11,21,22] no inner electrostatic field could be induced over TiN or TiN with visible light irradiation, as they possess symmetrical electrostatic potential distributions (Figure 4.12 and 4.13), which leads to their photothermal conversion capacities. In addition to ZrN and TiN, group VIII metals also possess strong photothermal conversion capacity.[23] The thermal energy transformed from photon energy (visible light) could not make itself be distinguished from the thermal energy supplied by the heater and it would be ultimately compensated with the heater to the stable reaction temperature 500 $^{\circ}$C. Then, photo-induced temperature increase or local heating could be excluded as reasons for the

enhanced catalytic performance of Pt/TaN with visible light irradiation.

Figure 4.9 Catalytic performance of Pt/ZrN in CRM. Reaction conditions: 0.10 g catalyst, 500 °C, reactant 20.0 mL min^{-1}, with or without 0.420 W cm^{-2} visible light irradiation.
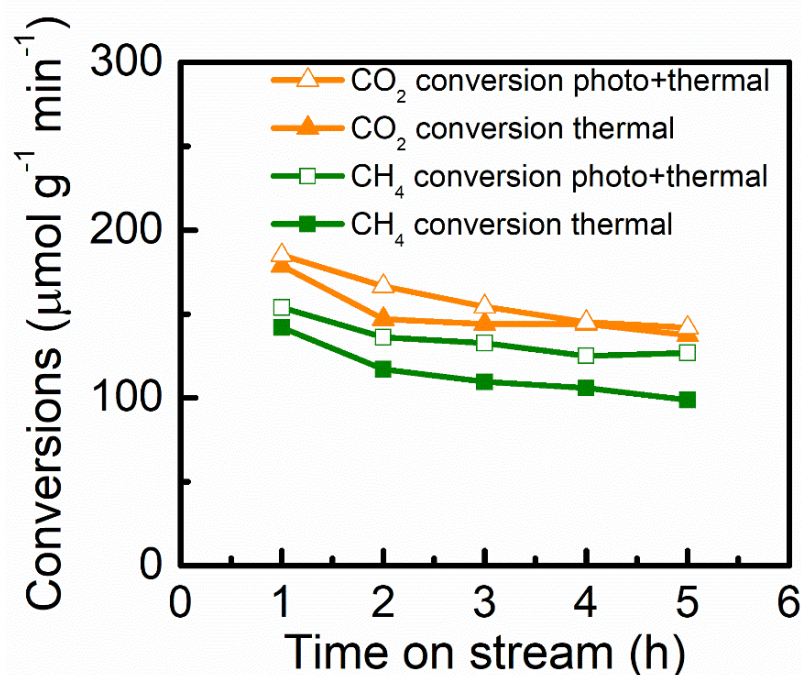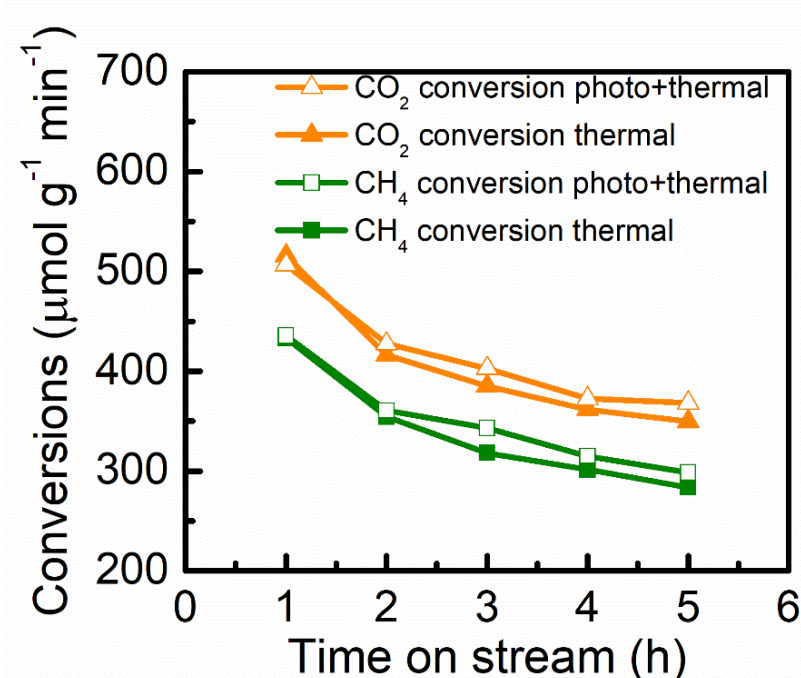

Figure 4.10 Catalytic performance of Pt/TiN in CRM. Reaction conditions: 0.10 g catalyst, 500 °C, reactant 20.0 mL min^{-1}, with or without 0.420 W cm^{-2} visible light irradiation.
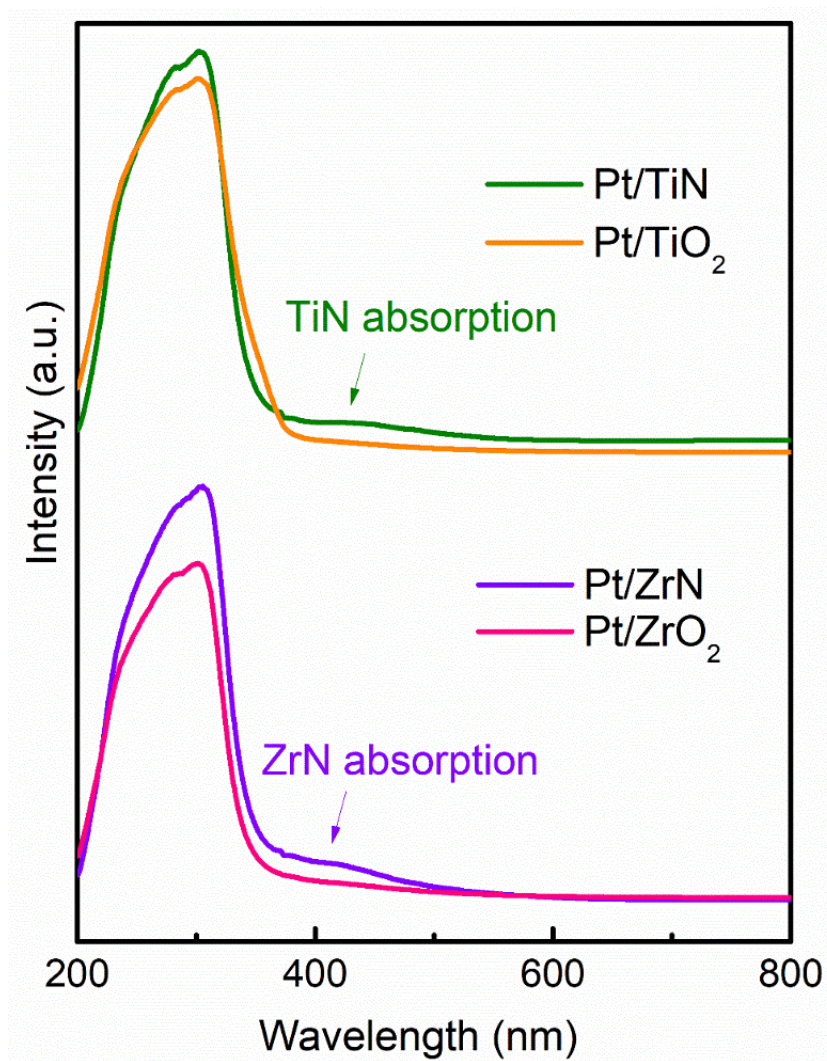
Figure 4.11 UV-visible spectra of Pt/TiN, Pt/TiO$_2$, Pt/ZrN and Pt/ZrO$_2$.
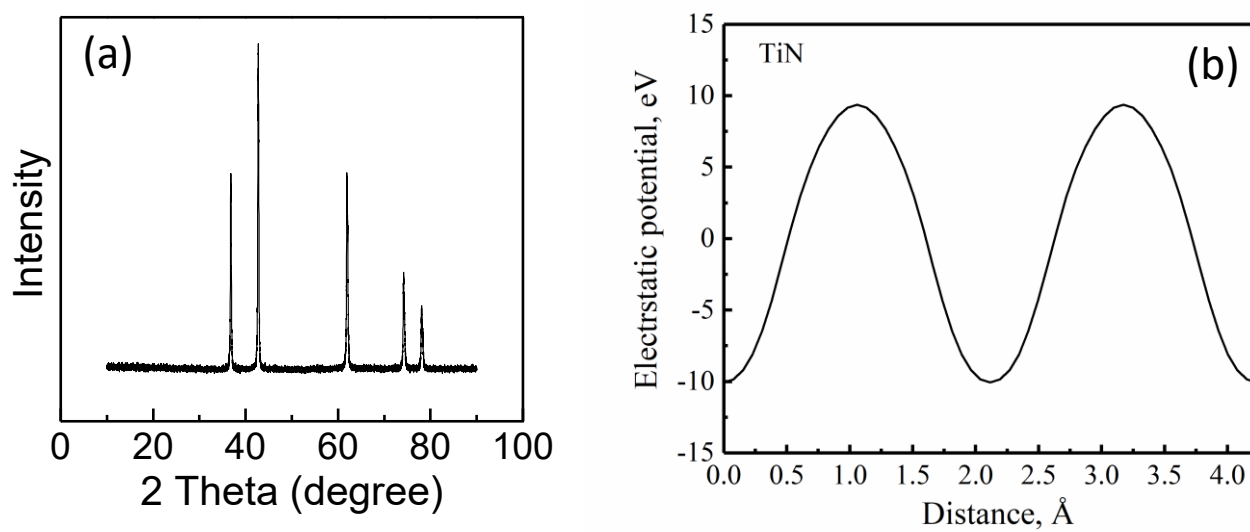
Figure 4.12 (a) XRD pattern and (b) electrostatic potential of TiN.
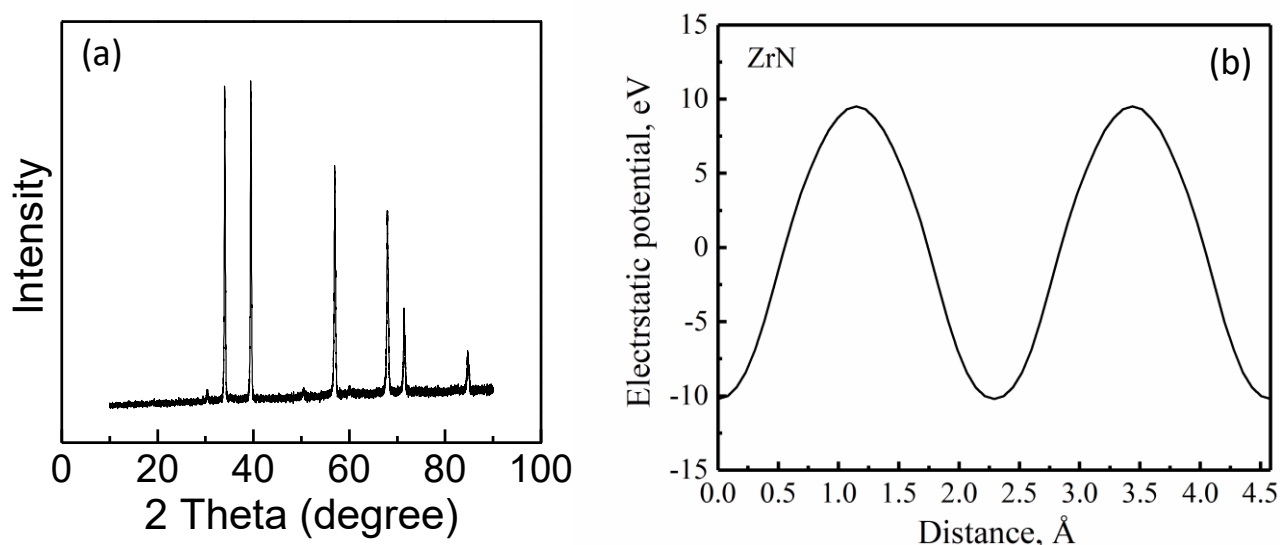
Figure 4.13 (a) XRD pattern and (b) electrostatic potential of ZrN.
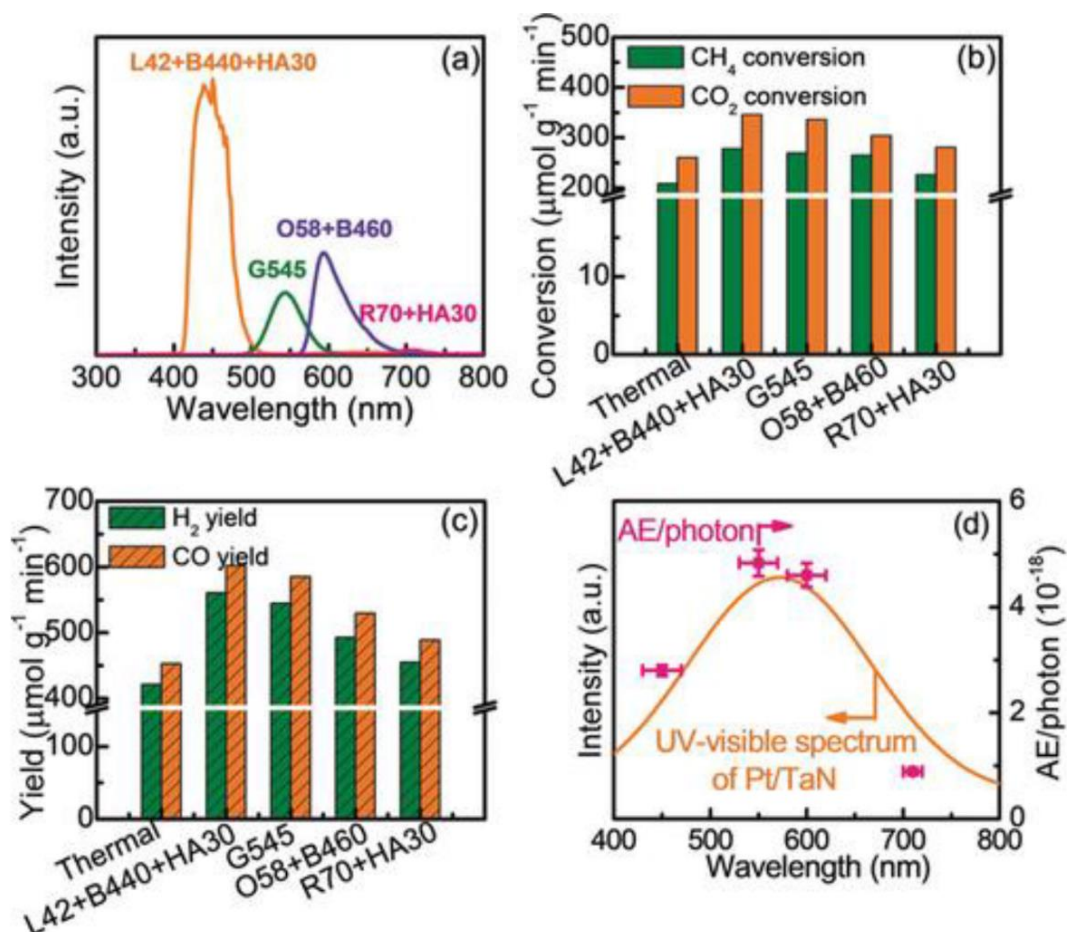
Figure 4.14 (a) Wavelength range obtained with different filter sets, (b) CH$_4$ and CO$_2$ conversions and (c) H$_2$ and CO yields without or with light irradiation of different wavelength range, and (d) UV-visible spectra of Pt/TaN and the activity enhancement induced by one photon AE/photon.

In order to identify whether the enhanced performance of Pt/TaN in CRM with visible light

assistance was stemmed from the optical property of TaN, the influence of light wavelength on the performance of Pt/TaN in CRM was investigated, with several types of filters employed to obtain the desired wavelength range (Figure 4.14a). Apparently, the activities of Pt/TaN were all more or less enhanced with the introduction of light of various regions (Figure 4.14b and c). Noticeably, with the irradiation of proper wavelength range of light (500-600 nm), the activity of Pt/TaN could be increased by about 29.0 % even at the light intensity as low as 0.023 W cm^{-2}. By roughly assuming the center of the introduced light and calculating the activity enhancement induced by one photon (AE/photon), a wavelength-dependent performance was obtained (Figure 4.14d), which follows the trend of TaN absorption in the visible light region within detection error. The results in Figure 4.14 confirmed that it was the optical property of TaN that enhanced the performance of Pt/TaN under light irradiation.

The origination of the optical property of TaN was simulated via first-principle density functional theory (DFT) with the structure displayed in Figure 4.15a as the model. It could be seen that, the simulated UV-visible spectrum of TaN exhibited an obvious light absorption peak at around 540 nm, consistent with the characterized one within detection error (Figure 4.15b and Figure 4.1d). Energy band diagram in Figure 4.15d revealed the energy levels of several key electrons over TaN, which indicated that the optical absorption of TaN in visible light region was complicated and probably originated from the electron transfer between several orbitals.
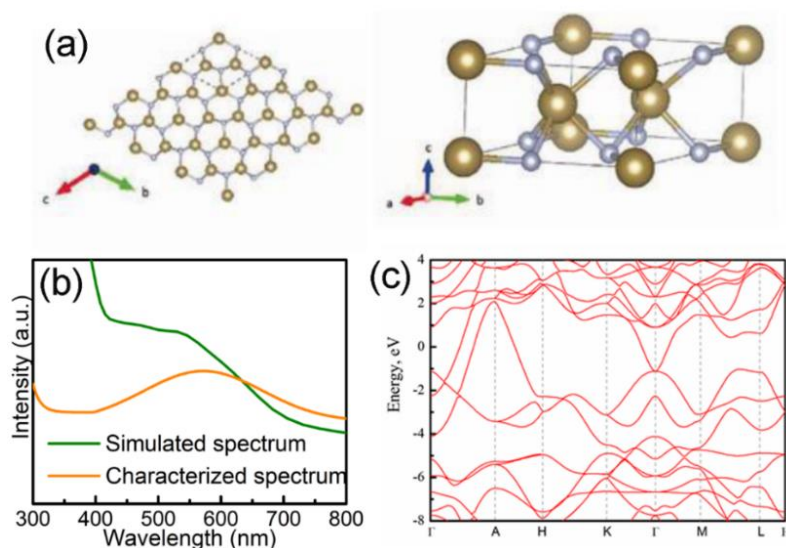

Figure 4.15 (a) TaN model used for DFT simulation, (b) comparison between simulated and characterized UV-visible spectra over TaN, (c) energy band diagram of TaN
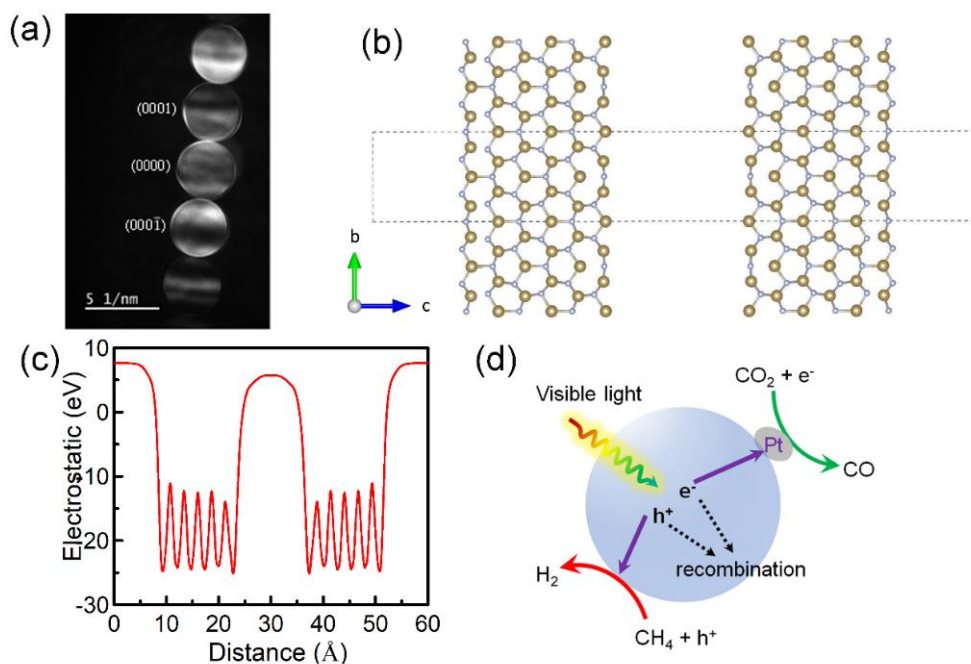
Figure 4.16 (a) CBED pattern of TaN giving asymmetric contrast between (0001) and (000$\bar{1}$) diffraction spots. It indicates a polarity of (0001) plane for non-symmetric crystal structure like TaN with space group P-62m. (b) Structure of TaN for electrostatic field simulation, (c) the distribution of the electrostatic field over TaN, and (d) mechanism study for visible light assisted CRM over Pt/TaN catalyst.

Generally, with visible light irradiation, electron-hole pairs will be created over visible light responsive materials, then the electrons and holes will be separated and transferred to catalyst surface to drive reaction occurrence. Considering the facts that not all the visible light sensitive materials supported catalysts exhibited improved performances with visible light irradiation (Figure 4.9, 4.10 and 4.11), then it could be proposed that the characteristics of TaN played important roles for the enhanced catalytic performance in this study. The convergent beam electron diffraction (CBED) method of TEM technique demonstrated that TaN is a polar material. As shown in Figure 4.16a, the CBED pattern was taken near to [1$\bar{1}$00] zone. Then the electron diffraction from (0001)$_{TaN}$ and (000$\bar{1}$)$_{TaN}$, which are assumed to be Ta or N terminations, respectively, could be distinguished by the fringes in the CBED disks. The CBED pattern in Figure 4.16a below revealed that, the center fringes at (0001)$_{TaN}$ and (000$\bar{1}$)$_{TaN}$ disks are bright and dark, respectively, because (0001)$_{TaN}$ face could reflect the electron beams more strongly than the (000$\bar{1}$)$_{TaN}$. The unsymmetrical fringes at (0001)$_{TaN}$ and (000$\bar{1}$)$_{TaN}$ of the CBED disks suggested that TaN is polar, with Ta and N terminated at different surfaces. This is because that TaN has space group P-62m. It indicates a six-fold inverse axis along

Z-axis, a two-fold rotation symmetric axis along [11-20] and a mirror plane perpendicular to [1-100] axis. Electrostatic field simulation also confirmed that TaN is polar. The polarity of TaN induced an electrostatic field (Figure 4.16b and c), which could facilitate the photo-induced electron-hole pairs separation and transfer.[24-26] Then the electrons, with the assistance of co-catalyst Pt, preferentially reduced CO_2 to CO under visible light irradiation.[27,28] Meanwhile, the holes oxidized CH_4 to H_2 (Figure 4.16d). The photo-induced supernumerary CO_2 reduction and CH_4 oxidation (Figure 4.16d) is responsible for the activity enhancements over TaN supported group VIII catalysts with visible light irradiation. Comparing with the non-improved activities of TiN or ZrN supported catalysts with visible light irradiation (the lacking of inner electrostatic fields over TiN or ZrN might lead to the easy recombination of the separated electron-hole pairs and ultimately the nearly unchanged catalytic performance with visible light irradiation), it could be concluded that, the polarity induced electrostatic field over TaN was critical in enhancing the activities with visible light irradiation.

4.4 Conclusions

To sum up, in this chapter, I provided strong evidence for the potential application of TaN in photo-thermocatalytic CRM. It was found that, the activities of TaN supported group VIII metal-based catalysts could be greatly enhanced with visible light assistance, and the activity enhancement ratios (2.3-2.7 times) were much higher than that achieved by adopting expensive Au as plasmonic promoter to an optical-inert catalyst (1.6 times). Polarity of TaN is regarded to facilitate electron-hole separation and ultimately be responsible for the activity enhancement. The study is expected to guide TaN to various photocatalytic areas and wider optical application domains.

References

1. Choudhary, T.V., and Choudhary, V.R. (2008). Energy-efficient syngas production through catalytic oxy-methane reforming reactions. Angew. Chem. Int. Ed. *47*, 1828-1847.

2. Pakhare, D., and Spivey, J. (2014). A review of dry (CO_2) reforming of methane over noble metal catalysts. Chem.Soci. Rev. *43*, 7813-7837.

3. Ma, Y., Wang, X., Jia, Y., Chen, X., Han, H., and Li, C. (2014). Titanium dioxide-based nanomaterials for photocatalytic fuel generations. Chem. Rev. *114*, 9987-10043.

4. Morris, A.J., Meyer, G.J., and Fujita, E. (2009). Molecular approaches to the photocatalytic reduction of carbon dioxide for solar fuels. Accounts of chemical research *42*, 1983-1994.

5. Sarina, S., Zhu, H.Y., Xiao, Q., Jaatinen, E., Jia, J., Huang, Y., Zheng, Z., and Wu, H. (2014). Viable Photocatalysts under Solar-Spectrum Irradiation: Nonplasmonic Metal Nanoparticles. Angew. Chem. Int. Ed. *53*, 2935-2940.

6. Marimuthu, A., Zhang, J., and Linic, S. (2013). Tuning selectivity in propylene epoxidation by plasmon mediated photo-switching of Cu oxidation state. Science *339*, 1590-1593.

7. Bian, Z., Tachikawa, T., Zhang, P., Fujitsuka, M., and Majima, T. (2013). Au/TiO_2 superstructure-based plasmonic photocatalysts exhibiting efficient charge separation and unprecedented activity. J. Am. Chem. Soc. *136*, 458-465.

8. Kale, M.J., Avanesian, T., Xin, H., Yan, J., and Christopher, P. (2014). Controlling catalytic selectivity on metal nanoparticles by direct photoexcitation of adsorbate–metal bonds. Nano Lett. *14*, 5405-5412.

9. Liu, H., Meng, X., Dao, T.D., Zhang, H., Li, P., Chang, K., Wang, T., Li, M., Nagao, T., and Ye, J. (2015). Conversion of Carbon Dioxide by Methane Reforming under Visible-Light Irradiation: Surface-Plasmon-Mediated Nonpolar Molecule Activation. Angew. Chem. Int. Ed. *54*, 11545-11549.

10. Matenoglou, G., Koutsokeras, L., Lekka, C.E., Abadias, G., Camelio, S., Evangelakis, G., Kosmidis, C., and Patsalas, P. (2008). Optical properties, structural parameters, and bonding of highly textured rocksalt tantalum nitride films. J. Appl. Phys. *104*, 124907.

11. Kumar, M., Umezawa, N., Ishii, S., and Nagao, T. (2015). Examining the performance of refractory conductive ceramics as plasmonic materials: a theoretical approach. ACS Photonics *3*, 43-50.

12. Naik, G.V., Shalaev, V.M., and Boltasseva, A. (2013). Alternative plasmonic materials: beyond gold and silver. Adv. Mater.*25*, 3264-3294.

13. Kumar, M., Umezawa, N., and Imai, M. (2014). (Sr, Ba)(Si, Ge) 2 for thin-film solar-cell applications: First-principles study. Journal of Applied Physics *115*, 203718.

14. Ehrenreich, H., and Philipp, H. (1962). Optical properties of Ag and Cu. Phys. Rev.*128*, 1622.

15. Laref, S., Cao, J., Asaduzzaman, A., Runge, K., Deymier, P., Ziolkowski, R.W., Miyawaki, M., and Muralidharan, K. (2013). Size-dependent permittivity and intrinsic optical anisotropy of nanometric gold thin films: a density functional theory study. Opt. Express *21*, 11827-11838.

16. Kresse, G., and Furthmüller, J. (1996). Efficient iterative schemes for ab initio total-energy calculations using a plane-wave basis set. Phys. Rev.B *54*, 11169.

17. Perdew, J.P., Chevary, J.A., Vosko, S.H., Jackson, K.A., Pederson, M.R., Singh, D.J., and Fiolhais, C. (1992). Atoms, molecules, solids, and surfaces: Applications of the generalized gradient approximation for exchange and correlation. Phys. Rev. B *46*, 6671.

18. Chen, M., Wu, B., Yang, J., and Zheng, N. (2012). Small Adsorbate-Assisted shape control of Pd and Pt nanocrystals. Adv. Mater.*24*, 862-879.

19. Langhammer, C., Yuan, Z., Zorić, I., and Kasemo, B. (2006). Plasmonic properties of supported Pt and Pd nanostructures. Nano letters *6*, 833-838.

20. Haag, S., Burgard, M., and Ernst, B. (2007). Beneficial effects of the use of a nickel membrane reactor for the dry reforming of methane: comparison with thermodynamic predictions. J. Catal. *252*, 190-204.

21. Guler, U., Ndukaife, J.C., Naik, G.V., Nnanna, A.A., Kildishev, A.V., Shalaev, V.M., and Boltasseva, A. (2013). Local heating with lithographically fabricated plasmonic titanium nitride nanoparticles. Nano Lett. *13*, 6078-6083.

22. Roux, L., Hanus, J., Francois, J., and Sigrist, M. (1982). The optical properties of titanium nitrides and carbides: Spectral selectivity and photothermal conversion of solar energy. Sol. Energy Mater.*7*, 299-312.

23. Meng, X., Wang, T., Liu, L., Ouyang, S., Li, P., Hu, H., Kako, T., Iwai, H., Tanaka, A., and Ye, J. (2014). Photothermal conversion of CO_2 into CH_4 with H_2 over Group VIII nanocatalysts: an alternative approach for solar fuel production. Angew. Chem. Int. Ed. *53*, 11478-11482.

24. Li, L., Salvador, P.A., and Rohrer, G.S. (2014). Photocatalysts with internal electric fields. Nanoscale *6*, 24-42.

25. Andreev, A., and O'Reilly, E. (2000). Theory of the electronic structure of GaN/AlN hexagonal quantum dots. Phys. Rev. B *62*, 15851.

26. Waltereit, P., Brandt, O., Trampert, A., Grahn, H., Menniger, J., Ramsteiner, M., Reiche, M., and Ploog, K. (2000). Nitride semiconductors free of electrostatic fields for efficient white light-emitting diodes. Nature *406*, 865.

27. Xie, S., Wang, Y., Zhang, Q., Deng, W., and Wang, Y. (2014). MgO-and Pt-promoted TiO_2 as an efficient photocatalyst for the preferential reduction of carbon dioxide in the presence of water. ACS Catal. *4*, 3644-3653.

28. Iizuka, K., Wato, T., Miseki, Y., Saito, K., and Kudo, A. (2011). Photocatalytic reduction of carbon dioxide over Ag cocatalyst-loaded $ALa_4Ti_4O_{15}$ (A= Ca, Sr, and Ba) using water as a reducing reagent. J. Am. Chem. Soc. *133*, 20863-20868.

Chapter 5 Direct photocatalytic oxidation of methane to liquid oxygenates with molecular oxygen over nanometals/ZnO catalysts

5.1 Introduction

Methane is an abundant and promising feedstock for the synthesis of various commodity chemicals, especially after the recent discovery of large reserves of shale gas and methane hydrate.[1-3] The industrial approaches for transforming methane into liquid chemicals are performed indirectly through the production of syngas (a mixture of carbon monoxide and hydrogen) by energy-intensive steam methane reforming, followed by further conversion of syngas to liquid hydrocarbons through Fischer-Tropsch synthesis or methanol (CH_3OH) synthesis.[4-6] Direct partial oxidation of methane into value-added oxygenates such as CH_3OH and formaldehyde (HCHO) at low temperature or even room temperature remains a grand challenge in increasing conversion and controlling over-oxidation.[7-9] Although high methane conversion and CH_3OH selectivity favored by product protection against over-oxidation could be achieved over organo-transition metal complexes in heated oleum (ca. 200 °C),[10,11] the corrosive nature of this homogeneous system is an restriction for operation.

In heterogeneous system, thermocatalysis with widely used Fe and Cu based zeolites could convert CH_4 to CH_3OH with N_2O, O_2 or H_2O in gas phase in stepwise or one-step process.[12-15] Relatively high temperatures (200 to 500 °C) is necessary to activate the zeolites by oxidant for C-H activation and water stream has to be introduced to improve the methanol selectivity. Water stream is crucial in the gas phase reaction to guide methoxy intermediates formation and avoid the direct over-oxidation of methyl species.[15,16] Direct methane conversion in liquid phase overcome the intrinsic flaw of gas phase system where methane tends to be over-oxidized. Indeed, impressive oxygenates selectivity in methane conversion has been demonstrated in liquid phase with hydrogen peroxide (H_2O_2) as an oxidant in the presence of single site catalysts (confined transition metal in zeolites, oxides, graphene, metal-organic frameworks, etc.),[17-20] where H_2O_2 could assist the active site formation for C-H activation at low temperature. Higher cost of H_2O_2 than the oxygenated products make the systems of this kind uneconomical.[21] Hutchings and co-workers reported the oxidation of

methane to CH_3OH by molecular oxygen over colloidal gold-palladium nanoparticles at 50 °C in the presence of H_2O_2.[18]. Activation of first C-H bond of methane into methyl radical by oxidative intermediate derived from H_2O_2 favored the incorporation of O_2 in the subsequent reaction steps. Moreover, in the presence of CO, methane oxidation to CH_3OH or acetic acid was catalyzed by molecular oxygen over isolated Rh catalysts in aqueous solution under mild condition (150 °C).[22,23] H_2O_2 is also reported to be an efficient oxidant in photocatalytic CH_4 oxidation to CH_3OH with high selectivity over iron species modified TiO_2 at ambient condition.[24]

From the economic and environmental aspects, significant progress should be made in exploring photocatalysts for methane oxidation to oxygenates directly by abundant molecular oxygen, the ideal oxidants, at room temperature. In photocatalysis, the reactive oxygen species (ROS), such as hydroxyl radical (˙OH) and alkoxyl radicals (˙OR),[25,26] are readily formed upon the excitation of photons with the energy of several eV. Then C-H bond dissociation would be potentially initiated by the ROS at much lower or even room temperature.[18,26]

In this chapter, I reported the direct conversion of methane solely with molecular oxygen in pure water at room temperature over ZnO photocatalysts. The water could help to form hydroperoxyl (˙OOH) radicals, an important intermediate for oxygenate production, through protonation effect in O_2 reduction. In addition, solvation effect of water will promote desorption of oxygenates from active site into the bulk solution to avoid over-oxidation and improve product selectivity. Experimental results demonstrated that methane is photo-activated by the hole center, (active oxygen O^-), to form methyl radical (˙CH_3) via hydrogen abstraction. The oxygen in the oxygenated products originates from molecular oxygen incorporation in 100%.

5.2 Experimental section

5.2.1 Chemicals and materials

Zinc oxide (ZnO, 0.02 µm) was purchased from Wako. Commercial TiO_2 (AEROXIDE TiO_2 P25, Lot No. 614041498) was supplied from Evonik-Degussa. TiO_2 (Anatase nanopowder, <25 nm particle size) and TiO_2 (rutile nanopowder, <100 nm particle size) were purchased from Sigma-Aldrich. Tungsten oxide (WO_3), strontium titanate ($SrTiO_3$) were purchased from Wako. $Bi(NO_3)_3 \cdot 5H_2O$, urea (CN_2OH_4) and V_2O_5 were purchased from Wako. All materials were used as

received without further purification. The deionized water with a resistivity of 18.2 MΩ cm^{-1} was utilized in all experiments.

5.2.2 Preparation of the catalysts

Synthesis of metal (Pt, Pt, Au and Ag)/ZnO and metal (Pt, Pt, Au and Ag)/TiO$_2$ photocatalysts. Cocatalysts (Pt, Pd, Au and Ag) were loaded on ZnO and TiO$_2$ photocatalysts via NaBH$_4$ reduction method. The precursors of cocatalysts were H$_2$PtCl$_6$·6H$_2$O (Wako, 99.9%), Na$_2$PdCl$_4$ (Sigma-Aldrich, 99.99%), HAuCl$_4$·4H$_2$O (Wako, 99.9%) and AgNO$_3$ (Wako, 99.8%). Typically, for synthesis of 0.1 wt% Pt/ZnO photocatalyst, 1 g of ZnO was dispersed into 100.0 mL of aqueous H$_2$PtCl$_6$ solution (0.051 mM) by ultrasonication. After stirring for 1 h, a certain amount of aqueous NaBH$_4$ solution was added dropwise into the solution. After further stirring for 1h, the samples were filtered, washed with water for three times and then dried at 70 °C. The synthesis of 0.1 wt% Pd/ZnO, 0.1 wt% Au/ZnO, 0.1 wt% Ag/ZnO, 0.1 wt% Pt/TiO$_2$, 0.1 wt% Pd/TiO$_2$, 0.1 wt% Au/TiO$_2$, 0.1 wt% Ag/TiO$_2$, 1.0 wt% Pt/ZnO, 1.0 wt% Pd/ZnO, 1.0 wt% Au/ZnO and 1.0 wt% Ag/ZnO was similar to the above method in addition to changing the corresponding metal precursors.

Synthesis of BiVO$_4$ photocatalyst. 9.7 g of Bi(NO$_3$)$_3$·5H$_2$O and 1.82 g of V$_2$O$_5$ were added into 100.0 mL of aqueous HNO$_3$ solution (0.5 M). After stirring for 72 h, the obtained BiVO$_4$ photocatalyst were filtered, washed and dried at 70 °C for 6 h.

Synthesis of BiOCl photocatalyst. 1.46 g of Bi(NO$_3$)$_3$·5H$_2$O and 0.22 g of KCl were added into 20.0 mL of ethylene glycol solution. The mixture was then added into a 50 mL Teflon-line stainless autoclave. Then the autoclave was heated at 160 °C for 12 h and cooled to room temperature. After that, the obtained BiOCl was collected, washed with water and ethanol for three times, dried at 70 °C for 6 h, and calcined in a muffle oven at 300 °C for 4 h.

Synthesis of C$_3$N$_4$ photocatalyst. 5 g of urea was placed into a crucible and calcined in a muffle oven at 550 °C for 4 h with a heating rate of 2 °C min^{-1}, and then cooled to room temperature naturally. Then C$_3$N$_4$ photocatalyst was obtained without further modification.

5.2.3 Characterization

Powder XRD were carried out on an X-ray diffractometer with Cu Kα radiation (PANalytical

B.V., Netherlands). TEM and HR-TEM were perfomed on a Tecnai G 2 F30 S-Twin microscope operated at 300 kV. The actual loading amouts of cocatalysts (Pt, Pd, Au and Ag) were measured by inductively coupled plasma optical emission spectrometry (ICP-OES, HORIBA Jobin Yvon, Ultima2). The Brunauer-Emett-Teller surface area were measured by nitrogen adsorption-desorption experiment (BELsorp II mini, BEL Japan Inc.). UV-visible diffuse reflectance spectra were measured by a Shimadzu UV-2600 spectrophotometer, and transformed into absorption sepectra via Kubelka-Munk transformation. The fluorescence spectra were collected by JASCO FP-6500 fluorescence spectrophotometer. Electron paramagnetic resonance (EPR) spectroscopy measurement was performed on Magnettech MS-5000X with 5, 5-Dimethyl-1-pyrroline-N-oxide (DMPO) as the radical trap. The samples were dispersed in water dissolved CH_4 and O_2 to detect methyl radical ($^{\bullet}CH_3$) and hydroxyl radical ($^{\bullet}OH$), as well as in methanol dissolved O_2 to detect hydroperoxyl ($^{\bullet}OOH$) radicals. The light intensity and wavelength of the irradiation light source were detected by USR-40 spectrophotometer.

5.2.4 Photocatalytic activity measurements

The photocatalytic methane oxidation reaction tests were conducted in a batch-reactor equipped with a quartz window to allow light irradiation (Figure S1). Typically, 10 mg catalyst was dispersed in 100 mL water by ultrasonication for 5 min. Then, the mixture was added into the glass cell and the batch-reactor was purged with O_2 for several times to exhaust air. After that, the reactor vessel was pressurized with 0.1 MPa O_2 (purity, 99.99995%) and 2 MPa CH_4 (purity, 99.9995%). Subsequently, the reactor was loaded into a cold-water bath and the solution was stirred at 1000 rpm. 300 W Xe lamp equipped with a reflector, which can reflect most of the visible light and all the infrared light, was used as the light source. The incident light wavelength was from 300 to 500 nm and light intensity was 100 mW cm^{-1} (Figure S2). A thermocouple was inserted into the solution to directly detect the temperature of the liquid solution. During the reaction process, the temperature of the liquid solution was maintained at 25 ± 2 °C. After the reaction, the reactor was cooled in an ice bath to a temperature below 10 °C. Then the gas product was collected and analyzed by gas chromatograph (GC, Shimadzu) equipped with methanizer and flame ionization detector. The liquid phase of the reaction mixture product was collected by centrifugation. The liquid product was analyzed by nuclear magnetic resonance spectroscopy (NMR, JEOL) and colorimetric method.

For isotopic labeling experiments, 1 MPa ^{13}C enriched CH$_4$ (Tokyo Gas Chemicals, ^{13}C enrichment: > 99 atom%), 0.1 MPa ^{18}O enriched O$_2$ (Taiyo Nippon Sanso Corporation, ^{18}O enrichment: ≥ 98 atom%) and 10 mL water-^{18}O (Taiyo Nippon Sanso Corporation, ^{18}O enrichment: ≥ 98 atom%) were used.

In the cycling tests, we used 10 mg 0.1 wt% Au/ZnO from a total of 100 mg for the photocatalytic methane oxidation. After each cycling measurement reaction, a parallel experiment was conducted using the rest of the photocatalyst under the identical reaction conditions. After that, all the photocatalysts were mixed, washed, collected and dried at 200 °C for 2 h to remove any organic chemicals adsorbed on catalysts. Then 10 mg of photocatalyst was used from the collected samples for the next cycling experiment until a total of 5 cycles.

Turnover number (TON) is generally defined by the number of moles of products to that of active sites. However, it is difficult to determine the number of moles of active sites for ZnO photocatalysts, therefore, a conservative method that the number of moles of ZnO is considered to be the number of active sites was used for the calculation of TON through the following equation.

$$TON = \frac{\text{Number of moles of } (CH_3OOH + CH_3OH + HCHO + CO_2)}{\text{Number of moles of ZnO}}$$
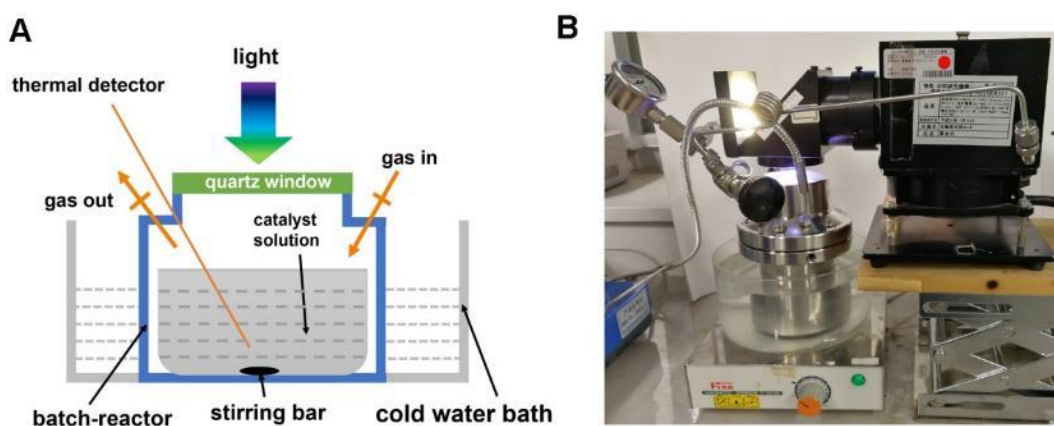

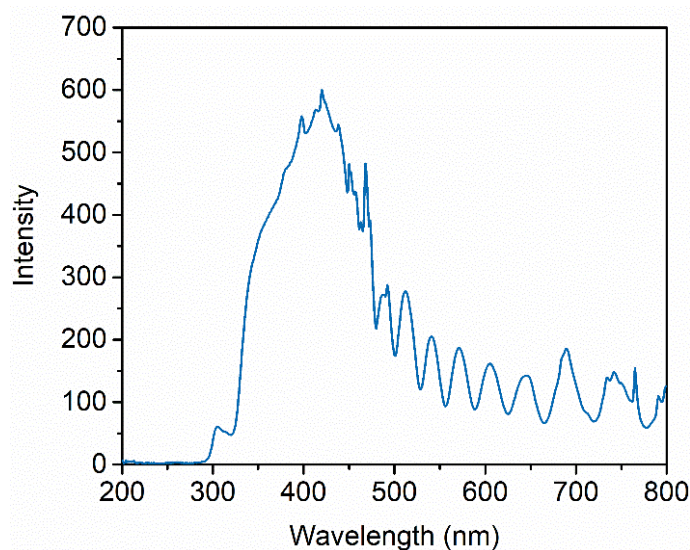**Figure 5.1** Schematic diagram (a) and picture (b) of home-made batch-reactor system.

Figure 5.2 The spectrum of the incident light.

5.2.5 Products analysis

The concentration of CH_3OOH and CH_3OH in the liquid was quantified by ^1H NMR (JEOL ECS 400 MHz). Typically, 0.5 mL liquid product was mixed with 0.1 mL of D_2O and 0.05 µl dimethyl sulfoxide (DMSO, Wako, 99.99%) was added as an internal standard. The products were quantified by comparing the ^1H NMR signal against calibration curves.

The concentration of liquid product HCHO was quantified by colorimetric method.[27] Typically, the reagent solution was firstly prepared by adding 15 g of ammonium acetate, 0.3 mL of acetic acid and 0.2 mL of pentane-2,4-dione into 95 mL water. Then, 0.5 mL of liquid product was mixed with 2.0 mL of water and 0.5 mL of reagent solution. The mixed solution was maintained at 35 °C in a water bath and measured by UV-Vis absorption spectroscopy until the absorption intensity at 412 nm did not further increase. The concentration of HCHO in the liquid product was determined by the standard curve. In addition, the amount of formed HCHO was also quantified by high-performance liquid chromatography (HPLC),[28] and the error between colorimetric method and HPLC analysis was within 5%.

Analysis of hydroxyl radicals (˙OH). The generation of hydroxyl radicals (˙OH) was measured by the photoluminescence (PL) technique using coumarin (COU) as a probe molecule.[29] COU can easily react with ˙OH to form 7-hydroxycoumain (7HC), which has high fluorescence with a PL signal at around 454 nm. The PL intensity of 7HC was proportional to the amount of ˙OH generated. Briefly.

10 mg of catalyst was dispersed in 50 mL of a 1.0 mM COU aqueous solution. The above mixture solution was stirred for 1 h in dark to reach an adsorption-desorption equilibrium. A 300 W Xe lamp equipped with a U340 filter was used as a light source. After light illumination for a certain time, the reaction solution was collected by centrifugation. The PL spectra of 7HC produced were measured by fluorescence spectrophotometer (JASCO FP-6500) with excitation wavelength at 332.0 nm. The PL intensity was recorded at 454 nm.

5.2.6 Computation methods

All calculations in this work were performed with first principle calculations based on density functional theory using Vienna Ab initio Simulation (VASP) package.[30,31] The pseudopotential was generated from the projected augmented wave method. And the exchange-correlation functional was treated by the generalized gradient approximation with the Perdew-Burke-Ernzerhof (GGA-PBE) functional.[32] To avoid the interaction between neighboring slab models with five atomic layers, a vacuum layer of 16 Å was used along the Z-axis direction. The in-plane parameter of surface supercell mode for ZnO (101) is a = 10.886Å, b= 11.328Å while that of TiO$_2$ (101) is a = 12.273Å, b= 6.49860Å. The kinetic cutoff energy for the plane-wave expansion was set to 400 eV, and the 3×3×1 and 2×4×1 k-point mesh set was used for the above surface models. All the structural models were fully relaxed to the ground state with the convergence of energy and forces setting to 1×10^{-5} eV and 0.02 eV Å^{-1}, respectively. In addition, the D2 method proposed by Grimme was adopted to describe the van der Waals interactions. The reaction path energy barrier was calculated from the total energy difference between after and before reaction with the reaction equations below, where * represents the catalysts.

$$*+ CH_4 \rightarrow CH_3 + *H \tag{1}$$

$$CH_3 + *H + O_2 \rightarrow *CH_3OOH \tag{2}$$

$$*CH_3OOH + 2H^+ + 2e^- \rightarrow *CH_3OH + H_2O \tag{3}$$

$$*CH_3OOH \rightarrow *HCHO + H_2O \tag{4}$$

$$*CH_3OH + 1/2O_2 \rightarrow *HCHO + H_2O \tag{5}$$
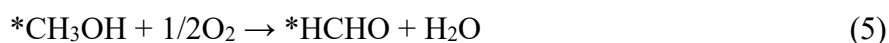
5.3 Results and discussion

5.3.1 Catalyst characterization

The commercial ZnO were used as photocatalyst to investigate photocatalytic conversion of CH_4. The transmission electron microscopy (TEM) and scanning transmission electron microscopy (STEM) images of ZnO showed that the particle size of ZnO is in the range of 15-50 nm (Figure 5.3). The X-ray diffraction (XRD) pattern and high resolution TEM (HRTEM) image of ZnO (Figure 5.4) showed that they were highly crystalline with wurtzite phase (JCPDS No. 36-1451). Additionally, for comparison, different kinds of commercially available semiconductors (TiO_2, WO_3, $SrTiO_3$ and CdS) and several semiconductors (C_3N_4, $BiVO_4$ and BiOCl) synthesized by procedures reported elsewhere were also used (see supplementary materials).
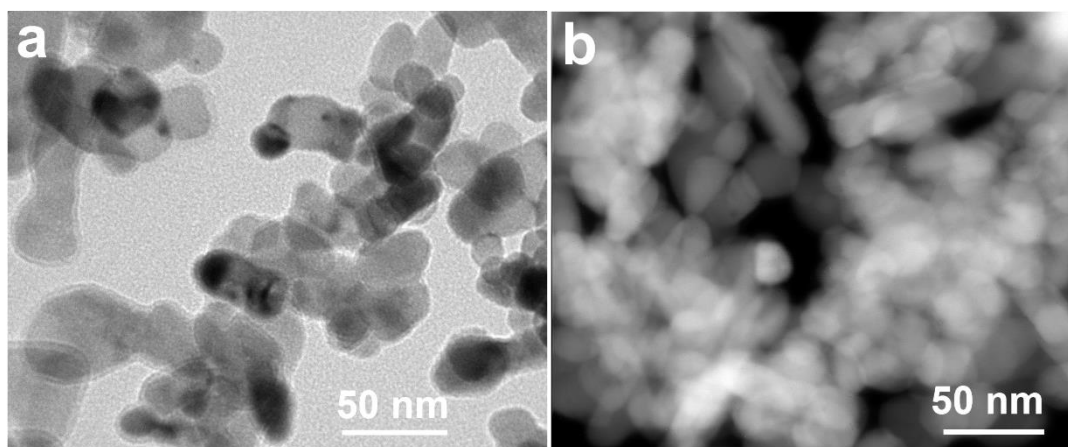

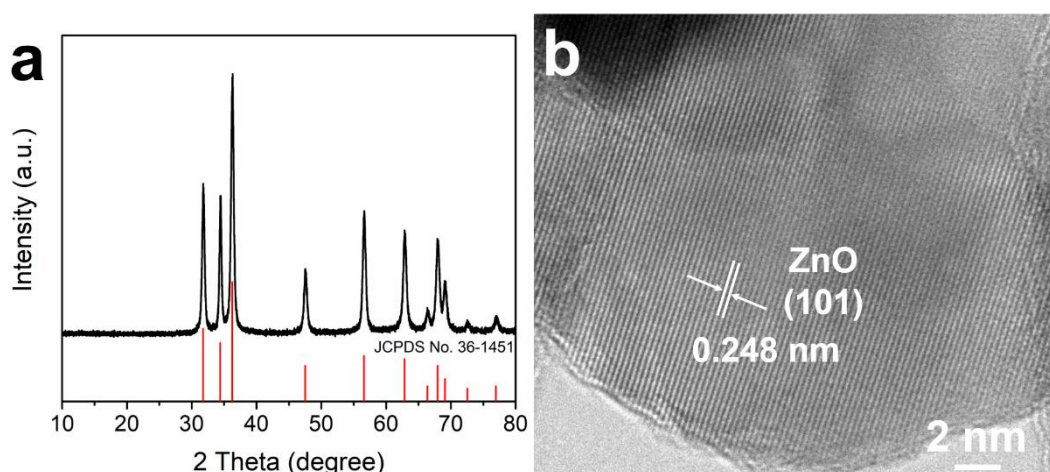**Figure 5.3** TEM (A) and STEM (B) images of ZnO NPs.

Figure 5.4 XRD pattern (A) and HRTEM image (B) of ZnO.

5.3.2 Photocatalytic oxidation of methane

The photocatalytic reactions were carried out at room temperature (25±2 °C) under 2 MPa of CH_4 and 0.1MPa of O_2 in a batch-type reactor, in which the photocatalysts were suspended in 100 mL water. The reactions were proceeded for 2h under irradiation of 300 W Xe lamp (wavelength λ = 300-500 nm) with light intensity of 100 mW cm^{-2} as the light source. No product or only little amounts of CO_2 was produced over most of photocatalysts, while oxygenate product (HCHO) was only produced on ZnO and TiO_2 (Table 5.1, entry 1-10). TiO_2 P25 (composed of anatase and rutile crystallites) showed a higher activity for HCHO production than ZnO, yet with a low selectivity. Analysis of the reaction solution failed to detect other oxygenates such as methyl hydroperoxide (CH_3OOH), CH_3OH and formic acid (HCOOH) by ^1H nuclear magnetic resonance (NMR).

Then, I further loaded co-catalysts on photocatalysts and investigated their influences on the photocatalytic CH_4 oxidation. Depositing co-catalysts Pt, Pd, Au or Ag NPs on ZnO with 0.1 weight percent (wt%) (Figure 5.5 and Table 5.2) promoted the production of oxygenated products (CH_3OOH and CH_3OH) (Table 5.1, entry 11-14); whereas loading these co-catalysts had little contribution to the formation of liquid oxygenates over TiO_2 (Table 5.1, entry 15-18). The total production of liquid oxygenates including CH_3OOH, CH_3OH and HCHO over 0.1 wt% Pt, Pd or Au/ZnO all exceeded 210 μmol with more than 90% selectivity. Compared with these photocatalysts, yields of oxygenates over 0.1 wt% Ag/ZnO was relatively lower (138.7 μmol) but with a higher selectivity to HCHO. For 0.1 wt% Au/ZnO, the generation rate of liquid oxygenates amounts to approximately 12.6 micromoles per gram catalyst per hour ($mmol_{oxygenates}$ $g_{catalyst}^{-1}$ hour^{-1}), with nearly 96% selectivity. This activity substantially overtakes the rates of many other photo- or thermo- catalytic systems where H_2O_2 or CO is necessary for oxygenates formation from CH_4 oxidation at or above room temperature,[18,23,24] and is even higher than that of biological system over methane mono-oxygenase from Methylococcus capsulatus (Bath).[33] When the irradiation time increased to 4 h, the measured amount of total liquid oxygenates over 0.1 wt% Pt, Pd, Au or Ag/ZnO increased accordingly while maintaining high selectivity (~90%) (Table 5.3). Increasing the loading amount of co-catalysts to 1.0 wt% has little impact on the total amount of oxygenated products, indicating that 0.1 wt% is a proper cocatalyst loading amount for the ZnO used in this study (Table 5.4). Control experiments without photocatalysts, light or CH_4, (Table 5.1, entry 19-21) showed no formation of oxygenated products,

demonstrating that the oxygenates were formed via photocatalytic CH_4 oxidation.

Table 5.1 Catalytic activity. Comparison of photocatalytic activity of different photocatalysts, co-catalyts/ZnO and co-catalyst/TiO_2 for oxidation of methane using O_2 as oxidant. Reaction conditions: 10 mg catalyst, 2 MPa CH_4, 0.1 MPa O_2, 100 mL water, 25±2 °C reaction temperature, 2 h reaction time; light source, 300 W Xe lamp, $300 < \lambda < 500$ nm, light intensity 100 mW cm^{-2}.

Entry	Catalyst	Amount of product (μmol)					Liquid products (μmol)	All products (μmol)	Liquid products sel. (%)
		CH_3OOH	CH_3OH	HCHO	CO	CO_2			
1	ZnO	0	0	25.2	0.04	1.2	16.0	26.4	95.3
2	TiO_2 (P25)	0	0	43.0	0.06	6.5	48.5	49.6	86.7
3	TiO_2 (anatase)	0	0	7.5	0	2.1	9.6	10.4	84.6
4	TiO_2 (rutile)	0	0	2.5	0	0.8	3.3	4.3	81.4
5	$SrTiO_3$	0	0	0	0	0.2	0.2	0.2	-
6	WO_3	0	0	0	0	0.2	0.2	0.2	-
7	$BiVO_4$	0	0	0	0	0	0	0	-
8	BiOCl	0	0	0	0	0	0	0	-
9	CdS	0	0	0	0	0	0	0	-
10	C_3N_4	0	0	0	0	0	0	0	-
11*	0.1 wt% Pt/ZnO	65.6	44.5	101.1	0.6	20.7	211.2	232.5	90.8
12*	0.1 wt% Pd/ZnO	41.3	60.7	110.3	0.3	19.5	212.3	232.1	91.5
13*	0.1 wt% Au/ZnO	123.4	41.2	86.3	0.4	11.6	250.9	262.9	95.4
14*	0.1 wt% Ag/ZnO	19.3	7.3	112.1	0.8	7.1	138.7	146.6	94.6
15	0.1 wt% Pt/TiO_2	0	0	36.6	0.1	13.4	36.6	50.1	73.1
16	0.1 wt% Pd/TiO_2	0	0	34.1	0.1	12.4	34.1	46.6	73.2
17	0.1 wt% Au/TiO_2	0	0	44.1	0.1	14.3	44.1	58.5	75.4
18	0.1 wt% Ag/TiO_2	0	0	45.2	0.1	12.9	45.2	58.2	77.7
19	-	0	0	0	0	0	0	0	-
20§	0.1 wt% Au/ZnO	0	0	0	0	0	0	0	-
21†	0.1 wt% Au/ZnO	0	0	0	0	0	0	0	-

| 22 ‡ | 0.1 wt% Au/ZnO | 0 | 0 | 0 | 0 | 0 | 0 | 0 | - |

*Entries 11 to 14: Trace amount of C_2H_6 was detected

§Entry 20: 2 MPa Ar gas was used instead of CH_4

†Entry 21: Without light irradiation

‡Entry 22: Visible light irradiation ($420 < \lambda < 500$ nm)
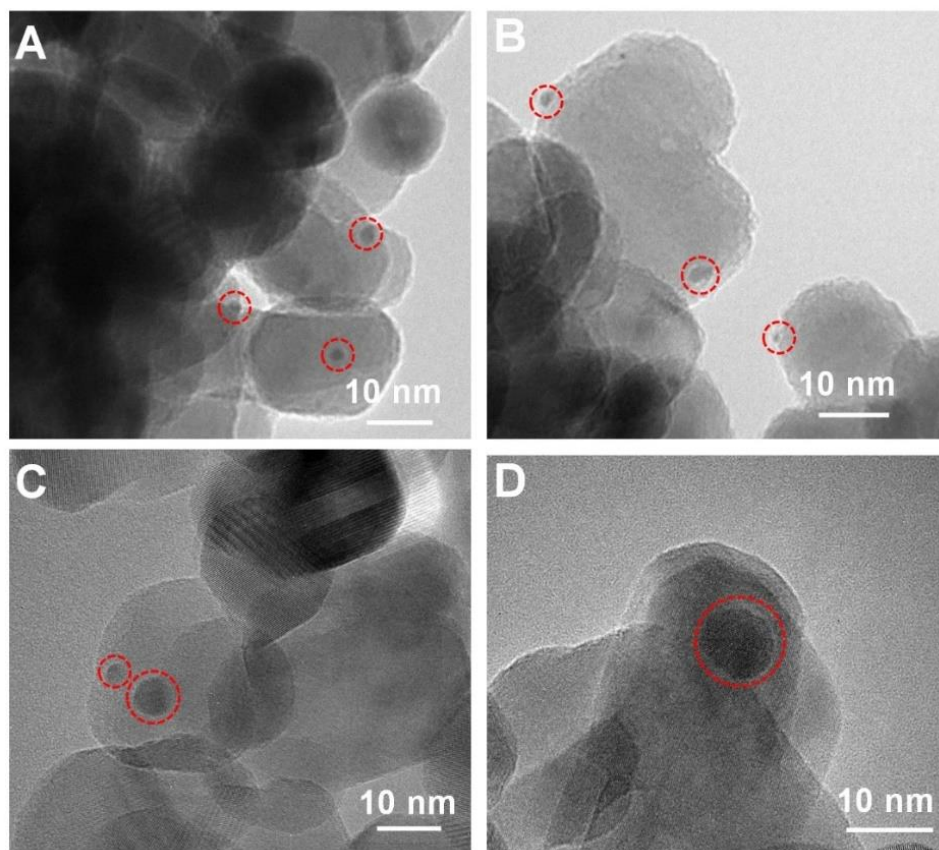

Figure 5.5 TEM images of (A) 0.1 wt% Pt/ZnO, (B) 0.1 wt% Pd/ZnO, (C) 0.1 wt% Au/ZnO and (D) 0.1 wt% Ag/ZnO.

Table 5.2 Physicochemical properties of ZnO- and TiO$_2$-based photocatalysts.

Catalyst	S_{BET} (m^2 g^{-1})	Metal loading (wt%)
ZnO	28.5	-
TiO$_2$	56..8	-
0.1 wt% Pt/ZnO	27.5	0.12
0.1 wt% Pd/ZnO	27.1	0.11

0.1% wt Au/ZnO	27.7	0.12
0.1 wt% Ag/ZnO	27.3	0.10
0.1 wt% Pt/TiO$_2$	55.8	0.12
0.1 wt% Pd/TiO$_2$	56.2	0.11
0.1 wt% Au/TiO$_2$	56.1	0.12
0.1 wt% Ag/TiO$_2$	55.9	0.10

Table 5.3 Catalytic activity of different photocatalysts. Reaction conditions: 10 mg catalyst, 2 MPa CH$_4$, 0.1 MPa O$_2$, 100 mL water, 25±2 °C reaction temperature, 4 h reaction time; light source, 300 W Xe lamp, 300 < λ < 500 nm, light intensity 100 mW cm^{-2}.

Entry	Catalyst	Amount of product (μmol)					Liquid products (μmol)	All products (μmol)	Liquid products sel. (%)
		CH$_3$OOH	CH$_3$OH	HCHO	CO	CO$_2$			
1	0.1 wt% Pt/ZnO	117.6	85.3	113.2	1.3	35.7	316.1	353.1	89.5
2	0.1 wt% Pd/ZnO	35.5	108.2	122.5	0.1	35.5	266.2	301.8	88.2
3	0.1 wt% Au/ZnO	170.1	58.6	104.9	1.25	28.4	333.6	363.3	91.8
4	0.1 wt% Ag/ZnO	48.7	23	140	1.4	12.9	211.7	226.0	93.6

Table 5.4 Catalytic activity of different photocatalysts. Reaction conditions: 10 mg catalyst, 2 MPa CH$_4$, 0.1 MPa O$_2$, 100 mL water, 25±2 °C reaction temperature, 2 h reaction time; light source, 300 W Xe lamp, 300 < λ < 500 nm, light intensity 100 mW cm^{-2}.

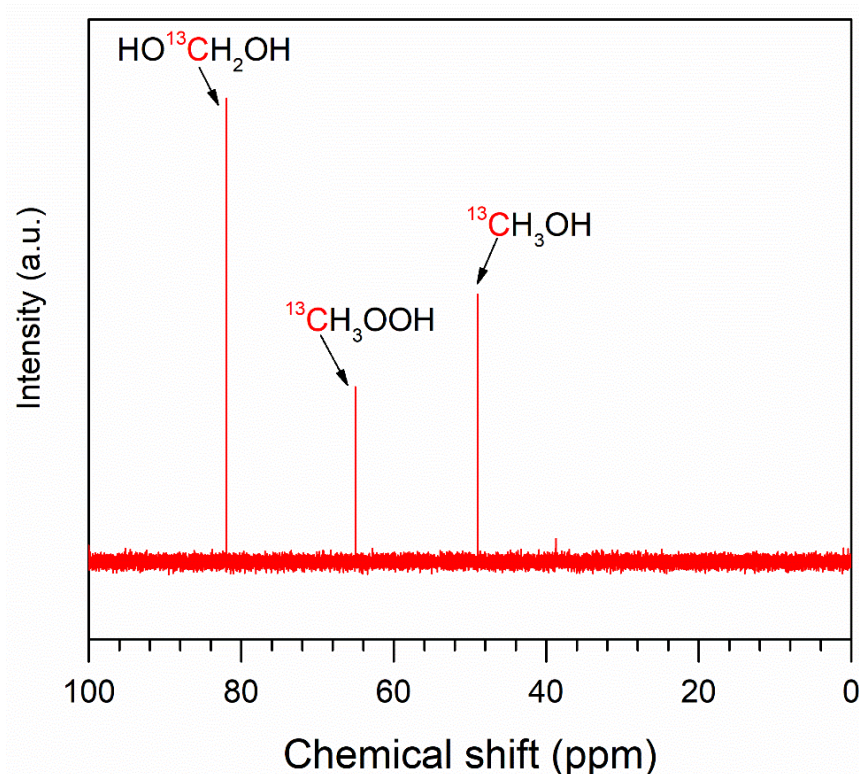| Entry	Catalyst	Amount of product (μmol)					Liquid products (μmol)	All products (μmol)	Liquid products sel. (%)
		CH$_3$OOH	CH$_3$OH	HCHO	CO	CO$_2$			
1	1.0 wt% Pt/ZnO	52.3	77.2	82.9	0.2	32.9	212.4	245.5	86.5
2	1.0 wt% Pd/ZnO	33.6	114.1	79.7	0.1	30.9	227.4	258.4	88.0
3	1.0 wt% Au/ZnO	107.2	85.3	64	0.1	13.2	256.5	269.8	95.1
4	1.0 wt% Ag/ZnO	45.3	30.3	113.8	0.4	8.2	189.4	198	95.7

Figure 5.6 ^{13}C NMR spectra obtain from photocatalytic methane oxidation using ^{13}CH$_4$. Reaction conditions: 10 mg 0.1 wt% Pt/ZnO, 1 bar O$_2$, 10 bar ^{13}CH$_4$, 10 mL water, 25±2 °C reaction temperature, 4 h reaction time; light source, 300 W Xe lamp, 300 < λ < 500 nm, light intensity 100 mW cm^{-2}. It is worthy to note that in aqueous solutions of formaldehyde, formaldehyde undergoes hydration to generate methylene glycol (MG, HO-CH$_2$-OH), which is the major species, leaving only traces of the molecular formaldehyde (HCHO). The peak at 82.02 ppm attributes to MG.

To confirm the carbon source of the oxygenated products, isotope labelling experiments using ^{13}CH$_4$ was conducted. 1 MPa ^{13}CH$_4$ was mixed with 0.1 MPa O$_2$ for isotope experiment over 0.1 wt% Pt/ZnO in 10 mL water for 4 h. Three obvious ^{13}C NMR signals at 49.1, 65.1, 82.0 and 171.0 ppm are attributed to CH$_3$OH, CH$_3$OOH, and HOCH$_2$OH (methylene glycol, the major species in aqueous solutions of HCHO[34]), respectively, confirming that all the oxygenates indeed originate from CH$_4$ conversion (Figure 5.6). When increasing the CH$_4$ solubility in water by elevating its pressure, the yields of oxygenated products increased accordingly with high selectivity (>95%) (Figure 5.7). The catalyst could even show appreciable activity under simulated sunlight (AM 1.5G, 100 mW cm^{-2}) and the production of oxygenates increases with irradiation time (Figure 5.8). The total oxygenated products reached 235.3 μmol with approximately 97% selectivity after 4 hours' irradiation. Only little decrease in activity was observed over 0.1 wt% Au/ZnO after 5-run cycling tests (10 h in total) and

the corresponding turnover number (TON) of all products reached 10.4 (Figure 5.9), confirming that CH_4 oxidation is a genuine photocatalytic process with good stability.
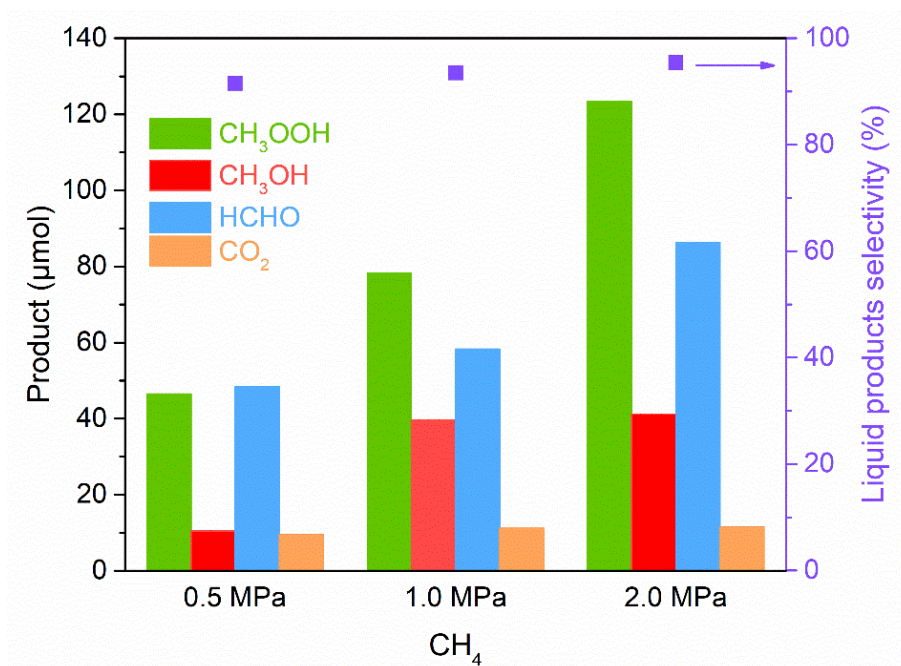

Figure 5.7 Product yields and liquid oxygenates selectivity for 0.1 wt.% Au/ZnO under different CH_4 pressure. Reaction conditions: 10 mg catalyst, 100 mL water, 0.1 MPa O_2, 25±2 °C reaction temperature; light source, 300-W Xe lamp, 300 < λ < 420 nm, light intensity 100 mW cm^{-2}.
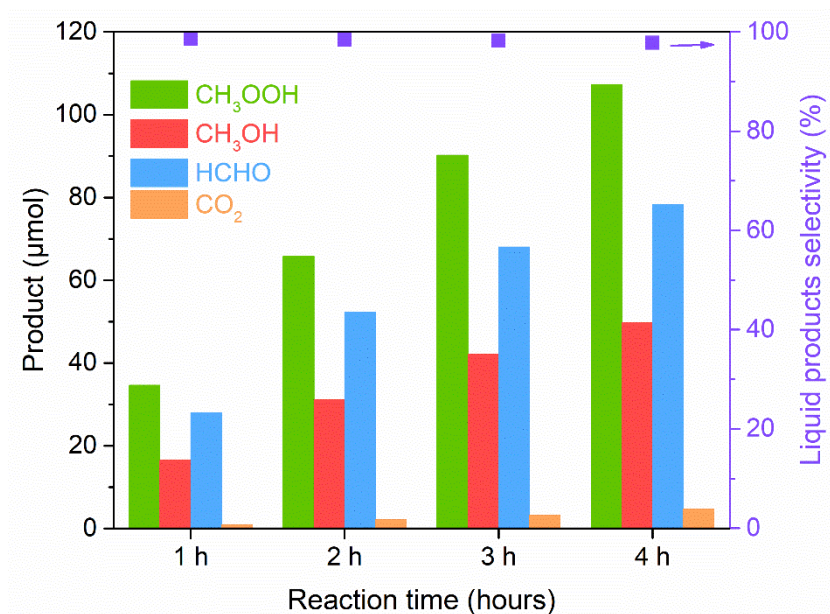

Figure 5.8 Time course of product yields and liquid oxygenates selectivity for 0.1 wt% Au/ZnO under simulated sunlight irradiation. Reaction conditions: 10 mg catalyst, 100 mL water, 0.1 MPa O_2, 2.0 MPa CH_4, 25±2 °C reaction temperature; light source, solar simulator (AM 1.5G), light intensity 100 mW cm^{-2}.
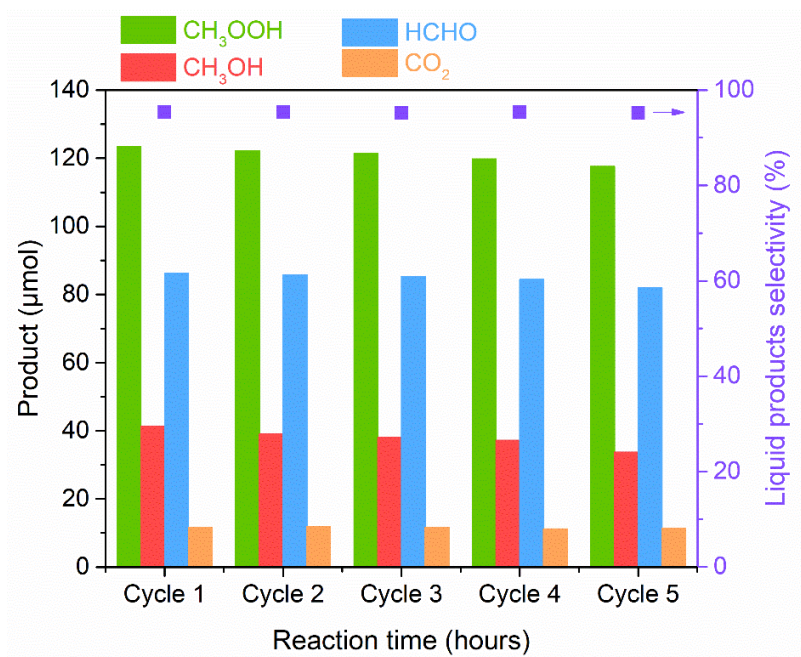
Figure 5.9 Cycling measurements of photocatalytic oxidation of methane over 0.1 wt% Au/ZnO. Reaction conditions: 10 mg catalyst, 2 MPa CH_4, 0.1 MPa O_2, 100 mL water, 25±2 °C reaction temperature, 2 h reaction time; light source, 300 W Xe lamp, $300 < \lambda < 500$ nm, light intensity 100 mW cm^{-2}.
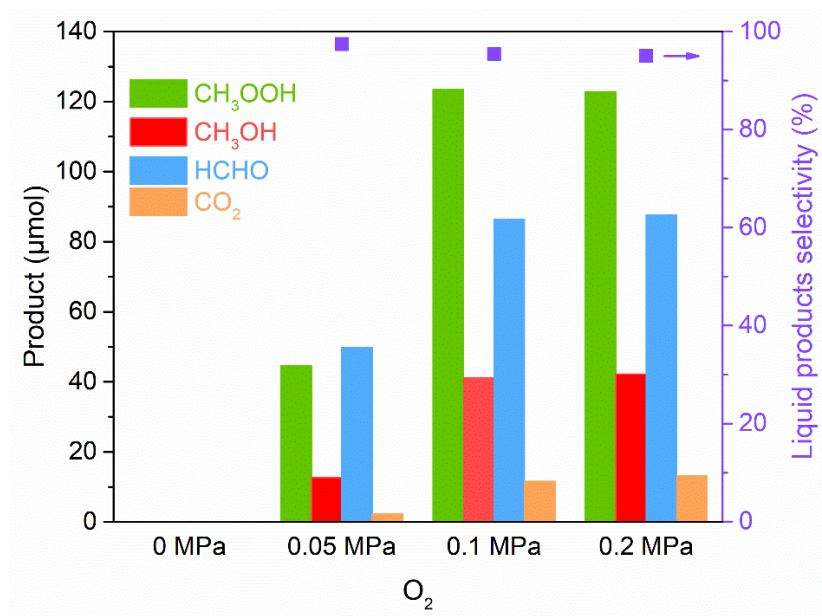
5.3.3 Mechanism discussion

Figure 5.10 Product yields and liquid oxygenates selectivity over 0.1 wt% Au/ZnO under different O_2 pressure. Reaction conditions: 10 mg catalyst, 100 mL water, 2.0 MPa CH_4, 25±2 °C reaction temperature, 2 h reaction time; light source, 300-W Xe lamp, $300 < \lambda < 420$ nm, light intensity 100 mW cm^{-2}.

Figure 5.11 GC-MS spectra of CH_3OH generated over 0.1 wt% Au/ZnO with $^{18}O_2$ + $H_2^{16}O$ or $^{16}O_2$ + $H_2^{18}O$ in photocatalytic methane oxidation.
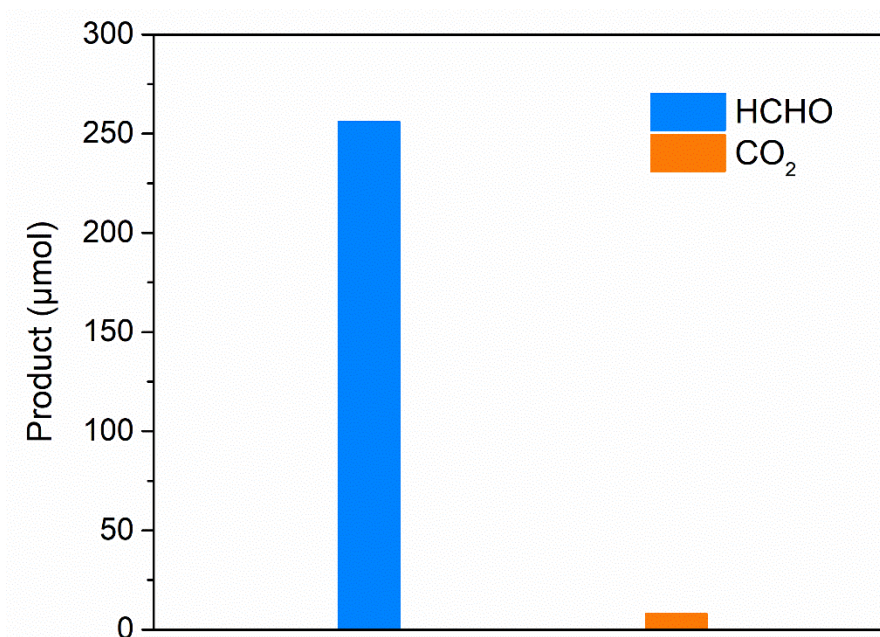
Figure 5.12 Product yields in photocatalytic oxidation of methanol. Reaction conditions: 10 mg 0.1 wt% Au/ZnO, 0.1 MPa O_2, 100 mL of 100 mM CH_3OH water, 25±2 °C reaction temperature, 1 h reaction time; light source, 300 W Xe lamp, 300 < λ < 500 nm, light intensity 100 mW cm^{-2}.

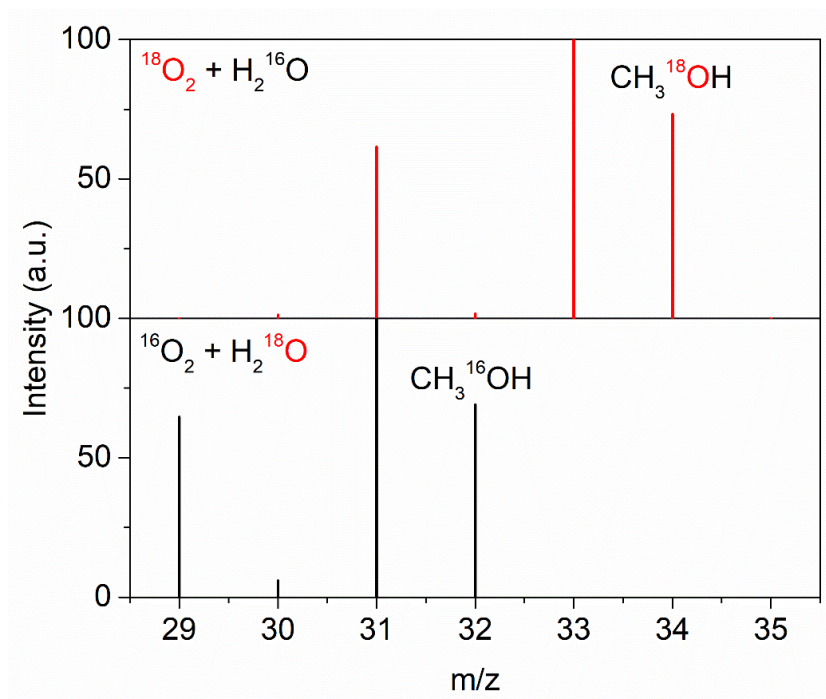None of carbonaceous products can be identified in the water in the absence of O_2 (Figure 5.10) in the control experiment, indicating that O_2 is indispensable for the photocatalytic reaction. The

yields of oxygenated products are boosted until the pressure of O_2 reaches 0.1 MPa, beyond which O_2 pressure contributes little to the photocatalytic activity. It is reasonable that, in the photocatalytic CH_4 oxidation with O_2 in water, in contrast to the relatively higher O_2 solubility and facile reaction kinetics of O_2 reduction, the overall reaction rate is limited by the low CH_4 solubility in water and its well-known tough C-H activation kinetics. Therefore, the overall photocatalytic activity is more sensitive to the pressure of CH_4 than that of O_2. To confirm the direct participation of O_2 in forming oxygenated products, the isotope experiments using ^{18}O-labelled oxygen ($^{18}O_2$) or ^{18}O-labelled water ($H_2{}^{18}O$) in the reaction were conducted and oxygenated products were analyzed by gas chromatography-mass spectrometry (GC-MS). Previous studies have shown that CH_3OOH can decompose into CH_3OH in the presence of air during the GC-MS analysis, resulting in a low extent of ^{18}O incorporation.[18,35] To avoid the thermal decomposition of CH_3OOH, $NaBH_4$ were used to reduce CH_3OOH to CH_3OH before conducting GC-MS analysis according to the reported method.[18] The results show that 100% of ^{18}O has been incorporated into CH_3OH, while $CH_3{}^{18}OH$ was not found in the oxidation reactions with $^{16}O_2$ and $H_2{}^{18}O$ (Figure 5.11). Due to its low equipment sensitivity of HCHO to mass spectrometer, it is unable to detect the HCHO to analyze it isotope information. However, it has been widely known that HCHO can be readily produced in photocatalytic CH_3OH dehydrogenation without removing O atoms.[36,37] Experiments using CH_3OH as the reactant also clearly confirmed the formation of HCHO (Figure 5.12). Thus, the O atoms of HCHO should also be derived from molecular O_2. All these results explicitly reveal that ZnO photocatalysts can catalyze direct CH_4 conversion into oxygenated products in pure water by solely using molecular O_2.

To study the mechanism of methane photo-oxidation, *in-situ* electron paramagnetic resonance (EPR) spin-trapping technique with the spin traps 5,5-Dimethyl-1-pyrroline *N*-oxide (DMPO) were used. Before the introduction of CH_4, the 1:2:2:1 quartet signal ascribed to DMPO-OH adduct was observed on illuminated various ZnO photocatalysts (Figure 5.13), revealing the presence of ˙OH.[38] When introducing CH_4 and O_2, both ˙CH_3 and ˙OH were detected (Figure 5.14), which indicates that the photocatalytic methane oxidation over ZnO photocatalysts is radical-based and involves the participation of ˙CH_3.[20] Depositing co-catalysts (Pt, Pd, Au and Ag NPs) on ZnO led to significant increase in the amounts of ˙CH_3 and ˙OH radicals, suggesting that these co-catalysts facilitate the H abstraction of methane. The increased signals of ˙CH_3 also matched well with the enhanced

photocatalytic activity after the introduction of co-catalysts. The intermediate of O_2 photo-reduction was also measured by ESR spin-trapping technique, in which methanol was used to scavenge $^\bullet OH$. The results clearly show the signal of hydroperoxyl radical ($^\bullet OOH$) formed via Eq. 1 over various ZnO photocatalysts (Figure 5.15).[38,39] Likewise, introduction of co-catalysts loaded ZnO also produced more $^\bullet OOH$. The increase in $^\bullet OOH$ production generally results from the contribution of improved separation of photo-excited carriers and lowered reaction barriers of these co-catalysts to oxygen reduction. The produced $^\bullet OOH$ could couple with $^\bullet CH_3$ to generated CH_3OOH (Eq. 2). CH_3OOH is also probably produced via the reaction of $^\bullet CH_3$ and O_2 to form $CH_3O_2^\bullet$ at first which then undergoes a further single electron coupled proton reduction process (Eqs. 3 and 4).[18,20]

$$e^- + O_2 + H^+ \rightarrow {}^\bullet OOH \tag{1}$$

$$^\bullet CH_3 + {}^\bullet OOH \rightarrow CH_3OOH \tag{2}$$

$$^\bullet CH_3 + O_2 \rightarrow CH_3O_2^\bullet \tag{3}$$

$$CH_3O_2^\bullet + H^+ + e^- \rightarrow CH_3OOH \tag{4}$$

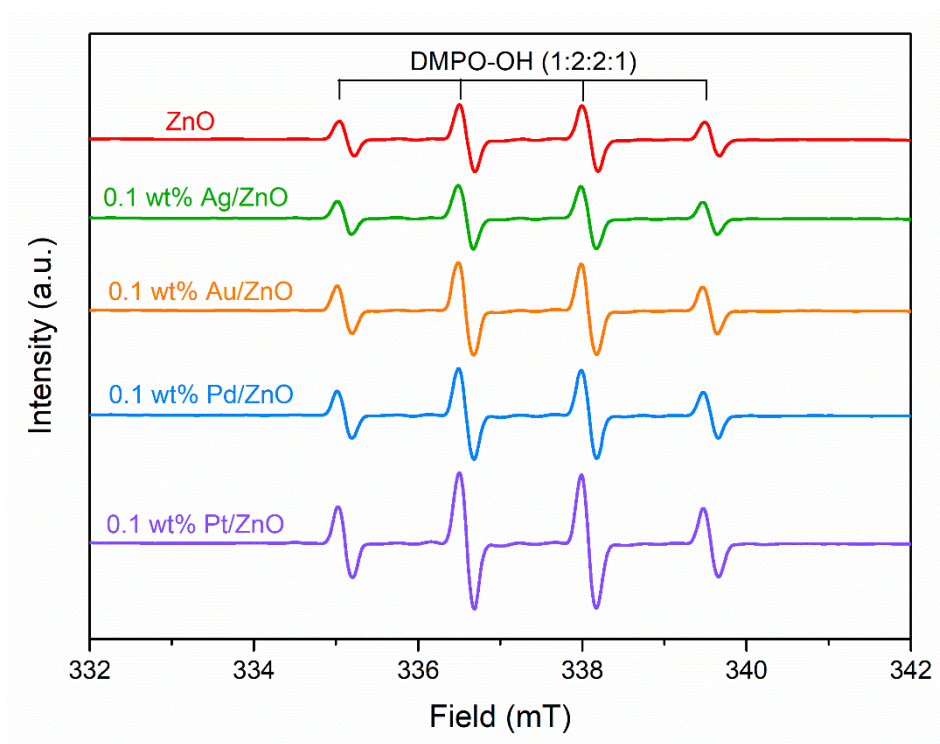$$^\bullet CH_3 + {}^\bullet OH \rightarrow CH_3OH + H_2O \tag{5}$$
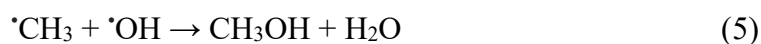
Figure 5.13 EPR spectra of co-catalysts/ZnO under light irradiation for 10 min in aqueous solution. DMPO was added into the reaction mixture as the radical trapping agent.
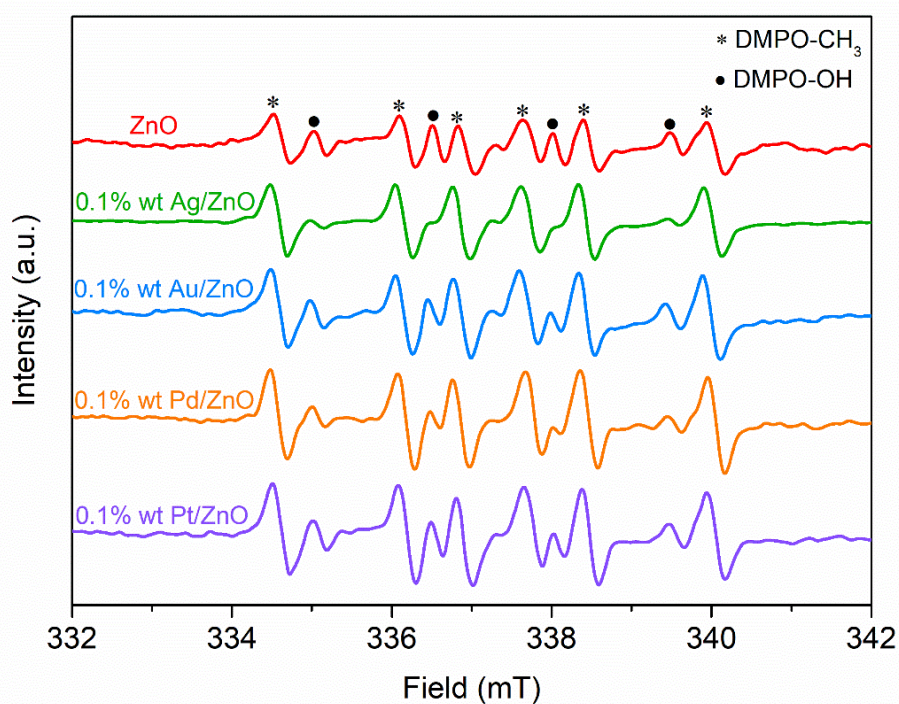
Figure 5.14 In situ EPR spectra of co-catalysts/ZnO under light irradiation of 10 min in the presence of CH_4 and O_2. Signals marked by stars are attributed to DMPO-CH$_3$ adducts; signals marked by solid dots are attributed to DMPO-OH adducts.

Figure 5.15 In situ EPR spectra of co-catalysts/ZnO under light irradiation of 10 min in the presence of O_2 and CH_3OH (as $^\bullet$OH scavenger).

Figure 5.16 Comparison of PL intensity over different catalysts in 1 mM COU aqueous solution.

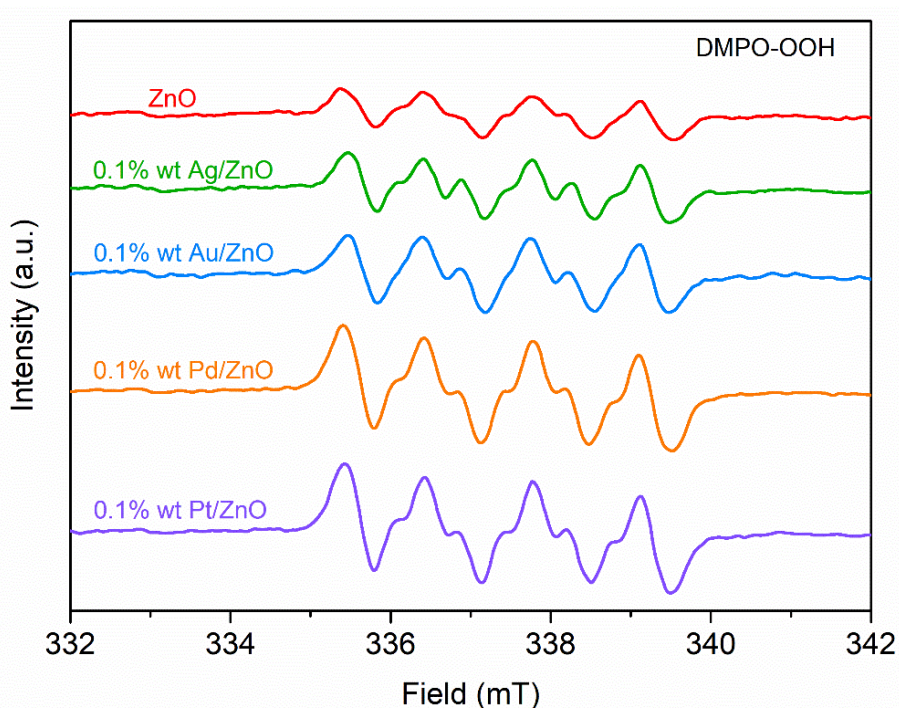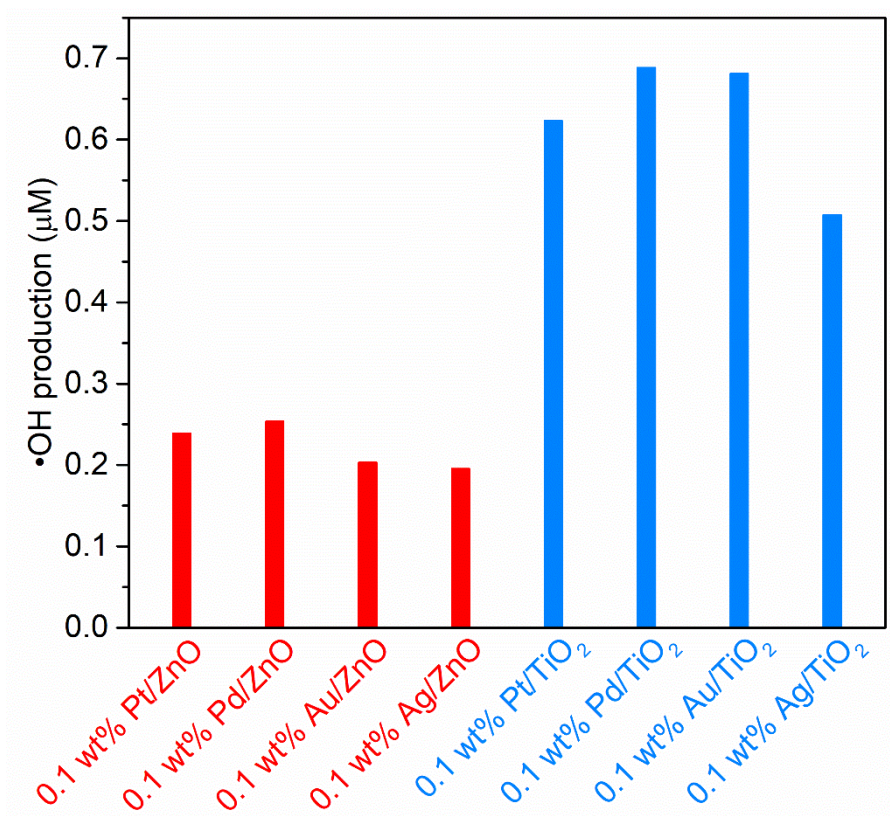Although cocatalysts loaded TiO_2 are more efficient than cocatalysts loaded ZnO in $^{\bullet}OH$ production (Figure 5.16), the former photocatalytic activities are much lower than the latter. It is thus plausible that the C-H bond activation of CH_4 for $^{\bullet}CH_3$ formation is more likely to be initiated by photo-generated hole centers (O^-) at photocatalyst surface rather than $^{\bullet}OH$ radicals. DFT calculations (Figure 5.17a) confirm that the reaction energy barrier of H abstraction of CH_4 by oxygen atom on ZnO is obviously lower than that of TiO_2, which is accordance with the experimental results of photocatalytic methane oxidation. Therefore, photocatalytic CH_4 activation over oxide semiconductors probably undergoes a different mechanism from the widely reported liquid phase thermocatalytic systems where CH_4 is activated by $^{\bullet}OH$ derived from H_2O_2.[18,20] After the formation of $^{\bullet}CH_3$, a series of oxygenated products would be readily generated without thermodynamic limitations. According to ESR results and very negative $\Delta G_{(CH3OOH)}$ (-5.17 eV), the main product CH_3OOH would be generated by coupling $^{\bullet}CH_3$ with $^{\bullet}OOH$ once CH_4 and O_2 are activated by irradiated photocatalysts at initial reaction stage.[20] Considering the fact that no oxygenated products were delivered in the absence of oxygen and a 100% $CH_3^{18}OH$ was obtained in isotope experiment with $^{18}O_2$, CH_3OH should be derived from CH_3OOH precursor through a photo-reduction process

rather than the coupling of $^•CH_3$ and water photo-oxidation derived $^•OH$ (Eq. 5). Finally, HCHO can be produced from the photo-oxidation of CH_3OH by photogenerated holes or $^•OH$, which has been thoroughly investigated.[33,34] Alternatively, HCHO is also possibly produced from the direct decomposition of CH_3OOH, according to previous study (Figure 5.17b).[40]
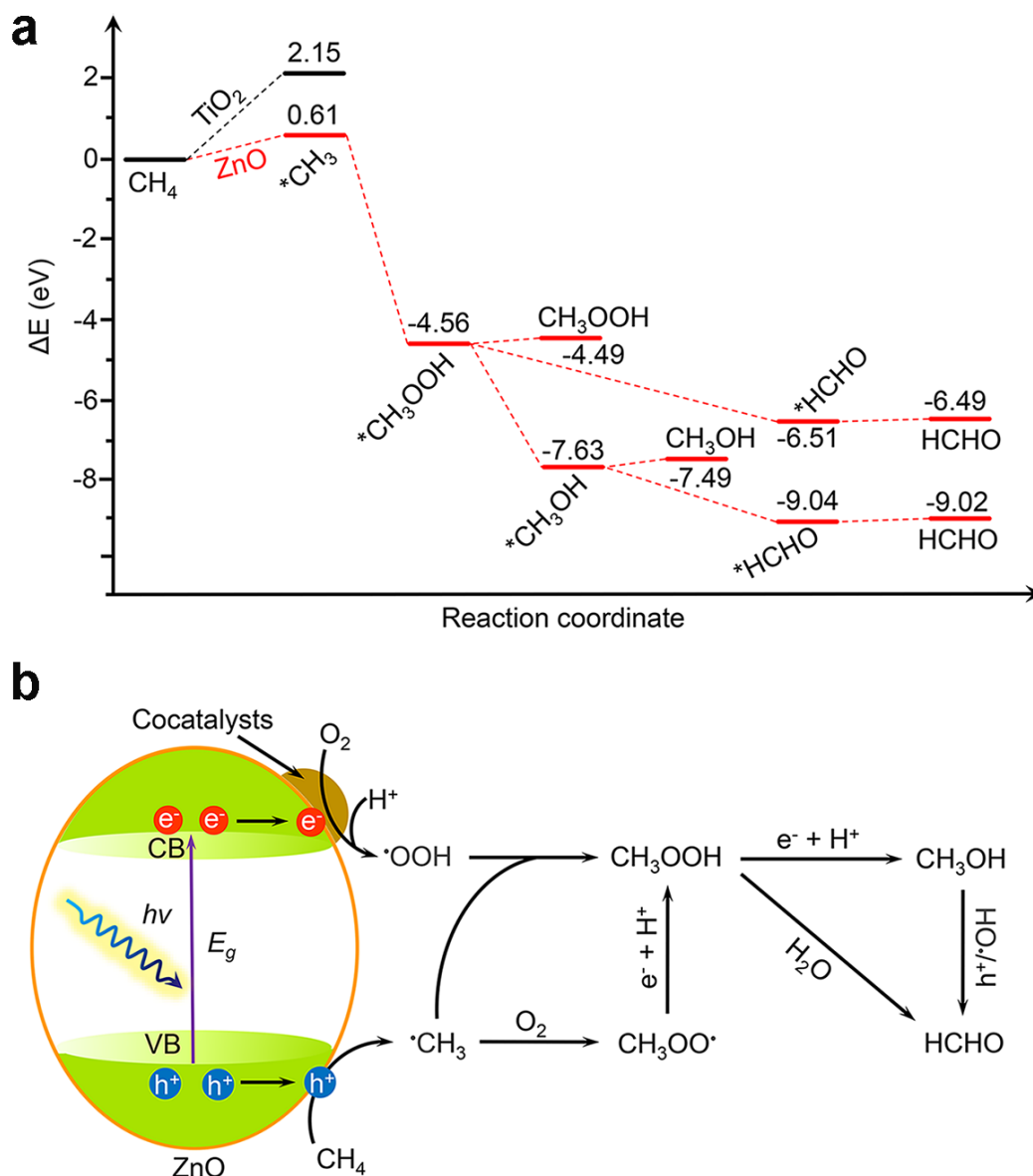
Figure 5.17 Reaction pathways for photocatalytic oxidation of methane with oxygen. (a) The results of DFT calculations for the production $^•CH_3$, CH_3OOH, CH_3OH and HCHO in methane oxidation on ZnO (101) and TiO_2 (101). ΔE (eV) in the diagram represents the reaction energy of different intermediate products. Zn, Ti, O, H and C atoms are shown in blue, purple, red, white and gray, respectively. (b) Sketch of the proposed reaction mechanism for photocatalytic CH_4 oxidation to CH_3OOH, CH_3OH, and HCHO.

Additionally, experimental results also show that the selectivity towards CH_3OOH or CH_3OH is closely related to the type of cocatalysts. In comparison with Pt and Pd loaded ZnO, Au and Ag loaded samples give higher selectivity towards CH_3OOH. From another perspective, photocatalytic CH_4 oxidation reduction with O_2 is also a photocatalytic oxygen reduction reaction (ORR). The cocatalyst-determined CH_3OOH and CH_3OH selectivity in photocatalytic reaction of this work displays similar trend to that of H_2O_2 and H_2O selectivity in general electrocatalytic ORR, i.e., Pt and Pd are more selective to $4e^-$ ORR process to produce CH_3OH or H_2O, while Au and Ag are relatively more efficient for $2e^-$ ORR process to produce CH_3OOH or H_2O_2.[41] This would be an instructive insight for exploring more efficient photocatalysts by loading selective co-catalysts for methane conversion into target products, with oxygen as oxidant at room temperature.

5.4 Conclusions

In conclusion, I report that ZnO loaded with co-catalysts (Pt, Pd, Au or Ag) directly oxidize methane to methanol and formaldehyde using molecular oxygen as oxidant in aqueous solution under mild light irradiation at room temperature. High catalytic activity (12.6 micromoles per gram catalyst per hour) and selectivity (95%) were achieved. Experiments with isotopically labeled oxygen and water reveal that molecular oxygen, rather than water, was the oxygen source of methanol formed. Results of isotopic labelling, electron paramagnetic resonance, and density functional theory calculations demonstrate that the photocatalytic oxidation of methane to liquid oxygenates is a radical process, and surface lattice oxygen ions (O^-) of ZnO induced by photo-generated holes play the dominate role for the activation of methane to methyl radicals, a rate-limiting step for methane oxidation, with selectivity for methanol controlled by co-catalysts.

References

1. Sattler, J.J., Ruiz-Martinez, J., Santillan-Jimenez, E., and Weckhuysen, B.M. (2014). Catalytic dehydrogenation of light alkanes on metals and metal oxides. Chem. Rev. *114*, 10613-10653.

2. McFarland, E. (2012). Unconventional chemistry for unconventional natural gas. Science *338*, 340-342.

3. Malakoff, D. (2014). The gas surge. Science *334*, 1464-1467.

4. Labinger, J.A. (2018). Comment on "Selective anaerobic oxidation of methane enables direct synthesis of methanol". Science *358* eaan5970.

5. Schwach, P., Pan, X., and Bao, X. (2017). Direct Conversion of Methane to Value-Added Chemicals over Heterogeneous Catalysts: Challenges and Prospects. Chem. Rev. *117*, 8497-8520.

6. Olivos-Suarez, A.I., Szécsényi, À., Hensen, E.J.M., Ruiz-Martinez, J., Pidko, E.A., and Gascon, J. (2016). Strategies for the Direct Catalytic Valorization of Methane Using Heterogeneous Catalysis: Challenges and Opportunities. ACS Catal. *6*, 2965-2981.

7. Ravi, M., Ranocchiari, M., and van Bokhoven, J.A. (2017). The direct catalytic oxidation of methane to methanol-A critical assessment. Angew. Chem. Int. Ed. *56*, 16464-16483.

8. Gunsalus, N.J., Koppaka, A., Park, S.H., Bischof, S.M., Hashiguchi, B.G., and Periana, R.A. (2017). Homogeneous functionalization of methane. Chem. Rev. *117*, 8521-8573.

9. Schwarz, H., Shaik, S., and Li, J. (2017). Electronic Effects on Room-Temperature, Gas-Phase C-H Bond Activations by Cluster Oxides and Metal Carbides: The Methane Challenge. J. Am. Chem. Soc. *139*, 17201-17212.

10. Periana, R.A., Taube, D.J., Evitt, E.R., Löffler, D.G., Wentrcek, P.R., Voss, G., and Masuda, T. (1993). A mercury-catalyzed, high-yield system for the oxidation of methane to methanol. Science *259*, 340-343.

11. Periana, R.A., Taube, D.J., Gamble, S., Taube, H., Satoh, T., and Fujii, H. (1998). Platinum catalysts for the high-yield oxidation of methane to a methanol derivative. Science *280*, 560-564.

12. Snyder, B.E., Vanelderen, P., Bols, M.L., Hallaert, S.D., Bottger, L.H., Ungur, L., Pierloot, K., Schoonheydt, R.A., Sels, B.F., and Solomon, E.I. (2016). The active site of low-temperature methane hydroxylation in iron-containing zeolites. Nature *536*, 317-321.

13. Groothaert, M.H., Smeets, P.J., Sels, B.F., Jacobs, P.A., and Schoonheydt, R.A. (2005). Selective oxidation of methane by the bis (μ-oxo) dicopper core stabilized on ZSM-5 and mordenite zeolites. J. Am. Chem. Soc. *127*, 1394-1395.

14. Tomkins, P., Mansouri, A., Bozbag, S.E., Krumeich, F., Park, M.B., Alayon, E.M.C., Ranocchiari, M., and van Bokhoven, J.A. (2016). Isothermal Cyclic Conversion of Methane into

Methanol over Copper-Exchanged Zeolite at Low Temperature. Angew. Chem. Int. Ed. *55*, 5467-5471.

15. Sushkevich, V.L., Palagin, D., Ranocchiari, M., and van Bokhoven, J.A. (2017). Selective anaerobic oxidation of methane enables direct synthesis of methanol. Science *356*, 523-527.

16. Lustemberg, P.G., Palomino, R.M., Gutiérrez, R.A., Grinter, D.C., Vorokhta, M., Liu, Z., Ramírez, P.J., Matolín, V., Ganduglia-Pirovano, M.V., Senanayake, S.D., et al. (2018). Direct Conversion of Methane to Methanol on Ni-Ceria Surfaces: Metal-Support Interactions and Water-Enabled Catalytic Conversion by Site Blocking. J. Am. Chem. Soc. *140*, 7681-7687.

17. Cui, X., Li, H., Wang, Y., Hu, Y., Hua, L., Li, H., Han, X., Liu, Q., Yang, F., He, L., et al. (2018). Room-Temperature Methane Conversion by Graphene-Confined Single Iron Atoms. Chem *4*, 1902-1910.

18. Agarwal, N., Freakley, S.J., McVicker, R.U., Althahban, S.M., Dimitratos, N., He, Q., Morgan, D.J., Jenkins, R.L., Willock, D.J., and Taylor, S.H. (2017). Aqueous Au-Pd colloids catalyze selective CH_4 oxidation to CH_3OH with O_2 under mild conditions. Science *358*, 223-227.

19. Ceri, H., M., F.M., Hasbi, A.R.M., Adam, T., Qian, H., L., J.R., Nikolaos, D., A., L.-S.J., F., D.N., M., M.D., et al. (2012). Direct Catalytic Conversion of Methane to Methanol in an Aqueous Medium by using Copper-Promoted Fe-ZSM-5. Angew. Chem. Int. Ed.*51*, 5129-5133.

20. Hasbi, A.R.M., M., F.M., L., J.R., Ceri, H., Qian, H., Nikolaos, D., Antonio, L.-S.J., F., C.A., H., T.S., J., W.D., et al. (2013). Oxidation of Methane to Methanol with Hydrogen Peroxide Using Supported Gold–Palladium Alloy Nanoparticles. Angew. Chem. Int. Ed.*52*, 1280-1284.

21. Hutchings, G.J. (2016). Methane Activation by Selective Oxidation. Topics in Catalysis *59*, 658-662.

22. Tang, Y., Li, Y., Fung, V., Jiang, D.-e., Huang, W., Zhang, S., Iwasawa, Y., Sakata, T., Nguyen, L., Zhang, X., et al. (2018). Single rhodium atoms anchored in micropores for efficient transformation of methane under mild conditions. Nat. Commun. *9*, 1231.

23. Shan, J., Li, M., Allard, L.F., Lee, S., and Flytzani-Stephanopoulos, M. (2017). Mild oxidation of methane to methanol or acetic acid on supported isolated rhodium catalysts. Nature *551*, 605-608.

24. Xie, J., Jin, R., Li, A., Bi, Y., Ruan, Q., Deng, Y., Zhang, Y., Yao, S., Sankar, G., and Ma, D. (2018). Highly selective oxidation of methane to methanol at ambient conditions by titanium dioxide-supported iron species. Nat. Catal. *1*, 889.

25. Chen, X., Li, Y., Pan, X., Cortie, D., Huang, X., and Yi, Z. (2016). Photocatalytic oxidation of methane over silver decorated zinc oxide nanocatalysts. Nat. Commun. *7*, 12273.

26. Hu, A., Guo, J.-J., Pan, H., and Zuo, Z. (2018). Selective functionalization of methane, ethane, and higher alkanes by cerium photocatalysis. Science, eaat9750.

27. Chen, J., Stepanovic, S., Draksharapu, A., Gruden, M., and Browne, W.R. (2018). A Non-Heme Iron Photocatalyst for Light-Driven Aerobic Oxidation of Methanol. Angew. Chem. Int. Ed. *57*, 3207-3211.

28. Shankar, M.V., Kako, T., Wang, D., and Ye, J. (2009). One-pot synthesis of peroxo-titania nanopowder and dual photochemical oxidation in aqueous methanol solution. J. Colloid Interface Sci. *331*, 132-137.

29. Xiang, Q., Yu, J., and Wong, P.K. (2011). Quantitative characterization of hydroxyl radicals produced by various photocatalysts. J. Colloid Interface Sci. *357*, 163-167.

30. Kresse, G., Furthmüller, J. (1996). Efficiency of ab-initio total energy calculations for metals and semiconductors using a plane-wave basis set. *Comput. Mater. Sci.* **6**, 15-50.

31. Kresse, G., Hafner, J., (1993)Ab initio molecular dynamics for liquid metals. *Phys. Rev. B* **47**, 558.

32. Perdew, J. P., Burke, M. K., (1996). Ernzerhof, Generalized gradient approximation made simple. *Phys. Rev. Lett.* **77**, 3865.

33. Colby, J., Stirling, D.I., and Dalton, H. (1977). The soluble methane mono-oxygenase of Methylococcus capsulatus (Bath). Its ability to oxygenate n-alkanes, n-alkenes, ethers, and alicyclic, aromatic and heterocyclic compounds. Biochem. J. *165*, 395-402.

34. Nizova, G.V., Süss-Fink, G., and Shul'pin, G.B. (1997). Catalytic oxidation of methane to methyl hydroperoxide and other oxygenates under mild conditions. Chem. Commun. 397-398.

35. Wang, C.-y., Pagel, R., Bahnemann, D.W., and Dohrmann, J.K. (2004). Quantum yield of formaldehyde formation in the presence of colloidal TiO_2-based photocatalysts: effect of intermittent illumination, platinization, and deoxygenation. J. Phys.Chem. B *108*, 14082-14092.

36. Gaca, K.Z., Parkinson, J.A., Lue, L., and Sefcik, J. (2014). Equilibrium Speciation in Moderately Concentrated Formaldehyde-Methanol-Water Solutions Investigated Using ^{13}C and ^{1}H Nuclear Magnetic Resonance Spectroscopy. Ind. Eng. Chem. Res. *53*, 9262-9271.

37. Schneider, J., and Bahnemann, D.W. (2013). Undesired Role of Sacrificial Reagents in Photocatalysis. J. Phys. Chem. Lett. 4, 3479- 3483.

38. Wu, T., Lin, T., Zhao, J., Hidaka, H., and Serpone, N. (1999). TiO_2-assisted photodegradation of dyes. 9. Photooxidation of a squarylium cyanine dye in aqueous dispersions under visible light irradiation. Environ. Sci. Technol. *33*, 1379-1387.

39. Dvoranová, D., Barbieriková, Z., and Brezová, V. (2014). Radical intermediates in photoinduced reactions on TiO_2 (an EPR spin trapping study). Molecules *19*, 17279-17304.

40. Anglada, J.M., Crehuet, R., Martins-Costa, M., Francisco, J.S., and Ruiz-López, M. (2017). The atmospheric oxidation of CH_3OOH by the OH radical: The effect of water vapor. Phys. Chem. Chem. Phys. *19*, 12331-12342.

41. Siahrostami, S., Verdaguer-Casadevall, A., Karamad, M., Deiana, D., Malacrida, P., Wickman, B., Escudero-Escribano, M., Paoli, E.A., Frydendal, R., and Hansen, T.W. (2013). Enabling direct H_2O_2 production through rational electrocatalyst design. Nat. Mater. *12*, 1137.

Chapter 6 Selective photocatalytic oxidation of methane to methanol with molecular oxygen over nanometals/TiO$_2$ catalysts

6.1 Introduction

Methane is an abundant and inexpensive feedstock for fuels and chemicals production since its high availability from natural gas and shale gas.[1,2] In conventional processes, methane is firstly reformed by steam to synthesis gas which can be further converted into liquid hydrocarbons through methanol synthesis or Fischer-Tropsch synthesis. The first step of reforming is an energy-intensive process and results in high capital costs. The direct or partial oxidation of methane to methanol could address the disadvantage of the existing commercial technology.[3,4] In addition, methanol, as a transportable fuel, is among the top ten commodity chemicals (70 MMT in 2015) and is also used as a precursor to other commodity chemicals such as formaldehyde and acetic acid.[5]

Selective oxidation of methane to methanol has been intensively studied in many years. For example, partial oxidation of methane to methanol over zeolites containing Fe or Cu species by N_2O, O_2 and H_2O oxidants in the gas phase can be achieved, however, these systems require high temperatures (200 to 500 $^{\circ}$C) and multi-steps for CH_4 activation and CH_3OH desorption.[5] Conversion of CH_4 in liquid phase typically utilize milder reaction conditions. ZSM-5 supported isolated Rh catalysts can oxidize methane into methanol and acetic acid, but this system requires carbon monoxide participation in the reaction process.[6,7] Au-Pd colloids can catalyze CH_4 oxidation to CH_3OOH and CH_3OH with O_2 at 50 $^{\circ}$C.[8] However, H_2O_2 is required as an oxidant in this system and is typically more expensive than methanol, which limit its practical application. Molecular O_2 is an ideal oxidant for partial oxidation of methane from the economic and environmental aspects.

Semiconductor photocatalysis has also been used for catalyzing methane oxidation to methanol in recent years.[9-14] Methanol, hydrogen and ethane are common products in photocatalytic reactions. However, most of them suffered from low efficiency and poor sustainability. Deep ultraviolet (UVC, 100-280 nm) are also required in some works. For example, the production rate of methanol was only

around 20 μmol g^{-1} h^{-1} with only around 45% selectivity over $BiVO_4$ photocatalysts with UVC-visible irradiation.[9] Recently, a methanol production rate of 352 μmol g^{-1} h^{-1} was achieved over TiO_2-supported iron species photocatalysts with around 90% selectivity under 300 W Xe light irradiation that transform methane to methanol with high selectivity under light irradiation at ambient conditions.[14] However, H_2O_2 is required in this system, making this photocatalytic system less attractive. Developing photocatalysts that can efficiently convert methane to methanol using O_2 as oxidant at room temperature is highly desirable, however, few related works have been reported.

In this chapter, I report that TiO_2 loaded with 1.0 wt% Pt, Pd, Au and Ag as co-catalysts can oxidize methane to methyl hydroperoxide and methanol with O_2 as an oxidant under light irradiation at room temperature. The mechanism of photocatalytic methane oxidation is through radical pathways, and molecular oxygen is indeed incorporated into the primary products with around 100% of O incorporation degree. Intriguing, depositing Au nanoparticles (NPs) on the surface of TiO_2 via deposition-precipitation method leads to the formation of Au with high valence state, which reduce the concentration of ˙OH radicals generated in the reaction solution. Therefore, the over-oxidation of the primary products to formaldehyde and carbon dioxide was effectively inhibited. These results in this chapter provide a guideline for the design of efficient photocatalysts for partial oxidation of methane to methanol with high selectivity.

6.2 Experimental section

6.2.1 Chemicals and Materials

Commercially TiO_2 (AEROXIDE TiO_2 P25, Lot No. 614041498) was supplied from Evonik-Degussa. Chloroplatinic acid hexahydrate ($H_2PtCl_6 \cdot 6H_2O$), sodium tetrachloropalladate (II) (Na_2PdCl_4), gold chloride trihydrate ($HAuCl_4 \cdot 3H_2O$), and silver nitrate ($AgNO_3$) purchased from Wako Co. The deionized water with a resistivity of 18.2 MΩ cm^{-1} was utilized in all experiments.

6.2.2 Preparation of the catalysts

Preparation of co-catalysts (Pt, Pt, Au and Ag) /TiO_2-NBH. Metals (Pt, Pd, Au and Ag) were loaded on TiO_2 photocatalysts as co-catalyst via $NaBH_4$ reduction. Typically, for synthesis of Pt/TiO_2 photocatalyst, 1 g of TiO_2 was dispersed into 100.0 mL of aqueous H_2PtCl_6 solution by ultrasonication.

After stirring for 1 h, a certain amount of aqueous $NaBH_4$ solution was added dropwise into the solution. After further stirring for 1h, the samples were filtered, washed with water for three times and then dried at 70 °C. The preparation of Pd/TiO_2, Au/TiO_2, Ag/TiO_2 with different co-catalysts loading amount was similar to the above method in addition to adding the corresponding metal precursors. The samples prepared via $NaBH_4$ reduction method are denoted by cocatalysts/TiO_2-NBH.

Preparation of Au/TiO₂-DP. Au NPs were loaded on TiO_2 photocatalysts via deposition-precipitation method. Typically, 50 mL of an aqueous solution of $HAuCl_4$ (1.02 mM) was heated to 70 °C. The pH of this solution was adjusted to around 7.0 by using NaOH (0.1 M) solution. Then 50 mL of hot water (70 °C) was added into the above solution. After stirring for 15 min, 1 g of TiO_2 was added and the mixture was stirred for 1 h at 70 °C and then for 1 h at 25 °C. Finally, the mixture was filtered, washed 3 times with water and dried at 70 °C for 12 h. The Au/TiO_2 prepared via deposition-precipitation method is denoted by 1.0 wt% Au/TiO_2-DP.

6.2.3 Characterization

Powder XRD were carried out on an X-ray diffractometer with Cu Kα radiation (PANalytical B.V., Netherlands). TEM and HR-TEM were perfomed on a Tecnai G 2 F30 S-Twin microscope operated at 300 kV. Surface chemical analysis were characterized with XPS (PHI Quantera SXMULVAC-PHI, Japan). UV-visible diffuse reflectance spectra were measured by a Shimadzu UV-2600 spectrophotometer, and transformed into absorption sepectra via Kubelka-Munk transformation. Brunauer-Emett-Teller surface area were measured by nitrogen adsorption-desorption experiment (BELsorp II mini, BEL Japan Inc.). The fluorescence spectra were collected by JASCO FP-6500 fluorescence spectrophotometer. *In-situ* attenuated total reflectance Fourier transform infrared (ATR-FTIR) spectroscopy measurement was carried ou on JASCO FT-IR-6300. *In-situ* electron paramagnetic resonance (EPR) spectroscopy measurement was performed on Magnettech MS-5000X to detect methyl radical ($^\bullet CH_3$) and hydroxyl radical ($^\bullet OH$) with 5, 5-Dimethyl-1-pyrroline-*N*-oxide (DMPO) as the radicals trap. The light intensity and wavelength of the irradiation light source were detected by USR-40 spectrophotometer.

6.2.4 Photocatalytic activity measurements

The photocatalytic methane oxidation reaction tests were conducted in a home-made batch-

reactor which is the same as described in chapter 5. Typically, 10 mg catalyst was dispersed in 50 mL water. Then, the mixture was added into the glass cell and the batch-reactor was purged with O_2 for several times to exhaust air. After that, the reactor vessel was pressurized with 1 bar O_2 (purity, 99.99995%) and 20 bar CH_4 (purity, 99.9995%). Subsequently, the reactor was loaded into a cold-water bath and the solution was stirred at 1000 rpm. 300 W Xe lamp equipped with a reflector which can reflect most of the visible light and all the infrared light was used as the light source. The incident light wavelength was from 300 to 500 nm and light intensity was 100 mW cm^{-1}. A thermocouple was inserted into the solution to directly detect the temperature of the liquid solution. During the reaction process, the temperature of the liquid solution was maintained at 25±2 °C. After the reaction, the reactor was cooled in an ice bath to a temperature below 10 °C. Then the gas product was collected and analyzed by gas chromatograph (GC) according to the standard curves. The liquid phase of the reaction mixture product was collected by centrifugation. The liquid product was analyzed by colorimetric analysis, high-performance liquid chromatography (HPLC, Shimadzu) and nuclear magnetic resonance spectroscopy (NMR, JEOL ECS 400 MHz).

6.2.5 Products analysis

The concentration of CH_3OOH and CH_3OH in the liquid product was analyzed by ^1H NMR spectroscopy. The concentration of liquid product HCHO was quantified by colorimetric analysis and HPLC. The analysis details can be referred in chapter 5.

For isotopic labeling experiments, 10 bar ^{13}C enriched CH_4 (^{13}C enrichment: > 99 atom%), 1 bar ^{18}O enriched O_2 (^{18}O enrichment: ≥ 98 atom%) and 10 mL water-^{18}O (^{18}O enrichment: ≥ 98 atom%) were used.

Analysis of hydroxyl radicals ($^{\bullet}OH$). The generation of hydroxyl radicals ($^{\bullet}OH$) was measured by the photoluminescence (PL) technique using coumarin (COU) as a probe molecule. COU can easily react with $^{\bullet}OH$ to form 7-hydroxycoumain (7HC), which has high fluorescence with a PL signal at around 454 nm. The PL intensity of 7HC was proportional to the amount of $^{\bullet}OH$ generated. Briefly. 50 mg of catalyst was dispersed in 20 mL of a 1.0 mM COU aqueous solution. The above mixture solution was stirred for 1 h in dark to reach an adsorption-desorption equilibrium. A 300 W Xe lamp equipped with a U340 filter was used as a light source. After light illumination for a certain time, the

reaction solution was collected by centrifugation. The PL spectra of 7HC produced were measured by fluorescence spectrophotometer (JASCO FP-6500) with excitation wavelength at 332.0 nm. The PL intensity was recorded at 454 nm.

6.3 Results and discussion

6.3.1 Photocatalytic oxidation of methane

In chapter 5, I have demonstrated that TiO_2 loaded with co-catalysts (Pt, Pd, Au or Ag) with amount of 0.1 wt% can catalyze methane to HCHO in the presence of O_2 under light irradiation. Considering that HCHO is one of product of photocatalytic oxidation of CH_3OH, I speculated that cocatalysts/TiO_2 have the potential of photo-catalytically converting CH_4 to CH_3OH with O_2, and the failure of detecting CH_3OH by ^{1}H NMR is likely to the low concentration of CH_3OH formed. In order to detect the formation of CH_3OH, the volume of water was reduced to 50 mL on the basis of reaction conditions (2 MPa of CH_4 and 0.1MPa of O_2 at 25±2 °C for 2h) performed in chapter 5. Encouragingly, the formation of primary products (CH_3OOH and CH_3OH) was detected by ^{1}H NMR (Table 6.1, entry 2-5). For example, the measured yield of primary products over 0.1 wt% Pt/TiO_2-NBH was 9.6 μmol, yet with low selectivity (16.3%), since the yields of HCHO and CO_2 were 22.2 and 27.2 μmol. Interestingly, when the loading amount of co-catalysts was increased to 1.0 wt%, the amounts of primary products generated were remarkably increased (Table 6.1, entry 6-9). For 1.0 wt% Pt/TiO_2-NBH, the total amount of CH_3OOH and CH_3OH was 56.1 μmol. Although the amount of HCHO and CO_2 generated also increased, the selectivity for the production of primary products increased to 49.5%. In addition to 1.0 wt% Pt/TiO_2-NBH, the yield of primary products over 1.0 wt% Au/TiO_2-NBH was second (36.0 μmol), but the selectivity towards the primary products was quite low (39.6%) because of large extent of over-oxidation of the primary products to HCHO (21.4 μmol) and CO_2 (33.6 μmol). Surprisingly, when Au NPs were loaded on TiO_2 using deposition-precipitation method, the measured yields of the primary products increased to 56.9 μmol, and the yields of HCHO and CO_2 decreased to 10.2 and 10.5 μmol, respectively (Table 6.1, entry 10). The selectivity for the formation of primary products was up to 73.3 % in all products and 84.8 % in liquid oxygenated products. The activity of 1.0 wt% Au/TiO_2-DP for the production of primary products corresponds to 2,845 μmol g^{-1} h^{-1}. This photocatalytic activity was roughly 8 times higher than the best yield recently

reported for photocatalytic CH_4 oxidation to CH_3OH over FeO_x/TiO_2, where H_2O_2, rather than O_2, was used as the oxidant. Control experiments without photocatalysts, CH_4, or light (Table 6.1, entry 11-13) showed no formation of oxygenated products, demonstrating that the produced primary products were indeed generated via photocatalytic CH_4 oxidation. No product was produced under visible light irradiation, confirming that surface plasmon resonance of Au has no contribution to the photocatalytic activity (Table 6.1, entry 14).

Table 6.1 Catalytic activity. Comparison of photocatalytic activity of co-catalysts/TiO_2 for oxidation of CH_4 using O_2 as oxidant. Reaction conditions: 10 mg catalyst, 2 MPa CH_4, 0.1 MPa O_2, 50 mL water, 25±2 °C reaction temperature, 2 h reaction time; light source, 300 W Xe lamp, $300 < \lambda < 500$ nm, light intensity 100 mW cm^{-2}.

Entry	Catalysts	Amount of products (µmol)					All products (µmol)	Primary products sel. (%)
		CH_3OOH	CH_3OH	HCHO	CO	CO_2		
1	TiO_2	0	0	27.4	0.05	23.4	50.9	-
2	0.1 wt% Pt/TiO_2-NBH	8.5	1.1	22.2	0.03	27.2	59.0	16.3
3	0.1 wt% Pd/TiO_2-NBH	0.8	5.7	26.3	0.02	29.6	62.4	10.4
4	0.1 wt% Au/TiO_2-NBH	1.2	7.8	23.6	0.01	25.2	57.8	15.6
5	0.1 wt% Ag/TiO_2-NBH	1.3	5.4	32.0	0.1	22.5	61.3	10.9
6	1.0 wt% Pt/TiO_2-NBH	28.7	27.4	18.9	0.03	38.2	113.2	49.5
7	1.0 wt% Pd/TiO_2-NBH	2.5	22.1	23.7	0.02	39.4	87.7	28.0
8	1.0 wt% Au/TiO_2-NBH	15.8	20.2	21.4	0.01	33.6	91.0	39.6
9	1.0 wt% Ag/TiO_2-NBH	7.5	27.2	24.3	0.4	32.6	92.0	37.7
10	1.0 wt% Au/TiO_2-DP	27.4	29.5	10.2	0.01	10.5	77.6	73.3
11	-	0	0	0	0	0	0	-
12*	1.0 wt% Au/TiO_2-DP	0	0	0	0	0	0	-
13†	1.0 wt% Au/TiO_2-DP	0	0	0	0	0	0	-
14 ‡	1.0 wt% Au/TiO_2-DP	0	0	0	0	0	0	-

*Entry 12: 20 bar Ar gas was used instead of CH_4

†Entry 13: Without light irradiation

‡Entry 14: Visible light irradiation ($420 < \lambda < 500$ nm)

In order to prove the carbon source of the formed primary products, isotope labelling experiments using $^{13}CH_4$ was conducted. 1 MPa $^{13}CH_4$ was mixed with 0.1 MPa O_2 for isotope experiment on 1.0% wt Au/TiO_2-DP in 50 mL water for 4 h. In isotope labelling experiments carried out with $^{13}CH_4$, the products that form three obvious ^{13}C NMR signals at 49.1, 65.1 and 82.0 ppm are ascribed to CH_3OH, CH_3OOH and $HOCH_2OH$ (methylene glycol, the major species in aqueous solutions of HCHO), respectively, demonstrating that the primary products indeed come from CH_4 (Figure 6.1). Under milder conditions (1.0 MPa of CH_4), photocatalytic oxidation of methane to the primary products was also achieved over 1.0% wt Au/TiO_2-DP, yet with relatively low yield (15.1 μmol) and poor selectivity (approximately 47.2%) (Figure 6.1). These results reveal that increasing the concentration (solubility) of CH_4 in water plays the central role in achieving appreciable photocatalytic activity and selectivity. Low pressure of CH_4 limits the conversion of CH_4 to the primary products, and is favourable to deep-oxidation of the primary products to HCHO and CO_2.
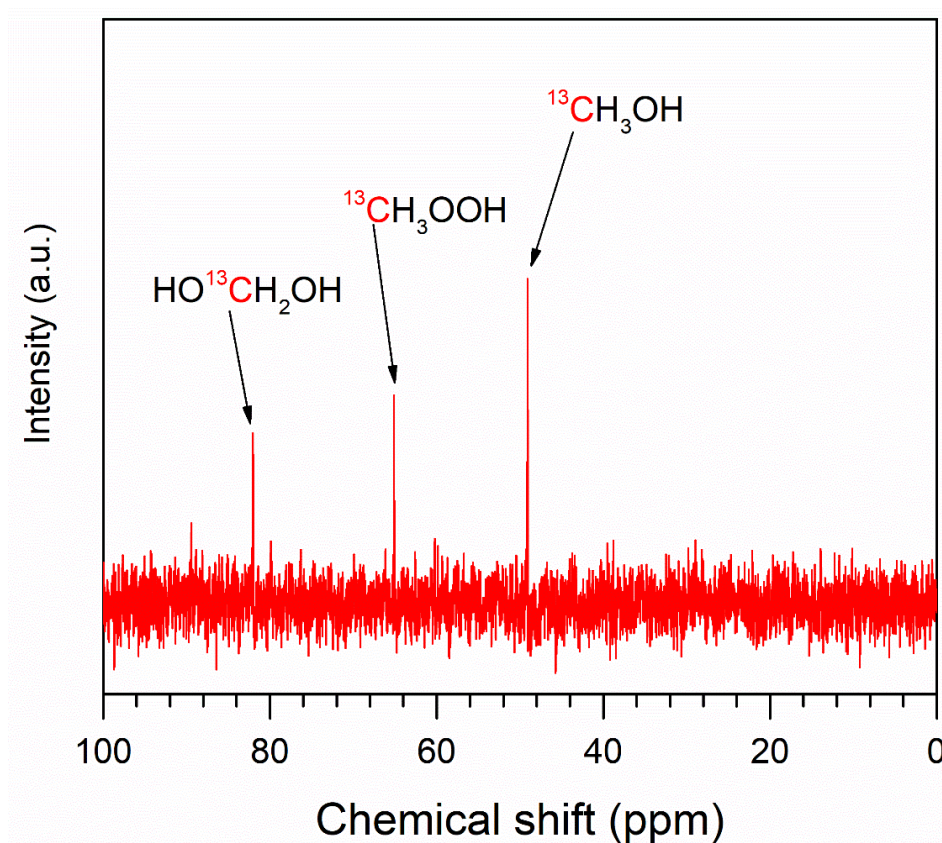

Figure 6.1 ^{13}C NMR spectra obtain from photocatalytic methane oxidation using $^{13}CH_4$. Reaction conditions: 1.0% wt Au/TiO_2-DP, 1 bar O_2, 10 bar $^{13}CH_4$, 50 mL water, 25±2 °C reaction temperature, 4 h reaction time; light source, 300 W Xe lamp, 300 < λ < 500 nm, light intensity 100 mW cm^{-2}.
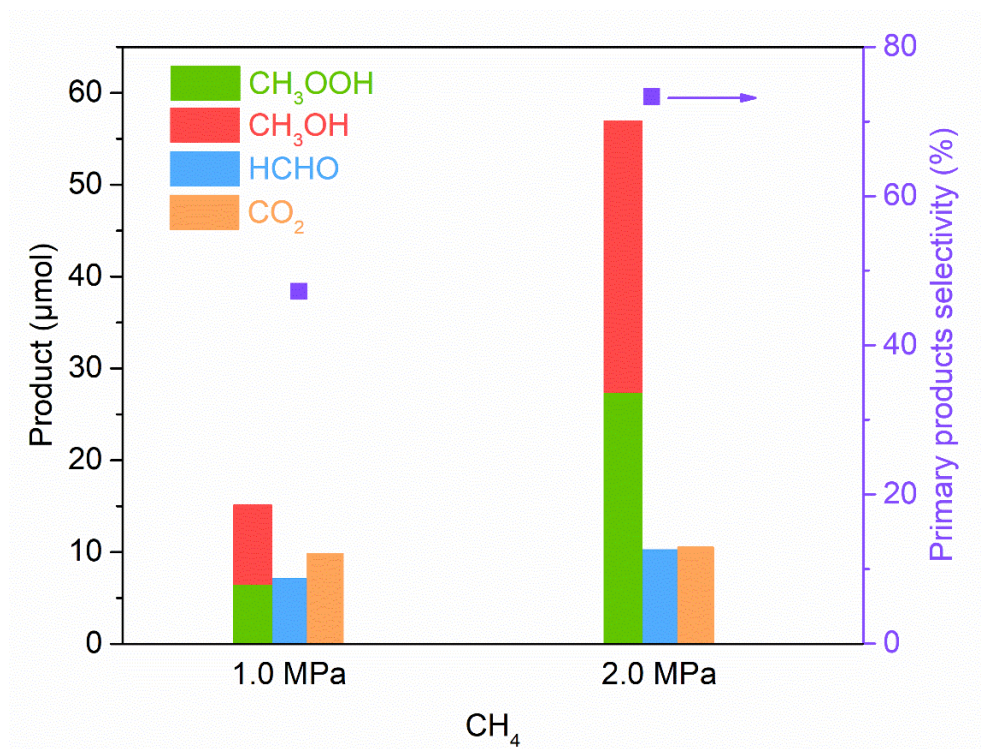
Figure 6.2 Product yields and primary products selectivity for 1.0 wt% Au/TiO_2-DP under different CH_4 pressure. Reaction conditions: 10 mg catalyst, 50 mL water, 0.1 MPa O_2, 25±2°C reaction temperature; light source, 300 W Xe lamp, 300 < λ < 420 nm, light intensity 100 mW cm^{-2}.

6.3.2 Characterization of photocatalysts

The morphology of 1.0 wt% Au/TiO_2-DP was investigated by transmission electron microscopy (TEM). As shown in Figure 6.3, the average size of TiO_2 NPs was around 20-40 nm. Figure 6.3 also reveals the formation of small Au NPs with an average Au diameter of 3 nm. While for 1.0 wt% Au/TiO_2-NBH, the average size of Au NPs was 10 nm, as shown in Figure 6.4. Therefore, for depositing catalytically active Au NPs onto the surface of TiO_2, deposition-precipitation is a good way to obtain Au NPs with small Au size, and $NaBH_4$ reduction method readily results in obvious agglomeration of the Au particles. The size of Au NPs possibly has an influence on the photocatalytic activity of methane oxidation. In addition, Figure 6.5, 6.6 and 6.7 show that the average size of Pt, Pd and Ag NPs via $NaBH_4$ reduction is around 4 nm, 3 nm and 10 nm, respectively. Table 6.2 shows the actual loading amount of co-catalyst by inductively coupled plasma atomic emission spectroscopy (ICP-AES). By utilizing the $NaBH_4$ reduction and deposition-precipitation methods, the Au loading amount was almost 1.0 wt% and the amounts of Pt, Pd and Ag were also almost 1.0 wt%.
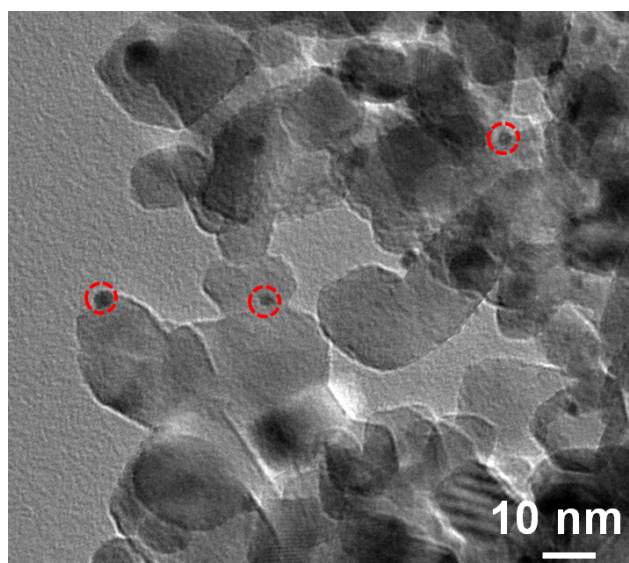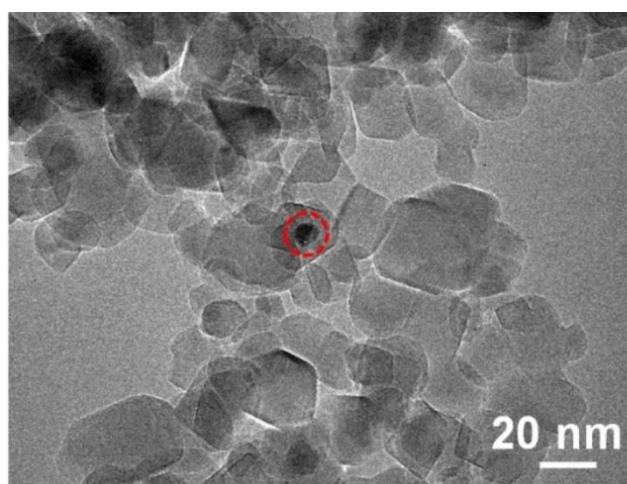
Figure 6.3 TEM image of 1.0% wt Au/TiO$_2$-DP.
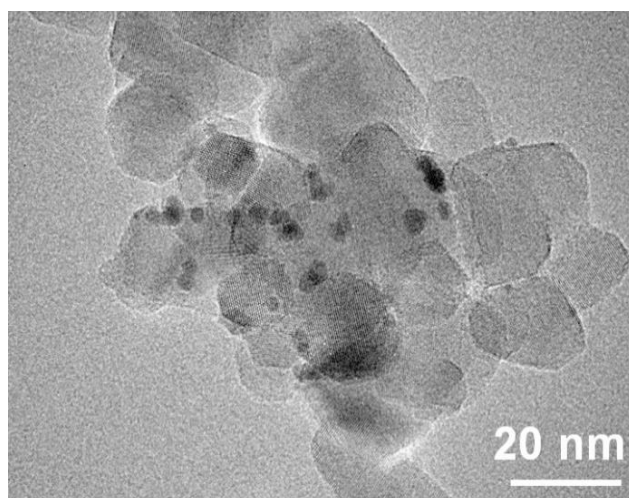

Figure 6.4 TEM image of 1.0% wt Au/TiO$_2$-NBH.

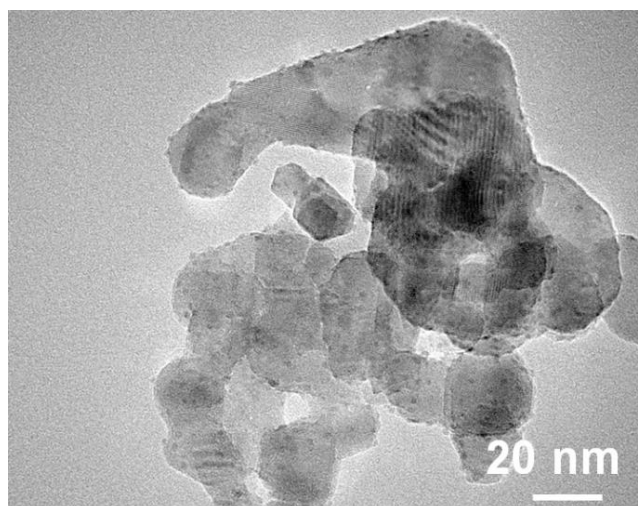**Figure 6.5** TEM image of 1.0 wt% Pt/TiO$_2$-NBH.

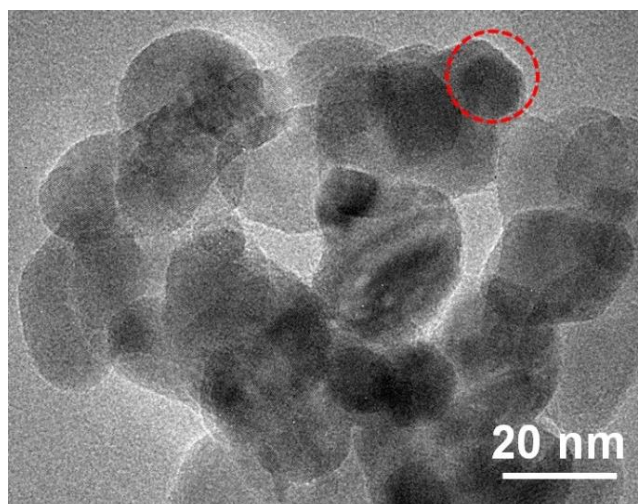**Figure 6.6** TEM image of 1.0 wt% Pd/TiO$_2$-NBH.

Figure 6.7 TEM image of 1.0 wt% Ag/TiO$_2$-NBH.

Table 6.2 Physicochemical properties of ZnO- and TiO$_2$-based photocatalysts.

Catalyst	Metal loading (wt%)
1.0 wt% Au/TiO$_2$-DP	0.99
1.0 wt% Au/TiO$_2$-NBH	1.02
1.0 wt% Pt/TiO$_2$-NBH	1.01
1.0 wt% Pd/TiO$_2$-NBH	1.03
1.0 wt% Ag/TiO$_2$-NBH	1.0

Figure 6.8 shows the UV-vis diffuse reflectance spectra of TiO_2, 1.0 wt% Au/TiO_2-DP and 1.0 wt% Au/TiO_2-NBH. It is clear that new peak appeared after loading Au NPs, which can be assigned to the absorption of Au surface plasmon resonance (SPR).[15] For 1.0 wt% Au/TiO_2-NBH, the SPR band was centered at 550 nm, while the SPR band of 1.0 wt% Au/TiO_2-DP positively shifted to 540 nm and intensity of absorption peak was significantly reduced. The intensity and position of SPR band of Au are influenced by the shape and size of Au nanostructures.[16] Decreasing Au particle size generally enable higher collective oscillation frequencies of the conduction electrons through interaction with the incident photons so that the SPR bands would shift to lower wavelengths. Thus, the SPR band positions of 1.0 wt% Au/TiO_2-DP (λ_{max} = 540 nm) and 1.0 wt% Au/TiO_2-NBH (λ_{max} = 550 nm) reveal that $NaBH_4$ reduction leads to larger particles than the deposition-precipitation method, consistent with the results of TEM images that the average particle sizes of 1.0 wt% Au/TiO_2-DP is 3 nm, smaller than that of 1.0 wt% Au/TiO_2-NBH (10 nm).
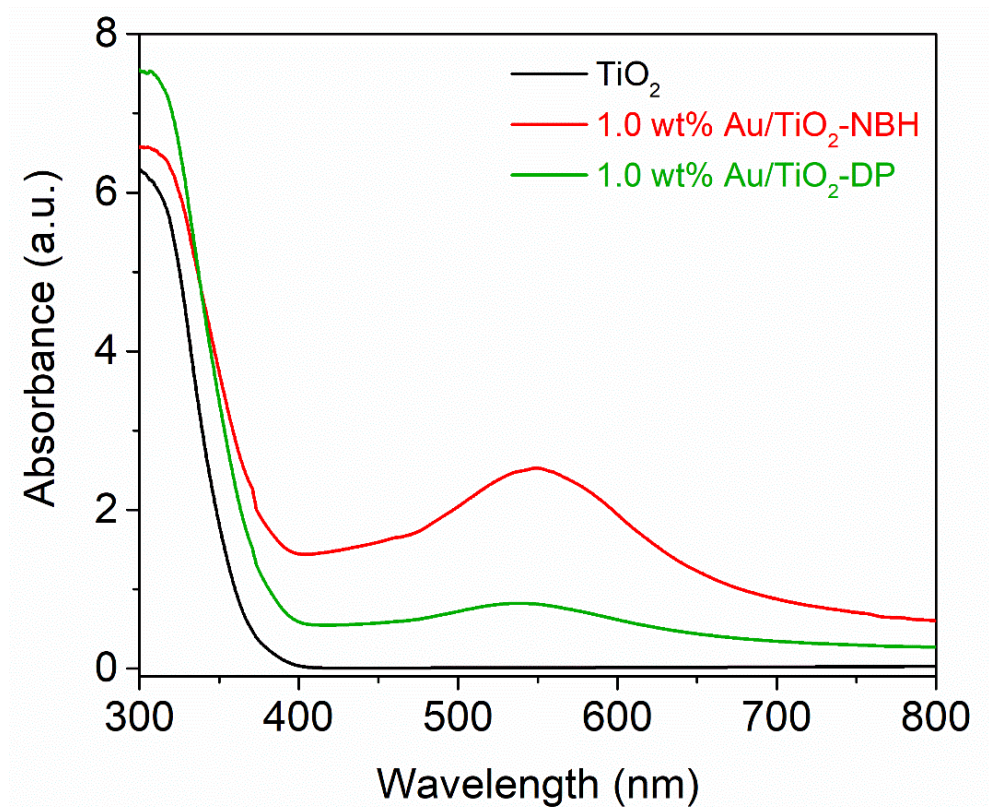

Figure 6.8 UV-vis diffuse reflectance spectra of TiO_2, 1.0 wt% Au/TiO_2-DP and 1.0 wt% Au/TiO_2-NBH.

To investigate the chemical states of Au on the TiO_2, we characterized 1.0 wt% Au/TiO_2-DP and 1.0 wt% Au/TiO_2-NBH by X-ray photoelectron spectroscopy (XPS) analysis. As shown in Figure 6.9,

the Au 4f spectra of 1.0 wt% Au/TiO$_2$-NBH consisted of two peaks located at the binding energies of 83.2 and 86.9 eV, attributed to Au 4f$_{7/2}$ and Au 4f$_{5/2}$, respectively, confirming that the Au species existed in the metallic state. Generally, the Au 4f$_{7/2}$ and Au 4f$_{5/2}$ binding energy peaks appeared at 83.8 and 87.5 eV, respectively.[17] The binding energy values of Au 4f in 1.0 wt% Au/TiO$_2$-NBH were significantly lower than that of bulk Au. The negative shift of binding energy possibly results from the electron transfer from TiO$_2$, since the Fermi level of TiO$_2$ is higher than that of Au NPs and electrons from TiO$_2$ would transfer to Au NPs for Fermi level equilibration when Au NPs are loaded on the surface of TiO$_2$. However, for 1.0 wt% Au/TiO$_2$-DP, the binding energies of Au 4f$_{7/2}$ and Au 4f$_{5/2}$ were located at 84.1 and 87.8 eV, respectively, resulting in a positive shift of 0.9 eV. The higher binding energies of Au 4f suggests that the presence of some partly oxidized Au$^{\delta+}$ species in 1.0 wt% Au/TiO$_2$-DP, in good agreement with the previous reported work.[18] The electron-deficient Au$^{\delta+}$ species may contribute to the high photocatalytic activity of formed primary products, which cannot be achieved by electron-rich Au NPs.
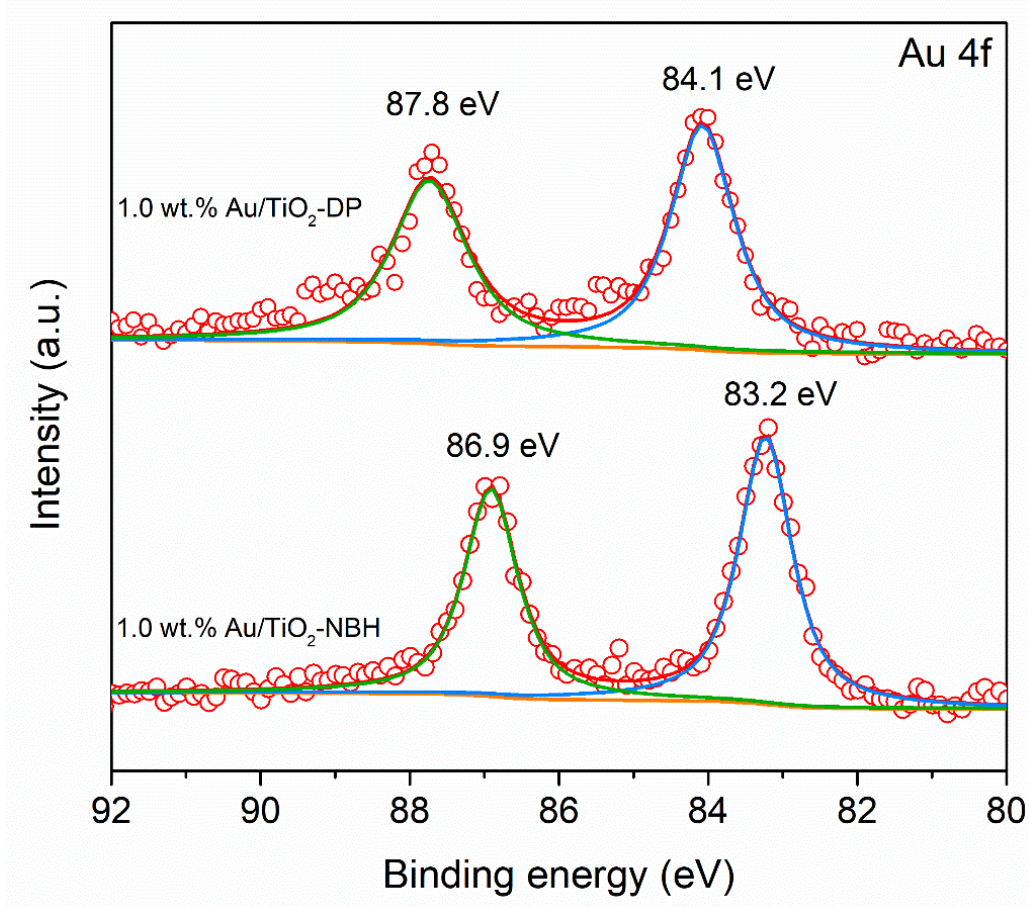

Figure 6.9 Au 4f XPS spectra of 1.0 wt% Au/TiO$_2$-DP and 1.0 wt% Au/TiO$_2$-NBH.
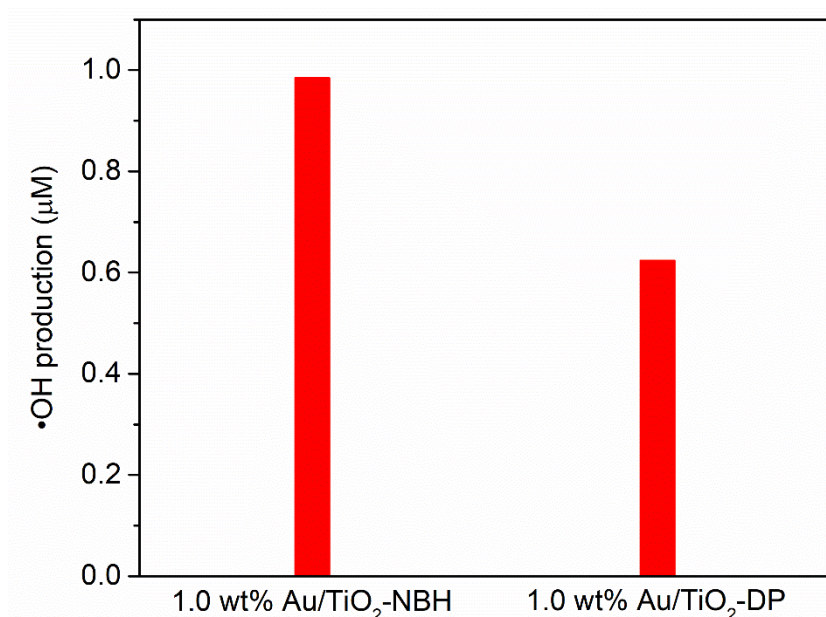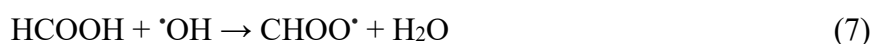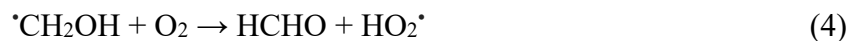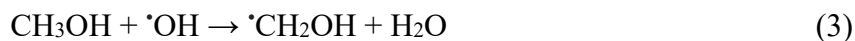
6.3.3 Mechanism discussion

Figure 6.10 Comparison of PL intensity of 1.0 wt% Au/TiO_2-DP and 1.0 wt% Au/TiO_2-NBH in 1 mM COU aqueous solution.

Table 3.1 show that the amounts of the primary products of 1.0 wt% Au/TiO_2-DP increased while the amounts of total products decreased, compared to those of 1.0 wt% Au/TiO_2-NBH, which reveal that the photocatalytic conversion of methane was limited to some extent, but more importantly, the over-oxidation of the primary products to formaldehyde and carbon dioxide was remarkably inhibited. It is well known that methanol can be oxidized to HCHO and CO_2 by photo-generated $\cdot$OH radicals (Equations 1-2) through a serious of oxidation process via Equations 3-8. We assume that the concentration of $\cdot$OH radicals in the reaction solution over 1.0 wt% Au/TiO_2-DP was obviously reduced, thereby resulting in low extent of over-oxidation of CH_3OH. In order to confirm this assumption, the experiments to measure the concentration of $\cdot$OH radicals of 1.0 wt% Au/TiO_2-DP and 1.0 wt% Au/TiO_2-NBH using coumarin (COU) as a probe molecule were preformed, since COU can easily react with $\cdot$OH to form 7-hydroxycoumain (7HC), which has high fluorescence with a PL signal at around 454 nm.[19] The PL intensity of 7HC is proportional to the amount of $\cdot$OH generated. As shown in Figure 6.10, the PL intensity of 1.0 wt% Au/TiO_2-DP was significantly lower than that of 1.0 wt% Au/TiO_2-NBH, demonstrating that 1.0 wt% Au/TiO_2-DP produced less $\cdot$OH radicals. The reason maybe that the Au NPs with high valence state in 1.0 wt% Au/TiO_2-DP could not be capable to effectively restrain the separation of photo-induced electrons and holes compared to metallic state

of Au in 1.0 wt% Au/TiO$_2$-NBH.

$$\text{Semiconductor} + h\upsilon \rightarrow e^- + h^+ \tag{1}$$

$$h^+ + H_2O \rightarrow {}^\bullet OH + H^+ \tag{2}$$

$$CH_3OH + {}^\bullet OH \rightarrow {}^\bullet CH_2OH + H_2O \tag{3}$$

$${}^\bullet CH_2OH + O_2 \rightarrow HCHO + HO_2{}^\bullet \tag{4}$$

$$HCHO + {}^\bullet OH \rightarrow HCO^\bullet + H_2O \tag{5}$$

$$CHO^\bullet + {}^\bullet OH \rightarrow HCOOH \tag{6}$$

$$HCOOH + {}^\bullet OH \rightarrow CHOO^\bullet + H_2O \tag{7}$$

$$CHOO^\bullet + {}^\bullet OH \rightarrow CO_2 + H_2O \tag{8}$$

In this experiment, molecular O$_2$ was utilized as the oxidant for the photooxidation of CH$_4$ to the primary products. To investigate the effect of O$_2$ on the formation of primary products, we carried out the experiments with different pressure of O$_2$ but all other reaction conditions were the same. Figure 6.11 shows the correlation of amounts of formed products (CH$_3$OOH, CH$_3$OH, HCHO, and CO$_2$) with the pressure of O$_2$ over 1.0 wt% Au/TiO$_2$-DP. No product including CH$_3$OOH and CH$_3$OH was produced in the absence of O$_2$. suggesting that O$_2$ was a necessary reactant for the formation of primary products. With increasing the O$_2$ pressure, the yields of products increased gradually and the selectivity for the formation of primary products also increased, which demonstrates that O$_2$ does participate in the generation of primary products. Further increasing the pressure of O$_2$ (large than 0.1 MPa) had little contribution to production of primary products, probably because the O$_2$ is up to the saturation concentration. Again, in order to further demonstrate the direct incorporation of O$_2$ into the primary products, the isotope experiments using ^{18}O-labelled oxygen (^{18}O$_2$) or ^{18}O-labelled water (H$_2$^{18}O) as the reaction mixture were performed. Gas chromatography-mass spectrometry (GC-MS) was utilized to analyzed the formed primary products. We used NaBH$_4$ to reduce CH$_3$OOH to CH$_3$OH before conducting GC-MS analysis to avoid the thermal decomposition of CH$_3$OOH in the presence of air. As shown in Figure 6.12, the reactions with ^{18}O$_2$ and H$_2$^{16}O showed that nearly 100% of ^{18}O was incorporated into CH$_3$OH, with only trace amount of CH$_3$^{16}OH detected. For the reactions with ^{16}O$_2$ and H$_2$^{18}O as the reactants, the detected CH$_3$^{16}OH accounted for nearly 100% while the ^{18}O labelling of CH$_3$OH was within the trace amount. Mass spectrometry cannot detect the signal of HCHO due to the low concentration of HCHO formed. Therefore, the above results suggest that the

oxygen atom in the generated primary products indeed originated from molecular oxygen and 1.0 wt% Au/TiO$_2$-DP enable the partial oxidation of methane to methanol with O$_2$ as the oxidant under light irradiation.
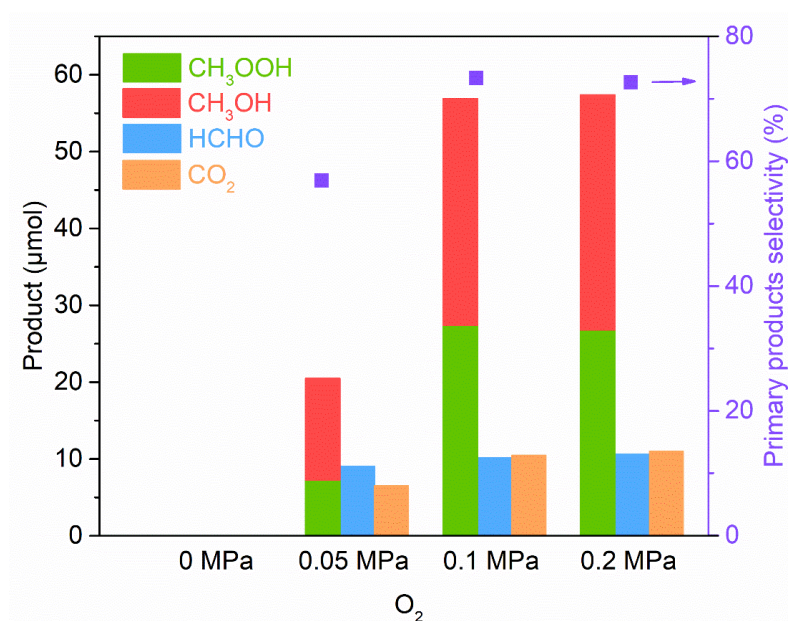
Figure 6.11 Product yields and primary products selectivity over 1.0 wt% Au/TiO$_2$-DP under different O$_2$ pressure. Reaction conditions: 10 mg catalyst, 50 mL water, 2.0 MPa CH$_4$, 25±2 °C reaction temperature, 2 h; light source, 300-W Xe lamp, 300 < λ < 420 nm, light intensity 100 mW cm^{-2}.

Figure 6.12 GC-MS spectra of CH$_3$OH generated over 1.0 wt% Au/TiO$_2$-DP with $^{18}O_2$ + H$_2$^{16}O or $^{16}O_2$ + H$_2$^{18}O in photocatalytic methane oxidation.

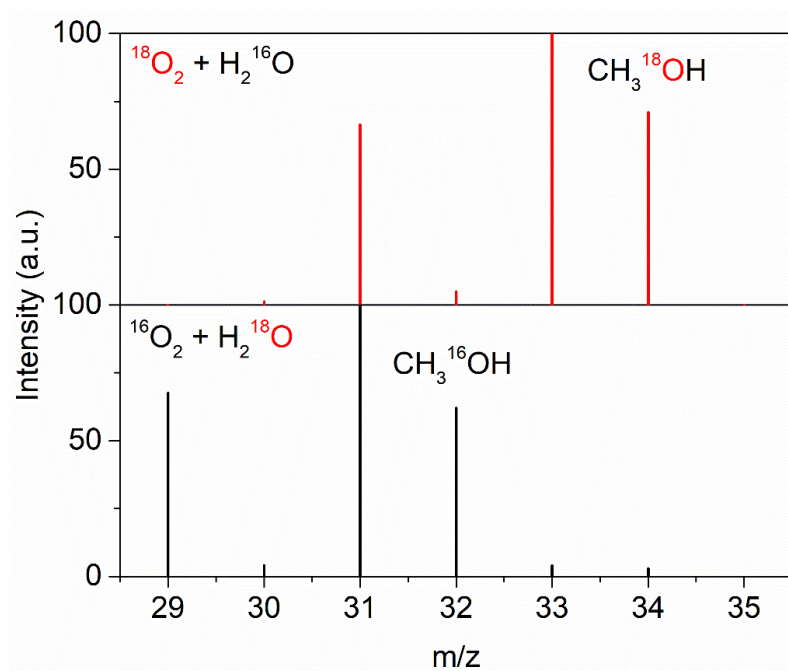To investigate the nature of photocatalytic partial oxidation to methane to the primary products with O_2, *in-situ* electron paramagnetic resonance (EPR) spin-trapping technique with the spin traps 5,5-Dimethyl-1-pyrroline *N*-oxide (DMPO) were employed. As shown in Figure 6.13, upon light irradiation, two radicals, methyl ($^{\bullet}CH_3$) and hydroxyl ($^{\bullet}OH$) radicals, were detected over 1.0 wt% Au/TiO$_2$-DP in the presence of CH_4 and O_2, suggesting that the mechanism of photocatalytic partial oxidation for TiO$_2$ photocatalysts is also radical-based and involves the participation of $^{\bullet}CH_3$ radicals. Increasing the illumination time led to the increase in the intensity of signals of $^{\bullet}CH_3$ and $^{\bullet}OH$ radicals. In order to capture the signals of $^{\bullet}OOH$ radicals by ESR spin-trapping technique, methanol was used to scavenge $^{\bullet}OH$. Figure 6.14 shows that the signals of $^{\bullet}OOH$ were detected over 1.0 wt% Au/TiO$_2$-DP and the intensity of signals also increased along the increase of illumination time. The termination reaction of $^{\bullet}CH_3$ and $^{\bullet}OOH$ would then produce methyl hydroperoxide, ultimately decomposition to CH_3OH.

Figure 6.13 In situ EPR spectra of 1.0 wt% Au/TiO$_2$-DP recorded under light irradiation of different time in the presence of CH_4 and O_2. DMPO was added into the reaction mixture as the radical trapping agent. Signals marked by stars are attributed to DMPO-CH$_3$ adducts; signals marked by solid dots are attributed to DMPO-OH adducts.
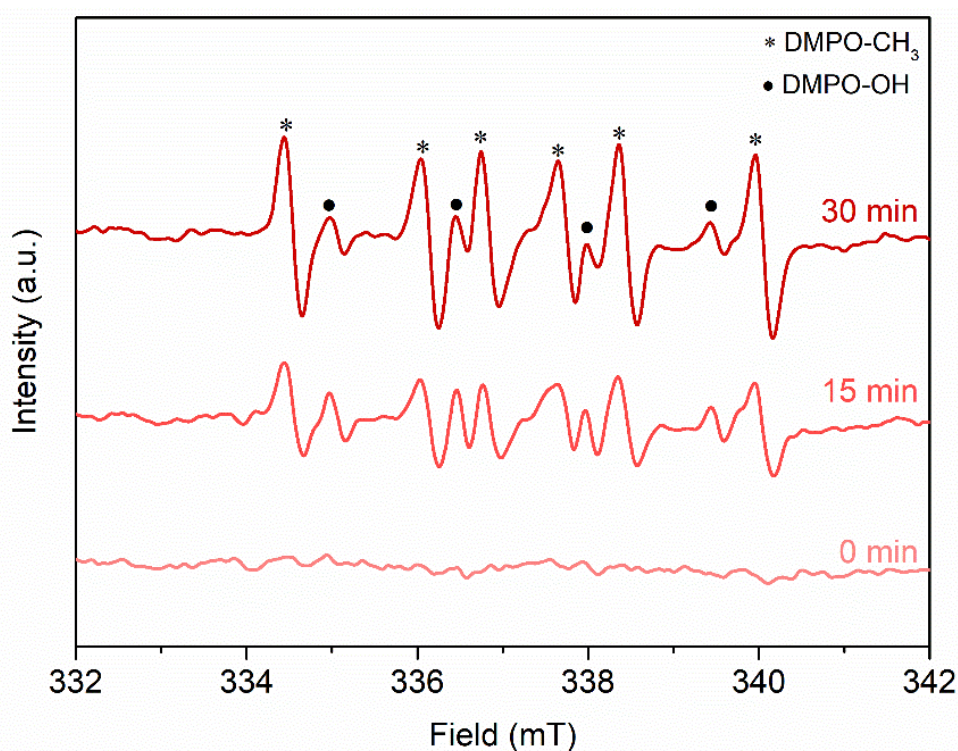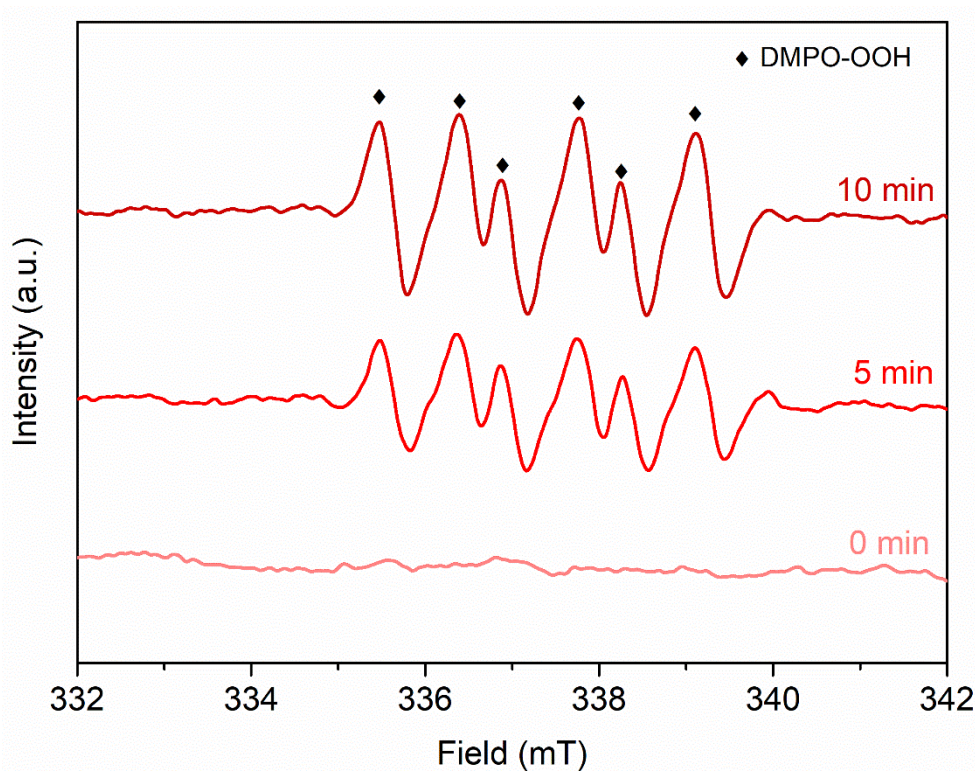
Figure 6.14 In situ EPR spectra of 1.0 wt% Au/TiO$_2$-DP recorded under light irradiation of different time in the presence of O$_2$ and CH$_3$OH (as ˙OH scavenger) (B). DMPO was added into the reaction mixture as the radical trapping agent. Signals marked by solid diamonds are attributed to DMPO-OOH adducts.

Based on the above results, we propose the reaction mechanism for photocatalytic partial oxidation of methane to primary products using molecular O$_2$ as oxidant. As we discussed in chapter, the initial activation of CH$_4$ to form ˙CH$_3$ radicals on ZnO was achieved by the high electrophilic surface lattice O$^-$ ions which was produced through the photo-excited holes. We also think that the surface lattice O$^-$ ions of TiO$_2$ drive the activation of CH$_4$ to ˙CH$_3$ radicals (Equation 9). Molecular O$_2$ can be readily reduced to form ˙OOH radicals by photo-excited electrons, as demonstrated in Figure 6.14. Experiments with isotopically labeled oxygen confirmed that the oxygen atom of formed methanol originated from molecular oxygen, rather than water. Therefore, the CH$_3$OOH was produced through the termination reaction of coupling of ˙CH$_3$ and ˙OOH (Equation 10), then the formed CH$_3$OOH can decomposed to CH$_3$OH. The production of CH$_3$OH through the direct termination reaction of ˙CH$_3$ with ˙OH is very limited (Equation 11). While the ˙OH radicals produced by photo-excited holes can further oxidize the formed CH$_3$OOH and CH$_3$OH to HCHO and CO$_2$. Since 1.0 wt% Au/TiO$_2$-DP produce less ˙OH radicals, the over-oxidation of the primary products

was avoided to a certain extent with maintain relatively high selectivity. Therefore, controlling the concentration of $^{\bullet}$OH radicals in the reaction solution play a central role in achieving high selectivity towards methanol for photocatalytic partial oxidation of methane.

$$CH_4 + O^- \rightarrow {}^{\bullet}CH_3 + \text{-}OH \tag{9}$$

$$^{\bullet}CH_3 + {}^{\bullet}OOH \rightarrow CH_3OOH \tag{10}$$

$$^{\bullet}CH_3 + {}^{\bullet}OH \rightarrow CH_3OH + H_2O \tag{11}$$

6.4 Conclusions

In this chapter, I report that methane can be transformed into methanol over 1.0 wt% Pt, Pd, Au or Ag/TiO$_2$ photocatalysts with O$_2$ as an oxidant under light irradiation at room temperature. The activity for the production of methyl hydroperoxide and methanol over the optimized photocatalysts amounts to 2,845 µmol g^{-1} h^{-1} with approximately 73.3% selectivity. This photocatalytic activity is highest among the previous reported yields for photocatalytic CH$_4$ oxidation to CH$_3$OH. In addition, reducing the concentration of $^{\bullet}$OH radicals generated in the reaction solution via the formation of Au with high valence state on the surface of TiO$_2$ is capable of avoiding the over-oxidation of the primary products to formaldehyde and carbon dioxide. These results provide a guideline for achieving efficient photocatalytic partial oxidation of methane to methanol with high selectivity.

References

1. Olivos-Suarez, A.I., Szécsényi, À., Hensen, E.J.M., Ruiz-Martinez, J., Pidko, E.A., and Gascon, J. (2016). Strategies for the Direct Catalytic Valorization of Methane Using Heterogeneous Catalysis: Challenges and Opportunities. ACS Catal. *6*, 2965-2981.

2. Schwach, P., Pan, X., and Bao, X. (2017). Direct Conversion of Methane to Value-Added Chemicals over Heterogeneous Catalysts: Challenges and Prospects. Chem. Rev. *117*, 8497-8520.

3. Ravi, M., Ranocchiari, M., and van Bokhoven, J.A. (2017). The direct catalytic oxidation of methane to methanol-A critical assessment. Angew. Chem. Int. Ed. *56*, 16464-16483.

4. Tang, P., Zhu, Q., Wu, Z., and Ma, D. (2014). Methane activation: the past and future. Energy Environ. Sci. *7*, 2580-2591.

5. Sushkevich, V.L., Palagin, D., Ranocchiari, M., and van Bokhoven, J.A. (2017). Selective anaerobic oxidation of methane enables direct synthesis of methanol. Science *356*, 523-527.

6. Shan, J., Li, M., Allard, L.F., Lee, S., and Flytzani-Stephanopoulos, M. (2017). Mild oxidation of methane to methanol or acetic acid on supported isolated rhodium catalysts. Nature *551*, 605-608.

7. Tang, Y., Li, Y., Fung, V., Jiang, D.-e., Huang, W., Zhang, S., Iwasawa, Y., Sakata, T., Nguyen, L., Zhang, X., et al. (2018). Single rhodium atoms anchored in micropores for efficient transformation of methane under mild conditions. Nat. Commun. *9*, 1231.

8. Agarwal, N., Freakley, S.J., McVicker, R.U., Althahban, S.M., Dimitratos, N., He, Q., Morgan, D.J., Jenkins, R.L., Willock, D.J., Taylor, S.H., et al. (2017). Aqueous Au-Pd colloids catalyze selective CH_4 oxidation to CH_3OH with O_2 under mild conditions. Science *358*, 223-227.

9. Murcia-López, S., Villa, K., Andreu, T., and Morante, J.R. (2014). Partial Oxidation of Methane to Methanol Using Bismuth-Based Photocatalysts. ACS Catal. *4*, 3013-3019.

10. Murcia-López, S., Bacariza, M.C., Villa, K., Lopes, J.M., Henriques, C., Morante, J.R., and Andreu, T. (2017). Controlled Photocatalytic Oxidation of Methane to Methanol through Surface Modification of Beta Zeolites. ACS Catal. *7*, 2878-2885.

11. Zhu, W., Shen, M., Fan, G., Yang, A., Meyer, J.R., Ou, Y., Yin, B., Fortner, J., Foston, M., and Li, Z. (2018). Facet-Dependent Enhancement in the Activity of Bismuth Vanadate Microcrystals for the Photocatalytic Conversion of Methane to Methanol. ACS Appl. Nano Mater. *1*, 6683-6691.

12. Villa, K., Murcia-López, S., Andreu, T., and Morante, J.R. (2015). Mesoporous WO_3 photocatalyst for the partial oxidation of methane to methanol using electron scavengers. Appl. Catal., B *163*, 150-155.

13. Villa, K., Murcia-López, S., Morante, J.R., and Andreu, T. (2016). An insight on the role of La in mesoporous WO_3 for the photocatalytic conversion of methane into methanol. Appl. Catal., B *187*, 30-36.

14. Xie, J., Jin, R., Li, A., Bi, Y., Ruan, Q., Deng, Y., Zhang, Y., Yao, S., Sankar, G., and Ma, D. (2018). Highly selective oxidation of methane to methanol at ambient conditions by titanium dioxide-supported iron species. Nat. Catal. *1*, 889.

15.   Linic, S., Christopher, P., and Ingram, D.B. (2011). Plasmonic-metal nanostructures for efficient conversion of solar to chemical energy. Nat. Mater. *10*, 911-921.

16.   Zhang, Y., He, S., Guo, W., Hu, Y., Huang, J., Mulcahy, J.R., and Wei, W.D. (2017). Surface-Plasmon-Driven Hot Electron Photochemistry. Chem. Rev. *116*, 2927-2954.

17.   Hao, C.-H., Guo, X.-N., Pan, Y.-T., Chen, S., Jiao, Z.-F., Yang, H., and Guo, X.-Y. (2016). Visible-light-driven selective photocatalytic hydrogenation of cinnamaldehyde over Au/SiC catalysts. J. Am. Chem. Soc. *138*, 9361-9364.

18.   Priebe, J.B., Radnik, J.r., Lennox, A.J., Pohl, M.-M., Karnahl, M., Hollmann, D., Grabow, K., Bentrup, U., Junge, H., and Beller, M. (2015). Solar hydrogen production by plasmonic Au-TiO$_2$ catalysts: impact of synthesis protocol and TiO$_2$ phase on charge transfer efficiency and H$_2$ evolution rates. ACS Catal. *5*, 2137-2148.

19.   Xiang, Q., Yu, J., and Wong, P.K. (2011). Quantitative characterization of hydroxyl radicals produced by various photocatalysts. J. Colloid Interface Sci. *357*, 163-167.

Chapter 7 General Conclusion and Future Prospects

7.1 General conclusion

In this thesis, the main work is to develop nanometals/semiconductors-based photocatalysts for efficient conversion of methane to higher-value chemicals and upgraded fuels such as hydrogen, carbon monoxide, methanol, and formaldehyde under mild conditions. The detaild study could be concluded in the following parts.

1. Visible-light-mediated methane activation for steam methane reforming over Rh/TiO_2 catalysts under mild conditions

TiO_2 supported Rh nanoparticles (NPs) catalysts were constructed for steam methane reforming under visible light irradiation at mild operating temperature (below 300 °C). Methane conversion was significantly enhanced over Rh NPs/TiO_2, with a ~50% decrease in apparent activation energy compared to that of pure thermal process. Femtosecond time-resolved infrared spectroscopic measurement and density functional theory calculation show an ultrafast separation of hot carriers at the Rh-TiO_2 interface, resulting in the formation of electron-deficient state of $Rh^{\delta+}$ at surface for the successive CH_4 activation at low temperatures. Wavelength-dependent activities and kinetic isotope experiments validate that the photoexcited hot carriers in the Rh nanoparticles play a critical role in facilitating the rate-determining steps, i.e., the cleavage of C-H bond in CH_4.

2. Light-enhanced carbon dioxide reforming of methane by effective plasmonic coupling effect of Pt and Au nanoparticles

Bimetal plasmonic catalysts consisting of Pt and Au NPs were developed for CRM reaction using UV-vis light illumination at 400 °C. The activation energy for CH_4 conversion are reduced ~30% below thermal activation energies and the reaction rate is 2.3 times higher than that of the thermocatalytic reaction rate. UV-vis absorption spectra and wavelength-dependent performances show that not only UV but also visible light play important roles in promoting CO_2 reduction because of effective local surface plasmon resonances (LSPR) coupling between Pt and Au NPs. Finite-difference time-domain (FDTD) simulations and in situ diffuse reflectance infrared Fourier transform

spectroscopy (DRIFTS) spectra results further reveal that the effective coupling LSPR effect generates strong local electric fields and produce high concentration of hot electrons to activate the reactants and intermediate species, reduce the activation energies and accelerate the reaction rate.

3. Visible light-promoted carbon dioxide reforming of methane over Pt/TaN catalysts

TaN was employed as an optical support to investigate the activities of its supported Pt and other group VIII metal catalysts in carbon dioxide reforming of methane (CRM) with visible light assistance at 500 °C. The activities of TaN supported group VIII metal-based catalysts were enhanced with visible light assistance, and the activity enhancement ratios (2.3-2.7 times) were much higher than that achieved by adopting expensive Au as plasmonic promoter to an optical-inert catalyst (1.6 times). Theoretical results reveal polarity of TaN is regarded to facilitate electron-hole separation and ultimately be responsible for the activity enhancement.

4. Direct photocatalytic oxidation of methane to liquid oxygenates with molecular oxygen over nanometals/ZnO catalysts

ZnO loaded with co-catalysts (Pt, Pd, Au or Ag) were constructed and can directly oxidize methane to methanol and formaldehyde using molecular oxygen as oxidant in pure water under mild light irradiation at room temperature. The activity for production of total liquid oxygenates including methyl hydroperoxide, methanol and formaldehyde on 0.1 wt% Au/ZnO reached approximately 12,545 micromoles per gram catalyst per hour ($\mu mol\ g^{-1}\ h^{-1}$), with 95% selectivity. Experiments with isotopically labeled oxygen and water reveal that molecular oxygen, rather than water, was the oxygen source of methanol formed. Experimental and theoretical results demonstrate that the photocatalytic oxidation of methane to liquid oxygenates is a radical process, and surface active oxygen (hole center, O^-) of photo-excited ZnO play the dominate role for the activation of methane to methyl radicals, a rate-limiting step for methane oxidation, with selectivity for methanol controlled by co-catalysts.

5. Selective photocatalytic oxidation of methane to methanol with molecular oxygen over nanometals/TiO$_2$ catalysts

Methane can be partial oxidation into methanol over 1.0 wt.% Pt, Pd, Au or Ag/TiO$_2$ photocatalysts with O$_2$ as an oxidant under light irradiation at room temperature. The activity for the

production of methyl hydroperoxide and methanol over the optimized photocatalysts amounts to 2,845 µmol g^{-1} h^{-1} with approximately 73.3% selectivity. The mechanism of photocatalytic methane oxidation over TiO$_2$ is through radical pathways, and molecular oxygen is indeed incorporated into the primary products. In addition, reducing the of ˙OH radicals generated in the reaction solution via the formation of Au with high valence state on the surface of TiO$_2$ is capable of avoiding the over-oxidation of the primary products to formaldehyde and carbon dioxide.

7.2 Future prospects

Although some achievements have been made in solar energy mediated conversion of methane to valuable chemicals and fuels over nanometals/semiconductors, research on the still remain in the primary stage, there are still a number of challenges towards the efficiency of methane conversion, the utilization of solar energy, the selectivity of targeted products and the mechanism of photo-activation of methane, which have to be solved, as discussed in the following.

First, although solar energy mediated methane conversion can proceed under mild conditions, the efficiencies of the reported processes are still low. One solution is to efficiently utilize solar light (i.e., UV, visible and infrared light) through the development of photocatalysts. It includes the development of semiconductor and plasmonic nanometals catalysts. Most of reported semiconductors for methane conversion are UV-responsive photocatalysts. The development of visible-light-active semiconductors is highly necessary. The reported plasmonic nanometals catalysts such as Au and Ni mainly absorb visible light for producing hot carriers. In addition, catalysts featured by black color have the ability to utilize visible and infrared light to photothermally heat catalysts. That is, semiconductor and plasmonic nanometals can utilize UV and visible light, whereas the apparently black catalysts can utilize the visible and infrared light. Therefore, by rationally designing multicomponent or multifunctional catalysts, the maximum utilization of solar light and efficient conversion of methane could be achieved simultaneously.

Second, the selectivity of photocatalytic methane oxidation to desired liquid products such as methanol and formaldehyde remains challenging since the reactivity of oxygenates is higher than that of methane under reaction conditions. Development of low-temperature or room-temperature photocatalytic conversion of methane in the liquid phase is a promising pathway to improve the

selectivity to oxygenates compared to that in the gas phase. The oxygenates absorbed on the catalyst surface in gas-phase reactions are prone to be deeply oxidized to CO_2. In contrast, in the liquid phase, water can facilitate the formation and desorption of oxygenates such as methanol to mitigate complete oxidation.[148] As photogenerated reactive oxygen species (such as O^- and $^{\bullet}OH$) can oxidize both methane and produced oxygenates, the design of multicomponent photocatalysts, in which one component is responsible for methane activation and the others for stabilizing products, is also a potential approach to improve the selectivity of methane conversion. Moreover, selective functionalization of methane to inert derivates through a radical reaction mechanism can be deemed a potential method for product protection in methane conversion, thus improving product selectivity.

Finally, at present, the mechanism investigations of methane activation and conversion both on semiconductors and plasmonic metal nanoparticles remain in the preliminary stages due to the complicated reaction pathways and the limited characterization techniques for photocatalytic reaction systems with a liquid phase as well as photothermal reaction systems with relatively high temperatures. C-H bond dissociation is regarded as the vital step for methane activation and conversion. However, few studies have been reported regarding the thermodynamic requirements of CB or VB potentials for methane conversion and the mechanism of photoinduced C-H bond cleavage on the surfaces of catalysts. In addition, the essence of the photogenerated reactive species over semiconductors responsible for C-H bond activation remains to be clarified in more detail. *In situ* characterization methods such as femtosecond time-resolved infrared spectroscopic measurement, X-ray absorption techniques, EPR and diffuse reflectance infrared Fourier transform spectroscopy could be employed to give a deep understanding of methane activation at the molecular level. Density functional theory calculations can be used to reveal the photoenergy-promoted methane conversion mechanism and explore the reaction pathways.

Acknowledgement

First of all, I would like to express my deep and sincere gratitude to my supervisor, Prof. Jinhua Ye for her continuous support and valuable suggestions both in my Ph.D. study and in my personal life. Prof. Ye gave me insightful direction about my research. Prof. Ye also help me analyze the experimental results, discuss research strategies and revise my research papers in the last three years. Her kind understanding, constant encouragement and helpful guidance made my achievements in my Ph.D. study.

Second, I am also very grateful to Dr. Tetsuya Kako. He gave me a lot of detailed and constructive suggestions on my research based on his abundant experience and knowledge of photocatalysis. His rigorous scientific attitude deeply impressed and influenced me. He also taught me a lot about Japanese culture. I want to thank Dr. Mitsutake Oshikiri. He also taught me a lot about photocatalysis, especially about density functional theory calculations. Their supports are very helpful and precious for my Ph.D. study.

Then, I would like to thank Dr. Xianguang Meng, who taught me a lot about the fundamental knowledge of photocatalysis and thermocatalysis. He also gave me a lot of advice for my research. Without his help, it would be difficult for me to finish my Ph.D. thesis. Then I want to thank the all members in Photocatalytic Materials Group in NIMS, Dr. Huimin Liu, Dr. Zhoujun Wang, Dr. Shengyao Wang, Dr. Li Shi, Dr. Xiao Hai, Dr. Hong Pang, Mr. Ichihara Fumihiko, Mr. Yunxiang Li, Ms. Haruna, for their help both in academics and life. I wish my warmest thanks to During Ph.D. course, provided me with best assistances in my experiments and daily life.

I would like to thank State Scholarship Fund by China Scholarship Council (CSC) to support me to pursue a doctoral degree in Japan.

Finally, I would like to thank my parents for their support. Their hard-working quality have always inspired me in my life. They are my most important life mentors. I also want to thank my brother, sister and my relatives for their constant support and encouragement in all my Ph.D. endeavors.